High-Compression-Ratio; Atkinson-Cycle Engine Using Low-Pressure Direct Injection and Pneumatic-Electronic Valve Actuation Enabled by Ionization Current and Forward-Backward Mass Air Flow Sensor Feedback

Submitted to:

US Department of Energy
Final Report

By:

Michigan State University
Harold Schock, Farhad Jaberi, Ahmed Naguib, and Guoming Zhu
&
Visteon Corporation
David Hung

March 31, 2008

DISCLAIMER

Table of Contents

1. Introduction

This report describes the work completed over a two and one half year effort sponsored by the US Department of Energy. The goal was to demonstrate the technology needed to produce a highly efficient engine enabled by several technologies which were to be developed in the course of the work. The technologies included:

1. A low-pressure direct injection system
2. A mass air flow sensor which would measure the net airflow into the engine on a per cycle basis
3. A feedback control system enabled by measuring ionization current signals from the spark plug gap
4. An infinitely variable cam actuation system based on a pneumatic-hydraulic valve actuation

These developments were supplemented by the use of advanced large eddy simulations as well as evaluations of fuel air mixing using the KIVA and WAVE models. The simulations were accompanied by experimental verification when possible.

The next sections describe the details of this effort

2. Development of a Forward-Backward Mass Air Flow Sensor (FBMAFS)

The goal of this component of the investigation is to develop a mass air flow sensor (MAFS) that is capable of measuring unsteady direction, reversing mass flow rate. The following information reviews these accomplishments.

2.1. Accomplishments

Three different Forward-Backward Mass Air Flow Sensor (FBMAFS) concepts were evaluated based on the use of hotwire velocity sensors. The first concept is based on the use of a Michigan State University, (MSU) patented idea [1] where an oscillating hotwire (OHW) is employed to detect the flow velocity magnitude and direction. The second concept, referred to as the dual-sensor concept, was conceived during the investigation and it employs two hotwire sensors that are mounted behind one another with very small spacing along the flow direction. The final idea, which was also created during the course of this study, employs a variable-area insert as a 'fluidic rectifier' to detect the flow direction. A patent application on this idea [2] (abbreviated as VI-FBMAFS) is currently pending. All sensor concepts were realized and evaluated in the laboratory under steady and unsteady flow conditions. The evaluation took place in the 14" x 14" wind tunnel and 1" jet facilities in the Flow Physics and Control Laboratory, as well as in the unsteady air-intake test facility in the MSU, Automotive Research Experiment Station (ARES), Energy and Automotive Research Laboratory (EARL). The results showed that both the OHW and VI-FBMAFS concepts were successful when implemented, using fast, laboratory hotwires. The advantage of the VI-FBMAFS over the OHW approach is that the former is inexpensive, robust and has no moving parts. Hence, the VI-FBMAFS is well suited for use in real applications. The bottle neck, however, for technology transfer is the availability of robust, hotwire sensors that have faster response than existing ones. Future research should focus on the development of such sensing technology, as well as further optimization of the fluidic rectifiers of the VI-FBMAFS.

2.2. Oscillating Hotwire FBMAFS

The OHW oscillates at high frequency (a few kHz) and small amplitude (a few micrometers) with/against the flow. The imposed oscillation results in sinusoidal modulation of the hotwire output voltage at the oscillation frequency. The phase of this modulation signal, relative to the oscillating motion of the wire, provides the flow direction, while the magnitude of the un-modulated signal yields the velocity, and hence, flow rate information. A piezoelectric based OHW that fits within an existing Ford MAFS was designed and constructed. Figure 1 displays the sensor module, before insertion, into a Ford MAFS. Proper magnitude and direction response of the sensor was verified under steady and unsteady direction-reversing flow conditions. The unsteady response is demonstrated in Figure 2.

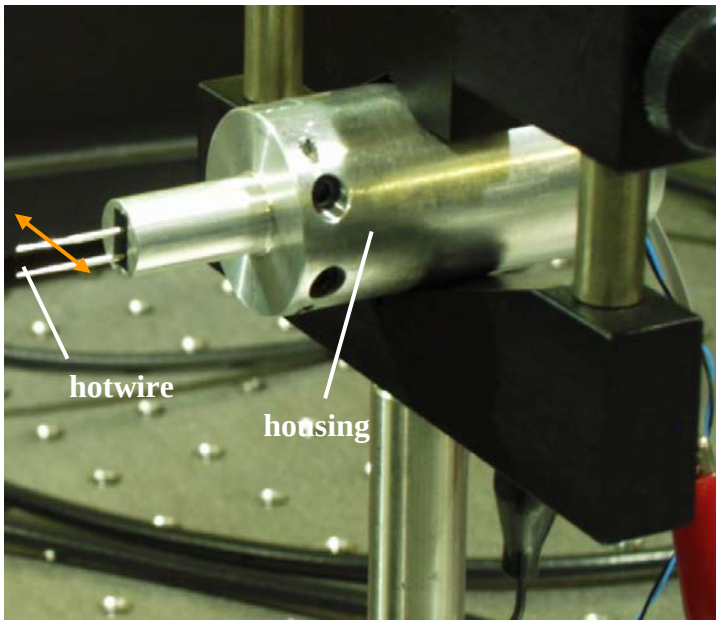

Figure 1. Image of the oscillating hotwire sensor used for engine research. Direction of oscillation is shown using orange, double-headed arrow. The oscillating mechanism is based on a cantilever piezoelectric mount that is embedded in the housing.

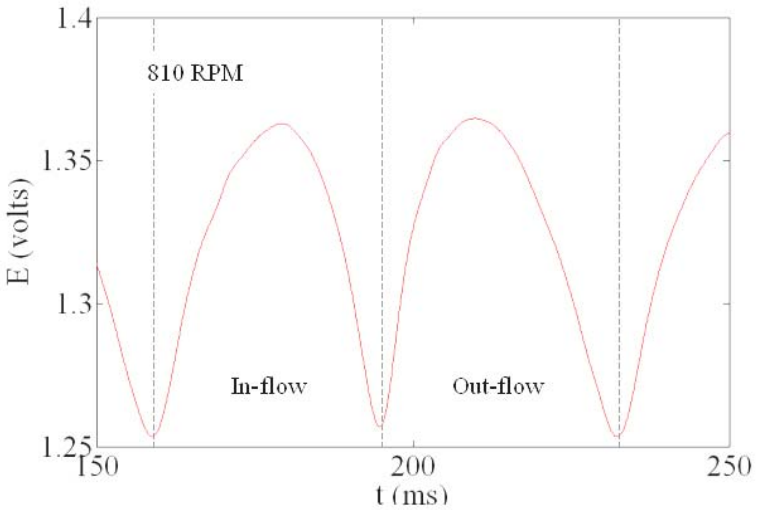

(a)

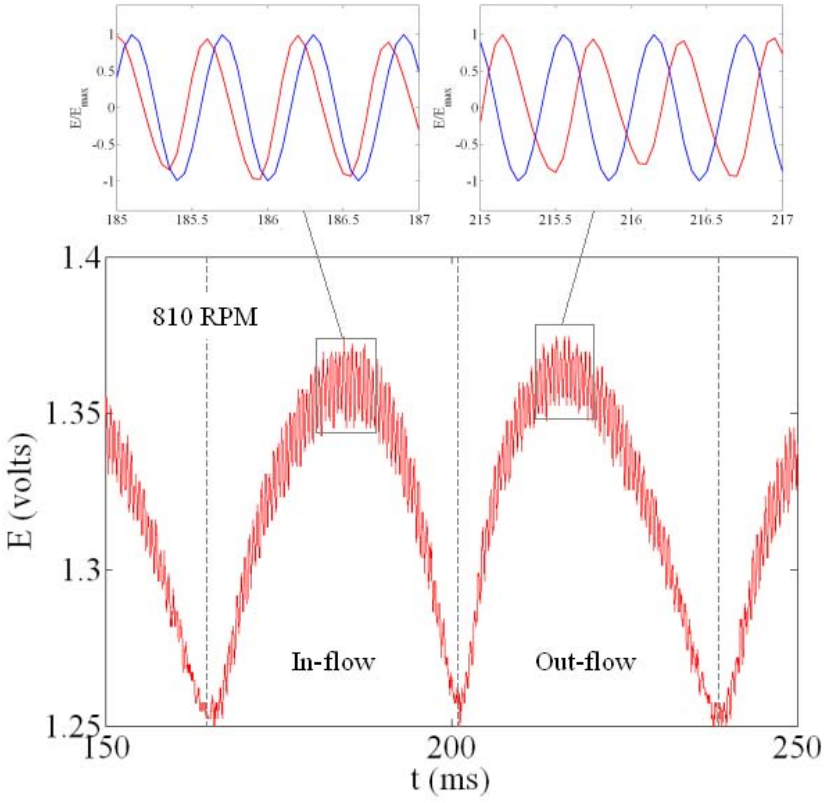

(b)

Figure 2. MAFS sensor output during one-cylinder, cold-engine operation at 810RPM: (a) conventional hotwire; (b) oscillating hotwire. Note the high-frequency (1675Hz) modulation signal seen in the oscillating sensor output. Close up view of this signal (top of part b) shows 180 degrees phase reversal (red line) relative to oscillation-driving signal (blue line) when the flow changes direction.

2.3. Dual-Sensor FBMAFS

In this concept, two hotwire sensors are mounted behind one another with very small spacing along the flow direction, as shown in Figure 3. Being in the wake of the upstream sensor, the downstream hotwire experiences less cooling by the airflow, generating a smaller output voltage than the upstream sensor. Thus, the sign of the difference between the voltage outputs from the two sensors can be used to provide the flow direction. On the other hand, the sum of the two voltages will be insensitive to the flow direction (assuming that the sensors are identical), and hence, it can be used to obtain the flow velocity magnitude. This concept remedies the need for the large-bandwidth sensors required by the OHW. More specifically, the OHW sensor oscillates at a frequency that is ten times larger or more than the frequency of unsteadiness of the intake air. To pick up these oscillations, the hotwire bandwidth needs to extend beyond 500Hz to properly measure the airflow unsteadiness at the fundamental frequency of an engine running at 3000RPM. Since the dual-sensor concept does not require such oscillations for its implementation, the hotwires' bandwidth needs to only extend beyond 50Hz.

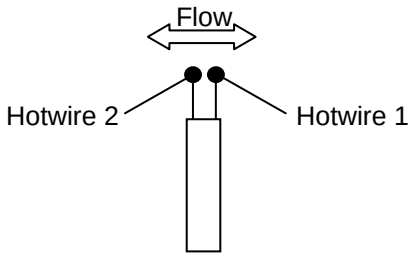

Figure 3. Dual-sensor concept

The dual-sensor idea worked quite well for measurement of the average-flow-velocity magnitude and direction (see Figure 4). Unfortunately, the same was not true when measuring the instantaneous velocity. The unsteady wake influence of the upstream sensor on the downstream sensor caused large variation in the instantaneous output of the downstream sensor. These variations were sufficiently large to cause errors in detecting the flow direction, as well as the velocity magnitude. There were two types of adverse wake effects: 1) thermal (caused by temperature fluctuations in the wake of the upstream sensor), and 2) hydrodynamic (caused by flow unsteadiness in the wake). It was possible to remedy thermal wake effects by incorporating a "shield" between the two sensors (Figure 5). However, the shield introduced its own hydrodynamic wake influences. To offset these, we experimented with various twists on the dual-sensor design, but none of these were successful.

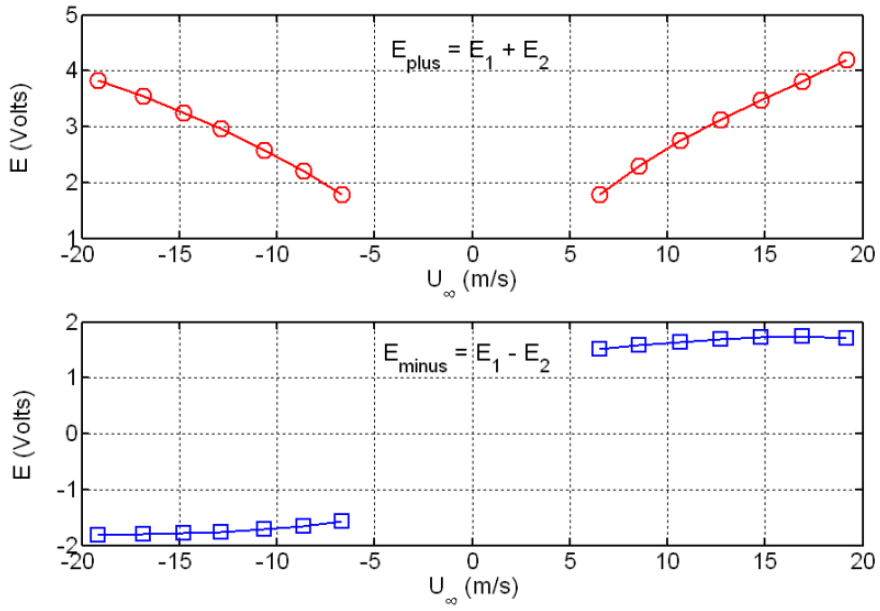

Figure 4. Steady response of the robust, dual-sensor probe: magnitude (top) and direction (bottom) response. Note the "flip" in sign of the difference between the two sensor outputs in response to flow-direction change.

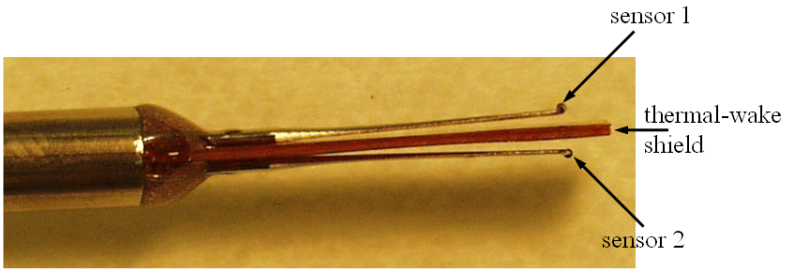

Figure 5. A picture of a dual-sensor probe fitted with provision to remedy thermal wake effects.

2.4. VI-FBMAFS

Here a 'fluidic rectifier' is employed to detect the flow direction. The rectifier consists of a nozzle (or diffuser, depending on the flow direction) that is fitted with a hotwire sensor at the center of the large area of the nozzle/diffuser. Figure 6 shows that if the flow is from right to left, the flow separates at the entrance of the diffuser (because of the steep angle of the diffuser) forming a jet. The hotwire is placed at the exit of the diffuser, which is typically about one diameter (d) downstream of the entrance; i.e., within the potential core, and hence the wire senses a velocity that is equal to or slightly faster than the free stream velocity. On the other hand, if the flow is from left to right, the flow accelerates through the nozzle. Since the velocity at the exit of the nozzle is approximately equal to the free stream velocity, the flow at the entrance will be lower than the free stream velocity by a factor equal to the area ratio (in the ideal case). For example, if an area ratio of 10 is utilized, the velocity sensed by the hotwire in the forward (left to right) will be more than order of magnitude smaller than in the backward direction; i.e., practically rectifying the flow through the nozzle/diffuser. The hotwire signal can be further conditioned to yield a 0/1 signal for forward/backward flow without ambiguity for flow velocities that are larger than 10% of the peak velocity. Larger area ratio could be used to lower the ambiguity threshold as desired.

The development effort of the VI-FBMAFS focused on optimizing the nozzle/diffuser geometry in order to achieve near perfect rectification.

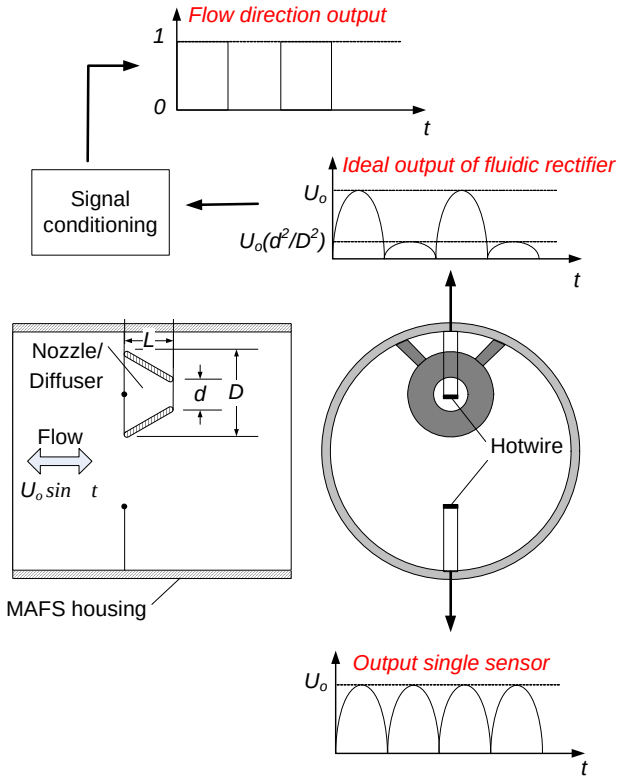

Figure 6. Illustration of the VI-FBMAFS concept.

For the purpose of optimizing the nozzle/diffuser geometry, three key parameters were considered. See Figure 7 for the schematic geometry showing these parameters.

- Area ratio (AR): $AR = D^2/d^2$ = 2, 4 and 8 were tested while keeping L = 5mm (where D is the large-area diameter, and L is the nozzle/diffuser length).
- Device length (L): L = "0" (washer), 2mm, 5mm and 10mm while keeping AR = 8 were tested.
- Straight extension on the large-area side: keeping AR = 8, a straight extension of 5mm length was used for devices with L = 5 and 10mm.

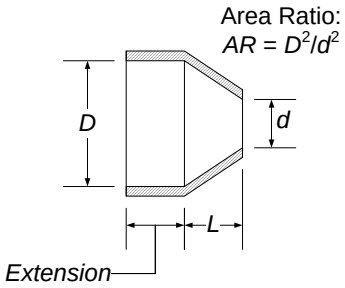

Figure 7. Geometry of the fluidic rectifier's nozzle.

The efficiency of the different nozzle/diffuser configurations in slowing down; i.e., rectifying, the flow in the forward direction, was tested. Figure 8 displays a plot of the velocity distribution along the streamwise direction on the centerline of the device for a steady flow in the direction of decreasing area. The vertical axis gives the measured velocity normalized by the free stream velocity (approx. 15m/s), and the horizontal one provides the streamwise distance (x) upstream of the small area, normalized by the small-area diameter. As expected, all results show deceleration of the flow to a minimum velocity followed by acceleration. The key question is: What is the smallest velocity (i.e., most effective slowing down of the flow) attained by each of the configurations? First, consider the red circles, blue triangles and purple diamonds. These cases represent nozzles with area ratio of 8, no extension, and length of "0", 5 and 10mm respectively. It is obvious that the longer the nozzle, the better the deceleration.

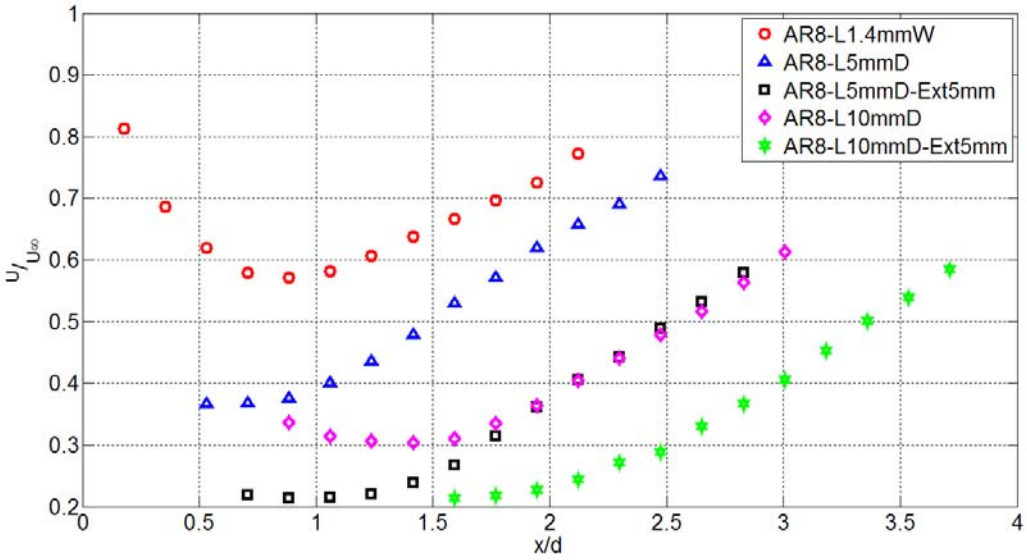

Figure 8. Streamwise distribution of the velocity on the centerline of the nozzle/diffuser.

However, even for the case with most deceleration, the minimum velocity remains higher than the theoretical minimum velocity of $1/AR$, or 0.125 in this case. The theoretical minimum can be approached by adding a 5mm extension, as seen in the cases represented by the black squares and green asterisks, where the minimum velocity is about 20% of the free stream velocity. Most interestingly, the data also show that the extension at the entrance may be more significant than the length of the nozzle, where the 5mm and 10mm long nozzles (black squares and green asterisks) perform equally well when both have an extension. Without the extension, the 10mm nozzle outperforms the 5mm nozzle (purple diamonds vs. blue triangles). All together, the results suggest that to attain the best possible rectification for a given area ratio, optimization of the nozzle profile is significant.

To examine the ability of the nozzle/diffuser to rectify the flow under unsteady, flow reversing conditions, experiments were conducted in the unsteady, air-intake facility. Sample time series are shown in Figure 9 for zero mean flow conditions (i.e. where the magnitude of the flow velocity through the facility is the same in the forward and backward direction). The time traces shown in this figure are obtained from nozzles with area ratio of 2 (red), 4 (blue) and 8 (black). As anticipated, the rectification effect of the device is evident when the peak velocity measured in one half of the cycle is lower than in the other half. It is also evident that the smaller peak gets smaller and the larger peak gets bigger; i.e., the rectification is enhanced, with increasing area ratio, demonstrating the controllability of the rectification

effect through area ratio change. Furthermore, by adding a 5mm extension at the entrance of the rectifier's nozzle, the rectification is further improved (see Figure 10)

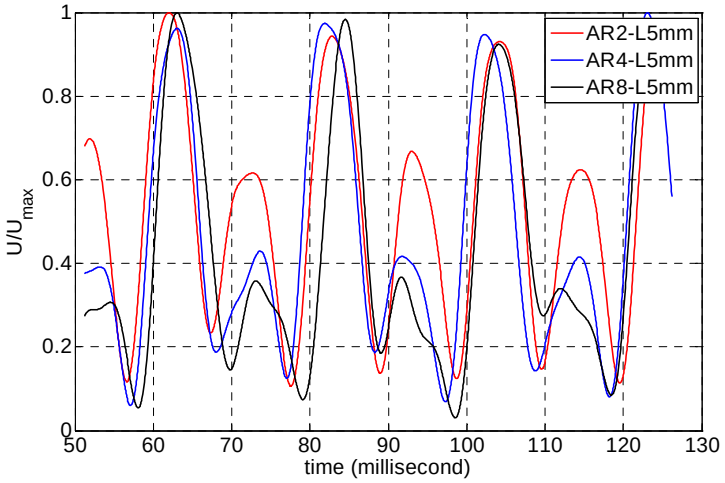

Figure 9. Sample hotwire signals under unsteady, direction-reversing flow conditions: Effect of the fluidic rectifier's area ratio. Area ratio - 2 (red), 4 (blue) and 8 (black).

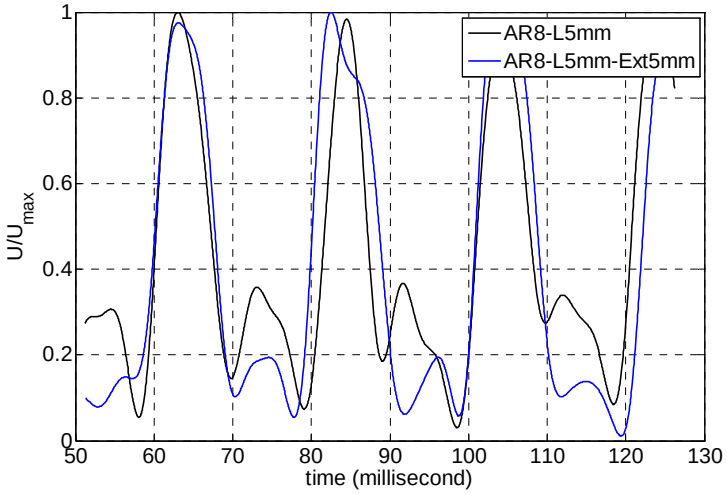

Figure 10. Sample hotwire signals under unsteady, direction-reversing flow conditions: Effect of the fluidic rectifier's extension length.

3. Injector Spray, In-Cylinder Fuel Mixture and Flame Combustion Visualization

The effect of spray pattern on fuel mixture preparation in a single-cylinder optical GDI engine under realistic speed and load conditions was documented. Four injector spray patterns were evaluated (Figure 11). Crank angle resolved images were taken using a newly acquired high-speed imaging system. Based on extensive image analysis, an optimal spray pattern was identified, which provided a good overall fuel distribution with minimal fuel impinged on the cylinder wall. A technical paper, based on the aforementioned research results, was written and submitted to the 2007 SAE World Congress [3].

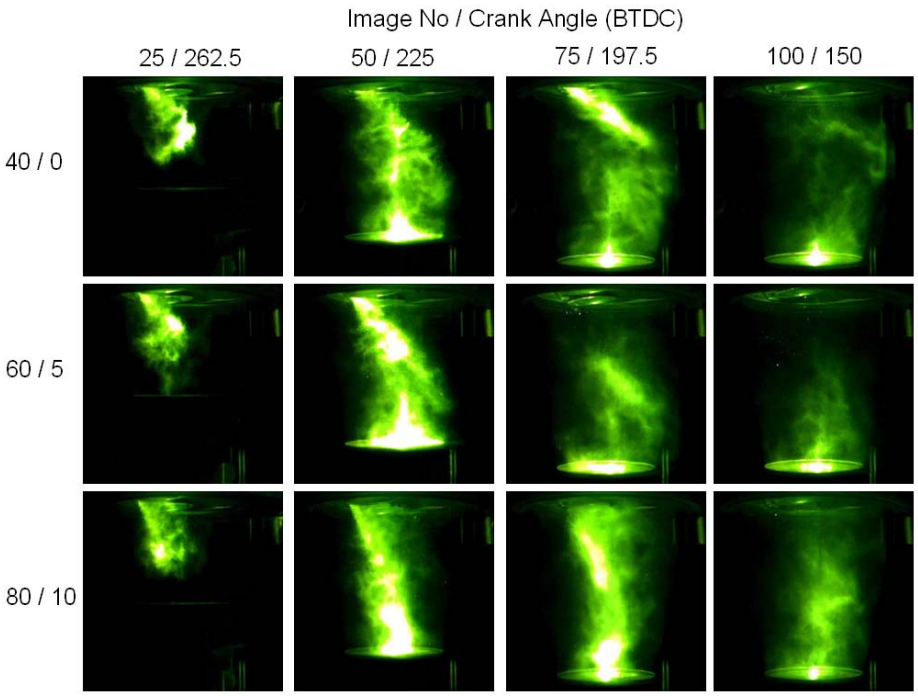

Figure 11. In-cylinder fuel mixture formation at 2500 RPM / WOT / 30 Bar Fuel Pressure/SOI at 300° CA BTDC.

In addition, high-speed visualization of in-cylinder flame distribution was achieved in a preliminary investigation. The color imagery allows the spray distribution, flame propagation, and fuel impingement to be studied in details. Both in-cylinder ionization and pressure data were also obtained in synchronization with the combustion images. The entire combustion event can be clearly visualized; from the beginning of spark ignition to flame propagation and to flame quenching at the cylinder wall. We believe that this is the first time that this specific combination of test data has ever been collected and evaluated simultaneously. We also developed a custom GUI (Graphical User Interface) to process the images. In Figure 12, the red line in the plot displays the image number (which can be related to crank angle) of the instantaneous combustion image with the corresponding pressure and ion voltage. The image depicts the premixed flame front (blue) propagating across the cylinder, with some small fuel-rich clusters (orange) scattered on the left side of the cylinder. Other test data can be extracted for further analysis.

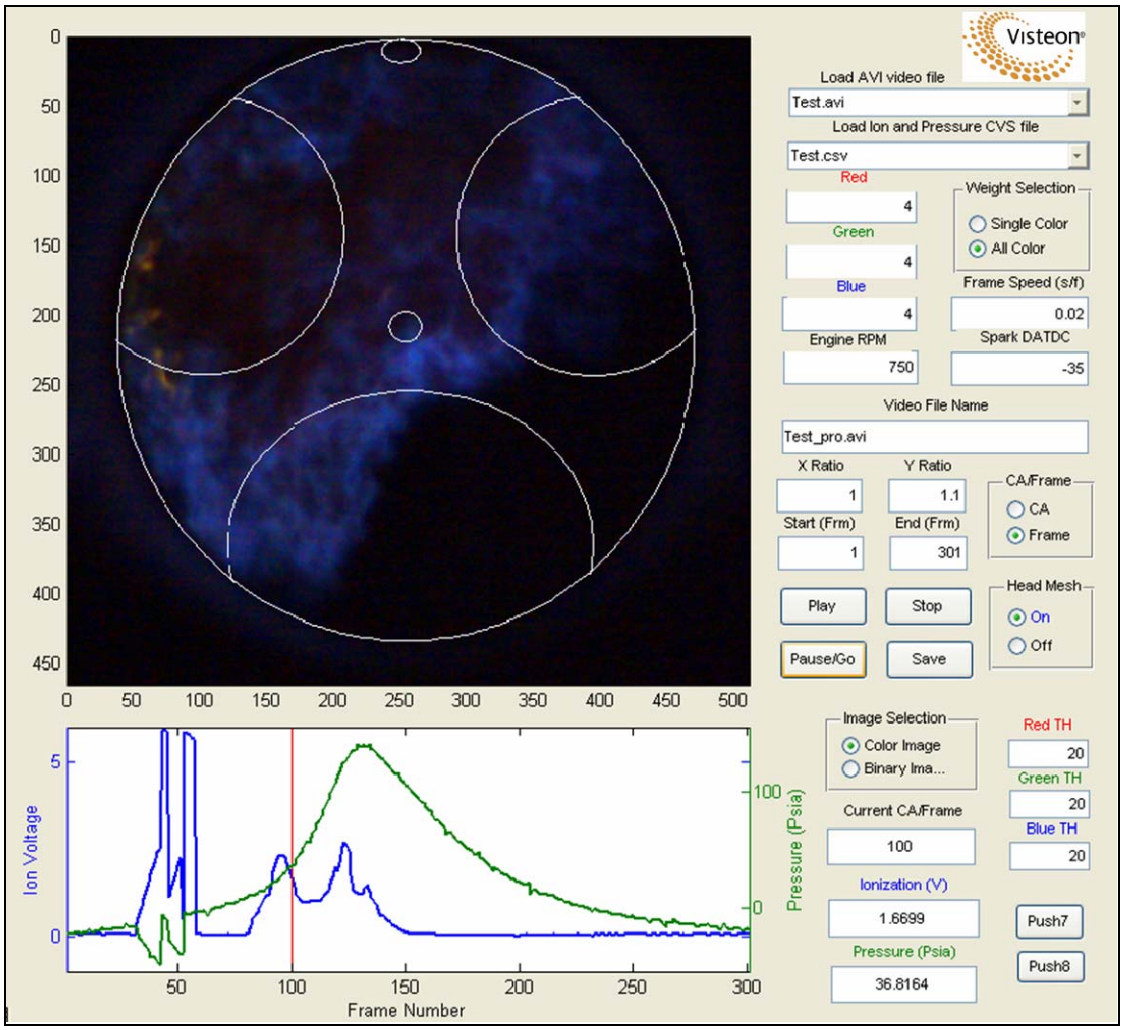

Figure 12. A schematic of custom-built GUI for flame image analysis. The combustion image with its corresponding pressure and ionization voltage data can be collected and evaluated simultaneously.

4. Large Eddy Simulation of Two-Phase Turbulent Reacting Flows in IC Engines

A new mathematical/computational methodology is developed and tested for large eddy simulation (LES) of turbulent flows in internal combustion (IC) engines. In this methodology, the filtered compressible Navier-Stokes equations in curvilinear coordinate systems are solved via a generalized, high-order; multi-block, compact differencing scheme and various subgrid-scale (SGS) stress closures. Both reacting and nonreacting flows with and without spray are considered. For nonreacting flows, the LES models have been applied to three flow configurations: (1) a fixed poppet valve in a sudden expansion, (2) a simple piston-cylinder assembly with a stationary open valve and harmonically moving flat piston, and (3) a realistic single-cylinder engine with moving intake and exhaust valves. The first flow configuration is the simplest one and is considered for studying the flow around the valves in IC engines and for the validation of LES and its SGS models. During the intake stroke of engine operation, large-scale unsteady turbulent flow motions are developed behind the intake valves that have significant effects on the flow field, mixing and combustion in the cylinder. The physical features of these turbulent motions and the ability of LES to capture them are studied and tested by simulating the flow around a fixed valve in the

sudden expansion geometry. The second flow configuration is closer to that in IC engines but is based on a single stationary intake/exhaust valve and relatively simple geometry. Nevertheless, it helps in better understanding of the effects of piston motion on the in-cylinder unsteady fluid motions and is considered here for further validation of our LES model. The third flow configuration includes all the complexities involved in a realistic single-cylinder IC engines such as the complex geometry and the moving valves and piston. The flow statistics predicted by LES are shown to compare well with the available experimental data. For the past few months we have worked on the modeling and simulation of spray and combustion in the MSU 3-valve engine. The spray combustion is simulated with the two-phase Filtered Mass Density Function (FMDF) method. Sample results obtained with LES/FMDF are presented in the report along with a brief description of the method.

4.1. Characterization of IC Engines

Internal Combustion (IC) engines are usually characterized by complex geometries, highly unsteady turbulent flows, shear layer and boundary layer instability, acoustic waves, spray and combustion. Additionally, the three-dimensional (3D) time-dependent in-cylinder turbulent flows in IC engines usually exhibit significant cycle-to-cycle variations [4]. Accurate numerical simulation of such flows requires a high fidelity turbulent flow solver with the ability to model complex geometries and deforming computational grids. Most of numerical results in the literature for in-cylinder flow/spray/combustion simulations have traditionally been based on Reynolds-averaged Navier-Stokes (RANS) models. RANS based models resolve the mean flow only and may not allow the prediction of cycle-to-cycle variations and phase-averaged flow statistics with usually simple (isotropic) turbulence models. Shortcomings of this type of models have been reported by some authors (see papers by EL Tahry and Haworth [5] for engine application of RANS models). However, due to transient nature, inherent unsteadiness, significant density/temperature variations and the presence of large-scale coherent vortical structures in these flows, large-eddy simulation (LES) models seem to be more promising than RANS models. In fact, more than 25 years ago Reynolds [4] suggested that the models based on spatial filtering is the best approach and should be used for in-cylinder flow/combustion calculations. However, it was not until 12 years after Reynolds suggestion that Naitoh et al. [6] reported the first application. In their simulations, Naitoh et al. used a coarse grid and a first-order Euler scheme for time differencing, a third-order upwind scheme for convective terms, and second-order central differencing for all other terms. The calculated SGS turbulence intensity was reported to be roughly 50 per cent of total turbulence intensity, indicating that their grid resolution was not sufficient for LES. Despite the limitations of their simulations, Naitoh et al. were able to capture the dynamics of large coherent structures. Other LES of IC engines have been reported by Haworth et al. [7]. Their simulations were performed using the Node-Centered Unstructured Topology, Parallel Implicit Advection (NO-UTOPIA [8]) scheme, which is at best second-order accurate in time and space. They used the standard SGS Smagorinsky model in their IC engine simulations. The simulated engine geometry was relatively simple, composed of an axisymmetric piston-cylinder assembly with a non-moving central valve and a low piston speed of 200RPM. Laser Doppler Anemometry (LDA) measurement of flow statistics for this simple engine was done by Morse et al. [9]. In another LES work, Haworth [10] used the boundary body force method [9] with orthogonal grids and several SGS stress models to simulate a two-valve Pancake-Chamber motored four stroke engine and the Morse et al. experiment [9]. Incompressible flow equations were discritized using second order spatial and third order temporal accuracy. Verzicco et al. [12, 13] used the boundary body force method in cylindrical grids to simulate Morce et al. experiment [9] at different Reynolds numbers. More recently, LES of an unsteady mixing process in a direct injection engine was conducted by Menon et al. [14] with a subgrid scale mixing model based on the one-dimensional linear-eddy model [15] and KIVA-3V [16] flow solver. In their simulations, liquid fuel mixing in the cylinder without combustion was investigated. The results obtained by LES were compared with those obtained by RANS and experimental data [9], and were found to be comparable with experimental data. Lee et al. [17] used the same SGS stress model to do LES of turbulent flow in a diesel engine. Moureau et al. [18] reported the application of the parallel

unstructured LES code to IC engines. It is second order finite volume and third order finite element convective schemes combined. In their first attempt, they simulated cold flow in a piston cylinder assembly. More recently, Dugue et al. [19] used industrial Star-CD code to study cycle-to-cycle variations in realistic IC engine configurations using both RANS and LES. They performed simulations for 5-10 cycles via RANS and LES and showed that volume averaged resolved turbulent kinetic energy calculated by LES increases in each cycle and slowly converges, but in RANS, as all turbulence is modeled, it is close to zero in all cycles. Rutland et al. [20] simulated turbulent combustion in an IC engine via a KIVA-based LES model. In their simulations, the KIVA-3V flow solver was used together with the one-equation SGS stress model of Menon [15], the dynamics structure model, and a CHEMKIN-based combustion model. Their simulations of flow in a CAT 3401 engine indicate that the LES models are able to predict some cycle to cycle variations, which the RANS model is unable to do. They also compared the heat release rate profiles as obtained by LES and RANS with the corresponding experimental data, and found that the LES results were closer to experimental data than those obtained by RANS. For more information on previous LES of IC engines see the recent review by Celik et al. [21].

In this work, three test cases were simulated with our newly developed high order LES model. Validation of the developed LES solver in complex geometries with moving grids was done in the first two test cases, and comparison of LES results for the last test case with experimental data will be presented in future papers. The Eulerian velocity field is calculated by generalized multi-block fourth order compact differencing for spatial derivatives and third order Runge-Kutta for the temporal derivatives. The predicted SGS turbulent viscosity in LES, which is smaller than the value estimated by RANS, can be highly affected by numerical viscosity. Numerical viscosity can become a serious issue in low order and especially in upwind schemes. For this work, we have only used high order schemes. The first test case considered is the flow around a poppet valve in axisymmetric sudden expansion geometry. This case helps in understanding the complex flow around and behind an intake valve during the intake stroke of real IC engines and is considered here for validation of LES model. Thobois et al. [22] used a second order Lax-Wendroff central differencing LES solver to simulate this problem. The second test case considered is the one simulated by Haworth et al. [7] and described briefly above. The geometry is somewhat closer to the first test case, but because of having a moving piston, it may be considered to be closer to realistic IC engines. The last test case considered is the flow in a 3-valve laboratory direct-injection spark-ignition (DISI) engine, built at the MSU, Automotive Research Experiment Station (ARES). This type of engines has been considered for the potential of generating low emission. Work is in progress to develop experimental data with the controlled and well-defined flow conditions for model validation.

4.2. Without Spray and Combustion - Governing Equations

The conservative form of filtered compressible Navier-Stokes equations in curvilinear coordinates system can be written in the following compact form

$$\frac{\partial (JU)}{\partial t} + \frac{\partial F}{\partial \xi} + \frac{\partial G}{\partial \eta} + \frac{\partial H}{\partial \varsigma} = JS_o \qquad (1)$$

where $J = \dfrac{\partial (x, y, z)}{\partial (\xi, \eta, \varsigma)}$ is the Jacobian of transformation, $U = (\rho, \rho u_i, \rho E)$ is the solution vector,

F, G, H are convection, diffusion and pressure terms, and S_o is the source term. The subgrid stress terms, which are appeared in equations after filtering, were closed by the Smagorinsky model. Total stress tensor is:

$$\tau_{ij} = -2(\mu + \bar{\rho}\nu_t)(\bar{S}_{ij} - \frac{1}{3}\bar{S}_{kk}\delta_{ij}) \qquad (2)$$

where μ is molecular viscosity and turbulent kinematic viscosity

$$\nu_t = (C_d\Delta)^2\left|\bar{S}\right| \qquad (3)$$

C_d is Smagorinsky model constant which varies between 0.1 and 0.2 or a dynamic procedure is used to calculate it, and $\Delta = (volume)^{1/3}$ is the filter size, and

$$\left|\bar{S}\right| = (2\bar{S}_{ij}\bar{S}_{ij})^{1/2} \qquad \bar{S}_{ij} = (\frac{\partial\bar{u}_i}{\partial x_j} + \frac{\partial\bar{u}_j}{\partial\bar{u}_i}) \qquad (4)$$

For dynamic computation of C_d, the smallest resolved scales are sampled [20]. SGS stress part of total stress tensor in equation (2) is written as:

$$\tau_{ij} - \frac{1}{3}\delta_{ij}\tau_{kk} = 2\bar{\rho}C_d\Delta^2 \mid \bar{S} \mid \bar{S}_{ij} \qquad (5)$$

and the subtest-scale stress is approximated by:

$$T_{ij} - \frac{1}{3}\delta_{ij}T_{kk} = 2\hat{\bar{\rho}}C_d\hat{\Delta}^2 \mid \hat{\bar{S}} \mid \hat{\bar{S}}_{ij} \qquad (6)$$

by subtracting the test-scale average of τ_{ij} from T_{ij} and minimizing its error using least squares approach [23], the C_d is evaluated as:

$$C_d = \frac{L_{ij}M_{ij}}{2M_{kl}M_{kl}} \qquad (7)$$

where L_{ij} and M_{kl} are second order tensors and calculated using the LES filter velocity field:

$$L_{ij} = \overline{\hat{u}_i u_j} - \hat{\bar{u}}_i\hat{\bar{u}}_j \qquad (8)$$

$$M_{ij} = \hat{\bar{\rho}}C_d\hat{\Delta}^2 \mid \hat{\bar{S}} \mid \hat{\bar{S}}_{ij} - \bar{\rho}C_d\Delta^2 \mid \bar{S} \mid \bar{S}_{ij} \qquad (9)$$

In order to avoid computational instability due to large value of calculated C_d, some averaging is necessary. Germano et. al. [23] averaged denominator and numerator of their derived equation for Cd over plates parallel to lower boundary to avoid singularity. And for general cases, they recommended local time and space averaging. In work, in addition to parallel plates averaging, local filtering of denominator and numerator of equation (7) was done and obtained results for both methods were compared.

The first term in the left hand side of equation (1) can be calculated using chain rule as:

$$\frac{\partial(JU)}{\partial t} = J\frac{\partial U}{\partial t} + U\frac{\partial J}{\partial t} \qquad (10)$$

Time derivative of Jacobian in fixed grid system is zero, but in the case of moving grid system this term should be added to governing equations to eliminate metric cancellation [22]. In order to calculate this term geometric conservation law (GCL) [22,23] was adopted:

$$\frac{\partial J}{\partial t} = -[(\hat{\xi}_t)_{\xi} + (\hat{\eta}_t)_{\eta} + (\hat{\varsigma}_t)_{\varsigma}] \qquad (11)$$

where

$$\begin{aligned} \hat{\xi}_t &= -[x_\tau(\hat{\xi}_x) + y_\tau(\hat{\xi}_y) + z_\tau(\hat{\xi}_z)] \\ \hat{\eta}_t &= -[x_\tau(\hat{\eta}_x) + y_\tau(\hat{\eta}_y) + z_\tau(\hat{\eta}_z)] \\ \hat{\varsigma}_t &= -[x_\tau(\hat{\varsigma}_x) + y_\tau(\hat{\varsigma}_y) + z_\tau(\hat{\varsigma}_z)] \end{aligned} \qquad (12)$$

(x_τ, y_τ, z_τ) is the grid speed vector which can be calculated analytically based on piston or intake/ exhaust valves speed.

4.3. Test Cases

As mentioned before, the LES model was applied to three flow configurations: (1) a fixed poppet valve in a sudden expansion, (2) a simple piston-cylinder assembly with a stationary open valve and harmonically moving flat piston, (3) a realistic single-cylinder engine with moving intake and exhaust valves and pistons, built at Michigan State University, Engine Research Laboratory. For each test case, schematic configuration and generated grids are illustrated and comparison of the predicted results and available experimental data are presented and discussed.

4.4. Flow Around a Poppet Valve

During the intake stroke in an IC engine, high vortical flow motions, which develop behind the intake valves have, significant effect on the flow field in the cylinder. As a first test case, the LES ability to capture these fluid motions was tested by simulating the flow in sudden expansion geometry with a fixed popper valve with 10 mm lift. The geometry details are shown in Figure 13. LDA data for this flow configuration are available [27]. For this problem, a 5-block grid system was generated. The 3D and 2D cross section of the grid is shown in Figure 14. Mean streamlines in a 2D cross section at the center line are shown in Figure 15. In order to avoid singularity in the center line of the cylinder a rectangular block was fitted. The mass flow rate was kept constant at 0.05kg/s and the Reynolds number was fixed at 30,000. Simulation was done with both dynamic and static Smagorinsky models. The results shown in Figure 15 confirm the generation of two large-scale vortical structures behind the valve. To make a quantitative comparison with the experimental data, the mean axial velocity and the root mean square values of the axial velocity at two locations, 20 and 70mm from the cylinder head were calculated and compared with the experimental data in Figure 16. Mean velocity values were calculated by time-averaging of the filtered velocities for about 0.03 second of physical time. Figure 16 shows that the mean axial velocity obtained with the dynamic model and local filtering of equation (8) was in good agreement with the experimental data. The RMS of axial velocity calculated with the same procedure also compares reasonably well with the LDA laboratory data in the middle of the cylinder and behind the poppet valve as shown in Figure 16 (between r/R=0 to r/R=0.5). The differences in the region close to the cylinder wall (between r/R=0.5 to r/R=1.0) can be attributed to not using a wall function and insufficient averaging process. Mean and rms values computed with constant coefficient Smagorinsky model with Cd = 0.12 in both distances from cylinder head are dissipative in compare with LDA data.

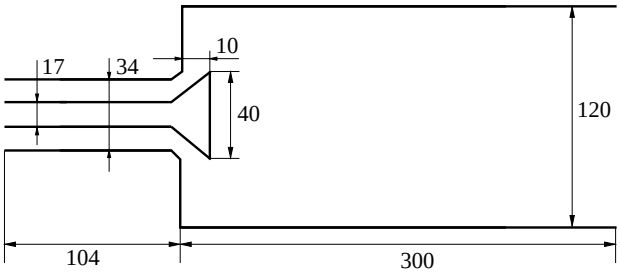

Figure 13. The geometrical details of the first test case (sudden expansion with fixed valve) considered in this study for validation of LES model. There is no piston and the valve is fixed.

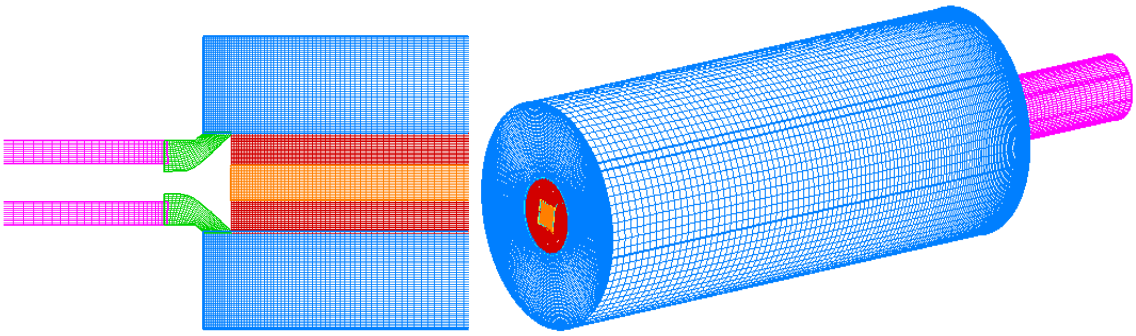

Figure 14. Two-dimensional top view and three-dimensional side view of the 5-block grid system for the sudden-expansion plus valve flow configuration.

Figure 15. Two-dimensional view of mean streamline profiles of the flow around the popper valve in sudden-expansion configuration.

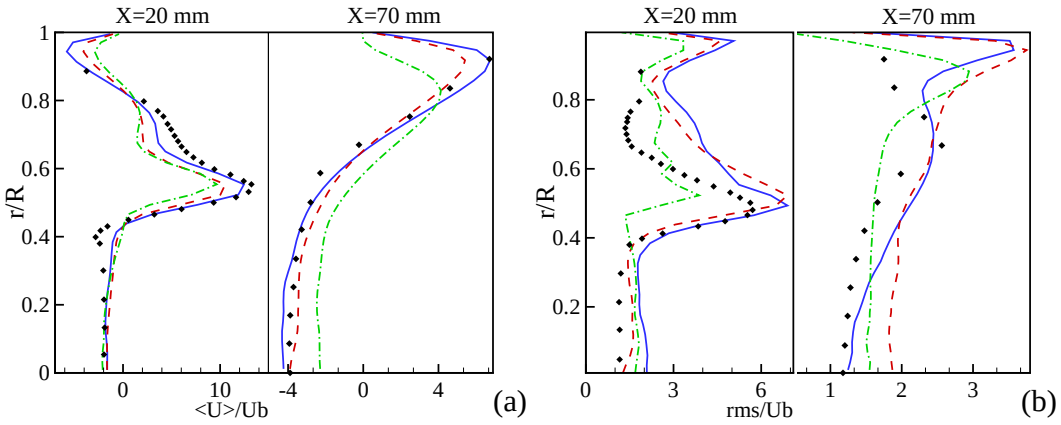

Figure 16. Mean axial velocity and RMS of axial velocity normalized with the bulk velocity. Solid lines and dashed lines are LES results with dynamic and static Smagorinsky (Cd = 0.1) respectively, and symbols are LDA data.

4.5. Simple IC Engine with One Intake/Exhaust Valve

As a second test case, the in-cylinder flow field in a piston-cylinder assembly was simulated via LES. The geometrical features of this idealized engine are shown in Figure 17. The piston is not shown. The engine is made of a fixed intake/exhaust valve with a piston that moves with simple harmonic motion and low RPM of 200. Average piston speed (Vp) is 0.4 m/s and the Reynolds number is 2000. Morse et al. [9] measured the radial profiles of the phase-averaged mean and RMS of axial velocity by LDA method. As mentioned in introduction, LES of this problem was conducted by some authors with a method very different from ours. Here, we have simulated the flow in this idealized flow configuration for further validation of the LES flow solver and SGS stress models. The generated 4-block grid system for this problem is shown in Figure 14. Simulation was initiated with zero velocity and continued for five cycles.

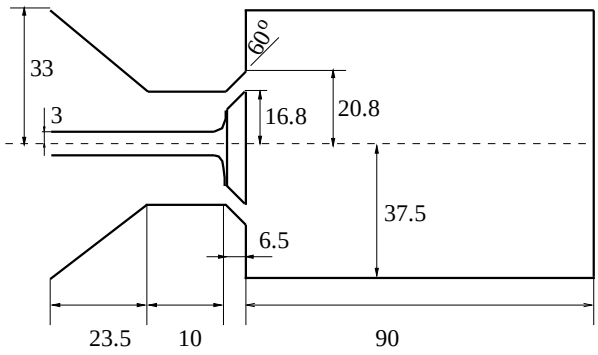

Figure 17. Morse et al.[9] Geometrical details of the second test case (cylinder-piston assembly with fixed valve) considered for validation of LES model. The piston is not shown.

Devesa et al. [28] used some initial conditions to avoid multiple cycle simulation. They simulated jet/tumble interaction as a phenomenon in IC engine. Here, we started with stationary condition and let the perturbations generated by the governing equations during the cycles. Constant pressure was set as inlet boundary condition. As piston started to accelerate downward, flow around the fixed valve accelerates and enters the cylinder like a jet flow. As the flow reaches the wall, the major portion of the jet is reflected downward toward the piston and a substantial fraction of that is recirculated back to the

cylinder head. Another smaller recirculating flow appears at the upper corner of the cylinder. This smaller vortex, which rotates in the opposite direction, persists until some crank angle before piston reaches to bottom dead center (BDC). As piston decelerates near BDC, the vortices become unstable and break up. Because the piston and therefore grids are moving, mean (time-averaged) velocity and its rms are obtained by averaging filtered velocity samples from specific crank angle over several cycles. Required data for any position in a specific crank angle in a cycle were gathered, and then mean velocities were calculated by ensemble or phase averaging of every cycle. Because of high computational cost, the number of simulated cycles is limited. This limits the accuracy of the averaging process. In this problem, the axisymmetric geometry configuration permits averaging in the azimuthal direction as well. For any radial position in each cycle, mean axial velocity and its fluctuations were calculated by azimuthally averaging filtered velocity. Ensemble or phase averaging of calculated values over some cycles produces mean axial velocity and its rms. The radial profiles of azimuthally and phase averaged axial velocity and rms of axial velocity at locations of 10, 20 and 30mm from the cylinder head are shown in Figure 19.

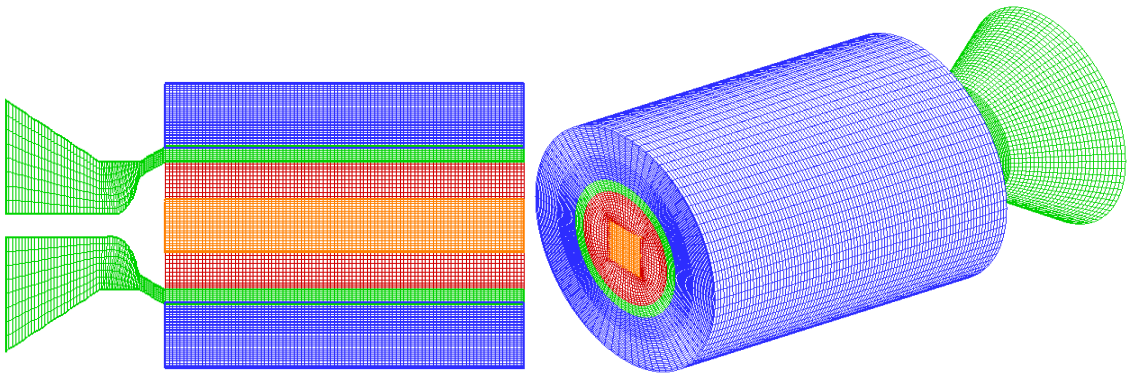

Figure 18. Two-dimensional (left) and three-dimensional (right) view of the 4-block grid system for the second test case. The piston is not shown.

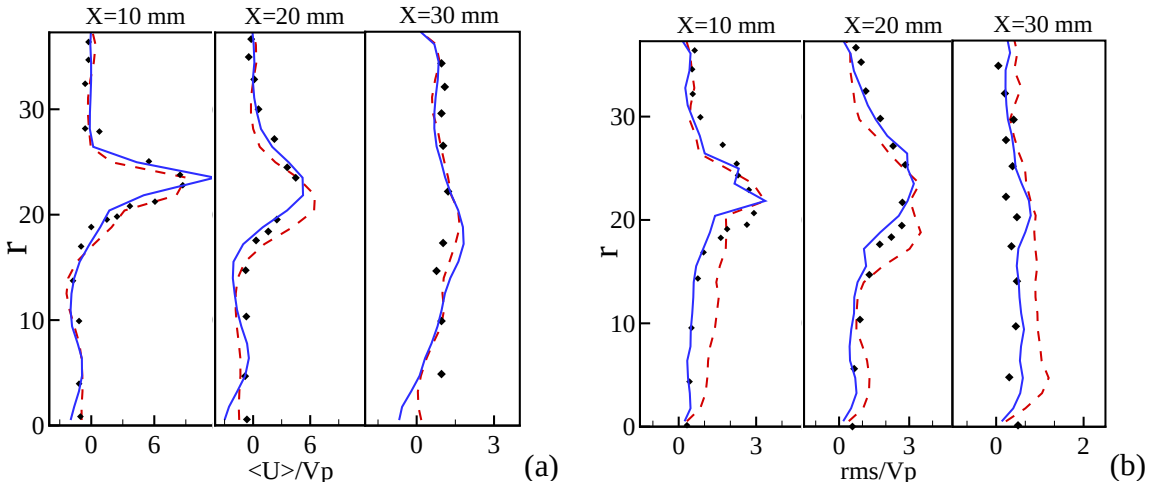

Figure 19. Mean axial velocity (a) and rms of axial velocity (b), normalized by the mean piston speed, at crank angle of 36°. Solid lines and dashed lines are LES results with dynamic procedure and constant coefficient Cd = 0.1, respectively, and symbols are LDA data.

The crank angle is 36°. The mean axial velocity computed with both static and dynamic Smagorinsky model are in good agreement with the experimental data. The dynamic procedure predicted the rms values better than the static Smagorinsky and they are in good agreement with LDA data. Also, in Figure 20, the mean and rms values of the axial velocity at every 10mm from cylinder head when crank angle was 144° are shown. Predicted axial mean velocities are in good agreement with LDA data. The LES is also able to capture the variation in the rms of the axial velocity. The two test cases reported above have some geometrical and flow features of realistic engines and are simulated here to assess the capabilities of the LES flow solver and its moving mesh technique. It is clear that the LES method is indeed able to predict the flow in these configurations. This gives us enough confidence to apply the model to more complex and more realistic engines.

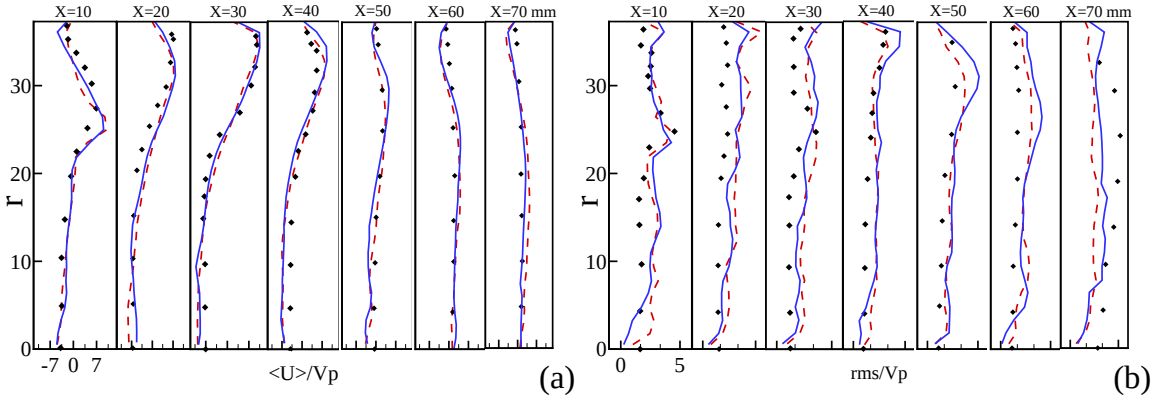

Figure 20. Mean axial velocity (a) and rms of axial velocity (b), normalized by the mean piston speed, at crank angle of 144°. Solid lines and dashed lines are LES results with dynamic procedure and constant coefficient Cd = 0.1 respectively, and symbols are LDA data.

4.6. Flow in a Real Internal Combustion Geometry

Here, we have considered the in-cylinder flow in a 3-valve IC engine that is built by our experimental group. This engine configuration is shown in Figure 21. It is a DISI engine which works with two intake and one bigger exhaust valve. In order to improve mixing during the intake stroke, intake valves were tilted. The same job was done for exhaust valve for helping the better discharge of burnt gases. This engine is tested in the fixed RPM equal to 2500. Mean piston speed during one stroke at that RPM is 8.82m/s. The maximum valve lift for intake and exhaust valves is 11 and 12mm respectively. To have a high quality grid for a moving piston, complex cylinder head and moving valves, a unique multi-block grid system is developed for the MSU 3-valve laboratory engine. A high quality grid system is required for accurate LES calculations. Inside the cylinder, the grid was made out of 31 initial parts. The 31 parts were then merged to form a nine block grid system, as shown in Figure 22 (left). In this grid system, each valve has a separate block to move in/out and there are three blocks for three intake/exhaust valves and the corresponding manifolds. Adding the valves and manifolds grid to cylinder grids, 18-block grid system was made, as shown in Figure 22 (right). Also, in order to show the grid for the valves and the position of the valves in the 18-block grid, cross sections of the grid at intake valve section and at center plane are shown in Figure 10 (center). In real engines, valve lifting is done by cam shaft. In this process, valve shanks cross the manifolds walls and come out as shown in Figure 21.

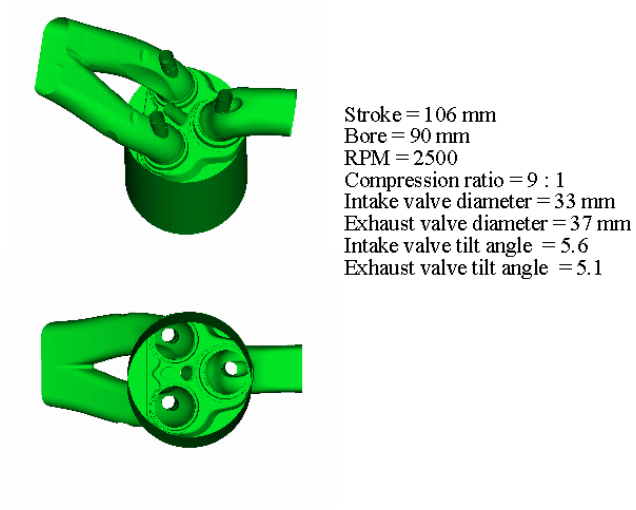

Figure 21. MSU 3-valve IC engine configuration.

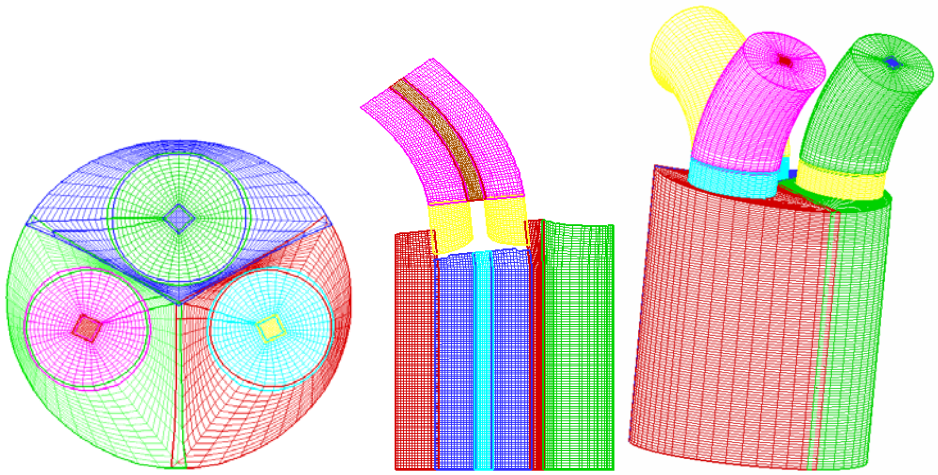

Figure 22. Two-dimensional top view (left), side view (center) and three-dimensional view (right) of the 18-block grid system for MSU 3-valve IC engine configuration.

For both keeping the grid quality high and simplicity, valve shanks were considered short. This simplification is shown in Figure 22 (center). As valves moves up and down, their corresponding blocks moves with different velocity (relative velocity of valve and piston) than the surrounded blocks which move with the piston speed. Therefore, overlap grids are no longer aligned and some interpolation for transferring the data between blocks is required. For standard car engines, the integral scale is about 1 mm at TDC [30, 31]. Accurate LES simulation of IC engines should have filter sizes smaller than those length scales. Here, it was tried to generate grid to have the satisfactory filter size. Dugue et al. [19] calculated Kolmogorov time scale in an IC engine with k-ϱ method, and found out that 5.56.10−6 is considerably lower than Kolmogorov time scale. In this problem, time steps were calculated based on CFL condition equal to one. Averaged time step during one cycle is about 1.5.10−7. A close examination of the 2D and 3D contours of velocity, vorticity, pressure, and temperature fields indicate that the results generated by the 18-block grid-system and the LES flow solver are physically sound and reliable. In Figures 23-26 contours of axial velocity in two planes (a): horizontal cross section with 20mm distance from cylinder head, (b): vertical cross sections from one intake valve center line.) are shown when the crank angles are

110^{o}, 145^{o}, 270^{o} and 560^{o} respectively. In this crank angle the intake valves are in maximum lift position. When crank angle is 110^{o}, valves are in maximum lift position, and in crack angle equal to 145^{o}, piston is decelerating downward while valves are closing; flow is still coming into the cylinder with high momentum. In both crank angle 110^{o} and 145^{o}, two vertical flow are present below the two intake valves, and maximum velocity of the flow are in the space between cylinder wall and intake valves rim. Two vortical flow structures are still present during the mid-compression stroke (Figure 25). Figure 26 shows the mid-exhaust stroke, in-cylinder flow is accelerating out of cylinder by piston passing through the exhaust valve and manifold.

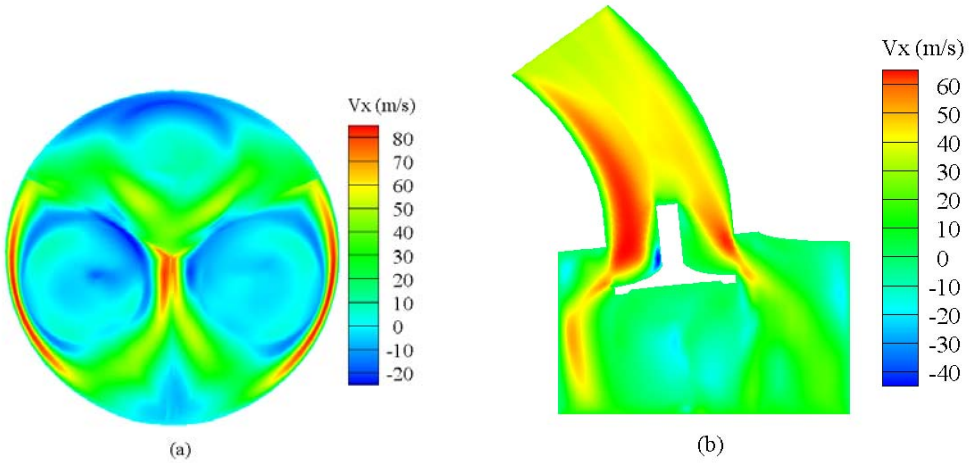

Figure 23. Axial instantaneous velocity in two-dimensional cross sections when crank angle is 110^{o}, (a): Y-Z plane in a distance 20 mm from cylinder head and, (b) X-Z plane from one intake valve center line.

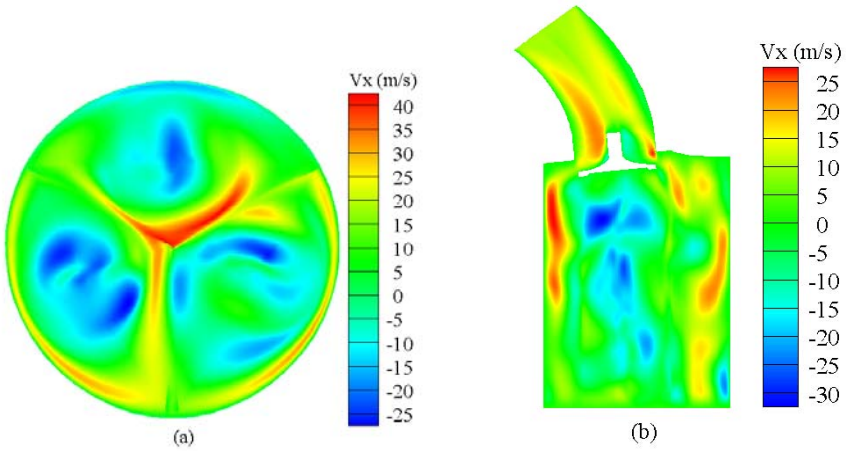

Figure 24. Axial instantaneous velocity in two-dimensional cross sections when crank angle is 145^{o}, (a): Y-Z plane in a distance 20 mm from cylinder head and, (b) X-Z plane from one intake valve center line.

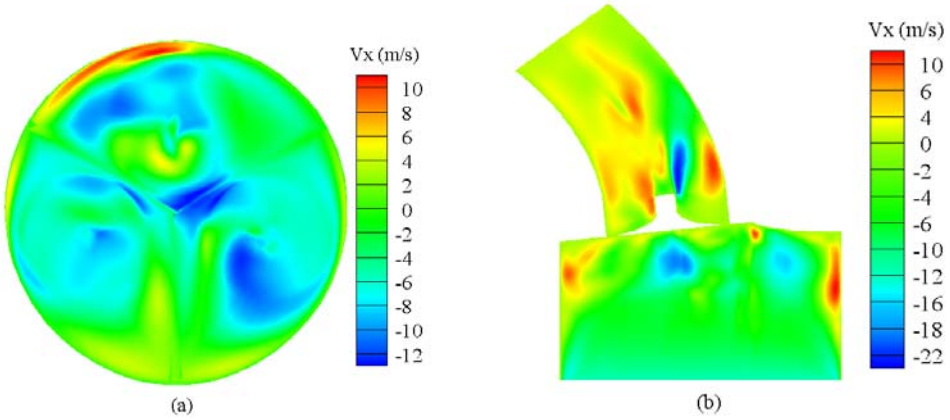

Figure 25. Axial instantaneous velocity in two-dimensional cross sections when crank angle is 270^{o}, (a): Y-Z plane in a distance 20mm from cylinder head and, (b) X-Z plane from one intake valve center line.

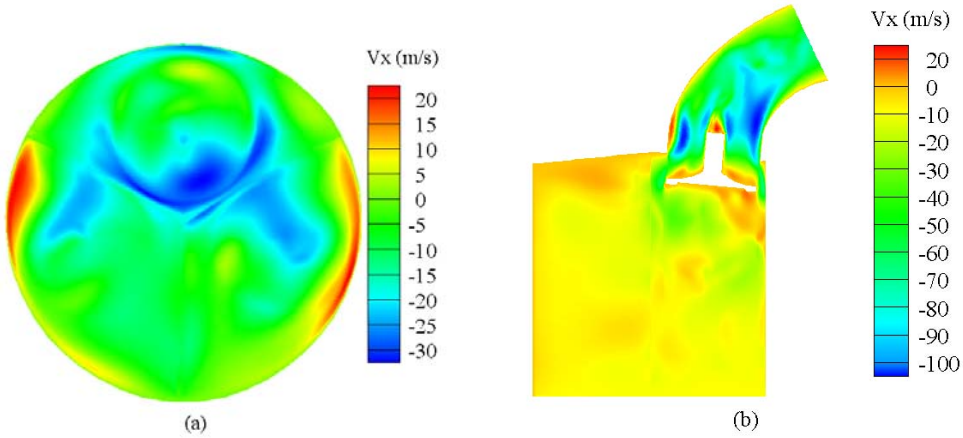

Figure 26. Axial instantaneous velocity in two-dimensional cross sections when crank angle is 560^{o}, (a) Y-Z plane in a distance 20mm from cylinder head and, (b) X-Z plane from one intake valve center line.

4.7. Spray and Combustion - LES/FMDF for Two-Phase Turbulent Reacting Flows

As mentioned before, the two-phase LES/FMDF model is based on an Eulerian-Lagrangian-Lagrangian mathematical/numerical methodology and can handle the two-way interactions between particle and fluid phases. The two-way and particle-particle interactions for low particle to fluid volume fraction ratio are also included. Figure 27 shows various elements of the model and its computational flow solver in a block diagram. The gas-phase part of the model is based on a high-order compact finite-difference numerical scheme. The subgrid gas-liquid combustion is modeled with the two-phase scalar Filtered Mass Density Function. The spray is simulated with a non-equilibrium Lagrangian model and stochastic SGS closures on mass, momentum, and energy coupling between phases are implemented through series of source/sink terms. The LES/FMDF employs variety of different fuels based on two combustion models: (1) a finite rate, reduced chemistry model for non-equilibrium flames, or (2) a near equilibrium model

employing detailed kinetics. In (1), system of nonlinear ordinary differential equations (ODEs) is solved together with the FMDF equation for all the scalars (mass fractions and enthalpy). Finite-rate chemistry effects are explicitly and "exactly" included in this procedure since the chemistry is closed in the formulation. In (2), the LES/FMDF is employed in conjunction with an equilibrium fuel-oxidation model. This model is enacted via "flamelet" simulations which normally consider a laminar counterflow (opposed jet) flame configuration. For two-phase flow calculations only non-equilibrium models based on (1) are used.

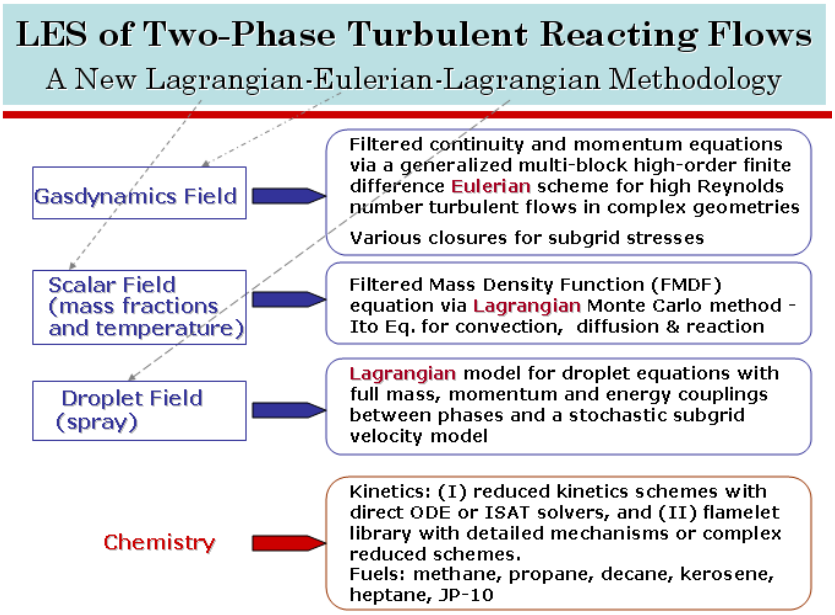

Figure 27. A block diagram showing different components of the LES/FMDF and its Lagrangian-Eulerian-Lagrangian flow solver.

The two-phase LES/FMDF model has been used for detailed and large-scale simulations of various droplet-laden turbulent systems with and without droplet evaporation and combustion. Figure 28 shows the vorticity and mass fraction contours and droplet distribution in one of the experiments we have simulated. In this experiment, a lean premixed preheated air-decane flame is controlled by injection of a relatively small amount of liquid n-decane fuel. Also shown in this figure are the interactions between Eulerian grid points, Lagrangian droplet phase and Monte Carlo Particles. There are basically three interacting fields: (i) the Eulerian finite difference field, describing the gas dynamic variables, (ii) the grid-free Lagrangian Monte Carlo field, describing gaseous species and temperature through Filtered Mass Density Function, and (iii) another Lagrangian field, describing liquid-fuel droplets and spray.

In "conventional" LES methods, the "resolved" flow variables are obtained by solving the filtered form of the compressible Navier-Stokes, energy and scalar equations with the filtered equations being closed by appropriate SGS stress and scalar flux models. In reacting flows, additional models are normally required for source/sink terms. Here, we use the FMDF, which has been implemented in two ways: (Formulation I) to consider only the SGS scalar quantities, and (Formulation II) to consider the SGS (velocity-scalar-pressure) quantities. Formulation I is more manageable computationally and Formulation II is more rigorous from the statistical standpoint. However, possible advantages or drawbacks of the joint velocity-composition (-pressure) FMDF formulation over the formulation which considers the composition FMDF alone for compressible reacting flows is not fully established at present time. Most of our previous

contributions are based on formulation I which considers the joint scalar (species and energy) FMDF. For two-phase flows, the modified version of the scalar FMDF is employed.

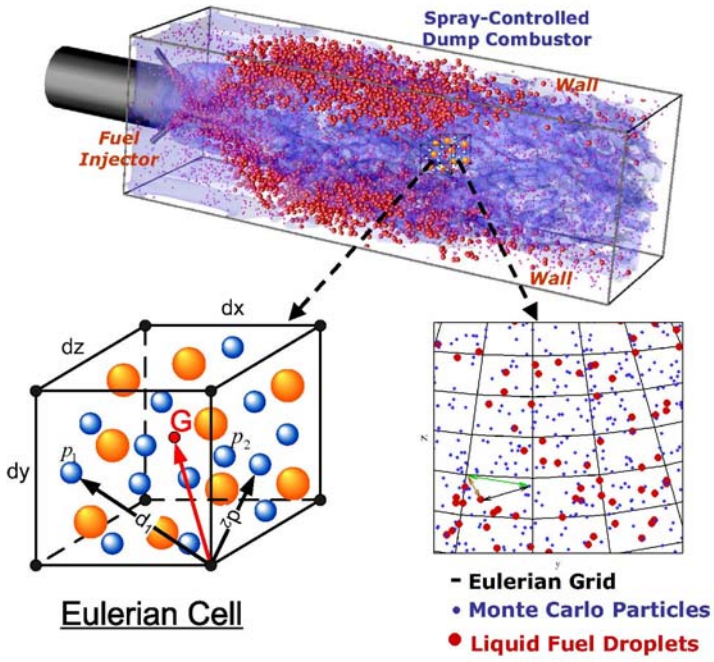

Figure 28. Contours of the instantaneous vorticity magnitude, droplet & Monte Carlo particle fields and grid layout in a spray-controlled dump combustor as obtained by LES/FMDF.

4.7.1 Filtered Mass Density Function (FMDF)

In conventional LES methods, the filtered equations for the scalars are solved together with other equations. In these equations, the filtered chemical source/sink terms are not closed and need modeling. Here, the subgrid combustion model is based on the FMDF methodology and the temperature and mass-fraction fields are obtained from the FMDF. The chemical source/sink terms are determined exactly with the knowledge of FMDF.

The scalar FMDF is the joint probability density function of the scalars at the subgrid-level and is defined as:

$$P_L(\underline{\Psi};\underline{x},t)=\int_{-\infty}^{+\infty}\rho(\underline{x}',t)\xi(\underline{\Psi},\underline{\Phi}(\underline{x}',t))G(\underline{x}'-\underline{x})d\underline{x}' \qquad (13)$$

where G denotes the filter function and ξ is the "fine-grained" density [31]. The scalar field, $\underline{\Phi}\equiv\phi_\alpha,\alpha=1,2,.....,N_s+1$, represents the mass fractions of the chemical species and the specific enthalpy ($\phi_\alpha,\alpha=N_s+1$), and is obtained from the joint scalar FMDF. The final form of the FMDF transport equation for a two-phase reacting system as derived from the original (unfiltered) governing equations is

$$\frac{\partial P_L}{\partial t}+\frac{\partial\left[\langle u_i\rangle_L P_L\right]}{\partial x_i}=\frac{\partial}{\partial x_i}\left[\langle\rho\rangle_l\left(\langle D\rangle_L+D_t\right)\frac{\partial\left(P_L/\langle\rho\rangle_l\right)}{\partial x_i}\right]+\sum_{\alpha=1}^{N_s+1}\frac{\partial}{\partial\Psi_\alpha}\left[\Omega_m\left(\Psi_\alpha-\langle\phi_\alpha\rangle_L\right)P_L\right]-\sum_{\alpha=1}^{N_s+1}\frac{\partial}{\partial\Psi_\alpha}\left[S_\alpha(\underline{\Psi})P_L\right]$$
$$-\frac{\partial}{\partial\Psi_\alpha}\left[\frac{\langle S_\rho^\alpha|\underline{\Psi}\rangle P_L}{\langle\rho\rangle_l}\right]+\frac{\partial}{\partial\Psi_\alpha}\left[\frac{\langle S_\rho|\underline{\Psi}\rangle\Psi_\alpha P_L}{\langle\rho\rangle_l}\right]+\left[\frac{\langle S_\rho|\underline{\Psi}\rangle P_L}{\langle\rho\rangle_l}\right] \qquad (14)$$

In Equations (13) and (14), S_α, Ψ, and Ω_m denote the production rate of species α, the "composition space" of scalar array Φ and the SGS mixing frequency, respectively. The molecular diffusivity coefficient and the SGS diffusivity coefficient are denoted by D and D_t. The effects of molecular/SGS mixing and SGS convection are modeled with closures similar to those used in LES/PDF methods [31-34].

4.7.2. Numerical Solution Method for FMDF

The filtered Eulerian carrier-gas equations are solved together with diffusivity-type closures for the SGS stress and the SGS scalar flux terms. The discretization procedure of the carrier fluid is based on the "compact parameter" finite difference scheme, which yields up to sixth order spatial accuracies. The time differencing is based on a third order low storage Runge-Kutta method. Once the fluid velocity, density and temperature fields are known, the droplet transport equations are integrated with second order time differencing. The evaluation of the fluid velocity at the droplet locations is based upon a fourth order accurate Lagrangian interpolation scheme. Also, for the droplet phase, a stochastic velocity model is considered by which the residual or subgrid velocity of the carrier fluid at the droplet location is constructed. The combined large- and small-scale fluid velocity is then used for calculations of droplet location and velocity.

From an operational standpoint, PDF or FMDF methods are implemented via stochastic differential equations. The full FMDF equation is a partial differential equation in physical, velocity and composition space. The connection to stochastic differential equations is via the Fokker-Planck equation: the Fokker-Planck equation of the stochastic model is a transport equation for the FMDF. Rather than solving that partial differential equation, and then computing statistics, the statistics can be obtained far more economically by averaging functions of the stochastic process. Hence, in FMDF modeling one actually solves a set of stochastic differential equations (SDEs), with the partial differential equations being a point of reference. The most convenient means of solving the SDE equations (Equation (14)) is via the "Lagrangian Monte Carlo" procedure [35]. With the Lagrangian procedure, the FMDF is represented by an ensemble of computational "stochastic elements" (or "particles") which are transported in the "physical space" by the combined actions of large scale convection and diffusion (molecular and subgrid). In addition, changes in the "composition space" occur due to chemical reaction, SGS mixing, and droplet evaporation. Again, all of these are implemented via a stochastic process described by a set of SDEs. These SDEs are fully consistent with the original FMDF transport equation. The Lagrangian FMDF represents the gas scalar and energy fields and is used to evaluate the local values of the temperature, density and species mass fractions at droplet location. The droplets in turn modify the species concentration and temperature values of the Monte Carlo particles or FMDF due to mass and energy coupling. Hence, the three-way coupling between the Carrier gas velocity field, FMDF scalar field and droplet field are included in the computations.

4.8. Numerical Simulation of Spray

The analytical methods that have been developed for two-phase turbulent flows are generally based on three different approaches: (i) Eulerian-Eulerian approach, (ii) Eulerian-Lagrangian approach, and (iii) Lagrangian-Lagrangian approach. In the first approach, the continuum transport equations for both phases are solved. These equations are somewhat similar and are often obtained by some sort of volume averaging which is conceptually different than the ensemble averaging in RANS or space averaging in LES. In the second approach, the continuum carrier fluid equations are solved in its "instantaneous" form in DNS or in its "averaged" form in RANS or LES over a fixed Eulerian grid system. However, the "dispersed" phase (particles, droplets, and micro bubbles) are described by a set of modeled Lagrangian equations which determine the position, velocity, temperature, and other properties of the dispersed phase.

In the third method, both phases are described in the Lagrangian context. The Eulerian-Eulerian and Eulerian-Lagrangian models have been employed for RANS, LES and DNS of a wide range of two-phase or two-fluid turbulent flows including free surface flows, or dispersed turbulent flows [36-39]. In comparison, there are limited numbers of models based on Lagrangian-Lagrangian approach.

Most of LES models are for isothermal two-phase turbulent flows; the application of LES models to non-isothermal flows with evaporating/reacting droplets was somewhat limited [40-48] and it has been only recently that LES models for realistic combustion systems are developed and tested. Among the limited number of LES studies on two-phase turbulent flows involving droplet evaporation and combustion, we refer here to the works by Okong'o & Bellan [49], Leboissetier et al. [50], Sankaran and Menon [51]; Patel et al. [52] Ham et al.[53] Mahesh [54], Afshari et al.[55] and Li & Jaberi [56], Cuenot et al. [57]. In the first two papers, [49-50] the DNS data for a temporal mixing layer laden with evaporating droplets are used to assess (a priori and a posteriori) different SGS models for carrier gas, droplet and evaporated vapor. It is shown that with the scale-similarity models for the carrier gas velocity, the predicted droplet distribution by LES compare reasonably well with that obtained from DNS data. However, the mass, momentum and heat transfer between evaporated droplets and carrier gas are not accurately represented by the proposed deterministic closures. The two-phase reacting LES model in References [51-52] is based on the Euelrian-Lagrangian approach. In this model, the carrier gas equations are solved for a fixed three-dimensional (3D) grid system. However, the mixing and reaction are implemented in one-dimensional (1D) domain via linear eddy model (LEM). The spray is based on a Lagrangian droplet model which includes empirical evaporation and secondary break-up submodel. The reaction is modeled with a global multi-step mechanism. The two-phase reacting LES model in Reference 20 is based on a similar hybrid Eulerian-Lagrangian approach. Here, the zero Mach number Navier-Stokes equations are solved on an unstructured grid system in the Eulerian part and the spray is modeled with Lagrangian method and some empirical droplet evaporation and break up submodels. The combustion is simulated with a flamelet/progress variable reaction submodel. The two-phase reacting LES model of Cuenot et al. [57] is fundamentally different than the above models as it solves the Eulerian equations for both phases. Our two-phase reacting LES/FMDF model [55-56] is also different than the other models mentioned above. It is based on an Eulerian-Lagrangian-Lagrangian methodology that is described in greater detail below.

In this work, the droplet field is obtained via a Lagrangian method. In this method, the evolution of the droplet displacement vector, the droplet velocity vector, the droplet temperature, and the droplet mass is governed by a set of non-equilibrium Lagrangian equations. The source terms appearing in the filtered carrier gas equations are evaluated based on the volumetric averaging of the Lagrangian variables and interpolation. Governing Lagrangian equations of transient position (X_i), velocity (v_i), temperature (T_d) and mass (m_i) of a single droplet are:

$$\begin{aligned}
&\frac{dX_i}{dt} = v_i \\
&\frac{dv_i}{dt} = \frac{f_1}{\tau_d}(u_i - v_i) \\
&\frac{dT_d}{dt} = \frac{Nu}{3\,\mathrm{Pr}}\left(\frac{C_{p,G}}{C_L}\right)\left(\frac{f_2}{\tau_d}\right)(T_G - T_d) + \left(\frac{\dot{m}_d}{m_d}\right)\frac{L_V}{C_L} \\
&\frac{dm_d}{dt} = -\frac{Sh}{3Sc_G}\left(\frac{m_d}{\tau_d}\right)\ln[1 + B_M]
\end{aligned} \tag{15}$$

Where subscript 'd' is the values for droplet and 'G' is for Carrier Gas field. In the equations, $\tau_d = \rho_L D^2/(18\mu_G)$ is particle time constant, D is the droplet diameter, L_v is the latent head of evaporation and C_L is the heat capacity of liquids. Drag of droplets is empirically corrected by the f_1 correlation function and f_2 is an analytical evaporative heat transfer correction function. Nu, Sh, Pr and Sc_G are Nusselt, Sherwood, Prandtl and Schmidt numbers of carrier gas respectively. Finally, B_M is the mass transfer number and is calculated using the non-equilibrium surface vapor function.

Mutual effects of droplets and carrier gas field on each other are considered via source terms (coupling terms) is continuity, momentums, energy and scalar field of carrier gas equations as:

$$
\begin{aligned}
S_I &= -\sum_{\alpha}\left\{\frac{w_\alpha}{\Delta V_\alpha}\left[\frac{d}{dt}(m_d)\right]_\alpha\right\} \\
S_{II,i} &= -\sum_{\alpha}\left\{\frac{w_\alpha}{\Delta V_\alpha}\left[\frac{d}{dt}(m_d v_i)\right]_\alpha\right\} \\
S_{III} &= -\sum_{\alpha}\left\{\frac{w_\alpha}{\Delta V_\alpha}\left[\frac{d}{dt}(m_d C_L T_d + \frac{1}{2} m_d v_i v_i)\right]_\alpha\right\}
\end{aligned}
\qquad (16)
$$

where subscript 'I' is for continuity and scalar equations, and 'II' and 'III' are for momentum and energy equations respectively.

4.9. Test Cases

In this section, we use the LES/FMDF methodology to simulate three single-phase and two-phase reactive flows in the MSU 3-valve engine configuration. First test case is premixed gaseous flame propagation in the cylinder using compressed turbulent flow, second is the evaporation of randomly distributed liquid fuel droplets using the same flow field as first test case, and the third case is concerned with the simulation of spray during the intake stroke in the engine. More cases are being simulated now but are not considered in this report.

4.10. Single-Phase Premixed Flame

In this case, the intake and compression stroke of the MSU engine without spray was simulated and the results of the flow field when the crank angle is 345 degrees (15 degrees before TDC during the compression stroke) were taken as initial condition. Then, it was assumed that there is a perfectly premixed propane mixture in the cylinder. Monte Carlo (MC) particles were distributed uniformly in the domain. Ignition was implemented by adding a source term to MC particle energy equations in the middle of cylinder on the cylinder head to increase the local temperature. Values of temperature predicted with both finite difference and Monte Carlo at different times were compared in Figure 29 at three different times. Figure 18 also shows comparison of instantaneous finite difference and MC predictions at the same time. Also, mean gas temperature in the cylinder is shown in Figure 29. Combustion starts at initial temperature of 620K, and then it was enhanced by increasing the temperature to 1100K with ignitor, and continues afterwards until all available fuel was burned. Evidently, there is a good consistency between the two methods which shows that both are accurately computed in LES/FMDF.

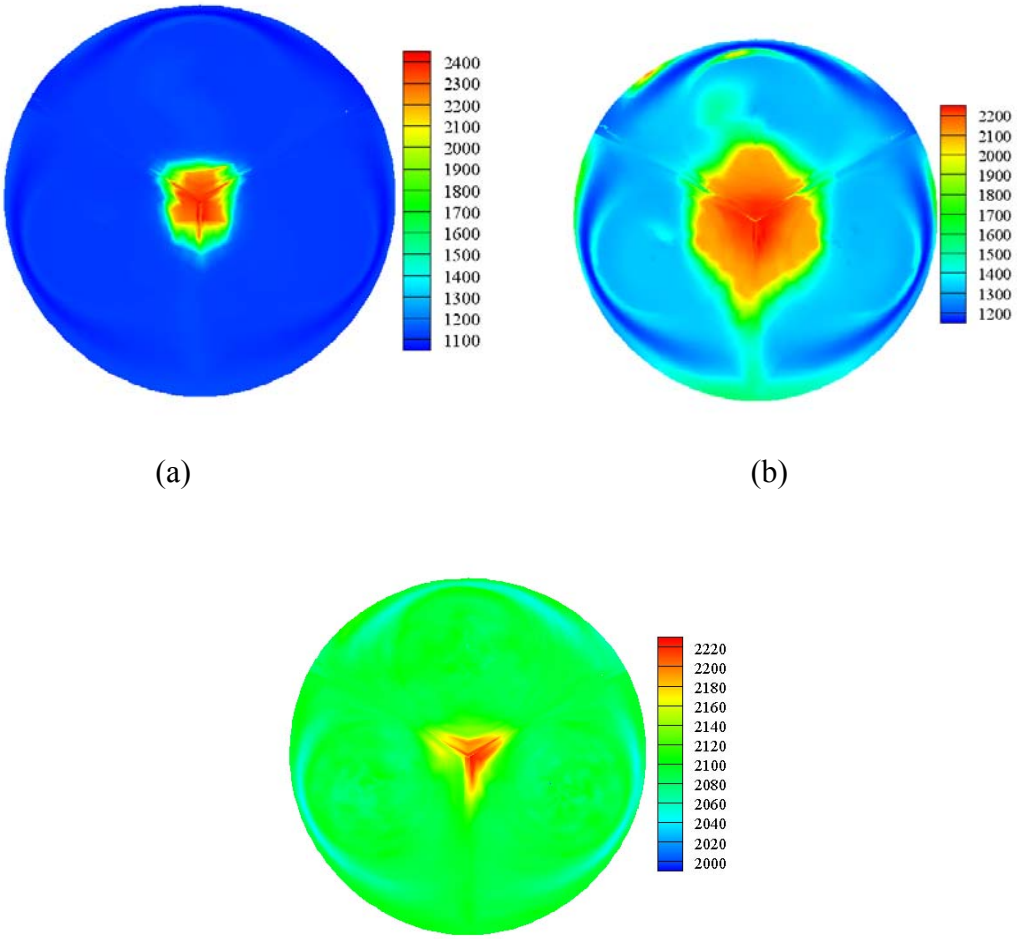

(a) (b)

(c)

Figure 29. Propane premixed flame, (a) 2×10^{-5} sec after ignition, (b) 6×10^{-5} after ignition and (c) 1.2×10^{-4} sec. after ignition.

4.11. Two-Phase Reaction

In this case, similar to previous test case, the results of flow field, when crack angle is 345^0, were taken as initial condition. Then, about 2.3×10^6 decane droplets with initial temperature of 300K were randomly distributed in the domain. Average temperature in the cylinder was 620K at the initial time, causing droplets to evaporate in the cylinder as gas temperature was higher that boiling temperature of the droplets. To check the consistency between finite difference and Monte Carlo values, the temperature and mass fraction of the evaporated fuel mass fraction predicted with these two methods were compared in Figures 32-34. In Figure 32, the contours of evaporated fuel are shown. In Figure 33.a, the mean temperature in the cylinder is shown during the evaporation. As droplets evaporated and received their energy from the carrier gas, the mean temperature in the cylinder was decreased. In Figure 33.b, good comparison of finite difference and Monte Carlo predictions of evaporated fuel mass fraction again indicate that the both methods are accurate.

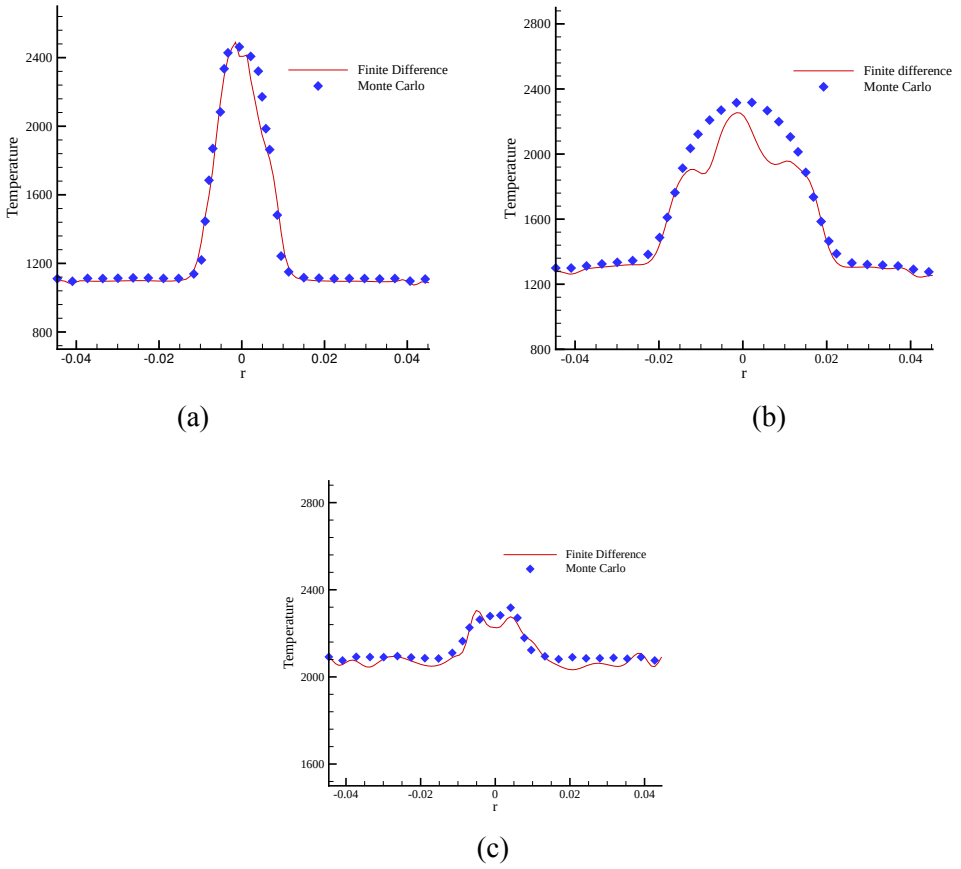

Figure 30. Comparison of finite difference and Monte Carlo prediction of temperature for propane premixed flame, (a) 2×10^{-5} sec after ignition, (b) 6×10^{-5} after ignition and (c) 1.2×10^{-4} sec. after ignition.

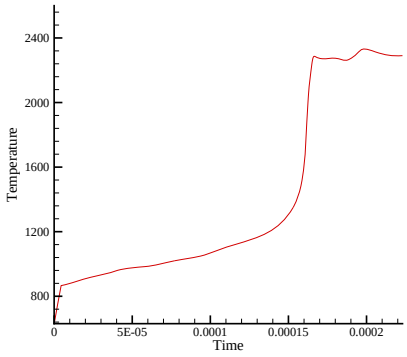

Figure 31. Mean in-cylinder temperature for propane premixed flame.

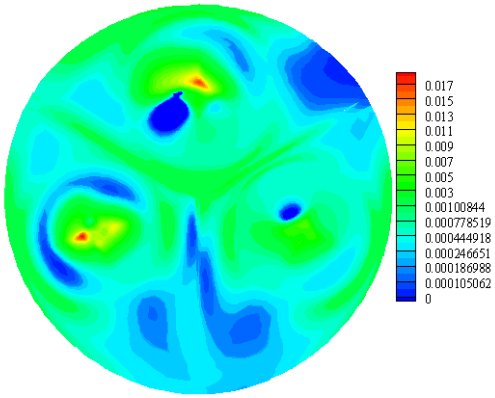

Figure 32. Evaporated fuel mass fraction contours.

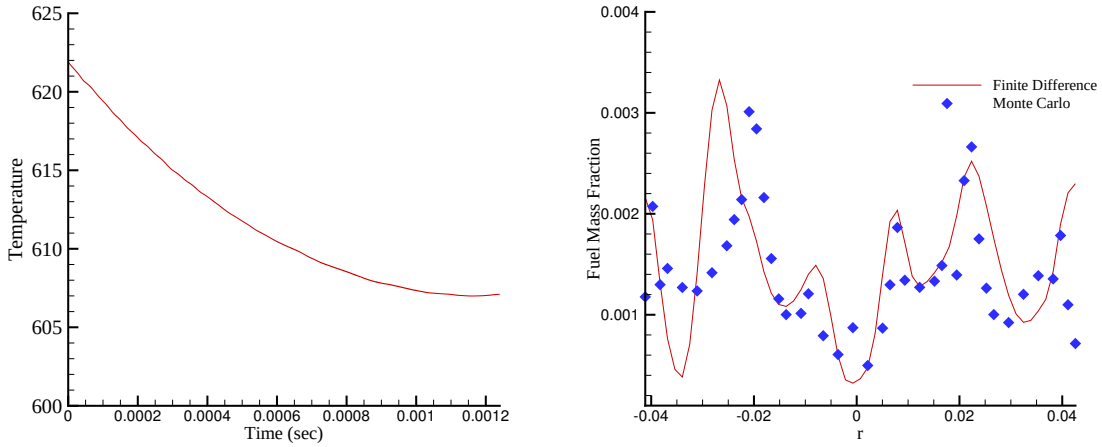

Figure 33. (a) Mean in-cylinder temperature during the evaporation of randomly distributed decane droplets and (b) comparison of evaporated fuel mass fraction as predicted by finite difference and Monte Carlo methods.

4.12. Simulation of Spray During the Intake Stroke

Simulations of spray and combustion in the MSU 3-valve, gasoline engine is an ongoing effort. Work is in progress to conduct complete simulations of burring engine with spray and combustion. In direct injection spark engines, fuel is injected into the cylinder during the intake stroke at sufficiently early times so that the fuel gets evaporated, mixed and compressed before ignition. The MSU, 3-valve engine, fuel injection is started when the crank angle is 79 and goes on up to 148 degrees. So, for this case, the flow after crank angle 79 is simulated with spray. In Figure 34, contours of axial velocity with streamlines around one of the intake valves together with fuel droplets are shown. During the intake the carrier gas temperature is around 300K and there is no considerable fuel evaporation. Fuel droplets are injected from the cylinder head with average initial velocity of 50m/s and a specified droplet size and velocity distribution. After a few crank angles, the droplets reach the piston. Here, two methods were applied to consider the interaction of the droplets with the piston. In these methods, the droplets can either stay on

the piston surface and make a liquid film or bounce back into the cylinder. Figure 34 shows that some of the droplets, which were bounced backed from the wall, are still close to piston. Currently, we are looking at the effects of turbulence on mixing and combustion for different fuels and flow conditions.

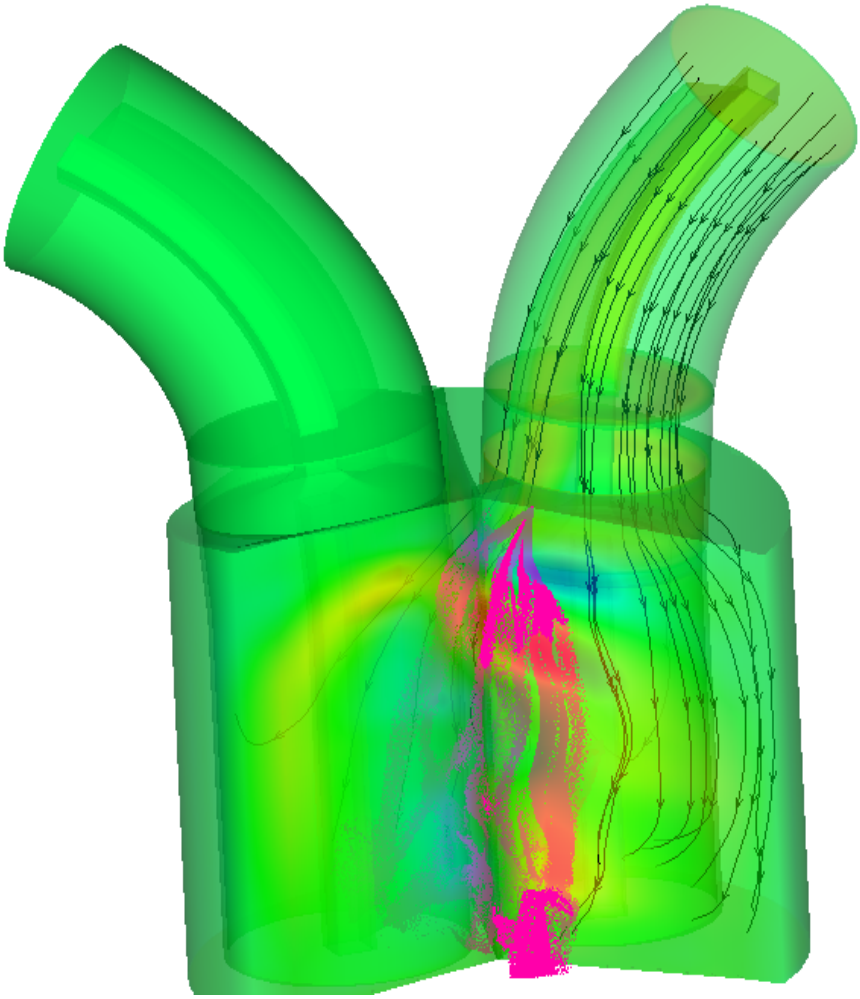

Figure 34. The spray pattern of fuel droplets during the intake stroke of the MSU 3-valve direct-injection gasoline engine (contours of axial velocity and streamlines are also shown).

5. Control System Development for Electro-Pneumatic Valve Actuator (EPVA) - System Modeling

The valve actuator's main function is to provide variable valve timing and variable lift in an automotive engine. The design of the combination of pneumatic and hydraulic mechanisms allows the system to operate under low pressure with an energy saving mode. A system dynamics analysis is provided and is followed by a mathematical model. This modeling approach uses Newton's law, mass conservation and thermodynamic principles. The air compressibility and liquid compressibility in the hydraulic latch are modeled. The discontinuous nonlinearity of the compressible flow due to choking is carefully considered. Provision is made for the nonlinear motion of the mechanical components due to the physical constraints. Validation experiments were performed on a Ford 5.4 liter 4-valve V8 engine head with different air supply pressures and different solenoid pulse inputs. Results of the experiments were satisfactory and the simulation responses agreed with the experimental results.

5.1. EPVA Control System Development for Intake Valves

Electro-pneumatic valve actuators are used to eliminate the cam shaft of a traditional internal combustion engine. They are used to control the opening timing, duration, and lift of both intake and exhaust valves. A control oriented model was developed to reduce computational throughput for real-time implementation. The developed control oriented model was validated by experimental data. An adaptive valve lift control strategy was developed to improve lift repeatability. A model reference adaptive system identification technique was employed to calculate system parameters needed for generating closed-loop control signals. The convergence of the derived adaptive parameter identification algorithm was verified using the valve test bench data. The bench test data covers engine speed from 1200RPM and 5000RPM. Parameter identification convergence was achieved within 40 cycles. The closed-loop lift control algorithm was developed and implemented in a prototype controller, and validated on a valve test bench with multiple reference valve lift set points at both 1200RPM and 5000RPM engine speeds. The experiment results showed that the actual valve lift reached the reference lift within 0.5mm of lift error in one cycle at 1200RPM and in two cycles at 5000RPM. The maximum steady state lift errors are less than 0.4mm at high valve lift and less than 1.3mm at low valve lift. Furthermore, the closed-loop valve lift control improved valve lift repeatability with more than 30% reduction of standard deviation over the open-loop control.

5.2. EPVA Control System Development for Exhaust Valves

Variable valve actuation of internal combustion engines is capable of significantly improving their performance. It can be divided into two main categories: variable valve timing with cam shaft(s) and camless valve actuation. For camless valve actuation, research has been centered in electro-magnetic, electro-hydraulic, and electro-pneumatic valve actuators. This research studies the control of the electro-pneumatic valve actuator. The modeling and control of intake valves for the Electro-Pneumatic Valve Actuators (EPVA) was shown in early publications and this paper extends the EPVA modeling and control development to exhaust valves for the lift control, which is the key to the exhaust valve control, since an accurate and repeatable lift control guarantees a satisfactory valve closing timing control. Note that exhaust valve closing timing is a key parameter for controlling engine residual gas recirculation. The exhaust valve lift control challenge is the disturbance from the randomly varying in-cylinder pressure against which the exhaust valve opens. The developed strategy utilizes model based predictive techniques to overcome this disturbance. This exhaust valve lift control algorithm was validated on a 5.4 liter 3-valve V8 engine head with a pressurized chamber to imitate the in-cylinder pressure. The experimental results demonstrated that the exhaust valve lift tracked the step reference in one cycle with the lift error under 1mm and the steady state lift error was kept below 1mm.

6. Engine Control Development for HCCE Engine - Baseline Engine Controller Development

The development of our Opal-RT based prototype engine controller has been completed. It has been *validated in both our engine HIL (Hardware-In-the-Loop) simulation and in the engine dynamometer. The baseline engine controller contains the following control features:

- Dual fuel control system for both PFI (Port Fuel Injection) and DI (Direct Injection) fuel systems.
- Ionization detection ignition control and feedback.
- Crank synchronized EPVA (Electro-Pneumatic Valve Actuator) control reference generation.

6.1. Decentralized Engine and EPVA Control Development

Communication between Opal-RT engine and EPVA controllers has been established and validated. The basic control principle is that the Opal-RT engine controller sends the crank synchronized desired valve lift, opening and closing signals to the EPVA Opal-RT controller; and the EPVA controller conducts the

valve lift, opening and closing timing control, based upon the reference signals from the engine controller, in a closed loop.

Both engine and EPVA controllers have been validated using our engine HIL simulation station and EPVA test bench, see diagram in Figure 35. EPVA valve control strategy is under development using this setup. Dynamometer validation tests of both engine and EPVA control strategies are the last task to be completed.

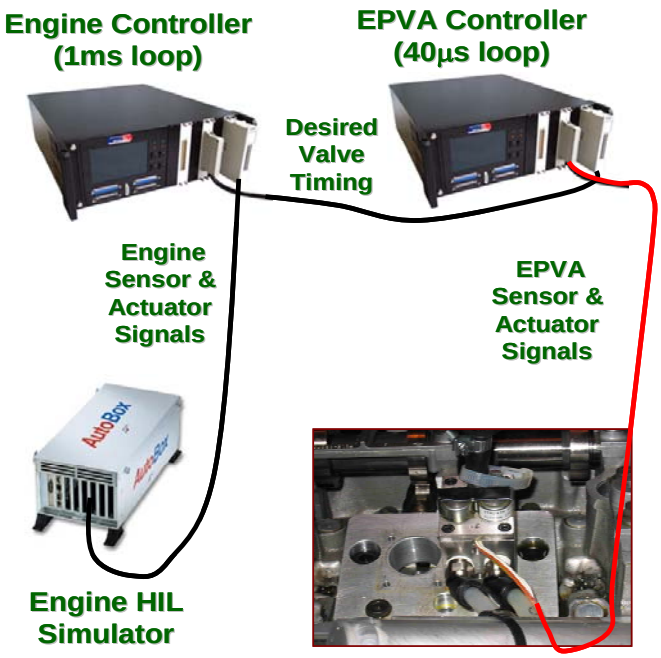

Figure 35. Decentralized engine and EPVA control architecture.

7. Publications and Patent Activity

Patent activity and publications that have resulted from this effort are listed below:

Patent: Jia Ma, George Zhu, Harold Schock and Tom Stuecken, “Method and Apparatus for Enhancing the Performance of a Camless Valve Actuator,” Application made November 1, 2007. US Patent pending.

Patent: A.M. Naguib, A. Aditjandra, B. Trosin, H.J. Schock, T.R. Stuecken, and E. Timm, “Mass Air Flow Sensor,” US Patent pending (MSU ID#07-019F).

Hung, D.L.S., Zhu, G., Winkelman, J., Stuecken, T., Schock, H., and Fedewa, A., "A High Speed Flow Visualization Study of Fuel Spray Pattern Effect on a Low Pressure Direct Injection Gasoline Engine," SAE Technical Paper No. 2007-01-1411, 2007. SAE World Congress, Detroit Michigan, April 2007.

Zhang, Y., Schock, H, and Hung, D.L.S., "Numerical Study of the Mixture Preparation Process in a 5.4L V8 GDI Engine," ILASS-Americas, 20th Annual Conference on Liquid Atomization and Spray Systems, Chicago, IL, 2007.

Ma, Jia and Schock, H., Michigan State University, Carlson, U., Hoglund, A., and Hedman, M. Cargine Engineering AB, Helsingborg, Sweden. "Analysis and Modeling of an Electronically Controlled Pneumatic Hydraulic Valve for an Automotive Engine," SAE Paper No. 2006-01-0042, SAE World Congress, Detroit, Michigan, April 16-19, 2006.

Ma, Jia, Stuecken, T., and Schock, H., Michigan State University, Zhu, G. and Winkelman, J. Visteon Corporation, "Model Reference Adaptive Control of a Pneumatic Valve Actuator for Infinitely Variable Valve Timing and Lift," SAE Paper No. 2007-01-1297, SAE World Congress, Detroit, Michigan, April 3-6, 2007.

Ma, Jia, Zhu, G., Schock, H., and Winkelman, J. "Adaptive Control of a Pneumatic Valve Actuator for an Internal Combustion Engine," Proceedings of 2007 American Control Conference, New York, NY, July 11-13, 2007.

Ma, Jia, Zhu, G., Hartsig, A., and Schock, H., "Model-Based Predictive Control of an Electro-Pneumatic Exhaust Valve for Internal Combustion Engines," Proceedings of 2008 American Control Conference, Seattle, WA, June11-13, 2008.

Ma, Jia, Zhu, G., Stuecken, T., Hartsig, A., and Schock, H., "Electro-Pneumatic Exhaust Valve Modeling and Control for an Internal Combustion Engine," Proceedings of ICES 2008 ASME 2008 International Combustion Engine Spring Technical Conference, ICES2008-1653, April 21-23, 2008, Chicago, IL.

8. Summary

In this effort a solid base has been established for continued development of the advanced engine concepts originally proposed. Due to problems with the valve actuation system a complete demonstration of the engine concept originally proposed was not possible. Below are the highlights that were accomplished during this effort:

1. A forward-backward mass air flow sensor has been developed and a patent application for the device has been submitted. We are optimistic that this technology will have a particular application in variable valve timing direct injection systems for IC engines.

2. The biggest effort on this project has involved the development of the pneumatic-hydraulic valve actuation system. This system was originally purchased from Cargine, a Swedish supplier and is in the development stage. To date we have not been able to use the actuators to control the exhaust valves, although the actuators have been successfully employed to control the intake valves. The reason for this is the additional complication associated with variable back pressure on the exhaust valves when they are opened. As a result of this effort, we have devised a new design and have filed for a patent on a method of control which is believed to overcome this problem. The engine we have been working with originally had a single camshaft which controlled both the intake and exhaust valves. Single cycle lift and timing control was demonstrated with this system.

3. Large eddy simulations and KIVA based simulations were used in conjunction with flow visualizations in an optical engine to study fuel air mixing. During this effort we have devised a metric for quantifying fuel distribution and it is described in several of our papers.

4. A control system has been developed to enable us to test the benefits of the various technologies. This system used is based on Opal-RT hardware and is being used in a current DOE sponsored program.

9. References

[1] Patent: A.M. Naguib and Y. Li, “Oscillating Hotwire or Hotfilm Flow Sensor,” US Patent No. 6,901,795, June 7, 2005.

[2] Patent: A.M. Naguib, A. Aditjandra, B. Trosin, H.J. Schock, T.R. Stuecken, and E. Timm, “Mass Air Flow Sensor,” US Patent pending (MSU ID#07-019F).

[3] Hung, D.L.S., Zhu, G., Winkelman, J., Stuecken, T., Schock, H., and Fedewa, A., "A High Speed Flow Visualization Study of Fuel Spray Pattern Effect on a Low Pressure Direct Injection Gasoline Engine," SAE Technical Paper No. 2007-01-1411, 2007.

[4] Reynolds W. C., “Modeling of Fluid Motions in Engines - An Introductory Review,” (Plenum Press, NY) Combustion Modeling in Reciprocating Engines (Eds. N. Mattavi and C. A. Amann), 52, 1980.

[5] E.I. Tahry, S.H., and Haworth, D.C. “Directions in Turbulence Modeling for In-Cylinder Flows in Reciprocating IC Engines,” AIAA Journal, Prop and Power, 50, 8:1040-8, 1992.

[6] Naitoh, K., Itoh, T. and Takagi, Y. “Large Eddy Simulation of Premixed-Flame in Engine Based on the Multi-Level Formulation and the Renormalization Group Theory,” SAE International Congress and Exposition, Detroit, Michigan, 53, 24-28 February 1992, SAE Technical Paper No. 920590.

[7] D.C. Haworth and K. Jansen, “Large-Eddy Simulation on Unstructured Deformation Meshes: Towards Reciprocating IC Engines,” Computers Fluids, 54, 29: pp.493-524, 2000.

[8] ORourke, P. and Sahota, M.S. “A Variable Explicit/Implicit Numerical Method for Calculating Advection on Unstructured Meshes,” Journal of Computational Physics, 55, 142:312-45, 1998.

[9] A.P. Morse, J.H. Whitelaw, and M. Yianneskia, “Turbulent Flow Measurement by Laser Doppler Anemometry in a Motored Reciprocating Engine,” Imperial College, Dept. Mechanical Engineering, Report FS/78/24, 1978.

[10] D.C. Haworth, “Large-Eddy Simulation of In-Cylinder Flows, Oil Gas Science and Technology,” 54, 2: pp.175-185, 1999.

[11] J. Mohd Yusof, “Interaction of Massive Particles with Turbulence,” PhD Thesis, Cornell Univ. 1996.

[12] R. Verzicco, J. Mohd-Yusof, P. Orlandi and D. Haworth, “Large Eddy Simulation in Complex Geometric Configuration Using Boundary Body Forces,” AIAA Journal, 38, No. 3. pp.427-433, 2000.

[13] R. Verzicco, J. Mohd-Yusof, P. Orlandi and D. Haworth, “LES in Complex Geometric Using Boundary Body Forces,” Proceedings of the Summer Program of the Center for Turbulence Research, Stanford University/NASA Ames Center for Turbulence Research, pp.171-186, 1998[14] K. Sone and S. Menon, “Effect of Subgrid, Modeling on the In-Cylinder Unsteady Mixing Process in a Direct Injection Engine,” Journal of Eng for Gas Turbines and Power, 56, 125: pp.435-443, 2003.

[15] Menon, S., Yeung, P.K. and Kim, W., “Effect of Subgrid Models on the Computed Interscale Energy Transfer of Isotropic Turbulence,” Computers Fluids, 57, 25, No. 2; 65-180, 1996.

[16] Amsden, A., “KIVA-3: A KIVA Program with Block Structured Mesh for Complex Geometries,” Los Alamos National Laboratory Report, LA-12503-MS, 58, 1993.

[17] Lee, D., Pomraning, E. and Rutland, C.J., “LES Modeling of Diesel Engines,” SAE Paper No. 2002-01-2779.

[18] Moureau, V., Barton, I. Angelberger, C. and Poinsot, T., “Towards Large Eddy Simulation in Internal-Combustion: Simulation of a Compressed Tumble Flow,” SAE Paper No. 2004-01-1995.

[19] Dugue, V., Gauchet, N. and Veynante, D., “Applicability of Large Eddy Simulation to the Fluid Mechanics in a Real Engine Configuration by Means of an Industrial Code,” SAE Paper No. 2006-01-1194.

[20] R. Jhavar and C. J. Rutland, “Using Large Eddy Simulations to Study Mixing Effects in Early Injection Diesel Engines Combustion,” SAE 2006 World Congress, Detroit, MI, 59, SAE Paper No. 2006-01-0871.12.

[21] Celik, I., Yavuz, I. and Smirnov, A, “Large Eddy Simulations of In-Cylinder Turbulence for Internal Combustion Engines: A Review,” International Journal of Engine Research, 60, 2 No. 2:119-148. 1997.

[22] L. Thobois, G. Rymer, T. Souleres and T. Poinsot, “Large Eddy Simulation for the Prediction of Aero-Dynamics in IC Engines,” International Journal of Vehicle Design, 39, No. 4:368-382. 2005.

[23] R. Germano, U. Piomelli, P. Moin, and W. H. Cabot, "A Dynamic Subgrid-Scale Eddy Viscosity Model," Phy. Fluids A, 3, 1760, 1991.
[24] D. K. Lilly, "A Proposed Modification of the Germano Subgrid-Scale Closure Method," Phy. Fluids A, 3, 633, 1992.
[25] M. Visbal and D. Gaitonde, "On the Use of Higher-Order Finite-Difference Schemes on Curvilinear and Deforming Meshes," Journal of Computational Physics, (2002) 181, pp.155-185, 2002.
[26] P. D. Thomas and C. K. Lombard, "Geometric Conservation Law and its Application to Flow Computations on Moving Grids," 17, 10, 1030, 1979.
[27] L. Graftieaux, M. Michard and N. Grosjean, "Combining PIV, POD and Vortex Identification Algorithms for the Study of Unsteady Turbulent Swirling Flows Measurement Science and Technology," 12, pp.1422-1429, 2001.
[28] Devesa, A., Moreau, J., Hlie, J., Faivre, V. and Poinsot, T., "Initial Conditions for Large Eddy Simulations of Piston Engines Flows," Computers Fluids, 36, pp.701-713, 2007[29] Fraser, R.A. and Bracco, F.V., "Cycle-Resolved LDV Integral Length Scale - Measurements Investigating Clearance Height Scaling, Isotropy and Homogeneity in an IC Engine," SAE Paper No. 890615, 1989,
[30] Fraser, R.A. and Bracco, F.V., "Cycle-Resolved LDV Integral Length Scale Measurements in an IC Engine," SAE Paper No. 880381, 1988.
[31] James, S., and Jaberi, F. A., "Large Scale Simulation Two-Dimensional Nonpremixed Methane Jet Flames," Combustion and Flame, v.123, 2000, pp.465-487.
[32] Jaberi, F. A., "Large Eddy Simulation of Turbulent Pre-mixed Flame via Filtered Mass Density Function," 37th AIAA Aerospace Sciences Meeting and Exhibit, Reno, NV, January 1999.
[33] Givi, P., "Filtered Density Function for Subgrid Scale Modeling of Turbulent Combustion," AIAA Journal, v.44, No.1, January 2006, pp.16-23.
[34] Afshari, A., Jaberi, F.A. and Shih, T. I-P., "Large-Eddy Simulation of Turbulent Flow in an Axisymmetric Dump Combustor," AIAA Journal, 2007.
[35] Jaberi, F. A., Colucci, P. J., James, S., Givi, P. and Pope, S. B., "Filtered Mass Density Function for Large Eddy Simulation of Turbulent Reacting Flows," Journal of Fluid Mech. v.401, 1999, pp.85-121.
[36] Cressman, J. R., Davoudi, J., Goldburg, W. I. and Schumacher, J., "Eulerian and Lagrangian Studies in Surface Flow Turbulence," New Journal of Physics, v.6, No.53, 2004.
[37] Menon, S., "Subgrid Combustion Modeling for LES of Single and Two-Phase Reacting Flows," Adcances in LES of Complex Flows, edited by R. Friedrich and W. Rodi, Proceedings of the Euromech Colloquium 412, Munich, Germany, 2000, pp.329-351.
[38] Madnia, C.K., Jaberi, F.A. and Givi, P., "Large Eddy Simulation of Heat and Mass Transport in Turbulent Flows," Handbook of Numerical Heat Transfer, 2nd ed. edited by W. J. Minkowycz, E. M. Sparrow and J.Y. Murthy, Chapter 5, Wiley, New York, 2006, pp.167-189.
[39] Moin, P., "Large Eddy Simulation of Multi-Phase Turbulent Flows in Realistic Combustors," Progress in Computational Fluid Dynamics, International Journal, v.4, 2004, pp.237-240.
[40] Mashayek, F. and Pandya, R., "Analytical Description Particle/Droplet-Laden Turbulent Flows," Progress Energy Combustion Science, v.29, 2003, pp.329-378.
[41] Lakehal, D., "On the Modeling of Multiphase Turbulent Flows for Environmental and Hhydrodynamic Applications," International Journal of Multiphase Flow, v.28, 2002, pp.823-863.
[42] Herrmann, M., "Modeling Primary Breakup: Three-Dimensional Eulerian Level Set/Vortex Sheet Method for Two-Phase Interface Dynamics," Center for Turbulence Research, Stanford University, Annual Research Brief, 2003, pp.185-196.
[43] Cuenot, B., Boileau, M., Pascaud, S., Mossa, J.-B., Riber, E., Poinsot, T. and Berate, C., "Large Eddy Simulation of Two-Phase Reacting Flows," ECCOMAS CFD, Egmond Aan Zee, Netherland, 2006.
[44] Faeth, G. M., "Mixing, Transport and Combustion in Sprays," Progress Energy Combustion Science, v.13, 1987, pp.293-345.
[45] Shirolkar, J. S., Coimbra, C. F. M. and McQuay, M. Q., "Fundamental Aspects of Modeling Turbulent Particle Dispersion in Dilute Flows," Progress Energy Combustion Science, v.22, No.5, 1996, pp.363-399.

[46] Crowe, C. and Sommerfeld, M. and Tsuji, Y., "Multiphase Flows with Droplets and Particles," CRC Press, 1998.
[47] Sirignano, W. A., "Fluid Dynamics and Transport of Droplets and Sprays," Cambridge University Press, 1999.
[48] Bellan, J., "Perspectives on Large Eddy Simulations for Sprays: Issues and Solutions," Atomization and Sprays, v.10, 2000, pp.409-425.
[49] Okong'o, N. and Bellan, J., "Consistent Large Eddy Simulation of a Temporal Mixing Layer Laden with Evaporating Drops. Part 1: Direct Numerical Simulation, Formulation, and A Priori Analysis," Journal of Fluid Mechanics, v.499, 2004, pp.1-47.
[50] Leboissetier, A., Okong'o, N. and Bellan, J., "Consistent Large Eddy Simulation of a Temporal Mixing Layer Laden with Evaporating Drops. Part 2: A Posteriori Modeling," Journal of Fluid Mechanics, v.523, 2005, pp.37-78.
[51] Sankaran, V. and Menon, S., "LES of Spray Combustion in Swirling Flows," Journal of Turbulence, v.3, No.011, 2002, pp.1-23.
[52] Patel, N., Kırtaş, M., Sankaran, V. and Menon. S., "Simulation of Spray Combustion in a Lean-Direct Injection Combustor," Proceedings of the Combustion Institute, v.31, 2007, pp. 2327-2334.
[53] Mahesh, K., Constantinescu G., Apte, S., Iaccarino, G., Ham, F. and Moin, P., "Large-Eddy Simulation of Reacting Turbulent Flows in Complex Geometries," Journal of Applied Mechanics, v.73, 2006, pp.374-381.
[54] Ham, F., Apte, S.V., Iaccarino, G., Wu, X., Herrmann, M., Constantinescu, G., Mahesh, K. and Moin, P., "Unstructure LES of Reacting Multiphase Flows in Realistic Gas-Turbine Combustors," Center for Turbulence Research, Annual Research Briefs, Stanford University, Stanford, CA, 2003.
[55] Afshari, A., Almeida, T., Mehravan, K. and Jaberi, F. A., "Large Scale Simulation of Turbulent Combustion and Propulsion Systems," Proceedings of the Seventeenth ONR Propulsion Meeting, Boston, MA, June 2004.
[56] Li, Z. and Jaberi, F.A., "A New Two-Phase Stochastic Subgrid Model for Large Eddy Simulation of Spray Combustion," Journal of Fluid Mechanics.
[57] Cuenot, B., Boileau, M., Pascaud, S., Mossa, J.-B., Riber, E., Poinsot, T. and B'erat, C., "Large Eddy Simulation of Two-Phase Reacting Flows," ECCOMAS CFD, Egmond Aan Zee, Netherland, 2006.

10. Acronyms

AR	area ratio
ARES	Automotive Research Experiment Station
BDC	bottom dead center
BTDC.	Before top dead center
CA	crank angle?
CAT 3401	Caterpillar engine
Cd	constant coefficient
CFL	Computational Fluid Dynamics Laboratory
d	diameter
D	large area diameter
DISI	direct-injection spark-ignition
DNS	direct numerical simulation
E	volts
EARL	Energy and Automotive Research Laboratory
EPVA	Electro-Pneumatic Valve Actuator
FBMAFS	Forward-Backward Mass Air Flow Sensor
FMDF	Filtered Mass Density Function
GCL	geometric conservation law
GUI	Graphical User Interface

HIL	Hardware-In-the-Loop
Hz	hertz (unit)
IC	internal combustion
K	Kelvin
kg/s	kilograms per second
kHz	kilohertz
k-ϱ	turbulence model of two equations
L	divice length
LDA	Laser Doppler Anemometry
LEM	linear eddy model
LES	large eddy simulation
MAFS	mass air flow sensor
MC	Monte Carlo (particles)
mm	micrometer
ms	millisecond
m/s	meters per second
MSU	Michigan State University
NO-UTOPIA	Node-Centered Unstructured Topology, Parallel Implicit Advection
ODE	ordinary differential equation
OHW	oscillating hotwire
PDF	probability density function
PFI	Port Fuel Injection
RANS	Reynolds-averaged Navier-Stokes
RMS	root mean square
RPM	rate per minute
SDE	stochastic differential equation
SGS	subgrid-scale
SOI	start of ignition
TDC	top dead center
VI	variable-area insert
VI-FBMAFS	variable-area insert - Forward-Backward Mass Air Flow Sensor
Vp	average piston speed
WOT	wide open throttle
x	streamwise distance

2006-01-0042

Analysis and Modeling of an Electronically Controlled Pneumatic Hydraulic Valve for an Automotive Engine

Jia Ma, Harold Schock
Michigan State University, Automotive Research Experiment Station, 3361 Hulett Road, Okemos, MI 48864

Urban Carlson, Anders Hoglund, Mats Hedman
Cargine Engineering AB, Helsingborg, Sweden

ABSTRACT

This paper addresses the design and detailed modeling of a novel electronically controlled, pneumatic/hydraulic valve actuator (EPVA) for both the engine intake and engine exhaust valves. The valve actuator's main function is to provide variable valve timing and variable lift in an automotive engine. The design of the combination of pneumatic and hydraulic mechanisms allows the system to operate under low pressure with an energy saving mode. A system dynamics analysis is provided and is followed by a mathematical model. This modeling approach uses the Newton's law, mass conservation and thermodynamic principles. The air compressibility and liquid compressibility in the hydraulic latch are modeled. The discontinuous nonlinearity of the compressible flow due to choking is carefully considered. Provision is made for the nonlinear motion of the mechanical components due to the physical constraints. Validation experiments were performed on a Ford 5.4 liter 4-valve V8 engine head with different air supply pressures and different solenoid pulse inputs. Results of the experiments were satisfactory and the simulation responses agreed with the experimental results.

INTRODUCTION

In a camless valvetrain, the motion of each valve is controlled by an independent actuator. There is no camshaft or other mechanisms coupling the valve to the crankshaft as in a conventional valvetrain. This provides the possibility to control the valve events, i.e. timing, lift and duration, independent of crankshaft rotation. Various studies have shown that an engine using variable valve timing allows the reduction of pumping losses, control of the internal residual gas recirculation (RGR) and NOx emissions, along with improvement of performance over a wide operating range. All of these factors contribute to a considerable potential improvement in fuel economy. J.W.G.Turner et al. studied the strategies of camless valvetrain implementation [1]. Research has been conducted on different types of valve actuators, including electromagnetic, hydraulic and pneumatic actuators. Chihaya Sugimotoet et al. [2], Mark A.Theobald et al. [3] and F.Pischinger et al. [4] developed electromagnetic actuators. H.P.Lenz et al. [5] developed a hydraulic actuator. W.E.Richeson et al. presented a pneumatic actuator incorporated with a permanent magnet control latch in [6]. The advantages and disadvantages of a pneumatic actuator over a hydraulic actuator were addressed by John P.Watson and Russell J.Wakeman [7]. In their article, a pneumatic valve actuator with a physical motion stopper was presented and the simulations of the valve actuation system were shown. In [8], James E.Bobrow and Brian W.McDonell modeled a variable valve timing engine and discussed an engine control strategy. In order to provide an insight into the pneumatic actuator design and the control requirements, mathematical modeling was performed to a variety of actuation systems. In [9], J.M.Tressler et al. analyzed and modeled the dynamics of a pneumatic system consisting of a double-acting or single-acting cylinder and servovalve. A mathematical model of a pneumatic force actuator was presented by Edmond Richer and Yildirim Hurmuzlu in [10].

In this article, electronically controlled pneumatic/hydraulic valve actuators (EPVA) are employed to replace the traditional camshaft in an internal combustion engine. The EPVA is capable of varying valve lift height, valve timing and valve open duration as desired in a variable valve timing engine. In addition, the EPVA is designed to extract the maximum work from the air flow by incorporating a hydraulic latch mechanism to reduce the power consumption. A hydraulic damper mechanism is also added to produce a desirable slow and smooth seating velocity when the valve returns to the seat. Mathematical modeling was completed to give an insight of the design and control criteria.

The organization of this paper is as follows. First, the dynamics of the system are analyzed in the system dynamics section. Next, the model is derived in the mathematical modeling section. Third, the experimental setup is presented in the simula-

tions and experiments section where the experimental responses and the simulation results are compared. Finally, conclusions are drawn.

SYSTEM DYNAMICS

The EPVA consists of two solenoids, two spool valves, two port valves, an actuator piston, an actuator cylinder and a hydraulic latch/damper system. An actuator piston pushes the back of the poppet valve stem, causing the valve to open. Solenoid-controlled spool valves are used to control the flow of the air that enters and exits the actuator cylinder. In order to reduce the energy consumption, EPVA uses a hydraulic latch which allows the actuator to extract the full expansion work out of the air that is drawn into the actuator cylinder. Meanwhile, the actuator is still capable of holding the valve in an open position to obtain full variation of valve open duration. A hydraulic damping mechanism is added to provide a slow seating velocity for the valve. According to the events taking place in the actuator cylinder, the system dynamics are divided into three stages: air charging, expansion and dwell, and air discharging stage. Figure (6) illustrates their equivalent stages on the valve lift profile.

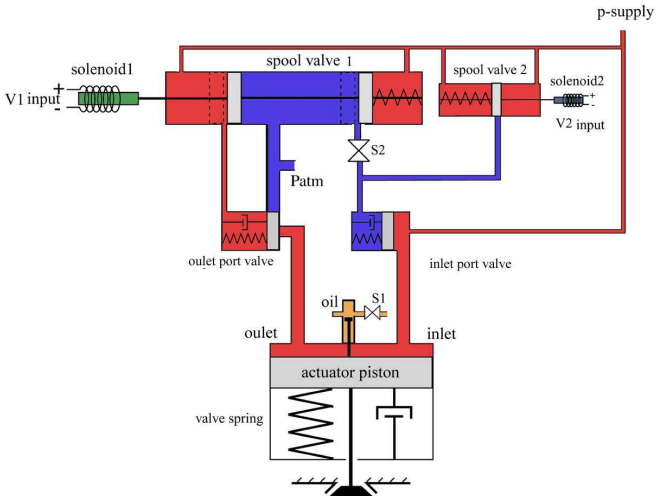

Figure 1: System dynamics at the air charging stage

Air Charging Stage Figure (1) depicts the system dynamics when the actuator cylinder is at the air charging stage. The red color represents the high pressure (supply pressure) air, the blue color represents the low pressure (atmospheric pressure) air, the yellow color represents the oil in the hydraulic latch/damper. $S1$ and $S2$ are two check valves that are corresponding to solenoid 1 and solenoid 2. When a solenoid is energized, its corresponding check valve is able to function as a one-way flow valve. When that solenoid is deactivated, then the check valve is held off its seat allowing two way flow. Green is an energized solenoid while blue is an de-energized solenoid.

During the charging stage, solenoid 1 is energized pushing the spool valve 1 slightly to the right. In this spool valve position, the high pressure air is sent to two places, the left of the outlet port valve and the right of the inlet port valve. The low pressure air is sent to the left of the inlet port valve. Therefore, the high pressure air closes the outlet port valve and opens the inlet port valve. The supply air now charges the cylinder, the actuator piston starts moving down and opens the poppet valve. Although the right side of the outlet port valve is then subject to high pressure air, it remains closed due to the area difference between the two sides of the port valve. The check valve $S1$ is activated at the moment when solenoid 1 is energized. This only allows the oil to flow down the passage and prevents it from returning to the reservoir. The oil supply pressure is the same as the air supply pressure.

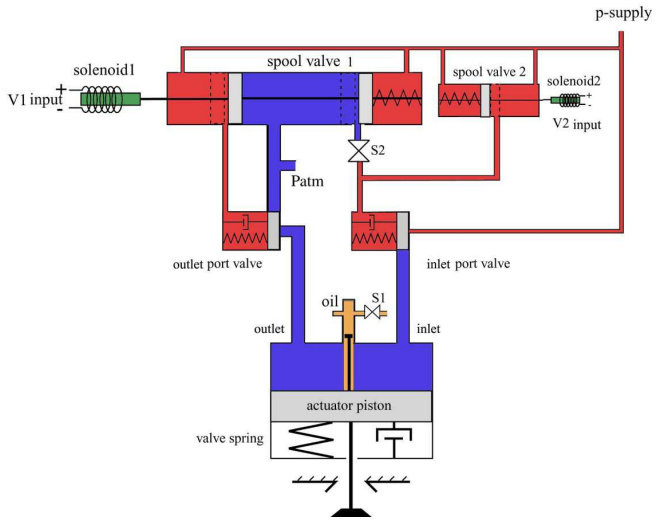

Figure 2: System dynamics at the expansion and dwell stage

Expansion and Dwell Stage In the expansion and dwell stage as shown in Figure (2), solenoid 2 is energized as well. The time delay between the activation of two solenoids is usually chosen from $2ms$ to $5ms$ depending on the desired valve lift height. The spool valve 2 is pushed slightly to the left so that the high pressure air can be sent to the left of the inlet port valve through the second spool valve. The check valve $S2$ is activated at the same time when solenoid 2 is energized to prevent the high pressure air from escaping to the atmosphere through the first spool valve. The inlet port valve is closed due to its area difference at two sides. Meanwhile, solenoid 1 remains energized, therefore, the outlet port valve remains closed. The air that was drawn into the actuator cylinder during the previous (air charging) stage is able to expand completely. The actuator piston and poppet valve both reach their maximum displacement. The high pressure oil (yellow color) trapped in the hydraulic latch (check valve $S1$ is still on) balances the valve spring force and keeps the poppet valve open at its maximum lift height as long as it is needed. This is also called energy saving mode. It allows the system to extract the full expansion work from the air which has entered the cylinder without losing the capability to vary the valve open duration.

Air Discharging stage In the air discharging stage, the air leaves the actuator cylinder and the valve returns to its seat. As displayed in Figure (3), both solenoids are de-energized. Consequently, both check valves, $S1$ and $S2$, are de-activated. The air flow and the oil flow can travel in two directions. Since both solenoids are off, the springs inside the two spool valves can return the spools to their original positions. The high pressure

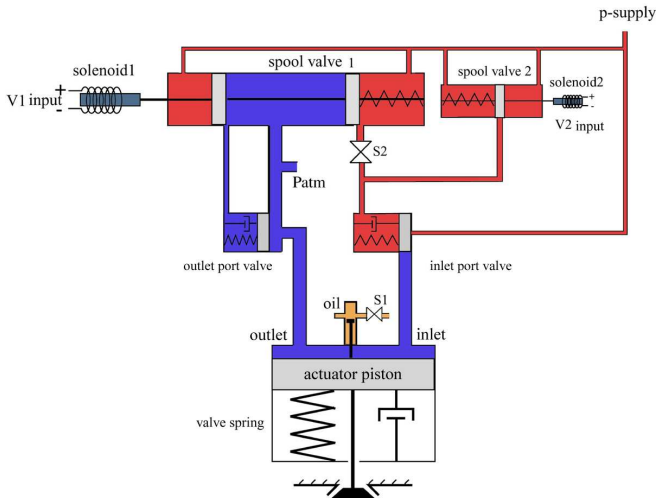

Figure 3: System dynamics at the air discharging stage

air is then sent to both sides of the inlet port valve. The area difference between two sides of this port valve causes it to remain closed. Meanwhile, the low pressure air is on both sides of the outlet port valve. Because the oil in the hydraulic latch is now able to flow back up to its reservoir, there is no resistance for the valve spring to return the actuator piston. The actuator piston comes back and the volume of the air in the actuator cylinder is then reduced. This results in an increase of the air pressure in the actuator cylinder and an increase of the air pressure at the right side of the outlet port valve. Therefore, the outlet port valve is pushed open, the air in the actuator cylinder is able to discharge and its pressure decreases immediately. The poppet valve now returns to the seat. The hydraulic damper starts to function when the poppet valve moves close to its seat. Due to the decreasing flow area where the oil leaves the passage, the velocity of the valve is reduced greatly to provide a smooth return.

MATHEMATICAL MODELING

The purpose of this section is to derive governing equations of the individual components of the pneumatic/hydraulic valve acutator, which consists of the actuator piston, the hydraulic latch/damper, the inlet and outlet port valves, two solenoids and two spool valves as displayed in Figure (1). These equations were used to simulate the behavior of the valve under different sets of operating conditions.

Actuator Piston In this section, energy conservation, mass conservation and Newton's second law were used to determine the following variables: the rate change of the gas pressure inside of the cylinder chamber $\dot{P}_p$, the rate change of density of the gas $\dot{\rho_p}$ and the acceleration of the actuator piston $\ddot{y}$. A sudden reduction in pressure occurs at the inlet port when it opens. This causes the air flow to expand in an explosive fashion. The flow is choked and the pressure at the port stays constant. The difference between the cylinder pressure and the supply pressure decreases as the pressure in the cylinder chamber builds up over time. The air then becomes unchoked and flows through the inlet with decreasing pressure. The flow exiting the outlet switches between a choked and unchoked pattern as well for the same reason. This discontinuous nonlinearity of the flow has to be taken into consideration in the actuator piston model. As

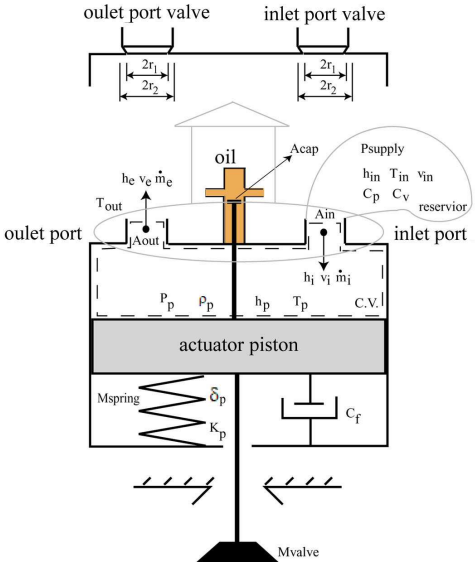

Figure 4: Actuator piston model

shown in Figure (4), considering the control volume above the actuator piston in the cylinder chamber including the inlet and outlet, the first law of thermodynamics can be written as:

$$\dot{Q} - \dot{W} + \dot{m}_i(h_i + \frac{v_i^2}{2}) - \dot{m}_e(h_e + \frac{v_e^2}{2}) = \frac{\partial E}{\partial t} \qquad (1)$$

where,

- $\dot{Q}$ is the heat transfer rate into the control volume
- $\dot{W}$ is the work rate delivered by the control volume to the actuator piston
- $\dot{m}_i$ is the mass flow rate entering the control volume
- $\dot{m}_e$ is the mass flow rate exiting the control volume
- $\dot{h_i}$ is the enthalpy of the gas entering the cylinder chamber
- $\dot{h_e}$ is the enthalpy of the gas exiting the cylinder chamber
- $\frac{\partial E}{\partial t}$ is the rate of change of the total energy of the control volume.

- Evaluation of $\dot{W}$

The rate of the work done on the actuator piston by the control volume is:

$$\dot{W} = A_p P_p \dot{y} \qquad (2)$$

where, A_p is the area of the actuator piston, P_p is the pressure of the control volume (the pressure on the actuator piston) and $\dot{y}$ is the velocity of the actuator piston movement.

- Evaluation of $h_i + \frac{v_i^2}{2}$ and $h_e + \frac{v_e^2}{2}$

The supply air entering the cylinder chamber from the inlet can be viewed as a gas coming from a reservoir. The gas in the reservoir has zero velocity, therefore, its enthalpy is stagnation enthalpy of the inlet supply air h_{in}. For the same reason, the air leaving the cylinder chamber from the outlet can be viewed as a gas leaving a reservoir, which is the control volume inside the chamber. Hence, the enthalpy of the air leaving the chamber can be represented by the stagnation enthalpy of the air in the actuator cylinder h_p.

$$h_i + \frac{v_i^2}{2} = h_{in} = C_p T_{in} \tag{3}$$

$$h_e + \frac{v_e^2}{2} = h_p = C_p T_p \tag{4}$$

Treating air as an ideal gas, we have:

$$P = \rho R T \tag{5}$$

Replacing T_p in Equation (4) with $\frac{P_p}{R\rho_p}$:

$$h_e + \frac{v_e^2}{2} = \frac{C_p P_p}{R\rho_p} \tag{6}$$

where,

- T_{in} is the temperature of the air at the inlet which equals to the ambient temperature $T_{atm} = 295K$
- C_p is the specific heat of the air at constant pressure
- R is the gas constant of the air
- ρ_p is the density of the air in the cylinder chamber above the actuator piston
- P_p is the pressure of the air in the cylinder chamber above the actuator piston
- T_p is the temperature of the air in the cylinder chamber above the actuator piston

- Evaluation of $\dot{m}_i$ and $\dot{m}_e$

In order to draw the equations for the mass flow rate when the air flow enters the inlet or leaves the outlet, we need to consider two cases, choked and unchoked gas flow. The proof of the derivation of the mass flow equation is shown by J. M. Tressler et al. in [9]. We assume that the gas flow in the valve actuator is adiabatic ($\dot{Q} = 0$) for now, and a term proportional to $\dot{W}$ will be subtracted from the total power that is delivered to the actuator piston to compensate the heat loss [10]. We also assume that the flow is isentropic everywhere except across normal shock waves.

Considering the mass flow rate $\dot{m}_i$ at the inlet, the flow patten depends on the cylinder pressure P_p and the supply pressure P_{supply} as follows:

$$\dot{m}_i = \gamma_{in} \sqrt{\frac{k}{RT_{in}}} P_{supply} A_{in} \tag{7}$$

If $P_p > 0.53 P_{supply}$, the unchoked case:

$$\gamma_{in} = \sqrt{\frac{2}{k-1}} \left(\frac{P_p}{P_{supply}}\right)^{\frac{k+1}{2k}} \left[\left(\frac{P_p}{P_{supply}}\right)^{\frac{1-k}{k}} - 1\right]^{\frac{1}{2}} \tag{8}$$

If $P_p \leq 0.53 P_{supply}$, the choked case:

$$\gamma_{in} = 0.58 \tag{9}$$

where, $k = \frac{C_p}{C_v}$ is the specific heat ratio, C_v is the specific heat of air at constant volume. A_{in} is the area of the inlet. Since the port valves open and close very fast, the effective flow area A_{in} can be approximated as:

$$A_{in} = \pi r_1^2, w > 0 \tag{10}$$

$$A_{in} = 0, w = 0 \tag{11}$$

where, r_1 is the inner radius of the inlet port valve. We can derive the mass flow rate $\dot{m}_e$ equation similarly as follows:

$$\dot{m}_e = \gamma_{out} \sqrt{\frac{k}{RT_p}} P_p A_{out} \tag{12}$$

If $P_{out} > 0.53 P_p$, the unchoked case:

$$\gamma_{out} = \sqrt{\frac{2}{k-1}} \left(\frac{P_{out}}{P_p}\right)^{\frac{k+1}{2k}} \left[\left(\frac{P_{out}}{P_p}\right)^{\frac{1-k}{k}} - 1\right]^{\frac{1}{2}} \tag{13}$$

If $P_{out} \leq 0.53 P_p$, the choked case:

$$\gamma_{out} = 0.58 \tag{14}$$

where, A_{out} is the area of the outlet, it follows the same expression as A_{in} except that it is dependent on z. The A_{out} expression can be given as below:

$$A_{out} = \pi r_1^2, z > 0 \tag{15}$$

$$A_{out} = 0, z = 0 \tag{16}$$

where, r_1 is the outer radius of the outlet port valve.

- Evaluation of $\frac{\partial E}{\partial t}$

The rate of change of the total energy of the control volume is the summation of the rate of change of the internal energy, the kinetic energy and the potential energy. The kinetic and potential energy of the control volume are negligible. Hence, the change of the total energy is approximated as the rate of change of the internal energy:

$$\frac{\partial E}{\partial t} = \frac{\partial U}{\partial t} = \frac{d}{dt}(m C_v T_p) \tag{17}$$

m is the mass of air in the control volume and C_v is the specific heat of air at constant volume. The expression for $\dot{m}$ is:

$$\dot{m} = \rho_p A_p \dot{y} \tag{18}$$

Expanding Equation (17), and using Equation (18) and Equation (5) results in:

$$\frac{\partial E}{\partial t} = \frac{A_p C_v}{R}(P_p \dot{y} + \dot{P}_p y) \tag{19}$$

The expression for $\dot{P}_p$ can be derived by substituting Equation (2), (3), (6), (7), (12) and (19) into Equation (1):

$$\dot{P}_p = \frac{1}{A_p y}[C_{din}A_{in}(w)P_{supply}\gamma_{in}\sqrt{k^3 RT_{in}} - C_{dout}A_{out}(z)\gamma_{out}\sqrt{\frac{k^3 P_p^3}{\rho_p}}] - \alpha_p k\frac{P_p\dot{y}}{y} \quad (20)$$

where, C_{din} and C_{dout} are the flow discharge coefficients at the inlet and outlet. α_p is multiplied by the rate change of work $\dot{W}$ because it is assumed that part of the work is dissipated as heat loss from the system. α_p is chosen to be between 0 to 1 depending on the actual heat loss during the process. This formulation is studied by Edmond Richer and Yildirim Hurmuzlu in [10].

Applying the law of mass conservation to the control volume above the actuator piston in the cylinder results in:

$$\dot{m}_i - \dot{m}_e = A_p(\rho_p\dot{y} + \dot{\rho_p}y) \quad (21)$$

Replacing $\dot{m}_i$ and $\dot{m}_e$ by Equation (7) and (12) to obtain the expression for $\dot{\rho_p}$:

$$\dot{\rho_p} = \frac{1}{A_p y}[C_{din}A_{in}(w)\gamma_{in}P_{supply}\sqrt{\frac{k}{RT_{in}}} - C_{dout}A_{out}(z)\gamma_{out}\sqrt{kP_p\rho_p}] - \frac{\rho_p\dot{y}}{y} \quad (22)$$

Now we invoke Newton's second law to obtain the $\ddot{y}$ equation:

$$M\ddot{y} + C_f\dot{y} + K_p(y+\delta_p) = A_pP_p + A_{cap}P_{oil} - (A_p + A_{cap})P_{atm} \quad (23)$$

$$M = M_{piston} + M_{valve} + \frac{1}{3}M_{spring} + M_{cap}$$

where,

- M_{piston} is the mass of the actuator piston
- M_{valve} is the mass of the intake valve
- M_{spring} is the mass of the valve spring. The effective spring mass equals one third of the total spring mass [11]
- M_{cap} is the mass of the cap on the top of the valve stem
- A_{cap} is the area of the cap on the top of the actuator piston stem
- $A_p = \pi r_p^2 - \pi r_{oil}^2$ with r_p as the radius of the actuator piston and r_{oil} as the radius of the oil passage
- C_f is the damping coefficient approximating the energy dissipation due to the friction
- K_p is the stiffness of the valve spring
- δ_p is the preload of the valve spring

Rearranging Equation (23):

$$\ddot{y} = \frac{1}{M}[A_pP_p + A_{oil}P_{oil} - (A_p + A_{oil})P_{atm} - C_f\dot{y} - K_p(y+\delta_p)] \quad (24)$$

Hydraulic Latch/Damper Another mechanism that has a direct impact on the dynamics of the actuator piston is the hydraulic latch/damper. The compressibility of the fluid in the hydraulic latch is considered and the mechanism of adjusting the valve seating velocity is modeled in detail. Figure (5) illustrates

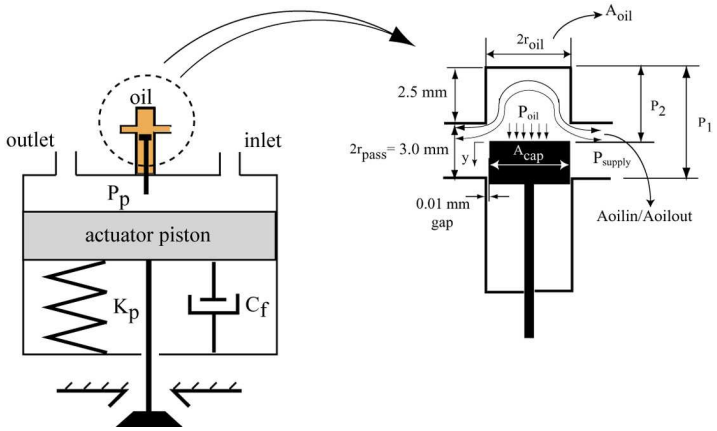

Figure 5: Hydraulic latch/damper model

this function. The oil sits on the top of the actuator piston stem with the supply pressure as the back pressure. Fluid enters or exits through area A_{oilin}/A_{oilout}. When the air that is drawn in at the air charging stage is fully expanded in the actuator cylinder, the actuator piston reaches to its maximum displacement. The check valve $S1$ is activated by solenoid 1 to prevent the oil from returning. (Recall system dynamics at the air charging stage, and expansion and dwell stage.) The pressurized oil is trapped in the passage and keeps the actuator piston at the maximum displacement until solenoid 1 is turned off. (Recall the air discharging stage). Hence, this hydraulic latch provides an adjustable valve open duration. Another function of this mechanism is to provide a low seating velocity for the valve. When the actuator piston approaches the original position, the cap on the top of the stem will partially block the exit area A. The actuator piston encounters a large resistant force due to the reduced flow area, which decreases the velocity tremendously. The smaller the area A, the lower the valve velocity.

Figure (6) shows a valve lift profile with the solenoid action chart. The solenoid itself has about $2ms$ to $3ms$ delay upon activation. These delays were not shown in this chart. As was explained earlier, one valve cycle consists of three stages: air charging, expansion and dwell, and air discharging stage. They will be called stage I, stage II and stage III in this section. Solenoid 1 is on at the beginning of stage I and off at the end of stage II. Solenoid 2 turns on before stage II. Solenoid 2 runs on the same frequency and the same duty cycle as solenoid 1 with a time delay. Both inlet and outlet are closed during the overlap of solenoid 1 and 2. The oil is modeled as an incompressible flow at stage I and III, while in stage II it is modeled as a compressible flow under high pressure with high incompressibility. The slight compressibility is what causes the volume change in the oil passage, hence the swing on the top of the valve lift profile.

- Stage I Air Charging (Incompressible Flow Model)

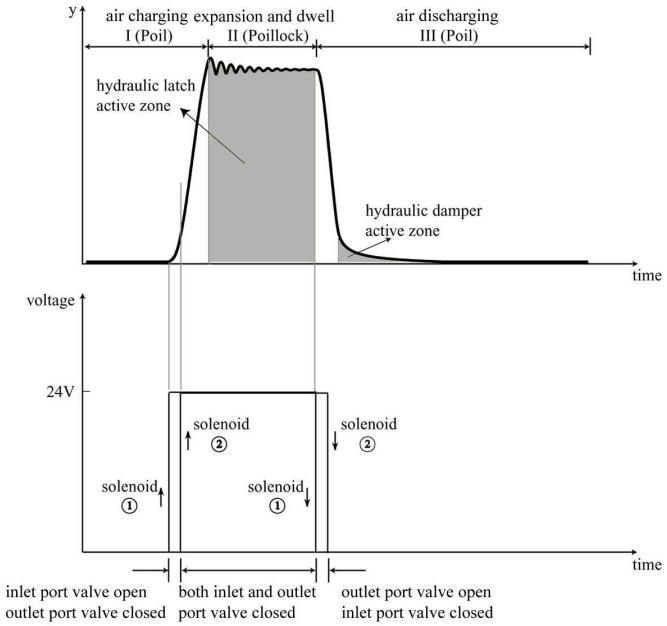

Figure 6: Valve lift profile with the solenoid action chart

$$q_{oil} = C_{d_{oilin}} A_{oilin} \sqrt{\frac{P_{supply} - P_{oil}}{\rho_{oil}}} = A_{cap}\dot{y} \tag{25}$$

Therefore, the pressure of the oil at air charging stage is:

$$P_{oil} = P_{supply} - \left(\frac{A_{cap}\dot{y}}{C_{d_{oilin}} A_{oilin}}\right)^2 \rho_{oil} \tag{26}$$

where,

- q_{oil} is the volumetric flow rate of the fluid
- $C_{d_{oilin}}$ is the discharge coefficient as the fluid enters the passage
- A_{oilin} is the area where the fluid enters the passage (it is calculated later)
- P_{supply} is the air supply pressure
- P_{oil} is the oil pressure and is at the same pressure as air supply
- ρ_{oil} is the density of the fluid

- Stage II Expansion and Dwell (Compressible Flow Model)

The state equation $PV^c = K = constant$ is used here by choosing c very large to represent the high level of incompressibility.

$$P_{oillock} V^c = P_i V_i^c \tag{27}$$

Substituting $V = A_{cap} y$ and $V_i = A_{cap} y_i$ into Equation (27) to obtain:

$$P_{oillock} = \frac{P_i y_i^c}{y^c} \tag{28}$$

Where,

- $P_{oillock}$ is the pressure of the oil at the dwell (lock) stage
- y_i is the maximum valve displacement
- V_i is the volume of the fluid at the maximum valve displacement y_i
- P_i is the oil pressure P_{oil} at the peak valve lift height y_i

- Stage III Air Discharging (Incompressible Flow Model)

Similarly, the equation of motion for stage III was obtained as follows:

$$q_{oil} = C_{d_{oilout}} A_{oilout} \sqrt{\frac{P_{oil} - P_{supply}}{\rho_{oil}}} = A_{cap}\dot{y} \tag{29}$$

Rearrange Equation (29):

$$P_{oil} = P_{supply} + \left(\frac{A_{cap}\dot{y}}{C_{d_{oilout}} A_{oilout}}\right)^2 \rho_{oil} \tag{30}$$

where,

- $C_{d_{oilout}}$ is the discharge coefficient as the fluid exits the passage
- A_{oilout} is the area where the fluid exits the passage A_{oilin}=A_{oilout}=A

Evaluation of A:

$$A = 2\pi r_{pass}^2 + (A_{oil} - A_{cap}), y \leq p_1 \tag{31}$$

$$A = 2\pi \left(\frac{y}{2}\right)^2 + (A_{oil} - A_{cap}), y < p_1 \tag{32}$$

The variables r_{pass}, A_{oil}, A_{cap} and p_1 are shown in Figure (5). The seating velocity is largely reduced while the stem enters the area where $y < p_1$. By adjusting p_1, we can alter its timing of entering the region where $y < p_1$ and consequently the slope of the response.

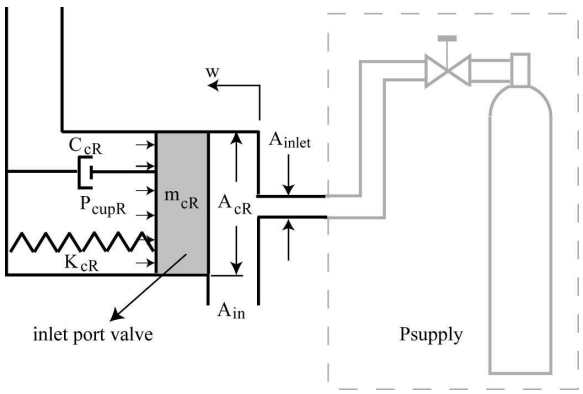

Figure 7: Inlet port valve model

inlet port valve As illustrated in Figure (7), the inlet port valve is modeled as a mass-spring-damper system driven by the air flow from the spool valve with pressure P_{cupR} and the supply with pressure P_{supply}. P_{cupR} alternates between atmosphere and supply pressure which is regulated by the spool valve. Due to the difference between the areas on which P_{cupR} and P_{supply} act, the port valve remains closed when P_{cupR} equals P_{supply} and the supply air pushes it open when P_{cupR} reaches atmosphere pressure. The supply air is treated as a stagnant flow with constant pressure. We obtain the equation of motion by Newton's second law as below:

$$m_{cR}\ddot{w} + C_{cR}\dot{w} + K_{cR}w = P_{supply}A_{inlet} - P_{cupR}A_{cR} \quad (33)$$
$$0 \leq w \leq w_{max}, A_{inlet} = \pi r_2^2 - \pi r_1^2, A_{cR} = \pi r_2^2$$

- m_{cR} is the mass of the inlet port valve
- C_{cR} is the damping coefficient compensating for the friction loss of the valve
- K_{cR} is the spring constant
- w, $\dot{w}$, $\ddot{w}$ are the displacement, velocity and the acceleration of the inlet port valve
- w_{max} is the maximum distance which the inlet port valve is allowed to travel. The discontinuous nonlinearity in the port valve dynamics caused by this physical limitation was considered.
- r_2 is the outer radius of the inlet and outlet port valve (see Figure (4)).

Rearranging Equation (33) to obtain expression for $\ddot{w}$:

$$\ddot{w} = \frac{1}{m_{cR}}(A_{inlet}P_{supply} - P_{cupR}A_{cR} - C_{cR}\dot{w} - K_{cR}w) \quad (34)$$

outlet port valve The outlet port valve functions in a similar way as the inlet port valve, except that the air that pushes the port valve open has the actuator cylinder pressure. The pressure in the actuator cylinder is unsteady, thus, the flow dynamics were modeled. The modeling process is similar to the actuator piston. The control volume used here is shown in Figure (8). Applying conservation of energy as shown in Equation (1), we evaluate $\dot{W}$, $\frac{\partial E}{\partial t}$, $h_i + \frac{v_i^2}{2}$ $h_e + \frac{v_e^2}{2}$ $\dot{m}_i$ and $\dot{m}_e$ as follows:

$$\dot{W} = A_{cL}P_{out}\dot{z} \quad (35)$$
$$A_{cL} = \pi r_2^2$$

where, P_{out} is the pressure on the outlet port valve in the control volume.

$$\frac{\partial E}{\partial t} = \frac{\partial U}{\partial t} = \frac{d}{dt}(mC_vT_{out}) = \frac{A_{cL}C_v}{R}(P_{out}\dot{y} + \dot{P_{out}}y) \quad (36)$$

where z is the displacement of the outlet port valve, T_{out} is the gas temperature in the control volume and P_{out} is the gas pressure in the control volume. The ideal gas law, Equation (5),

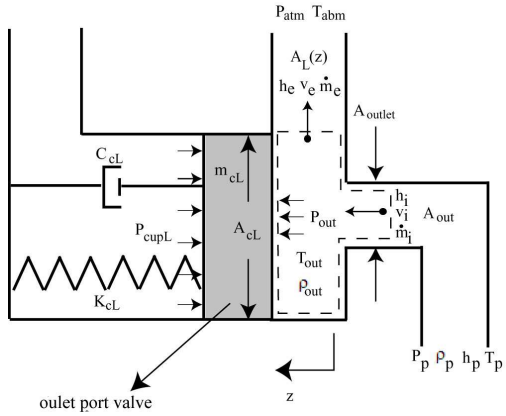

Figure 8: Outlet port valve model

was used to derive Equation (36). Treating the air flow from the actuator cylinder and the ambient air as stagnant flow we have:

$$h_i + \frac{v_i^2}{2} = h_p = C_pT_p = \frac{C_pP_p}{\rho_pR} \quad (37)$$

$$h_e + \frac{v_e^2}{2} = h_{atm} = C_pT_{atm} \quad (38)$$

$$\dot{m}_i = \gamma_{inL}\sqrt{\frac{k}{RT_p}}P_pA_{out} = A_{out}\gamma_{inL}\sqrt{k\rho_pP_p} \quad (39)$$

where A_{out} is the inlet area of the control volume. As it is drawn in Equation (15) and Equation (16), A_{out} can be approximated as:

$$A_{out} = \pi r_1^2, z > 0 \quad (40)$$
$$A_{out} = 0, z = 0 \quad (41)$$

If $P_{out} > 0.53P_p$, the unchoked case:

$$\gamma_{inL} = \sqrt{\frac{2}{k-1}}(\frac{P_{out}}{P_p})^{\frac{k+1}{2k}}\left[(\frac{P_{out}}{P_p})^{\frac{1-k}{k}} - 1\right]^{\frac{1}{2}} \quad (42)$$

If $P_{out} \leq 0.53P_p$, the choked case:

$$\gamma_{inL} = 0.58 \quad (43)$$

$$\dot{m}_e = \gamma_{outL}\sqrt{\frac{k}{RT_{out}}}P_{out}A_L = A_L\gamma_{outL}\sqrt{k\rho_{out}P_{out}} \quad (44)$$

where,

- T_{out} is the temperature of the gas in the control volume
- P_{out} is the is the pressure of the air in the
- ρ_{out} is the density of the air in the control volume

and A_L is the outlet area of the control volume and is also a function of geometry and the displacement of the outlet port valve.

$$A_L = 2\pi r_1 z \quad (45)$$

If $P_{atm} > 0.53P_{out}$, the unchoked case:

$$\gamma_{outL} = \sqrt{\frac{2}{k-1}}(\frac{P_{atm}}{P_{out}})^{\frac{k+1}{2k}}\left[(\frac{P_{atm}}{P_{out}})^{\frac{1-k}{k}} - 1\right]^{\frac{1}{2}} \quad (46)$$

If $P_{atm} \leq 0.53 P_{out}$, the choked case:

$$\gamma_{outL} = 0.58 \tag{47}$$

Here, the gas was assumed ideal and the nonlinearity of the flow was considered in Equations (42), (43), (46) and (47). One can obtain the equation of $\dot{P_{out}}$ in the following form by substituting Equation (35)-(47) into Equation (1) and letting $\dot{Q} = \alpha_L \dot{W}$ as it was treated in the actuator piston model:

$$\dot{P_{out}} = \frac{1}{A_{cL} z}[C_{dinL} A_{out}(z) P_p \gamma_{inL} k P_p \sqrt{\frac{kP_p}{\rho_p}} - C_{doutL} \tag{48}$$
$$A_L(z) \gamma_{outL} R k T_{atm} \sqrt{k \rho_{out} P_{out}}] - \alpha_L k \frac{P_{out} \dot{z}}{z}$$

Here, α_L is a number from 0 to 1 depending on heat loss, and C_{dinL} and C_{doutL} are the discharge coefficients. Applying mass conservation law to the control volume results in:

$$\dot{m_i} - \dot{m_e} = A_{cL}(\rho_{out} \dot{z} + \dot{\rho_{out}} z) \tag{49}$$

Replacing $\dot{m_i}$ with Equation (39) and replacing $\dot{m_e}$ with Equation (44) in the equation above, $\dot{\rho_{out}}$ equation can be written as below:

$$\dot{\rho_{out}} = \frac{1}{A_{cL} z}[C_{dinL} A_{out}(z) \gamma_{inL} \sqrt{k \rho_p P_p} \tag{50}$$
$$-C_{doutL} A_L(z) \gamma_{outL} \sqrt{k P_{out} \rho_{out}}] - \frac{\rho_{out} \dot{z}}{z}$$

Finally, Newton's Second Law yields the equation of motion of the outlet port valve:

$$m_{cL} \ddot{z} + C_{cL} \dot{z} + K_{cL} = A_{outlet} P_{out} - A_{cL} P_{cupL} \tag{51}$$
$$0 \leq z \leq z_{max}, A_{outlet} = \pi r_1^2, A_{cL} = \pi r_2^2$$

- m_{cL} is the mass of the outlet port valve
- C_{cL} is the damping coefficient compensating for the friction loss of the valve
- K_{cL} is the spring constant
- z, $\dot{z}$, $\ddot{z}$ are the displacement, velocity and the acceleration of the outlet port valve
- z_{max} is the maximum distance which the outlet port valve is allowed to travel. The discontinuous nonlinearity in the port valve dynamics was considered in the simulation.

Rearranging Equation (51) to obtain an expression for $\ddot{z}$ results in:

$$\ddot{z} = \frac{1}{m_{cL}}(A_{outlet} P_{out} - P_{cupL} A_{cL} - C_{cL} \dot{z} - K_{cL} z) \tag{52}$$

All the discharge coefficients that are involved in the flow equations were determined numerically and experimentally.

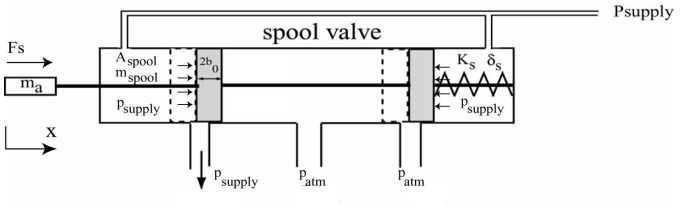

Figure 9: Spool valve model

Spool Valve The armature of the solenoid pushes the stem of the spool valve with the magnetic force F_s when the solenoid is energized and a pre-compressed spring returns the spool valve when the solenoid is de-energized. The spool valve is pressure balanced at two ends as shown in Figure (9). The equation of motion of the spool valve is:

$$m_{spool} \ddot{x} + C_s \dot{x} + K_s(x + \delta_s) = F_s, 0 < x < x_0 \tag{53}$$

Where m_{spool} is the mass of the spool valve, C_s is the damping coefficient modeling the frictional loss, K_s and δ_s are the stiffness and preload of the spring.

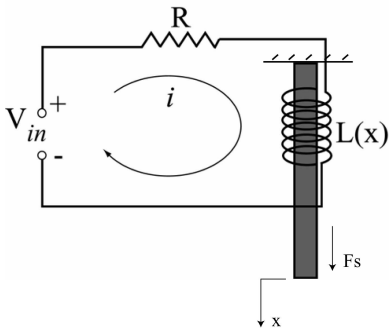

Figure 10: Solenoid model

Solenoid A solenoid can be modeled as an RLC circuit as shown in Figure (10). The Kirchoff law writes:

$$V_{in} - iR - L\frac{di}{dt} = 0 \tag{54}$$

Where, V_{in} is the pulse input voltage, i is the current, R and L are the resistance and the inductance of the solenoid. The relationship between the current i in the coils and the magnetic force F_s on the armature is assumed to take the following form:

$$F_s = L + \frac{bi^2}{1 + \frac{x}{a}} \tag{55}$$

Here, a and b are chosen to curve fit the empirical data provided by the manufacture.

SIMULATIONS AND EXPERIMENTS

Experimental Setup Figure (11) displays the devices that were used in the experiments. A Ford 5.4 liter 4-valve V8 engine head was used for the valve test. The camshaft was removed on the intake valve side and an EPVA was installed above one of the intake valves. A Micro-Epsilon optoNCDT 1605 point range laser sensor was used to measure the displacement of the test intake valve. The laser sensor was mounted on

an angle such that the laser beam from the emitter of the laser sensor would be perpendicular to the surface of the end of the valve stem. A dSPACE DS1104 PCI board was used for control and data acquisition. A switching circuit made of IGBT's (insulated gate bipolar transistor) amplified the signal from the computer and served as a driving circuit for the solenoids. Two STP2416-015 small push-pull solenoids were used to drive two spool valves in the EPVA. A DC power supply from Extech Instruments model 382203 was used to provide the electrical power for both the sensor and the circuit.

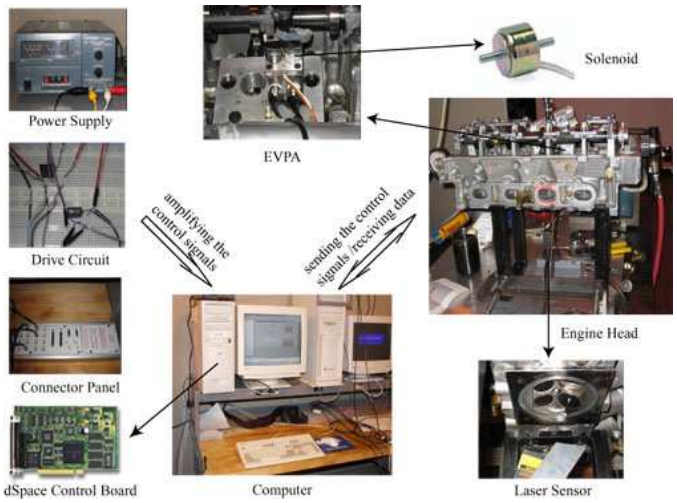

Figure 11: Experimental setup

The experiments were conducted under the combinations of various control parameters:

- $30psi$ and $40psi$ supply pressure
- $100ms$, $40ms$ and $24ms$ solenoid durations that were corresponding to $1200rpm$, $3000rpm$ and $5000rpm$ engine speeds
- 30% and 25% solenoid duty cycles
- $5ms$ and $3ms$ time delays between the first solenoid and the second solenoid

As given in Table 1, the experiment matrix listed 18 combinations of parameter sets under which the experiments were conducted, and the responses were compared with the simulation responses in the next section. The EPVA is aimed to tailor the engine intake flow without throttling. Therefore, in the experiments and simulations, the engine intake manifold pressure is considered to be close to atmospheric pressure. Since it is the intake valve that is being studied in here, no pressure loads are included on the valve head. In future studies where the exhaust valve will be studied, the valve will have to open against a high engine cylinder pressure. This model is capable of this type of simulation, but it is not included here since no experimental data is available for validation at this time.

Simulation The equations of motion derived previously were written in state space form and programmed in $Simulink^{TM}$. Figure (12) shows the schematic diagram programmed in $Simulink^{TM}$. The simulations were performed under the same

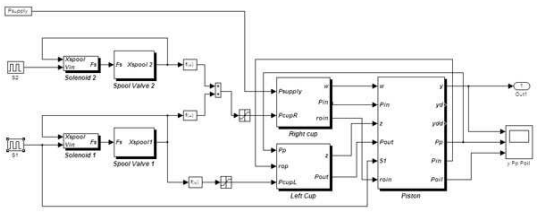

Figure 12: Schematic diagram of the model in $Simulink^{TM}$

parameter sets as were the experiments. The eighteen experiment and simulation responses are presented in Figure (13) through Figure (21). The dotted lines represent experimental responses and the solid lines represent the simulation responses. Figure (13) shows the responses under $30psi$ supply pressure, $100ms$ solenoid period with 30% duty cycle and $5ms$ vs. $3ms$ delay between two solenoids. The $100ms$ solenoid period corresponding to the engine speed at $1200rpm$. The response with $5ms$ delay had about $6ms$ rising time and the response with $3ms$ delay had about $5ms$ rising time. The maximum valve lift height was $6mm$ for the response with $5ms$ delay and $3.8mm$ for the response with $3ms$ delay. The swing motion on the top of the profile shows that the valve is in the dwell stage when the hydraulic latch is utilized to hold the valve open. The slight compressibility of the oil in the hydraulic latch causes the oscillation of the valve response which damps out eventually. The hydraulic damper is initiated at $3.7ms$, where the slope of the response is largely decreased and the response approaches to the original position gradually afterwards. The responses in Figure (14) were obtained under the same operating conditions as those in Figure (13) except that the solenoid period was reduced to $40ms$, corresponding to $3000rpm$. The rising time of the response with $5ms$ and response with $3ms$ were $6ms$ and $5ms$. As the solenoid period is reduced, the dwell stage is shorter. The maximum valve lift height is $6mm$ for the response with $5ms$ delay and $4mm$ for the response with $3ms$ delay. The solenoid period then was reduced to $24ms$, corresponding to $5000rpm$. The responses are shown in Figure (15). In this case, the maximum valve lift is $5mm$ and the rising time is $6ms$ for the response with $5ms$ delay. The maximum valve lift is $4mm$ and the rising time is $5ms$ for the response with $3ms$ delay. The maximum valve lift height in the $5ms$ delay case is decreased from $6mm$ to $5mm$. This happens because the solenoid is de-energized before the actuator piston can fully expand to its maximum displacement; the valve has to return without reaching its maximum lift. Moreover, the valve never enters the dwell stage in this pair of responses. The solenoid period is so short that the valve entered the air discharging stage immediately after the air charging stage. Hence, the swing motion disappears on the top of the profile. The experiment and simulation responses at $40psi$ pressure supply with 30% and 25% solenoid duty cycles are presented in Figure (16) through Figure (21). The response rising time of the valve varies from $4ms$ to $6ms$. The maximum valve lift is around $8mm$ for the response with $5ms$ delay and $6mm$ for the response with $3ms$ delay in this case. As was expected, the valve lift height could be controlled by regulating the supply pressure or varying the delay between two solenoids, and the valve open duration could be controlled by controlling

Control Parameters	The combinations of parameter sets Parameters																	
Supply Pressure (psi)	30						40											
Solenoid Period (ms)	100		40		24		100				40				24			
Solenoid Duty Cycle ($\%$)	30		30		30		30		25		30		25		30		25	
Time Delay Between Two Solenoids (ms)	3	5	3	5	3	5	3	5	3	5	3	5	3	5	3	5	3	5
In total 18 experiments were conducted under various combinations of parameter sets.																		

Table 1: The Experiment Matrix

the activation duration of the solenoid. The mathematical model was able to capture the dynamics of the EPVA closely.

CONCLUSIONS

This article presented a dynamic model for an electrically controlled pneumatic/hydraulic valve actuator. This model will be incorporated to develop criteria for both design and control of the valvetrain in a camless internal combustion engine. Two solenoids and two spool valves, a single acting cylinder, an inlet port valve, an outlet port valve, a hydraulic latch/damper and an intake valve with its valve spring were included in this model. The mathematical model employed Newton's law, mass conservation and principle of thermodynamics. The nonlinearity of the flow, incompressibility and compressibility of the hydraulic fluid and the nonlinearity of the motion due to the physical constraint was carefully considered in the modeling process. The control parameters were studied. The model was implemented in $Simulink/Matlab^{TM}$ under different combinations of operation conditions. Validation experiments were performed on a Ford 5.4 liter 4-valve V8 engine head with various air supply pressures, solenoid periods, solenoid duty-cycles and time delay between two solenoids. The numerical simulation results were compared with the experimental data and showed excellent agreement.

REFERENCES

[1] J.W.G.Turner, M.D.Bassett, R.J.Pearson, G.Pitcher and K.J.Douglas, "New Operating Strategies Afforded by Fully Variable Valve Trains", *SAE International 2004-01-1386*, 2004 Society of Automotive Engineers World Congress, Detroit, MI, April 2004.

[2] Chihaya Sugimoto, Hisao Sakai, Atsushi Umemoto, Yasuo Shimizu and Hidetaka Ozawa, "Study on Variable Valve Timing System Using Electromagnetic Mechanism", *SAE International 2004-01-1869*, 2004 Society of Automotive Engineers World Congress, Detroit, MI, April 2004.

[3] Mark A.Theobald, Bruno Lequesne and Rassem R.Henry, "Control of Engine Load via Electromagnetic Operating Actuator", *SAE paper number 940816*, 1994

[4] F.Pischinger and Rassem P.Kreuter, "Electromagnetically Operating Actuator", *U.S. Patent number 4,455,543*, June 19, 1984

[5] H.P.Lenz, B.Geringer and G.Smetana, "Initial Test Results of an Electro-Hydraulic Variable Valve Actuation System on a Firing Engine", *SAE paper number 890678*, 1989

[6] W.E.Richeson, and F.L.Erickson, "Pneumatic Actuator with Permanent Magnet Control Valve Latching", *U. S. Patent number 4,852,528*, August 1, 1989

[7] John P.Watson and Russell J.Wakeman, "Simulation of a Pneumatic Valve Actuation System for Internal Combustion Engine", *SAE International 2005-01-0771*, 2005 Society of Automotive Engineers World Congress, Detroit, MI, April 2005.

[8] James E.Bobrow and Brian W.McDonell, "Modeling and Control of a Variable Valve Timing Engine", *Proceedings of the American Control Conference*, Chicago, IL, June 2000.

[9] J.M.Tressler, T.Clement, H.Kazerooni and M.Lim, "Dynamic Behavior of Pneumatic Systems for Lower Extremity Extenders", *Proceedings of the 2002 IEEE International Conference on Robotics & Automation*, Washington, D.C., May 2002.

[10] Edmond Richer and Yildirim Hurmuzlu, "A High Performance Pneumatic Force Actuator System: Part I- Nonlinear Mathematical Mode", *Transactions of the ASME*, Vol. 122, pp. 416-425 September 2000.

[11] William T.Thomson, Theory of vibration with applications", *5th ed., Prentice Hall*, Upper Saddle River, New Jersey, c1998.

[12] Y.A.Cengel and M.A.Boles, "Thermodynamics: An Engineering Approach", *McGraw-Hill*, New York, N.Y., 1994.

[13] B.S.Massey, "Mechanics of fluids", *Wokingham*, Berkshire, England, 1983.

[14] A.M.Al-Ibrahim and D.R.Otis, "Transient Air Temperature and Pressure Measurement During the Charging and Discharging Processes of an Actuating Pneumatic Cylinder", *Proceedings of the 45th National Conference on Fluid Power*, 1992

[15] C.B.Schuder and R.C.Binder, "The Response of Pneumatic Transmission Lines to Step Inputs", *ASME Journal, Basic Engineering*, Vol 81, pp. 578-584, 1959.

[16] D.A.Hullender and R.L.Woods, "Modeling of Fluid Control Components", *Proceeding of the First Conference on Fluid Control and Measurement*, FLUCOME '85, Pregamon Press, London, 1985.

[17] D.Ben-Dov and S.E.Salcudean, "A Force-Controlled Pneumatic Actuator", *IEEE Transactions on Robotics and Automation*, Vol. 11, No. 6, pp. 906-911, 1995.

[18] John B.Heywood, "Internal Combustion Engine Fundementals", *McGraw-Hill*, Singapore, 1988.

[19] John P.Watson and Russell J.Wakeman, "Modeling, Identification, and Control of a Pneunatically Actuated Force Controllable Robot", *IEEE Transactions on Robotics and Automation*, Vol. 14, No. 5, October 1998

[20] J.O.Hougen, O.R.Martin and R.A.Walsh, "Dyanmics of Pneumatic Transmission Lines", *Energy Conservation Management*, Vol 35, No. 1, pp. 61-77, 1963.

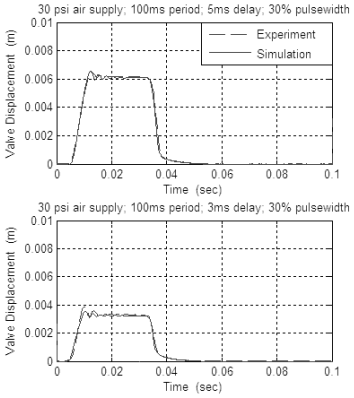

Figure 13: Simulation and experiment responses; $30psi$ pressure supply; $100ms$ solenoid period; 30% solenoid duty cycle; $5ms$ and $3ms$ time delay between two solenoids

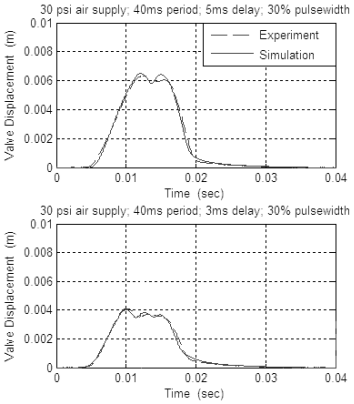

Figure 14: Simulation and experiment responses; $30psi$ pressure supply; $40ms$ solenoid period; 30% solenoid duty cycle; $5ms$ and $3ms$ time delay between two solenoids

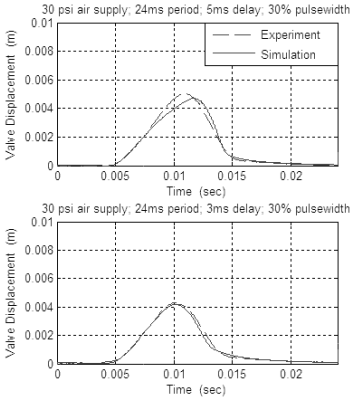

Figure 15: Simulation and experiment responses; $30psi$ pressure supply $24ms$ solenoid period; 30% solenoid duty cycle; $5ms$ and $3ms$ time delay between two solenoids

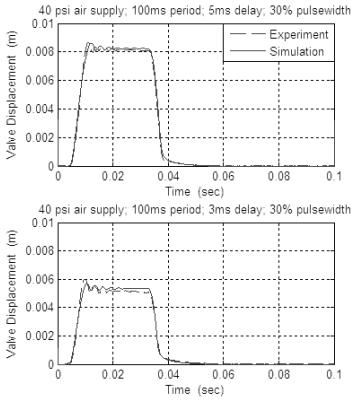

Figure 16: Simulation and experiment responses; $40psi$ pressure supply; $100ms$ solenoid period; 30% solenoid duty cycle; $5ms$ and $3ms$ time delay between two solenoids

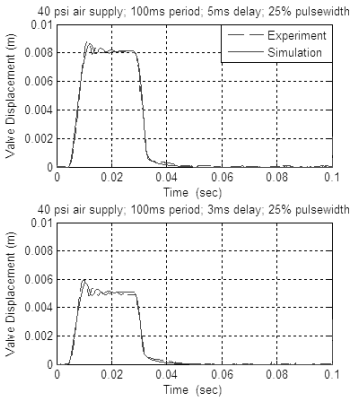

Figure 19: Simulation and experiment responses; $40psi$ pressure supply; $100ms$ solenoid period; 25% solenoid duty cycle; $5ms$ and $3ms$ time delay between two solenoids

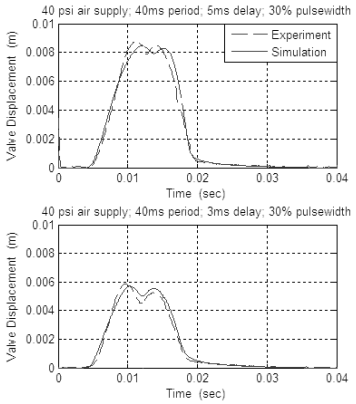

Figure 17: Simulation and experiment responses; $40psi$ pressure supply; $40ms$ solenoid period; 30% solenoid duty cycle; $5ms$ and $3ms$ time delay between two solenoids

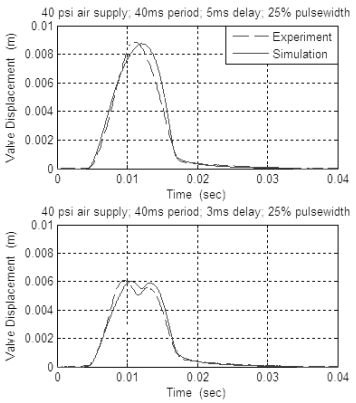

Figure 20: Simulation and experiment responses; $40psi$ pressure supply; $40ms$ solenoid period; 25% solenoid duty cycle; $5ms$ and $3ms$ time delay between two solenoids

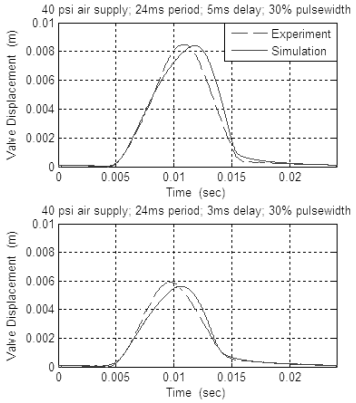

Figure 18: Simulation and experiment responses; $40psi$ pressure supply; $24ms$ solenoid period; 30% solenoid duty cycle; $5ms$ and $3ms$ time delay between two solenoids

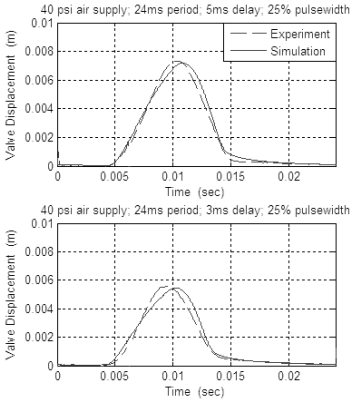

Figure 21: Simulation and experiment responses; $40psi$ pressure supply; $24ms$ solenoid period; 25% solenoid duty cycle; $5ms$ and $3ms$ time delay between two solenoids

2007-01-1297

Model Reference Adaptive Control of a Pneumatic Valve Actuator for Infinitely Variable Valve Timing and Lift

Jia Ma, Tom Stuecken, Harold Schock
Michigan State University, Automotive Research Experiment Station, 3361 Hulett Road, Okemos, MI 48864

Guoming Zhu, Jim Winkelman
Visteon Corporation, One Village Center Dr., Van Buren TWP, MI 48111

Abstract

Electro-pneumatic valve actuators are used to eliminate the cam shaft of a traditional internal combustion engine. They are used to control the opening timing, duration, and lift of both intake and exhaust valves. A physics based nonlinear mathematical model called the level one model was built using Newton's law, mass conservation and thermodynamic principles. A control oriented model, the level two model, was created by partially linearizing the level one model for model reference parameter identification. This model reduces computational throughput and enables real-time implementation. A model reference adaptive control system was used to identify the nonlinear parameters that were needed for generating a feedforward control signal. The closed-loop valve lift tracking, valve opening and closing timing control strategies were proposed. The closed-loop lift control algorithm was developed and implemented in a prototype controller, and validated on a valve test bench with multiple reference valve lift set points at both $1200rpm$ and $5000rpm$ engine speeds. The experiment results showed that the actual valve lift reached the reference lift within $0.5mm$ of lift error in one cycle at $1200rpm$ and in two cycles at $5000rpm$. The maximum steady state lift errors are less than $0.4mm$ at high valve lift and less than $1.3mm$ at low valve lift. Furthermore, the closed-loop valve lift control improved valve lift repeatability with more than 30% reduction of standard deviation over the open-loop control.

INTRODUCTION

The implementation of variable intake and/or exhaust valve timing and lift (VVT and VVL) in an Internal Combustion (IC) engine can significantly improve the fuel economy, emissions, and power output. A significant amount of research has been conducted to demonstrate the advantage of Variable Valve Actuation (VVA) over the traditional cam-based valve-train of both gasoline and diesel engines. The investigation of intake valve timing control of a Spark Ignited (SI) engine was conducted in [1]. It was found that at low and partial load conditions, engine pumping loss was reduced between 20% and 80% due to throttless operation. Fuel consumption was improved up to 10% at idle. Through simulation and experiments, reference [2] shows that SI engine efficiency can be improved up to 29% due to Variable Valve Timing (VVT), compared to a classic (throttled) engine. The engine torque output is also improved by up to 8% at low speed with wide open throttle. Research carried out in [3] demonstrates how VVT and VVL (Variable Valve Lift) affect the partial load fuel economy of a light-duty diesel engine. In this case, the indicated and brake-specific fuel consumptions were improved up to 6% and 19% respectively. The operation of an Otto-Atkinson cycle engine by late intake valve closing to have a larger expansion ratio than compression ratio was studied in [4]. A significant improvement of CO and NOx was obtained. Reference [5] also shows that the operational range of a Homogeneously Charged Compression Ignition (HCCI) engine can be expanded to both high and low load ranges through the adoption of VVT and VVL. The advantages of VVT and VVL engines lead to the development of their optimization over engine operational range. For example, reference [6] developed the VVT and VVL optimization methodology for an I4 2.0L camless ZETEC engine at various operational conditions including cold starts, cylinder deactivation, full load, idle and transient operations.

VVA or VVT and VVL can be achieved with mechanical (cam-based), electro-magnetic (electric mechanical), electro-hydraulic, and electro-pneumatic valvetrain mechanisms. The cam based variable valve actuation is able to provide either a multiple stepping or a continuously changing valve timing phase shift. The Honda mechanism [7] is a multiple-step actuator that allows switching between two cams. The Toyota system [8] allows the intake and exhaust cams to shift continuously without the flexibility of varying the valve lift and duration. BMW's valvetronic system [9] combines variable cam phasing with a continuously variable valve lift and duration actuation.

Infinitely variable valvetrain, often referred to camless valvetrain, includes electro-magnetic, electro-hydraulic, and electro-pneumatic actuation. The electro-magnetic systems, such as GM Magnavalve [10], FEV [11], Aura [12] and Visteon [13] systems, are capable of generating variable valve timing and duration but with fixed lift operation. The electro-hydraulic systems, such as the Sturman system [14], Ford and GM "camless" systems ([15] and [16]), provide infinitely variable valve timing, duration, and lift. The electro-pneumatic valve actuator (EPVA) [17] utilizes the supplied air pressure to actuate either the intake or exhaust valve by electronically controlling two solenoids. For both electro-hydraulic and electro-pneumatic valves, there is a potential issue of having a repeatable valve lift over the engine operational range and the life of an engine.

Valve lift control for electro-hydraulic valvetrain actuation has been investigated by number of researchers. Adaptive peak lift control was presented in [18], a digital valve technology was applied to control an hydraulic valve actuator in [19], and a sliding mode control method was utilized to vary valve timing in [20]. This paper proposed an adaptive valve lift and timing control schemes for an electro-pneumatic valve actuator (EPVA) to improve its transient and steady state responses. A control oriented electro-pneumatic valve model was developed to be used for adaptive parameter identification; and a PI (Proportional and Integral) closed-loop control strategy of valve lift and timing tracking was developed utilizing the identified parameters for feedforward control. The algorithm was implemented in a prototype controller and validated on a valve test bench using a 5.4 liter 3-valve V8 engine head modified for the EPVA valves. The detailed model reference adaptation technique used in the control system can be found in [21].

The paper is organized as follows. First, a physics based nonlinear model is introduced. A control oriented model is described in the Modeling section. Next, the adaptive parameter identification and the closed-loop valve lift and timing control strategies are discussed in the Control Strategy section. Third, the experimental responses of the open-loop valve operation at both low and high engine speeds are presented with their statistical analysis in the Experimental Implementation section. Then, the experimental results of the closed-loop valve lift control algorithm are shown and discussed at both low and high engine speed in the Closed-loop Valve Lift Control Experimental Responses section. Finally, conclusions are drawn.

MODELING

Two valve actuator models were developed prior to the controller design. First, a physics based mathematical model, called a level one model, was built component by component, where the air flow and oil fluid dynamics were considered. This is a sophisticated nonlinear valve model which requires heavy computational throughput and would be almost impossible to be implemented in a real time controller. But it provides a profound understanding of the pneumatic-mechanical system. This leads to the development of a control oriented second model, called a level two model. This control oriented model was utilized in real time implementation.

SYSTEM DYNAMICS Figure (1) is a schematic diagram of the valve actuator dynamics. EPVA consists of an actuator piston, a hydraulic latch (damper), inlet and outlet port valves, two solenoids and two spool valves. The actuator piston is driven by compressed air. It sits on the back of the valve stem, hence, its motion is equivalent to the valve motion.

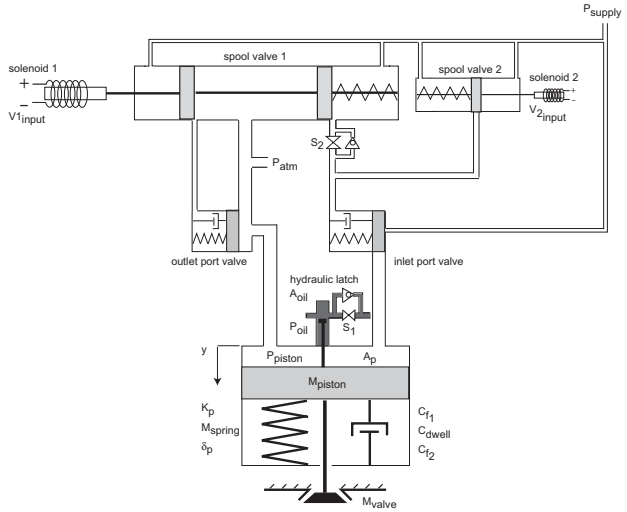

Figure 1: Level two model simulation and experiment responses

The system dynamics illustrated here focuses on the interrelation between the solenoid control commands and the actuator piston motion. As shown in Figure (2), the valve response can be divided into three stages. They are the open stage (I), dwell stage (II) and close stage (III). During the open stage, solenoid 1 is activated; the valve is pushed open by high pressure air. Solenoid 2 is then activated with a time lag δ_1 to stop air charging the cylinder, and at the same time, the controlled check valve $S2$ changed its state from a bypass valve to a check valve due to the activation of solenoid 2. Note that the interplay between two solenoids indeed results in a pulse force input from the supply air to the actuator system. The high pressure air enclosed in the cylinder expands until it balances with the valve spring force. During this period, the valve continues to open and reaches its reference valve lift. At the end of this period, the valve is held open and the system enters the dwell stage. The mechanism that holds the valve open is the hydraulic latch $S1$. It is a one-way check valve when solenoid 1 is active and a bypass valve when solenoid 1 is inactive. This means that in both opening and dwelling stages, the oil can flow from the reservoir into the passage above the piston stem but it can not flow back out. Thus, the pressurized oil applies to the back of the piston stem and holds the valve open at its reference lift. At the end of the dwell stage, solenoid 1 is deactivated to discharge the piston pressure. The hydraulic latch is switched from a one-directional check valve to a bypass one. It allows the oil to travel in and out of the passage. This begins close stage where the valve is returned by the spring force. The close stage can be divided into two sub-stages: during the first substage, the valve returns due to the valve spring force and creates a free vibration response with nonzero initial displacement; and in the second substage, the hydraulic damper is activated. It generates a hydraulic force against the piston return, and that consequently reduces the valve velocity while it approaches the seat. However, there are time delays between the activation of solenoids and the physical movement of the valve actuator. The diagnostic of

system delays and the effects of the system delays on the control commands are described in the level two model response sections. When the engine speeds up to a certain point, the solenoid period becomes so small that solenoid 1 deactivates before the valve reaches the equilibrium open position. The cylinder is discharged before the hydraulic latch has a chance to be engaged. Then the valve would not have a dwell stage or holding period and the lift profile would have a bell shape in this situation .

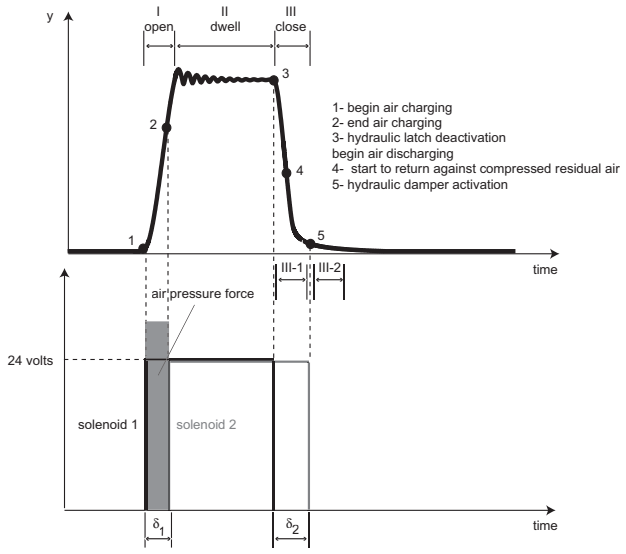

Figure 2: Valve lift profile with the solenoid action chart excluding system delays

LEVEL ONE MODEL The purpose of this section is to depict the technique used to derive the governing equations of the level one model. The complete formulation process and the validation of this level one model can be found in [17]. Control volumes are drawn and the mass conservation and thermodynamic principles are used to model the flow and fluid behavior in the individual components of the pneumatic/hydraulic valve actuator, which consists of the actuator piston, the hydraulic latch/damper, the inlet and outlet port valves, two solenoids and two spool valves (see Figure (1)). Although the hydraulic latch/damper mechanism is one component, it is essentially a hydraulic latch in dwell stage to hold the valve open and a hydraulic damper to slow down the valve seating velocity at the end of close stage. These two functionalities have to be modeled differently. The fluid in the hydraulic latch is modeled as an incompressible flow at the open and close stage but a compressible flow with low compressibility at the dwell stage due to a high pressure during this stage. This captures the swing on the top of the valve lift profile (see Figure (2)). At the end of the close stage, the hydraulic damper kicks in as the valve approaches the seat where the fluid is treated as an incompressible flow. The air is modeled as a compressible flow in all stages. Newton's law is used to model the physical motion of every moving part involved in the individual components.

The modeling of the actuator piston cylinder is highlighted here to illustrate the points. The rest of the component were modeled in a similar manner. A control volume is drawn on the top of the piston in Figure (3)). The following variables: the rate change of the gas pressure inside of the cylinder chamber $\dot{P}_p$, the rate change of density of the gas $\dot{\rho_p}$ and the acceleration of the actuator piston $\ddot{y}$ need to be determined. Equations (1), (2) and (3) are written based on the first law of thermodynamics, principle of mass conservation and Newton's law. After evaluating every element in the three fundamental equations with the only unknowns as P_p, ρ_p, y and their derivatives, Equations (4), (5) and (6) are obtained. A sudden reduction in pressure occurs at the inlet port when it opens. This causes the air flow to expand in an explosive fashion. The flow is choked and the pressure at the port stays constant. The difference between the cylinder pressure and the supply pressure decreases as the pressure in the cylinder chamber builds up over time. The air then becomes unchoked and flows through the inlet with decreasing pressure. The flow exiting the outlet switches between a choked and unchoked pattern as well for the same reason. This discontinuous nonlinearity of the flow are taken into consideration when the mass flow rate terms $\dot{m}_i$ and $\dot{m}_e$ in Equation (4) are evaluated. As shown in Figure (3), considering the control volume above

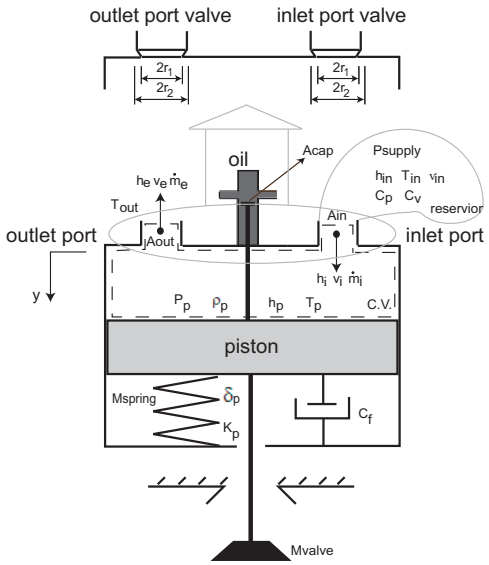

Figure 3: Actuator piston model

the actuator piston in the cylinder chamber including the inlet and outlet, the first law of thermodynamics can be written as:

$$\dot{Q} - \dot{W} + \dot{m}_i(h_i + \frac{v_i^2}{2}) - \dot{m}_e(h_e + \frac{v_e^2}{2}) = \frac{\partial E}{\partial t} \qquad (1)$$

where,

- $\dot{Q}$ is the heat transfer rate into the control volume
- $\dot{W}$ is the work rate delivered by the control volume to the actuator piston
- $\dot{m}_i$ is the mass flow rate entering the control volume
- $\dot{m}_e$ is the mass flow rate exiting the control volume
- $\dot{h_i}$ is the enthalpy of the gas entering the cylinder chamber
- $\dot{h_e}$ is the enthalpy of the gas exiting the cylinder chamber

- $\frac{\partial E}{\partial t}$ is the rate of change of the total energy of the control volume.

$$\dot{m}_i - \dot{m}_e = A_p(\rho_p \dot{y} + \dot{\rho_p} y) \tag{2}$$

$$M\ddot{y} + C_f\dot{y} + K_p(y + \delta_p) = A_p P_p + A_{cap} P_{oil} - (A_p + A_{cap}) P_{atm} \tag{3}$$

where,

- M is the sum of the actuator piston mass, the intake valve mass, one-third valve spring mass (or effective spring mass, see [22]), and the valve top cap mass.
- A_{cap} is the area of the cap on the top of the actuator piston stem
- $A_p = \pi r_p^2 - \pi r_{oil}^2$ with r_p as the radius of the actuator piston and r_{oil} as the radius of the oil passage
- C_f is the damping coefficient approximating the energy dissipation due to the friction
- K_p is the stiffness of the valve spring
- δ_p is the preload of the valve spring

$$\dot{P_p} = \frac{1}{A_p y}[C_{din} A_{in}(w) P_{supply} \gamma_{in} \sqrt{k^3 R T_{in}} - C_{dout} A_{out}(z) \gamma_{out} \sqrt{\frac{k^3 P_p^3}{\rho_p}}] - \alpha_p k \frac{P_p \dot{y}}{y} \tag{4}$$

where, C_{din} and C_{dout} are the flow discharge coefficients at the inlet and outlet; $k = \frac{C_p}{C_v}$ is the specific heat ratio, C_v is the specific heat of air at constant volume. α_p is chosen to be between 0 to 1 depending on the actual heat loss during the process.

$$\dot{\rho_p} = \frac{1}{A_p y}[C_{din} A_{in}(w) \gamma_{in} P_{supply} \sqrt{\frac{k}{R T_{in}}} - C_{dout} A_{out}(z) \gamma_{out} \sqrt{k P_p \rho_p}] - \frac{\rho_p \dot{y}}{y} \tag{5}$$

Rearranging Equation (3):

$$\ddot{y} = \frac{1}{M}[A_p P_p + A_{oil} P_{oil} - (A_p + A_{oil}) P_{atm} - C_f \dot{y} - K_p(y + \delta_p)] \tag{6}$$

The resulting equations were used to simulate the behavior of the valve under different operating conditions. The comparisons of the level one model responses and the valve bench test responses were presented in [17].

LEVEL TWO MODEL The level two model is divided into the open, dwell and close stages. It removes the flow and fluid dynamics from the level one model and is simplified to be a linear second order mass-spring-damper system at the open and close stages with two unknown damping coefficients C_{f_1} and C_{f_2}. A model reference adaptive identification system is designed to estimate these two parameters in real time and they are employed to construct control signals. The input to the system at the open stage is simplified to be a pulse force. However, it incorporates the hydraulic latch model in dwell stage and hydraulic damper model at the end of the close stage from the level one model.

Governing Equations Used in the Control System The detailed derivation and validation of the level two model can be found in [23]. Only the governing equations at the open and close stages are summarized in Equation (7) and (9) since they are going to be used for model reference adaptive closed-loop control.

Open stage

$$M\ddot{y} + C_{f_1}\dot{y} + K_p(y + \delta_p) = F(t) - F(t - \delta_1) \tag{7}$$

$$F(t) = \begin{cases} 0, & \text{if } t < 0 \\ A_p P_p - (A_p + A_{cap}) P_{atm} & \text{if } t \geq 0 \end{cases}$$

where $P_p = P_{oil} \approx P_{supply}$, C_{f_1} is the damping ratio approximating energy dissipation due to flow loss and frictional loss, δ_1 is the lag between the activation of solenoid 2 and solenoid 1 without system delays as illustrated in Figure (2), and δ_2 is the time needed for valve to return to the seat.

Close stage

Dynamics in the close stage was divided into two sub-stages (sub-stages III-1 and III-2) as illustrated in Figure (2). Substage III-1 can again be separated into two segments. The first segment is from point 3, where the piston starts returning, to point 4; and the second segment is from point 4 to point 5 where the hydraulic damper becomes effective. In the first segment, piston motion is a free return, however, in the second segment, the piston returns against certain pressure generated by compressed residual air. For simplicity, both segments were modeled as free returns. In substage III-2, the piston returns against largely increased hydraulic damping force that acts on the piston stem. The governing equations at this stage are in Equations (8) and (9). Equation (8) describes the response from point 3 to 5 (see Figure (2)).

$$M\ddot{y} + C_{f_2}\dot{y} + K_p y + K_p \delta_p = 0 \tag{8}$$

where $y(0) = y_{max}$, and $\dot{y} = 0$. The response beyond point 5 in hydraulic damping region follows the response of Equation (9).

$$M\ddot{y} + C_{f_2}\dot{y} + K_p(y + \delta_p) = A_p P_p + A_{cap} P_{oil} - (A_p + A_{cap}) P_{atm} \tag{9}$$

where P_{oil} is a constant in substage III-1. But it is a function of flow out area in the hydraulic damper in substage III-2. For detailed derivation of P_{oil}, see [17].

Level Two Model Response Figure (4) compares the simulation response of the level two model with its experimental response. The thin valve response is the experimental response; and the thick one is the simulated response. Damping ratio C_{f_1} at open stage and damping ratio C_{f_2} at close stage vary significantly and nonlinearly with respect to the temperature, fluid viscosity, and engine operational conditions. The adaptive identification of these two parameters can compensate the variation. The two curves close to the time axis are the measured solenoid currents, where the solid line is the dwell current of solenoid 1 and the dash line is that of solenoid 2. These solenoid current feedbacks are used to detect the delays from the activation of solenoids to the start of valve mechanical motions. As shown in Figure (4), total delays of each solenoid rises in two steps. Taking solenoid 1 current as an example, the first rise is from the starting point to the first peak which represents the electrical delay; and the second rise is from the first peak to the second peak which represents the magnetic delay. The total delay associated with solenoid 1 and solenoid 2 are defined as Δt_1 and Δt_2 respectively. Algorithms were developed to identify Δt_1 and Δt_2 at each cycle to be used for not only adjusting the opening and closing timing but also modifying δ_1 as a part of the valve lift control. The effect of the system delay, δ_1, and implementation of it in the control system are illustrated in the Control Strategy section.

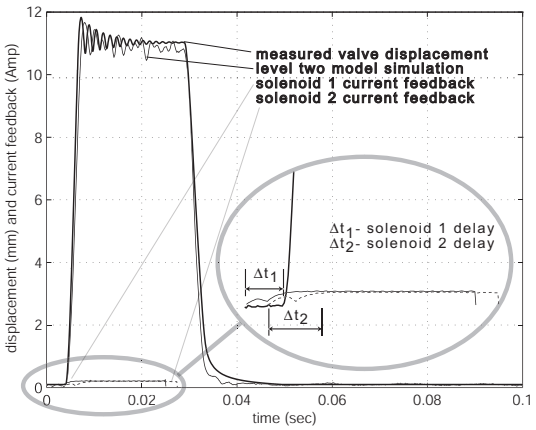

Figure 4: Level two model simulation and experiment responses

CONTROL STRATEGY

The goal of VVT and VVL control is to control valve opening timing, duration, and lift, or in other words, to control the valve opening, closing timing, and the valve lift. The strategy of achieving this goal is addressed in this section. An adaptive parameter identification algorithm using model reference technique and MIT rule [21] are used to estimate the two damping coefficients at both open and close stages. The identified parameters are used to modify the feedforward control of the closed-loop PI controller. Some approximations are used to obtain analytical solutions of control input in terms of the estimated parameters. Only stages I and III of the level two model were used in the real time controller to reduce the computational efforts. (see Figure (2)). The closed-loop control scheme aimed at real time implementation is discussed in this section.

VARIABLE DEFINITION Figure (5) defines the variables involved in the control strategy. At low engine speed, the valve lift profile has all three stages as shown in Figure (5), where the holding period exists. As engine speed increases, the holding period reduces. At certain engine speed, the holding period disappears, and the valve lift profile consists of only the open and close stages. In this case, solenoid 1 is deactivated shortly after its activation. It discharges the cylinder and allows the valve to return before the hydraulic latch can be engaged. In these two cases, both solenoids 1 and 2 are needed to control the valve event and the air supply pressure remains unchanged throughout the process. There is another special case in which only solenoid 1 is used. The cylinder is simply charged with supply air when solenoid 1 is energized and discharged when solenoid 1 is de-energized. This occurs when the engine speed is so high that the activation duration of solenoid 1 becomes very small. The valve lift control needs to be accomplished through regulating air supply pressure. This special case is not the subject of discussion in this paper. As displayed in Figure (5), the

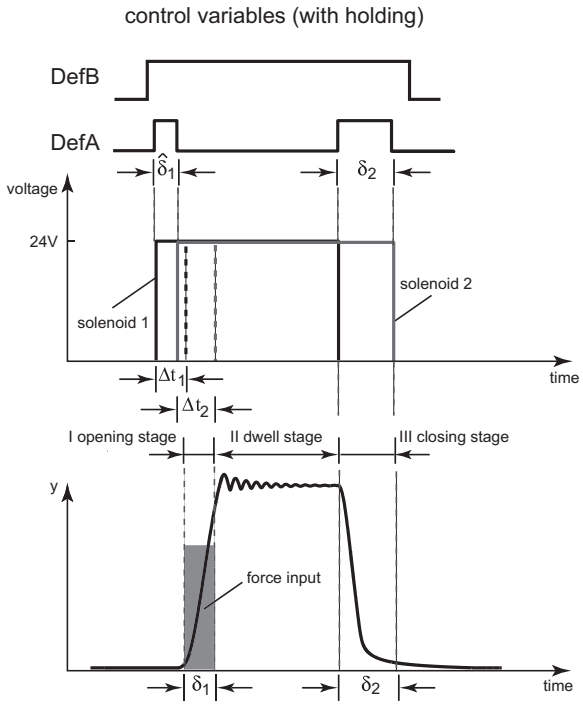

Figure 5: Control variable definition

control pulses for solenoids 1 and 2 are generated based upon crank synchronized $DefA$ and $DefB$ pulses from the engine control microprocessor. The rising and falling edges of $DefA$ and $DefB$ pulses occur at the reference crank angle degrees. When the controller needs to utilize both solenoids 1 and 2, the $DefB$ pulse is active over the $DefA$ window, and when only solenoid 1 is used, the $DefB$ is not active. $DefA$ and $DefB$ pulses carry the control information and they are converted to two solenoid pulses that actually control the valve actuator by the valve control microprocessor. The two time based solenoid pulses are synchronized with the crank angle after the transformation. Since the crank angle synchronized calculations and the time based algorithms are performed in separate CPU's, the convention of this transformation is defined as follows. The first rising and falling edges of $DefA$ correspond to the activation of

solenoids 1 and 2 respectively; and the second rising and falling edges of $DefA$ correspond to the deactivation of solenoids 1 and 2. The first pulse width of $DefA$ is denoted as $\hat{\delta}_1$ and the second pulse width of $DefA$ is denoted as δ_2. $\hat{\delta}_1$ is the time delay between the activation of two solenoids. The second falling edge of $DefA$, which is also the falling edge of solenoid 2 pulse, is defined to be the reference valve closing timing. δ_2 represents the time needed for the valve to return after the deactivation of solenoid 1 (at valve return point). Activation of solenoids 1 and 2 begins their impact on the system after time delays Δt_1 and Δt_2. The air pressure in the piston cylinder increases and forms a pulse force input to the system with a pulse width of δ_1. Therefore, $\hat{\delta}_1$ associates with δ_1 through the expression $\hat{\delta}_1 = \delta_1 + (\Delta t_1 - \Delta t_2)$, given the fact that Δt_1 is always greater than Δt_2. The reference valve opening, closing timing and reference valve lift are given by engine operational conditions. The timing of the first rising edge of $DefA$, the return time δ_2 and the lag between the activation of two solenoids, $\hat{\delta}_1$, are the controlled variables. The fist rising edge of $DefA$ is modified based on $\Delta t_1.\hat{\delta}_1$ and δ_2 are modified based on the identified parameter C_{f_1} and C_{f_2}. The control variable conventions for the other cases are similar to this case and are not repeated.

ADAPTIVE PARAMETER IDENTIFICATION The architecture of the model reference adaptive system (MRAS) for parameter identification is illustrated in Figure (6), where $G_m(S)$

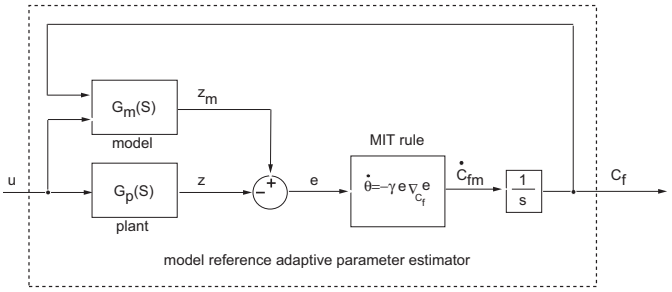

Figure 6: Model reference adaptive parameter identification scheme

is the level two model and $G_p(S)$ is the physical plant (EPVA). This adaptive estimator is applied to identify the damping ratios C_{f_1} and C_{f_2}, where C_{f_1} is for the open stage and C_{f_2} is for the close stage. The error e between model and plant outputs reduces as the estimated parameters converge. The excitation force u is a pulse input with PE of order infinity that meets the persistent excitation condition. The MIT rule uses the error between the model and plant outputs to generate an estimated C_{f_1} (or C_{f_2}), where C_{f_1} (or C_{f_2}) is updated at every time step. The adaption laws at open and close stages were established and the parameter convergence were verified using bench data in [23]. Both equations are summarized below:

Open stage

$$\begin{cases} \dot{C}_{fm_1} = -\gamma_1 p(t) e \\ \dot{p}(t) = \frac{1}{M}\big(z_m(t) - C_{fm_1} p(t) - K_p \int p(t)dt\big) \\ e = z - z_m = y - y_m \end{cases}$$

where $\gamma_1 > 0$ is the selected adaptive gain and C_{fm_1} is the model damping ratio (or estimated C_{f_1}). The adaptive algorithm utilizes the sampled data between point 1 and the first peak over the valve response shown in Figure (2).

Close stage

$$\begin{cases} \dot{C}_{fm_2} = -\gamma_2 q(t) e \\ \dot{q}(t) = \frac{1}{M}\big(z_m(t) - C_{fm_2} q(t) - K_p \int q(t)dt - \int z(0)dt\big) \\ e = z - z_m = y - y_m \end{cases}$$

where $\gamma_2 > 0$ is the selected adaptive gain and C_{fm_2} is the model damping ratio (or estimated C_{f_2}). The adaptive algorithm uses the sampled data between points 3 and 4 shown in Figure (2) due to free return characteristics of the valve response.

CLOSED-LOOP VALVE LIFT AND TIMING CONTROL The closed-loop valve closing timing and lift control schemes are created based upon the identified damping ratios C_{f_1} and C_{f_2}. The closed-loop valve opening timing control is a function of the detected solenoid 1 delay, Δt_1. The purpose of control is to make the system opening timing y track the reference input y_{ref}. $\hat{\delta}_{1_o}$ and δ_{2_o} are the nominal values of $\hat{\delta}_1$ and δ_2. They are computed from the estimated C_{f_1} and C_{f_2}.

Two first order systems are employed to approximate the second order systems for both open and close stages in the region of interest since the system damping ratios are between over-damped and slightly under-damped cases based upon the identified values. Hence, the analytical solutions of $\hat{\delta}_{1_o}(C_{f_1})$ and $\delta_{2_o}(C_{f_2})$ are developed based on the first order system. The formulas of computing $\hat{\delta}_{1_o}$ in terms of C_{f_1} are provided by Equations (10), (11) and (12).

$$\hat{\delta}_{1_o} = \delta_1 - (\Delta t_1 - \Delta t_2) \tag{10}$$

$$\delta_1 = \frac{2}{\sigma} \ln(\frac{a}{a - y_{max}}) \tag{11}$$

$$a = \frac{f_0}{K_p} - \delta_p \tag{12}$$

where $f_0 = A_p P_p + A_{cap} P_{oil} - (A_p + A_{cap}) P_{atm}$ is defined by Equation (7). The formula of solving δ_{2_o} in terms of C_{f_2} is provided in Equation (13).

$$\delta_{2_o} = \frac{100}{C_{f_2}\sigma} \ln(\frac{\delta_p}{y_{max} + \delta_p}) \tag{13}$$

In Equations (11) and (13), σ is derived accordingly for three cases as follows:

$$\sigma = \begin{cases} \frac{C_f}{2M}, C_f^2 < 4K_pM & \text{underdamped} \\ \frac{C_f}{2M}, C_f^2 = 4K_pM & \text{critically damped} \\ |\frac{-C_f + \sqrt{C_f^2 - 4K_pM}}{2M}|, C_f^2 > 4K_pM & \text{overdamped} \end{cases}$$

with $C_f = C_{f_1}$ at open stage or $C_f = C_{f_2}$ at close stage.

Closed-loop lift control The architecture of the closed-loop valve lift control is depicted in Figure (7). System inputs include reference valve displacement, solenoids 1 and 2 current measurements from the solenoid driving circuit (see Experimental Implementation section), air supply pressure, and oil pressure. The valve lift height is the output. The lift control consists of two parts, the open-loop parameter identification for feedforward control and the closed-loop lift control using a PI scheme. The system starts with a short period of open-loop valve operation where C_{f_1} is estimated using a high adaptive gain to achieve fast convergence. A subroutine checking the convergence of C_{f_1} switches the system from open-loop operation to closed-loop control as soon as the identification error stays below a given tolerance for a reference number of cycles. The open-loop identification period can take around 50 cycles. The open-loop identification scheme and the closed-loop lift tracking scheme are displayed in the upper and lower dotted line blocks respectively.

The open-loop parameter identification scheme includes the plant, the model plant, and a driving circuit. The inputs of the driving circuit are the solenoid command pulses from the prototype controller's D/A. The outputs of it are the amplified solenoid commands and the solenoid current feedbacks. Moreover, the parameter identification scheme comprises an algorithm that creates a C_{f_1} identification zone where the adaptive algorithm is active and the displacement error is detected to be used by the adaptation law. The open-loop scheme also contains the model reference adaptive system involving the MIT rule with a high adaptation gain γ_1. The direct force input to the model plant is computed from the solenoid pulses by a subroutine. It guarantees that the model plant output starts at the same point as the plant output. These subroutines complete C_{f_1} identification. Meanwhile, the $DefA$ and $DefB$ pulses are generated by a pre-determined $\hat{\delta}_{1_i}$. They are converted to two solenoid pulses amplified by the driving circuit for the EPVA actuators.

In addition to the subroutines used in the open-loop parameter identification period, additional algorithms were developed for the closed-loop valve lift tracking control. There are algorithms that compute the feedforward nominal control input ($\hat{\delta}_{1_o}$), detect system delay Δt_1 and Δt_2 and compute critical points including maximum valve lift, valve opening and closing locations, peak displacement, and so on. In this block, the model reference adaptive system (MRAS) uses a low adaptation gain γ_1 to maintain parameter convergence due to a sudden change of the valve displacement in a transient operational condition. The feedforward nominal control input $\hat{\delta}_{1_o}$ calculated from C_{f_1} needs to be sufficiently accurate to minimize the transient response time and the tracking error. The actual valve lift is a feedback signal to the system and it is subtracted from the reference valve lift to form the lift error. This error is the input of a proportional and integral (PI) controller with K_p as a proportional gain and K_i as an integral gain. The PI controller is updated every engine cycle. The output of the PI controller is then added onto the feedforward nominal input $\hat{\delta}_{1_o}$ to generate $\hat{\delta}_1$ as a controlled input to the system. The integral action is used to achieve the zero steady state tracking error. The $DefA$ pulse is generated based on $\hat{\delta}_1$. The $DefA$ and $DefB$ pulses are converted into solenoid commands. They are amplified by the solenoid driving circuit for the valve actuators.

As discussed in the Control System Hardware Configuration section, there are two CPU's in the prototype controller. CPU$\#1$ operates at a relatively slower rate (1 ms) than CPU$\#2$, but its outputs can be synchronized with the engine crank angle. CPU$\#2$ is dedicated to valve operation at a sample rate of 40 microseconds since the valve control algorithms require fast sample rate. The CPU$\#2$ also takes care of the conversion from the $DefA$ and $DefB$ pulses to the solenoid pulses. The PI controller is operated per engine combustion event. It is implemented in CPU$\#1$ to reduce the computational throughput of CPU$\#2$. $DefA$ and $DefB$ pulses are generated in CPU$\#1$ since they are crank synchronized.

Closed-loop opening timing control In order to track the reference valve opening timing calculated by the engine control CPU$\#1$, the valve control system needs to detect the magnetic delay of valve solenoid 1 Δt_1 which is equivalent to the time lag between the activation of solenoid 1 and the actual valve opening. With known Δt_1, the control system can track the reference opening timing by compensating the delay Δt_1. The main task of this control scheme is the system delay detection and its closed-loop PI controller. The solenoid delay Δt_1 is calculated using solenoid 1 current obtained from the solenoid driving circuit. It is used as feedforward control. The true valve opening timing is used as a feedback to the closed-loop controller, and it is subtracted from the reference valve opening timing to form an error signal of the PI controller. The output of the PI controller combined with feedforward control Δt_1 produces the final control input to the engine control system which updates the $DefA$ pulse. Most algorithms are implemented in CPU$\#2$, except for the crank angle synchronized $DefA$ and $DefB$ pulse generation and the combustion event based PI controller that are implemented in CPU$\#1$.

Closed-loop closing timing control The closed-loop valve closing timing control and valve lift control schemes share the similar approach. Figure (9) shows the open-loop parameter identification for detecting C_{f_2} and the closed-loop valve closing timing controller. The adaptive gain γ_2 is high in the open-loop operation and low in the closed-loop operation. A predetermined δ_{2_i} controls the valve closing timing in the open-loop operation. The system switches from open-loop to closed-loop control based upon the convergence criterion of the estimated C_{f_2} which is the same as the opening case. The feedforward control δ_{2_o} is computed from the identified C_{f_2}, and the system control output δ_2 consists of the feedforward control and the PI control output. Information from δ_2 is then used to generate $DefA$ pulse. The $DefA$ and $DefB$ pulses are sampled by CPU$\#2$ and converted to solenoid control commands that are sent to the valve driving circuit. Again, the PI control algorithm and the formation of $DefA$ and $DefB$ pulses are implemented in CPU$\#1$, and the rest of the algorithms are implemented in CPU$\#2$. The closed-loop timing control scheme allows the actuator to track the reference closing timing.

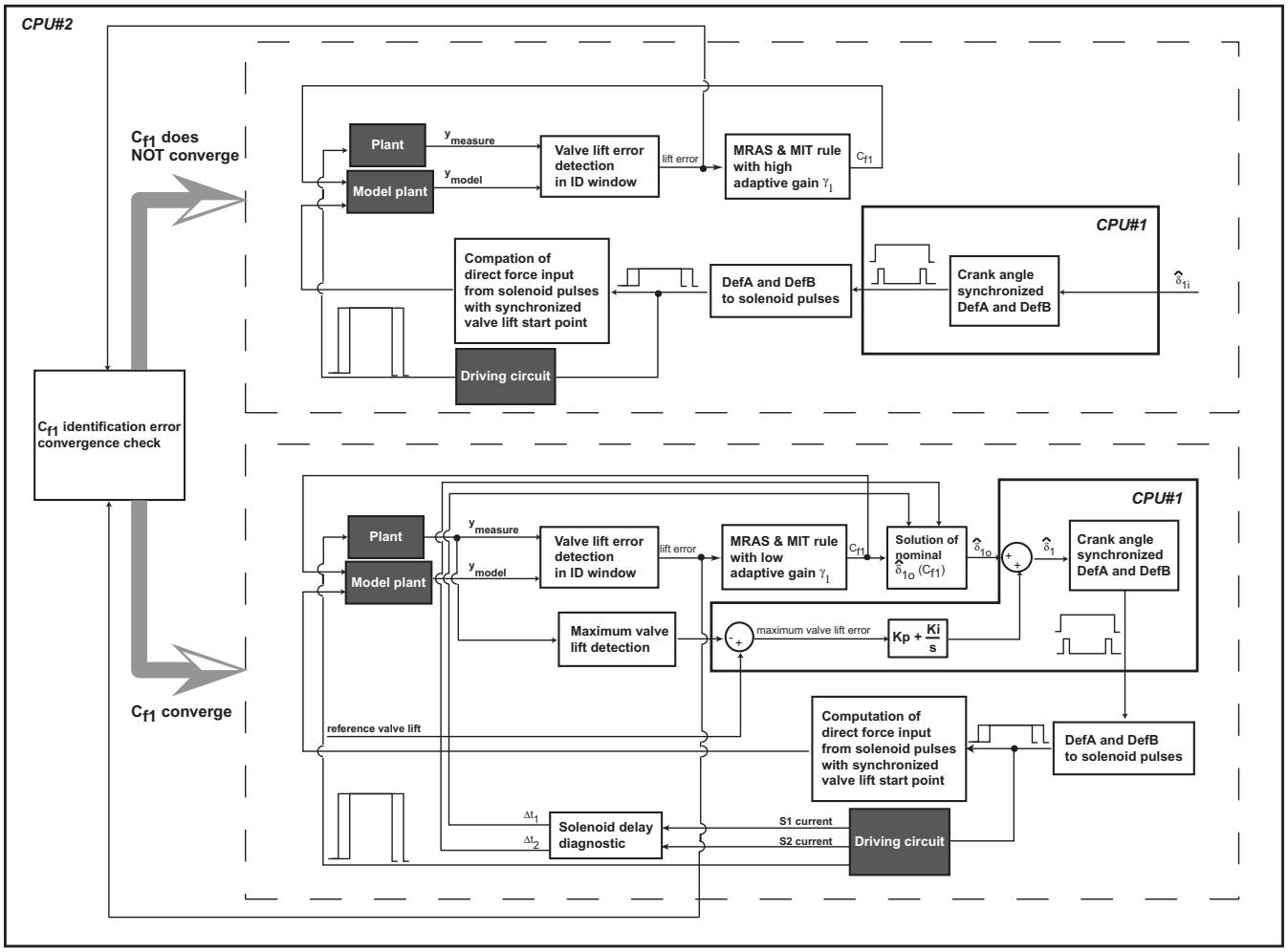

Figure 7: Schematics of closed-loop valve lift control

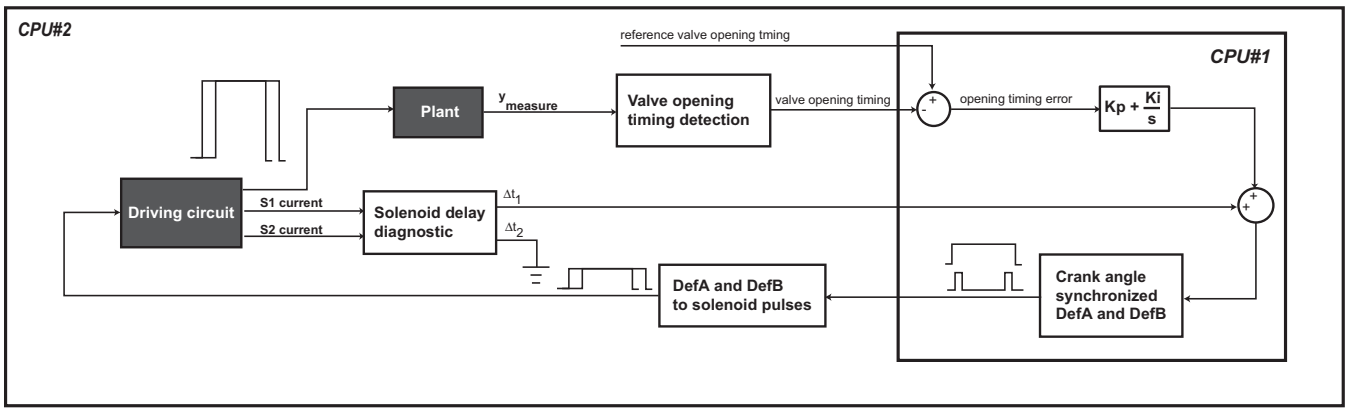

Figure 8: Schematics of closed-loop valve opening timing control

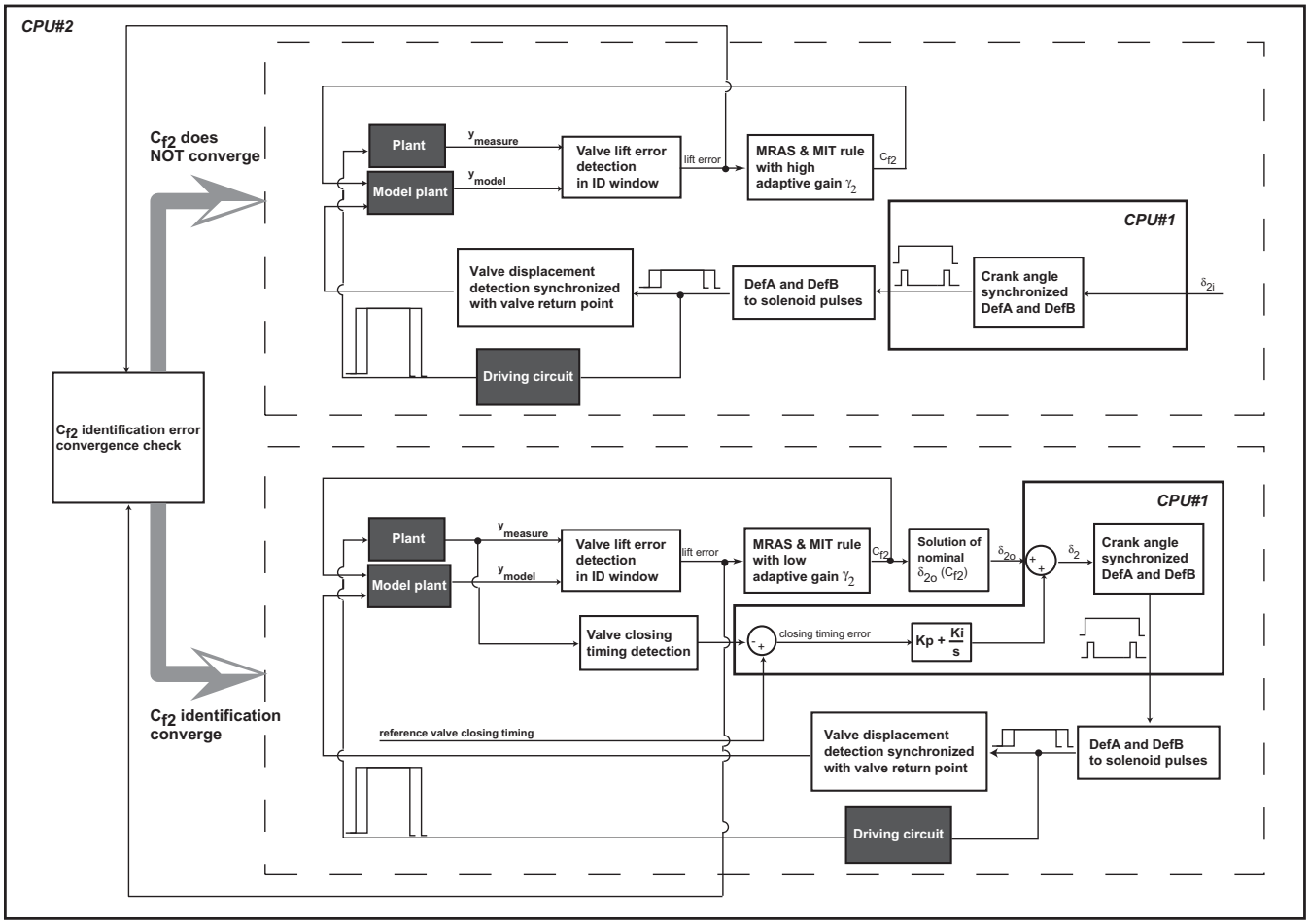

Figure 9: Schematics of closed-loop valve closing timing control

EXPERIMENTAL IMPLEMENTATION

CONTROL SYSTEM HARDWARE CONFIGURATION A real time modular control system was employed as a prototype controller for the EPVA bench tests. The system consists of:

- Two 3.2GHz CPU's
- An IEEE 1934 fire wire serial bus with the data transfer rate at 400MHz per bit
- Two 16 channel A/D and D/A boards with less than 1 μs conversion rate
- One 16 channel digital I/O board at 50 ns sampling rate

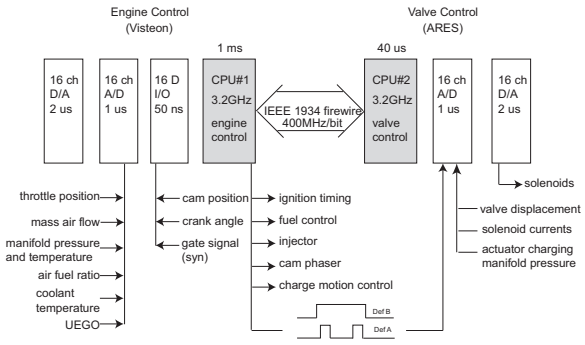

Figure 10: Modular control system configuration

Figure (10) displays the hardware configuration of the system. CPU $\#1$ is used for engine controls and CPU $\#2$ is dedicated to the valve actuator (EPVA) control. An IEEE 1934 fire wire serial bus is used for communication between CPU $\#1$ and CPU $\#2$. CPU $\#1$ is configured to be updated every $1ms$ and execute the engine control every combustion cycle. This means that this CPU updates input and updates analog outputs every $1ms$, but calculates the engine control parameters every engine combustion event. The digital outputs of CPU $\#1$ are synchronized with the engine crank angle with one-third crank degree resolution. The crank angle calculation is completed within the digital I/O card of CPU $\#1$ utilizing digital inputs from cam sensor, gate and crank signals from an encoder. The CPU $\#1$ digital outputs are spark pulse, fuel injection pulse, charge motion control, and intake and exhaust valve timing pulses, especially the valve control $DefA$ and $DefB$ pulses. The inputs of the 16 channel analog I/O board include ionization signal, pressure signal, throttle position, mass air flow rate, coolant temperature, manifold pressure and temperature, and air fuel ratio from universal exhaust gas oxygen (UEGO) sensor.

The valve control CPU $\#2$ is configured to operate at $40\mu s$ sample rate, which is close to one crank angle degree at $4000rpm$. CPU $\#2$ executes most of the valve control algorithms and generates the control signals for the pneumatic valve actuators. A 16 channel A/D board reads $DefA$ and $DefB$ pulse signals from CPU $\#1$, valve lift signal from valve lift position sensors, solenoid current signals from their drive circuits, and supply air pressure signal. The solenoid control pulses and supply air pressure regulation signal (which is needed to control valve lift for the special case where only solenoid 1 is used) are the output from a 16 channel D/A board.

VALVE ACTUATOR DRIVING CIRCUIT The solenoid driving circuit was designed to amplify the signal from the D/A controller outputs. Besides, it measures the solenoid current. The circuit is required to have a short solenoid release time and fast switching capability with low noise. A single channel driving circuit drawing is shown in Figure (11). This circuit consists of a switching MOSFET (Metal-Oxide Semiconductor Field-Effect Transistor) and a NPN BJT (Bipolar Junction Transistors). The solenoid current is measured across a 0.5Ω resistor in serial with the source of the MOSFET.

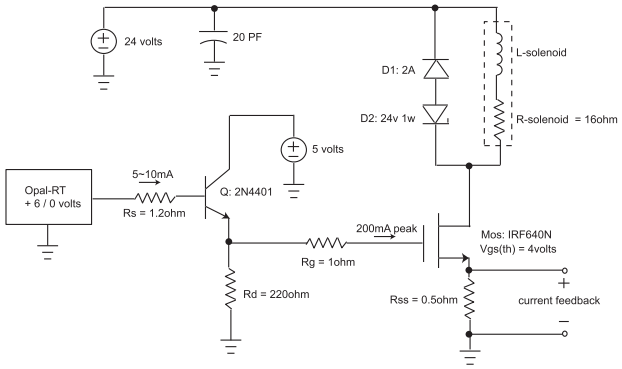

Figure 11: Solenoid driving circuit

STATISTICAL ANALYSIS OF OPEN-LOOP VALVE BENCH DATA Before the closed-loop valve lift and timing control bench tests were conducted, a statistical study focusing on the valve response repeatability was performed on test bench at both high and low engine speeds. The test bench uses the EPVA actuators installed on a 5.4 liter 3-valve V8 engine head. Results of this study will be used to compare with those of the closed-loop valve lift test data to evaluate the steady state closed-loop lift control performance in Closed-loop Valve Lift Control Experimental Responses session. The valve repeatability has a great impact on the adaptive estimation and steady state response. The operational conditions that were used in the open-loop parameter identification in valve lift tracking tests were the same for both the low and high engine speeds. They were applied to collect these sample data. This means that the lag between the activation of solenoids 1 and 2 is set to be a constant value $\hat{\delta}_{1_i}$ used in the open-loop period in the lift tracking tests. The solenoid pulse period and pulse width, the air supply pressure and the oil pressure were held constant in both types of experiments.

Low Engine Speed Open-loop Valve Bench Data Five bench tests were conducted using $80psi$ air supply pressure, $90psi$ oil pressure, $100ms$ solenoid period, which corresponds to the engine speed at $1200rpm$, with 25% pulse duty cycle and a lag of $5ms$ between the activation of two solenoids. The valve lift was targeted to be $9mm$ and there was a holding period on the valve lift profile under this experiment configuration (see Table 1). Two hundred-cycle data was collected from each experiment. The purpose of running these tests is to analyze statistical characteristics of the valve responses. Their histograms were plotted and the mean and standard deviation of responses were calculated. Taking data group $\#3$ as an example, Figure (12) shows

the histogram of data group $\#3$, where the top plot is the valve lift histogram which reflects the valve lift repeatability and the bottom one is the histogram of the valve lift integral during the valve opening which indicates the repeatability of the engine charged air. For the valve lift diagram, the horizontal axis is the valve lift ranging from $8.4mm$ to $9.8mm$ and the vertical axis is the number of occurrence for each valve lift; and for the bottom diagram, the horizontal axis is the integral area and the vertical axis is the number of occurrence. The mean μ and the standard deviation σ were calculated, and the mean of integral area of the valve lift was normalized to one. The 3σ value was used to indicate 95% occurrence.

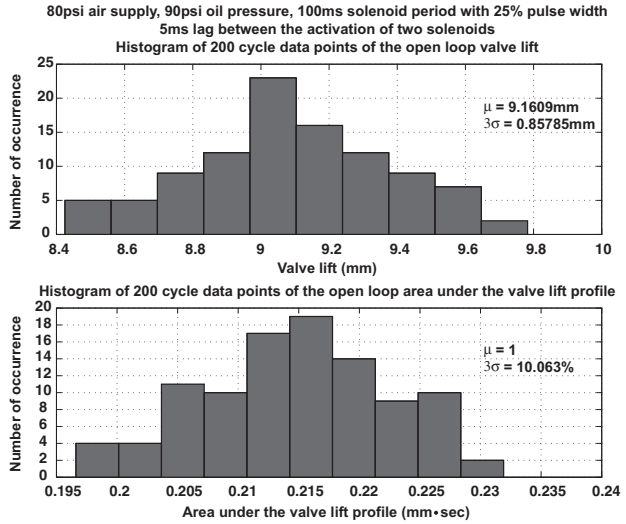

Figure 12: Histogram of open-loop valve lift bench test data points for $9mm$ target lift at $1200rpm$ in 200 cycles

The statistical analysis results of five data groups were summarized in Table 1. For the valve lift, group $\#5$ has the largest valve lift mean at $9.55mmm$ and group $\#2$ has the smallest mean at $8.83mmm$. The largest 3σ valve lift, $0.86mm$, is from data group $\#3$. The smallest 3σ valve lift ($0.44mm$) was from data group $\#1$. Regarding the analysis of the integral area of every cycle, the mean values were normalized to one, the 3σ values were calculated associated to normalized data and interpreted as percentage. Among the five data group, $\#3$ has the largest 3σ value of 10.06%. Group $\#3$ data provided the largest variation in both valve lift and the integral area. The corresponding histogram was displayed in Figure (12) and it will be compared with the closed-loop histogram of the largest variation operated with a $9mm$ reference lift to show the valve lift repeatability improvement at the same operational condition due to closed-loop control.

High Engine Speed Open-loop Valve Bench Data Similar to the low engine speed case, five bench tests were conducted using $80psi$ air supply pressure, $90psi$ oil pressure, $24ms$ solenoid period (which corresponds to the engine speed at $5000rpm$) with a 25% pulse duty cycle and a lag of $5ms$ between the activation of two solenoids. There is no holding pattern displayed in the valve lift profile when the engine is operated at $5000rpm$. In this case the valve returns before the hydraulic latch is engaged to hold the valve open (recall the discussion in the System Dynamics section). The desired valve lift was also set to be $9mm$ for this experiment (see Table 2). Two hundred-cycle data was collected for each experiment. The mean μ and the standard deviation σ were calculated. The mean of the valve lift integral was normalized to one as well. Again, the 3σ values were used to cover 95% sample data points.

Table 2 summarizes the statistical analysis results of five data groups. For the valve lift, data group $\#1$ has the largest mean valve lift at $9.14mm$ and group $\#5$ has the smallest mean valve lift at $8.59mm$. The largest 3σ valve lift was from data group $\#4$ at $0.63mm$ which is less than the largest 3σ valve lift ($0.86mm$) at low engine speed ($1200rpm$). The smallest valve lift 3σ value of $0.17mm$ was found from data group $\#2$. It is less than the largest valve lift 3σ value ($0.44mm$) from the $1200rpm$ tests. This indicates that the valve lift repeatability improves at high engine speed. For the integral area, data group $\#4$ has the largest 3σ value of 11.7%. The group $\#4$ test results show the largest variation in both valve lift and the integral area of the valve lift. Their histograms are shown in Figure (13), where the top histogram is for the valve lift and the bottom one is for the integral area. For the top diagram, the horizontal axis is the valve lift ranging from $8.9mm$ to $9.5mm$ and the vertical axis is the number of occurrence of each valve lift. For the bottom diagram, the horizontal axis is the integral area and the vertical axis is the number of occurrence of integral area. This histogram will be used to compare the corresponding closed-loop test data later.

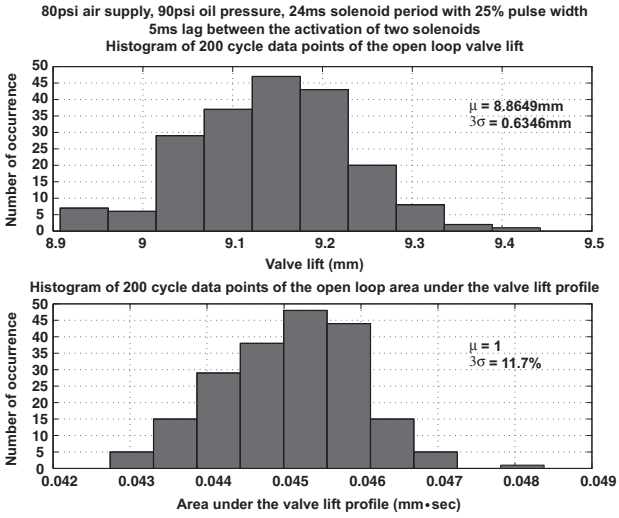

Figure 13: Histogram of open-loop valve lift bench test data points for $9mm$ target lift at $5000rpm$ in 200 cycles

Open-loop Low Valve Lift Bench Data The EPVA is capable of providing a valve lift as low as $3mm$. This subsection studies statistical property at low valve lift to determine if the low valve lift operation mode is acceptable for engine control. Since the valve lift repeatability improves as engine speed increases (from the previous analysis), we are going to study the low valve lift operation only at low engine speed ($1200rpm$). Five bench tests were conducted using the same experimental setup as high lift case at $1200rpm$ engine speed except the lag between the activation of two solenoids was reduced to $3.4ms$ to obtain the

Table 1: Statistical study of open-loop valve actuation data with $9mm$ target lift at $1200rpm$

Engine configuration	Data group	$y_{max} = \mu \pm 3\sigma\ (mm)$	$y_{area} = \mu \pm 3\sigma$
$80psi$ air supply pressure	#1	9.691 ± 0.43783	$1 \pm 4.639\%$
$90psi$ oil pressure	#2	8.8256 ± 0.80343	$1 \pm 10.87\%$
$100ms$ valve operation period	#3	9.1609 ± 0.85785	$1 \pm 10.063\%$
$25ms$ valve opening duration	#4	9.354 ± 0.5068	$1 \pm 6.7673\%$
$5ms$ lag of S2 (with holding)	#5	9.5495 ± 0.71124	$1 \pm 8.0833\%$

Table 2: Statistical study of open-loop valve actuation data with $9mm$ target lift at $5000rpm$

Engine configuration	Data group	$y_{max} = \mu \pm 3\sigma\ (mm)$	$y_{area} = \mu \pm 3\sigma$
$80psi$ air supply pressure	#1	9.1424 ± 0.26838	$1 \pm 6.1233\%$
$90psi$ oil pressure	#2	9.1281 ± 0.17305	$1 \pm 4.4528\%$
$24ms$ valve operation period	#3	9.0284 ± 0.39827	$1 \pm 8.339\%$
$6ms$ valve opening duration	#4	8.8649 ± 0.6346	$1 \pm 11.7\%$
$5ms$ lag of S2 (without holding)	#5	8.5943 ± 0.42403	$1 \pm 5.545\%$

targeted valve lift at $3mm$. The statistical results were shown in Table 3. The mean valve lift varies from $2.68mm$ to $3.51mm$. The largest valve lift 3σ value is $2.5mm$ from data group $\#3$ and the 3σ value is not less than $0.8mm$ among the rest of the data groups. Consequently, data group $\#3$ has a 3σ integral area value as high as 73.196%. Although the actuator is capable of providing a lift as low as $3mm$, its repeatability is not good enough to deliver a stable air flow when engine is operated at light load conditions. For this engine control project, the valve lift operational range is to be limited between $5mm$ and $11mm$ to ensure the desired repeatability. When the required valve lift is below $5mm$ at light load condition, a flap valve or a throttle would be used to reduce the intake air flow.

CLOSED-LOOP VALVE LIFT CONTROL EXPERIMENTAL RESPONSES

The closed-loop valve control algorithms were verified on the valve test bench utilizing the same engine head as open-loop cases. The experimental responses at both low and high engine speeds are presented in this section. Since both closed-loop valve opening and closing timing controls are similar to the valve lift control case, the results are not presented. Air and oil supply pressure for all tests are $80psi$ and $90psi$ respectively. The experimental parameter is $100ms$ solenoid period with $25ms$ solenoid active duration (25% duty cycle) corresponding to $1200rpm$ in the low engine speed tests and $24ms$ solenoid period with $6ms$ solenoid active duration (25% duty cycle) corresponding to $5000rpm$ in the high engine speed tests. The initial lag between the activation of solenoids 1 and 2 during the open-loop parameter identification period was $5ms$ at both low and high speed tests.

EXPERIMENTAL RESULTS AT LOW ENGINE SPEED
2500 cycles of valve responses were recorded with various reference valve lift points. The estimated parameter was converged in the first 25 cycles (or $2.5ms$). The reference valve lift varies every 500 cycles from $9mm$ to $6mm$, from $6mm$ to $10mm$, from $10mm$ to $7mm$, and from $7mm$ to $9mm$. Their steady state responses are presented in Figures (16), (18), (20) and (22). On the top diagram of every figure, the black line is the reference valve lift, and the grey line is the actual valve lift. The bottom diagram shows the lift error between the reference and the actual valve lifts. They start at 50 cycles before the reference valve lift step change and end right before the next reference valve lift change. The top diagrams of Figures (17), (19), (21) and (23) display the nominal input $\hat{\delta}_{1_o}$ (solid line) calculated based on the estimated C_{f_1} against the controlled input $\hat{\delta_1}$ (dotted line) which is the output of the PI feedback controller. Their enlarged transient responses are presented in the bottom diagrams, where the dark lines are the reference valve lift and the grey lines are the true valve displacement.

Open-loop Parameter Identification Valve Responses Figure (14) enlarges the first 80 cycle valve lift tracking responses. C_{f_1} identification error (the bottom diagram) converges to a set tolerance in about 25 cycles. It can be observed from the top diagram that the system switched from the open-loop to closed-loop control at the $65th$ cycle where the lift error jumps from zero to $0.7mm$ (the dark grey line in the top diagram). This indicates that the closed-loop controller is engaged.

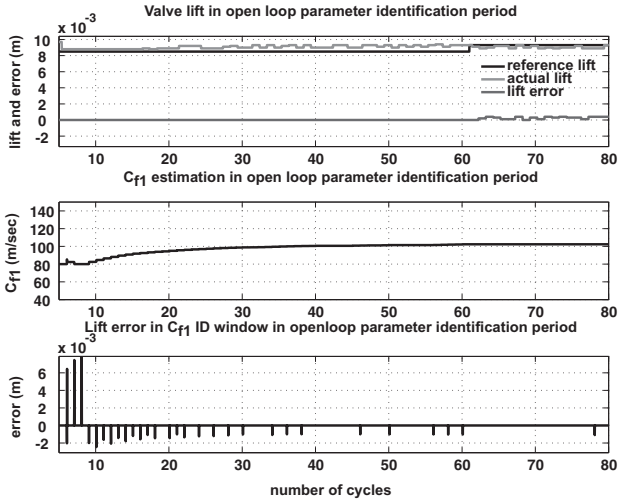

Figure 14: Open-loop parameter C_{f_1} identification at $1200rpm$

Steady state responses of valve lift tracking During the steady state operations, the valve lift tracks the reference valve lift and oscillates around the reference values. The responses

Table 3: Statistical study of open-loop valve actuation data with $3mm$ target lift at $1200rpm$

Engine configuration	Data group	$y_{max} = \mu \pm 3\sigma\ (mm)$	$y_{area} = \mu \pm 3\sigma$
$80psi$ air supply pressure	#1	2.6751 ± 0.89005	$1 \pm 15.71\%$
$90psi$ oil pressure	#2	3.3175 ± 0.79791	$1 \pm 18.745\%$
$100ms$ valve operation period	#3	3.3581 ± 2.4954	$1 \pm 73.196\%$
$25ms$ valve opening duration	#4	3.5056 ± 0.94671	$1 \pm 18.803\%$
$3.4ms$ lag of S2 (with holding)	#5	3.1683 ± 1.432	$1 \pm 41.194\%$

show good repeatability at high valve lifts. The maximum absolute valve lift error was bounded by $0.4mm$ at $10mm$ lift and $0.5mm$ at $9mm$ lift. The repeatability is relatively lower at low lift, however, the valve lift error falls mostly in the region of $\pm 0.5mm$ at $6mm$ and $7mm$ lift. This is partially due to the fact that the pneumatic valve actuator has a higher sensitivity at the low valve lift, which results in a high steady state lift error. The maximum absolute steady state error at these four set points are listed in Table 4.

Table 4: Maximum SS absolute valve lift error ($1200rpm$)

Reference valve lifts (mm)	6	7	9	10
Max. absolute lift error (mm)	0.75	1.3	0.5	0.4

The statistical performance of the valve lift responses with the closed-loop controller is also important to study. The statistical characteristics of the open-loop valve lift are analyzed in the earlier section of Statistical Analysis of Open-Loop Valve Bench Data. The results of the valve lift statistical study shown in both Figure (12) and Table (1) provide the worst lift 3σ value at $0.86mm$ and the worst integral area 3σ value at 10.87% with the valve lift at $9mm$ using five test data groups. The same statistical analysis is conducted for the closed-loop lift control. Five 200 cycle steady state valve lift responses at $9mm$ were used to calculate the means and standard deviations of the valve lift and its integrated area. These results are compared with the open-loop results. The diagrams displayed in Figure (15) depict the histograms of the lift and integral area of the valve lift profile. They are obtained from the data group with the largest variations among all five data groups (see group $\#1$ in Table (5)). Note that the axes ranges and the bin width of the valve lift (top) and integral area (bottom) histograms in Figure (15) are the same as those in Figure (12) for an easy comparison.

The five sets of means and 3σ values of valve lift and integral area were summarized in Table (5). The worst 3σ value of the valve lift reduced from the open-loop $0.86mm$ to the closed loop $0.45mm$, and the worst integral area 3σ value reduced from 10.87% to 5.45% (see both Table (5) and Table (1)). In other words, the worst case 3σ values of both valve lift and integral area were reduced by about 45%. This indicates that the closed-loop valve lift control reduces the valve lift variation, and hence, improves its lift repeatability.

Transient responses of valve lift tracking The feedforward nominal input $\hat{\delta}_{1_o}$ remains steady due to the fact that the parameter identification convergence is preserved in the closed-loop lift control operation. It takes about one cycle for the valve to reach the reference valve lift with less than $0.5mm$ of lift error.

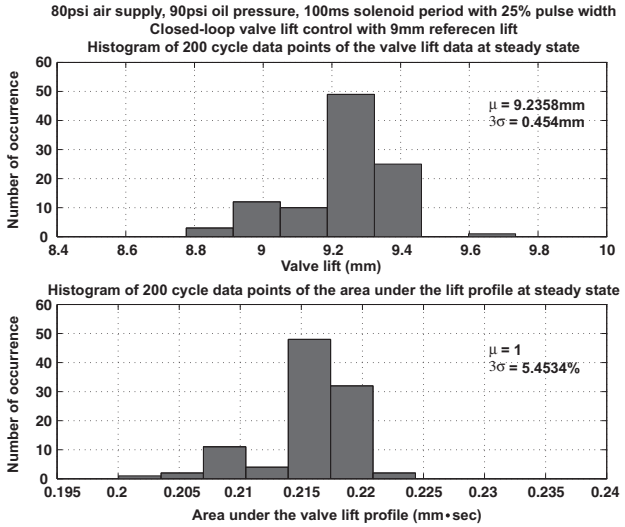

Figure 15: Histogram of closed-loop valve lift control test data points for $9mm$ reference lift at $1200rpm$ in 200 cycles

This is critical for transient air charge control. The controlled input $\hat{\delta}_1$ is close to the nominal input $\hat{\delta}_{1_o}$ which is sufficiently accurate to bring the valve lift close to the reference valve lift in the first cycle. In all four cases, the actual valve lift is within $0.5mm$ lift error region of the reference lift in one cycle.

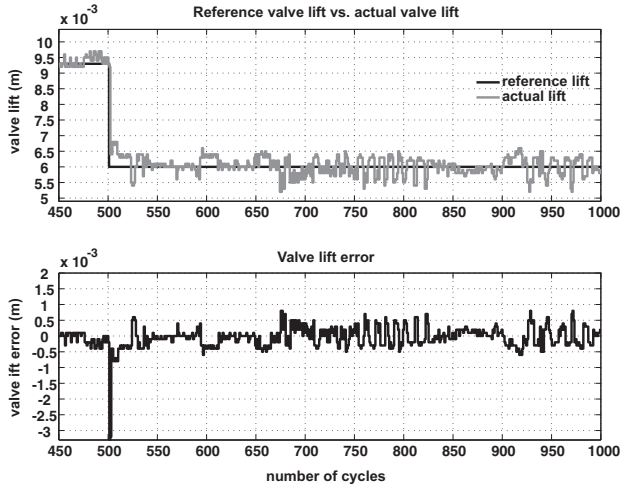

Figure 16: Steady state valve lift tracking responses from $9mm$ to $6mm$ lift at $1200rpm$

EXPERIMENTAL RESULTS AT HIGH ENGINE SPEED The high speed closed-loop valve lift tracking results are presented and discussed in this subsection. Similar to the low speed case, 2500 cycles of valve responses were collected with multiple reference valve lift set points the same as these in the low

Table 5: Statistical study of closed-loop valve actuation data at $1200rpm$

Engine configuration	Data group	$y_{max} = \mu \pm 3\sigma\ (mm)$	$y_{area} = \mu \pm 3\sigma$
$80psi$ air supply pressure	#1	9.2358 ± 0.454	$1 \pm 5.4534\%$
$90psi$ oil pressure	#2	9.2495 ± 0.3478	$1 \pm 2.9224\%$
$100ms$ valve operation period	#3	9.0984 ± 0.38628	$1 \pm 4.8195\%$
$25ms$ valve opening duration	#4	9.0549 ± 0.44419	$1 \pm 5.1670\%$
$9mm$ reference valve lift (with holding)	#5	9.1015 ± 0.41092	$1 \pm 4.1833\%$

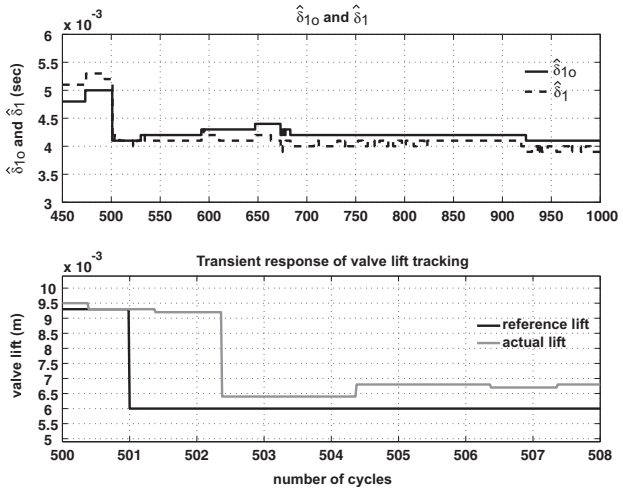

Figure 17: Controlled input and transient valve lift tracking responses from $9mm$ to $6mm$ lift at $1200rpm$

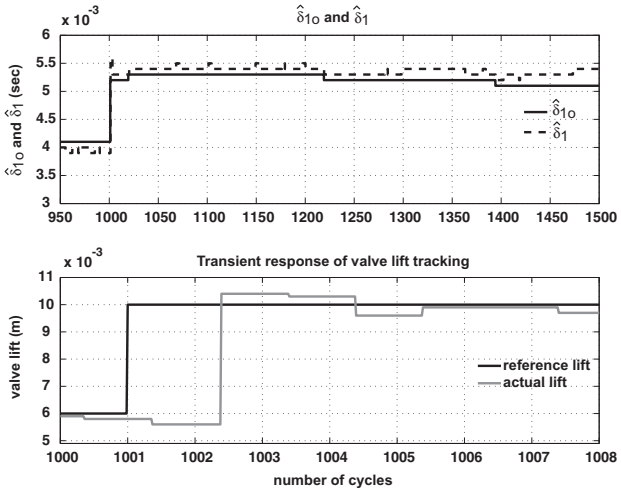

Figure 19: Controlled input and transient valve lift tracking responses from $6mm$ to $10mm$ lift at $1200rpm$

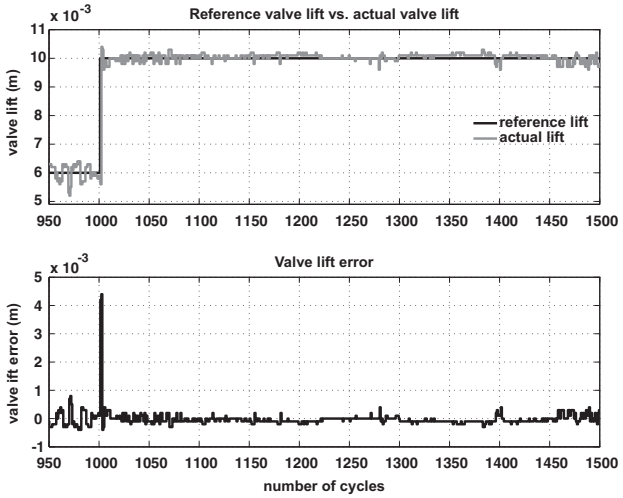

Figure 18: Steady state valve lift tracking responses from $6mm$ to $10mm$ lift at $1200rpm$

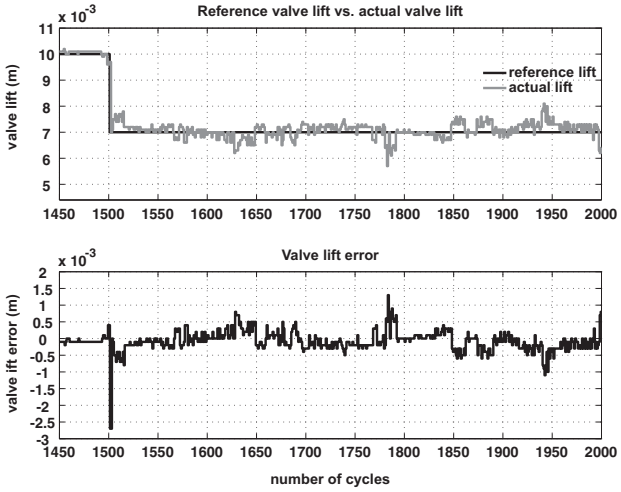

Figure 20: Steady state valve lift tracking responses from $10mm$ to $7mm$ lift at $1200rpm$

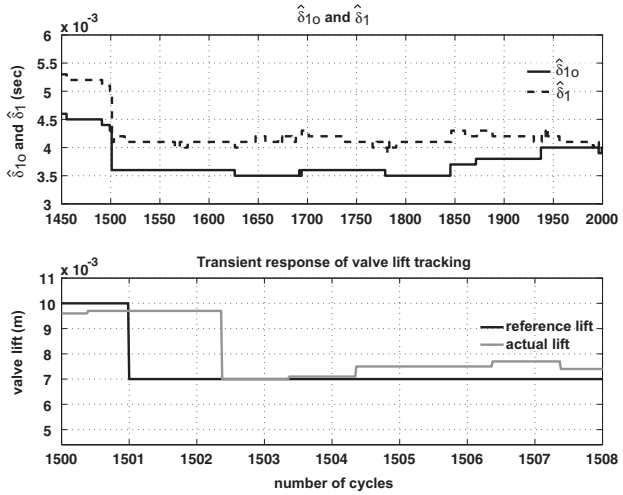

Figure 21: Controlled input and transient valve lift tracking responses from $10mm$ to $7mm$ lift at $1200rpm$

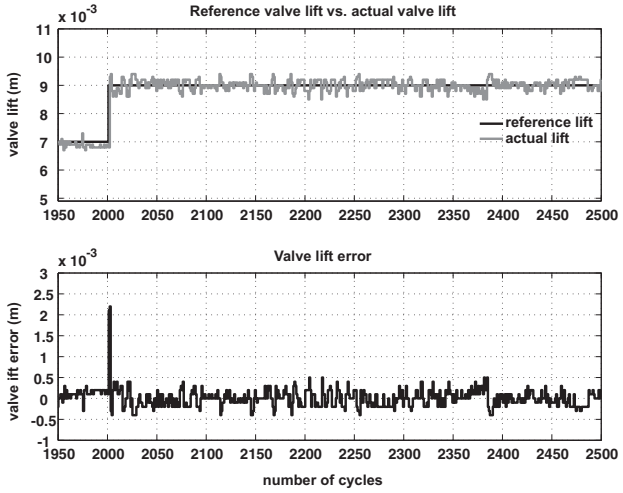

Figure 22: Steady state valve lift tracking responses from $7mm$ to $9mm$ lift at $1200rpm$

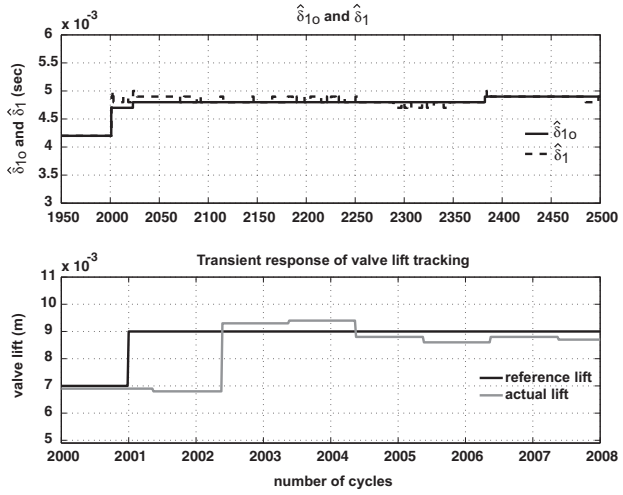

Figure 23: Controlled input and transient valve lift tracking responses from $7mm$ to $9mm$ lift at $1200rpm$

engine speed case. The entire 2500 cycle lift tracking responses and two enlarged transient responses are shown in Figure (24). The top diagram displays the reference valve lift in black line, the actual valve lift in light grey and the lift error in dark grey; the middle diagram shows the transient response at the reference lift change from $10mm$ to $6mm$, and the bottom diagram shows the transient response at the reference lift change from $7mm$ to $9mm$. All the horizontal axes are the number of engine cycles. The vertical axes are the valve lifts in m. The estimated parameter was converged within 100 cycles (or $2.4ms$) which was indicated by a small jump on the reference valve lift on the top diagram. In most of cases, it takes about one cycle for the valve to reach the reference valve lift with less than $0.5mm$ of lift error. However, when the reference lift has a relatively large drop, the actual lift would have a big undershoot during the transient response (see the transient response from $10mm$ to $7mm$ in the top diagram of Figure (24)). The undershoot is about $1.9mm$ in this case for the first step, and $0.5mm$ after the first step. This is partially due to the supply air pressure variations of different lift conditions at high engine speed. The high air flow requirement at high valve lift operational conditions reduces the actual supply air pressure close to the actuator, and supply air pressure increases as the valve lift reduces. When the valve is transient from high lift to low lift, the supply air pressure increases gradually, causing larger undershoot since the feedforward control assumes higher supply air pressure than actual one. This problem can be resolved by increasing the volume of the planum at the supply air manifold of the actuator cylinder.

The maximum absolute steady state error at these four set points are listed in Table 6. The steady state lift errors are less than $0.8mm$ at high valve lift and less than $1.1mm$ at low lift.

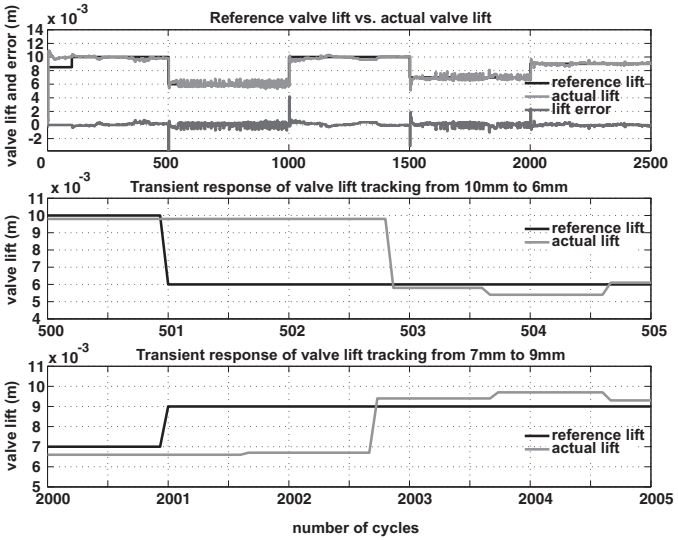

Figure 24: Valve lift tracking responses with multiple reference lift at $5000rpm$

Table 6: Maximum SS absolute valve lift error ($5000rpm$)

Reference valve lifts (mm)	6	7	9	10
Max. absolute lift error (mm)	0.8	1.1	0.8	0.7

The results of the valve lift statistical study at $5000rpm$ engine speed shown in both Figure (13) and Table 2 provide the worst lift 3σ value at $0.63mm$ and the worst integral area 3σ value at

Table 7: Statistical study of closed-loop valve actuation data at $5000rpm$

Engine configuration	Data group	$y_{max} = \mu \pm 3\sigma\ (mm)$	$y_{area} = \mu \pm 3\sigma$
$80psi$ air supply pressure	#1	9.0439 ± 0.45208	$1 \pm 9.4497\%$
$90psi$ oil pressure	#2	9.0832 ± 0.28338	$1 \pm 5.1215\%$
$100ms$ valve operation period	#3	9.1641 ± 0.313	$1 \pm 7.4794\%$
$25ms$ valve opening duration	#4	8.9544 ± 0.24869	$1 \pm 6.69\%$
$9mm$ reference valve lift (without holding)	#5	9.091 ± 0.37342	$1 \pm 8.2682\%$

11.7% with the target lift at $9mm$ using five test data groups. The same statistical analysis is performed for the closed-loop lift control. Five 200 cycle steady state valve responses at $9mm$ reference lift were used to calculate the means and standard deviations of the valve lift and its integral area. These results are compared with the open-loop results. The diagrams displayed in Figure (25) depict the histograms of the valve lift and integral area with the largest variations (data group $\#1$ in Table 7). For easy comparison, the axes ranges and the bin width of the valve lift (top) and integral area (bottom) histograms in Figure (25) are the same as those in Figure (13). The five sets of means and 3σ values of valve lift and integral area were summarized in Table (7). The worst 3σ value of the valve lift reduced from the open-loop $0.63mm$ to the closed-loop $0.45mm$ which was reduced by about 29%. The worst integral area 3σ value reduced from 11.7% to 9.45% which was reduced by about 19% (see both Table (7) and Table (2)). The low engine speed closed-loop lift control data showed a reduction of about 45% on both the 3σ values of the valve lift and integral area in their worst case. The reduction on the cycle to cycle lift variation at $5000rpm$ seems lower than that at $1200rpm$. We believe that low improvement at high engine speed is mainly due to the fixed control sample rate which reduces the valve control resolution as engine speed increases.

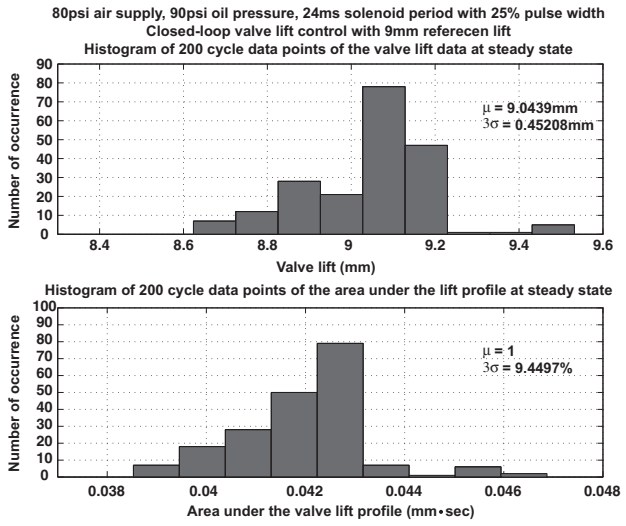

Figure 25: Histogram of closed-loop valve lift control test data points for $9mm$ reference lift at $5000rpm$ in 200 cycles

CONCLUSION

A nonlinear mathematical model called the level one model was developed for the electro-pneumatic valve actuator based on Newton's law, mass conservation and thermodynamic principles. A control oriented model, called level two model, was established using the physics based nonlinear model for model reference parameter identification. This level two model reduces computational throughput and enables real time implementation. A model reference adaptive scheme was employed to identify two key nonlinear system parameters. The identified parameters are then used to construct the feedforward control as part of the closed-loop valve PI controller. The closed-loop valve lift tracking, and valve opening and closing timing control strategies were developed and validated on an electro-pneumatic valve actuator test bench. The test data covers multiple reference lift points at both $1200rpm$ and $5000rpm$ engine speeds for both steady state and transient operations. The experiment results showed that the actual valve lift reached the reference lift within $0.5mm$ of lift error in one cycle at $1200rpm$ and in two cycles at $5000rpm$. The maximum steady state lift errors are less than $0.4mm$ at high valve lift and less than $1.3mm$ at low valve lift. Furthermore, the closed-loop valve lift control improved valve lift repeatability with more than 30% reduction of standard deviation over the open-loop control.

ACKNOWLEDGEMENT

The authors gratefully acknowledge the support for this work from the U.S. Department of Energy, National Energy Technology Laboratory, Energy Efficiency and Renewable Energy Division, Samuel Taylor, Project Manager.

REFERENCES

[1] Hans Peter Lenz, Klaus Wichart and Dusan Gruden, "Variable Valve Timing - A Possibility to Control Engine Load without Throttle," *SAE 880388*, 1988.

[2] Nichulae Negurescu, Constantin Pana, Marcel Ginu Popa and Alexandru Racovitza, "Variable Valve - Control Systems for Spark Ignition Engine," *SAE 2001-01-0671*, 2001.

[3] Tim Lancefield, "The Influence of Variable Valve Actuation on the Part Load Fuel Economy of a Modern Light-Duty Diesel Engine," *SAE 2003-01-0028*, 2003.

[4] D. L. Boggs, H. S. Hilbert and M. M. Schechter, "The Otto-Atkinson Cycle Engine-Fuel Economy and Emissions Results and Hardware Design," *SAE 950089*, 1995.

[5] Yasuhiro Urata, Moriyoshi Awasaka, Junichi Takanashi, Takashi Kakinuma, Takazou Hakozaki and Atushi Umemoto, "A Study of Gasoline-Fuelled HCCI Engine Equipped with an Electromagnetic Valve Train," *SAE 2004-01-1898*, 2004.

[6] Nate R. Trask, Mazen Hammoud, Mohammad Haghgooie, Thomas W. Megli and Wen Dai, "Optimization Techniques and Results for the Operating Modes of a Camless Engine," *SAE 2003-01-0033*, 2003.

[7] K. Inoue, K. Nagakiro, Y. Ajiki, and N. Kishi, "A High Power Wide Torque Range Efficient Engine with a Newly Developed Variable Valve Lift and Timing Mechanism," *SAE 890675*, 1989.

[8] Y. Moriya, A. Watanabe, U. Uda, H. Kawanura, M. Yoshioka, and Adachi, "A Newly Developed Intelligent Variable Valve Timing System Continuously Controlled Cam Phasing as Applied to a New 3 Liter Inline 6 Engine," *SAE 960579*, 1996.

[9] R. Flierl and M. Kluting, "The Third Generation of New Fully Variable Valvetrain for Throttle Free Load Control," *SAE 2000-01-1227*, 2000.

[10] M. Theobald, B. Lequesns, and R. Henry, "Control of Engine Load via Electromagnetic Valve Actuators," *SAE 940816*, 1994.

[11] C. Boie, H. Kemper, L. Kather, and G. Corde, "Method for Controlling a Electromagnetic Actuator for Achieving a Gas Exchange Valve On a Reciprocating Internal Combustion Engine," *US Patent 6,340,008*, 2000.

[12] L. Schneider, "Electromagnetic Valve Actuator with Mechanical End Position Clamp or Latch," *US Patent 6,267,351*, 2001.

[13] I. Haskara, L. Mianzo, and V. Kokotovic, "Method of Controlling an Electromagnetic Valve Actuator," *US Patent 6,644,253*, 2003.

[14] O. Sturman, "Hydraulic Actuator for an Internal Combustion Engine," *US Patent 5,638,781*, 1994.

[15] G. Wright, N. Schecter, and M. Levin, "Integrated Hydraulic System for Electrohydraulic Valvetrain and Hydraulicly Assisted Turbocharger," *US Patent 5,375,419*, 1994.

[16] Z. Sun and D. Cleary, "Dynamics and Control of an Electro-Hydraulic Fully Flexible Valve Actuation System," *Proceedings of American Control Conference*, Denver, Colorado, June, 2003.

[17] Jia Ma, Harold Schock, Urban Carlson, Anders Hoglund and Mats Hedman, "Analysis and Modeling of an Electronically Controlled Pneumatic Hydraulic Valve for an Automotive Engine," *SAE 2006-01-0042*, 2006.

[18] Mark D. Anderson, Tsu-Chin Tsao and Micheal B. Levin, "Adaptive Lift Control for a Camless Electrohydraulic Valvetrain," *SAE 981029*, 1997.

[19] K. Misovec, B. Johnson, G. Mansouri, O. Sturman, and S. Massey, "Digital Valve Technology Applied to the Control of an Hydraulic Valve Actuator," *SAE 1999-01-0825*, 1999.

[20] Hajime Hosoya, Hidekazu Yoshizawa, Satoru Watanabe, Naoki Tomisawa and Kenichi Abe, "Development of New Concept Control System for Valve Timing Control," *SAE 2000-01-1226*, 2000.

[21] Karl Johan Astrom and Bjorn Wittenmark, *Adaptive control (2nd edition)*, Addison-Wesley Publishing Company, Boston, MA, 1995.

[22] William T. Thomson, Theory of vibration with applications," *5th ed., Prentice Hall*, Upper Saddle River, New Jersey, 1998.

[23] Jia Ma, Guoming Zhu, Harold Schock and Jim Winkelman, "Adaptive Control of a Pneumatic Valve Actuator for an Internal Combustion Engine," accepted by the *Proceedings of American Control Conference*, New York, New York, June, 2007.

Adaptive Control of a Pneumatic Valve Actuator for an Internal Combustion Engine

Jia Ma*, Guoming Zhu**, Harold Schock* and Jim Winkelman**

***Abstract*— Electro-pneumatic valve actuators are used to eliminate the cam shaft of a traditional internal combustion engine. They are used to control the opening timing, duration, and lift of both intake and exhaust valves. A control oriented model was developed to reduce computational throughput for real-time implementation. The developed control oriented model was validated by experimental data. An adaptive valve lift control strategy was developed to improve lift repeatability. A model reference adaptive system identification technique was employed to calculate system parameters needed for generating closed-loop control signals. The convergence of the derived adaptive parameter identification algorithm was verified using the valve test bench data. The bench test data covers engine speed from 1200RPM and 5000RPM. Parameter identification convergence was achieved within 40 cycles. Error between the model and plant outputs were converged to given tolerances. Finally, a closed-loop control strategy was developed and validated in simulation.**

I. INTRODUCTION

Variable intake and/or exhaust valve actuation is capable of significantly improving the fuel economy, emissions, and power output of Internal Combustion (IC) engines. Variable valve actuation can be achieved with mechanical (cam-based), electro-magnetic (electric mechanical), electro-hydraulic, and electro-pneumatic valvetrain mechanisms. The cam based variable valve actuation is able to provide either a multiple stepping or a continuously changing valve timing phase shift. Honda mechanism [4] is a multiple-step actuator that allows a switch between two cams. The Toyota system [5] allows the intake and exhaust cams to shift continuously without the flexibility of varying the valve lift and duration. BWM's valvetronic system [6] combines variable cam phasing with a continuously variable valve lift and duration actuation.

Infinitely variable valvetrain, often referred to camless valvetrain, includes electro-magnetic, electro-hydraulic, and electro-pneumatic actuation. The electro-magnetic systems, such as GM Magnavalve [7], FEV [8], Aura [9], Visteon [10] systems, are capable of generating variable valve timing and duration but with fixed lift operation. The electro-hydraulic systems, such as the Sturman system [12], Ford and GM "camless" systems ([11] and [13]), provide infinitely variable valve timing, duration, and lift. The electro-pneumatic valve actuator (EPVA) [1] utilizes the supplied air pressure to actuate either the intake or exhaust valve by electronically controlling solenoids. For both electro-hydraulic and electro-pneumatic valves, there is a potential issue of having a repeatable valve lift over the life of an engine.

Valve lift control for electro-hydraulic valvetrain actuation has been investigated by number of researchers. Adaptive peak lift control was presented in [14], and digital valve technology was applied to control of an hydraulic valve actuator in [15]. This paper proposed an adaptive lift control scheme for the electro-pneumatic valve actuator to improve the EPVA lift repeatability. A control oriented electro-pneumatic valve model was developed and used for adaptive parameter identification; and a closed-loop control scheme of valve lift was developed, utilizing the identified parameters. The main control techniques used in the process include model reference adaptation and MIT rule that can be found in [3].

The paper is organized as follows. First, a control oriented model is presented in Section II. Next, the valve actuator parameter identification and its closed-loop control are discussed in Section III. Third, the experimental validation results are shown in Section IV where the adaptive parameter identification convergence was verified with test bench data. Finally, conclusions are drawn.

II. MODELING

A physics based mathematical model, called level one model, was built component by component where the flow and fluid dynamics were considered. The details of the level one model and its verification can be found in [1]. This model provides an insight into the hydraulic-mechanical system. The profound understanding of the system gained from this modeling process helped to develop a simplified model for control development purpose in the next step.

A. Level Two Model

The level one model is a sophisticated nonlinear model which requires heavy computational throughput and is almost impossible to be implemented in real time. A control oriented model, called level two model, is needed in this case.

1) System dynamics: EPVA consists of an actuator piston, a hydraulic latch (damper), inlet and outlet port valves, two solenoids and two spool valves. The actuator piston is driven by compressed air. It sits on the back of the valve stem, hence, its motion is equivalent to the valve motion. Figure 1 shows the schematic diagram of an EPVA.

The authors gratefully acknowledge the support for this work from the U.S. Department of Energy, National Energy Technology Laboratory, Energy Efficiency and Renewable Energy Division, Samuel Taylor, Project Manager.

Jia Ma* and Harold Schock* are with Mechanical Engineering, Michigan State University, Automotive Research Experiment Station, 3361 Hulett Road, Okemos, MI 48864-4205, USA majia1@msu.edu, schock@egr.msu.edu

Guoming Zhu** and Jim Winkelman** are with the Visteon Corporation, One Village Center Dr., Van Buren TWP, MI 48111, USA gzhu1@visteon.com, jwinkelm@visteon.com

A detailed description of EPVA dynamics and level one model can be found in [1]. The level two modeling work concentrates on the piston (end actuator) dynamics and omits the nonlinear flow dynamics. As illustrated in Figure 2, the valve operation process can be divided into three stages. They are opening stage I, dwell stage II and closing stage III.

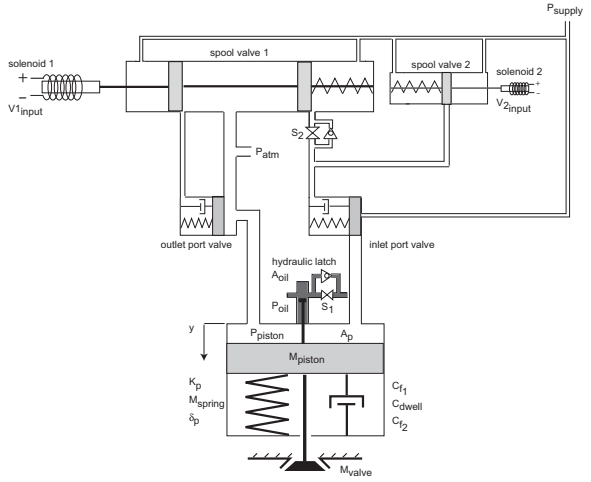

Fig. 1. Valve lift profile with the solenoid action chart excluding system delays

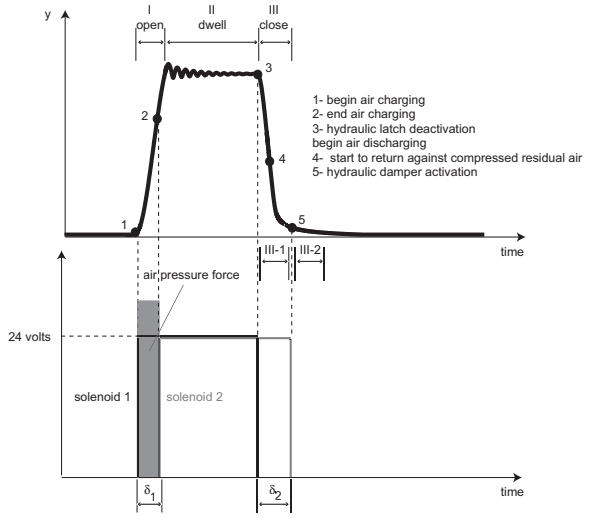

Fig. 2. Valve lift profile with the solenoid action chart excluding system delays

2) System modeling: Opening stage

In this stage the valve actuator is modeled as a second order mass-spring-damper system with zero initial conditions, see Equation (1).

$$M\ddot{y} + C_{f_1}\dot{y} + K_p(y + \delta_p) = F(t) - F(t - \delta_1) \quad (1)$$

$$F(t) = \begin{cases} 0, & \text{if } t < 0 \\ A_pP_p + A_{cap}P_{oil} - (A_p + A_{cap})P_{atm} & \text{if } t \geq 0 \end{cases}$$

where $P_p = P_{oil} \approx P_{supply}$, and

- $M = M_{piston} + M_{valve} + \frac{1}{3}M_{spring} + M_{cap}$, where M_{piston} is the mass of the actuator piston, M_{valve} is the mass of the intake valve and M_{spring} is the mass of the valve spring. The effective spring mass equals one third of the total spring mass [2], and M_{cap} is the mass of the cap on the top of the valve stem;
- $A_p = \pi r_p^2 - \pi r_{oil}^2$ with r_p as the radius of the actuator piston and r_{oil} as the radius of the oil passage;
- C_{f_1} is the damping ratio approximating energy dissipation due to flow loss and frictional loss;
- K_p is the stiffness of the valve spring;
- δ_p is the preload of the valve spring;
- P_p is the in-cylinder air pressure, P_{oil} is the oil pressure and is at the same pressure as air supply, and P_{supply} is the air supply pressure;
- A_{cap} is the area of the cap on the top of the actuator piston stem;
- δ_1 is the lag between the activation of solenoid 1 and 2 without system delays as illustrated in Figure 2, and δ_2 is the time needed for valve to return to the seat.

Dwell stage

The equation of motion at stage II is described as follows:

$$M\ddot{y} + C_{dwell}\dot{y} + K_p(y + \delta_p) = A_pP_p + A_{cap}P_{oillock} - (A_p + A_{cap})P_{atm} \quad (2)$$

where $P_p \approx P_{atm}$ since the supply pressure has been removed and the piston is fully extended at this stage, M is the total mass of the actuator system as described in Equation (1), C_{dwell} is the damping ratio approximating energy dissipation due to frictional loss at dwell (lock) stage, and $P_{oillock}$ is the oil pressure applied to piston stem in dwell stage. The state equation $PV^c = K = constant$ is used to obtain the expression for $P_{oillock}$ where a large c value was chosen to represent the low compressibility.

$$P_{oillock}V^c = P_iV_i^c \quad (3)$$

Substituting $V = A_{cap}y$ and $V_i = A_{cap}y_i$ into Equation (3) to obtain:

$$P_{oillock} = \frac{P_iy_i^c}{y^c} \quad (4)$$

where y_i is the maximum valve displacement, V_i is the volume of the fluid at the maximum valve displacement y_i, and P_i is the oil pressure P_{oil} at the peak valve lift height y_i.

Closing stage

Dynamic motion in the closing stage was divided into two sub-stages (sub-stages III-1 and III-2) as illustrated in Figure 2. Substage III-1 can again be separated into two segments. The first segment is from point 3, where the piston starts returning, to point 4; and the second segment is from point 4 to point 5 where the hydraulic damper becomes effective. In the first segment, piston motion is a free return, however, in the second segment, the piston returns against certain pressure due to in-cylinder compressed residual air. For simplicity, both segments were modeled as free returns.

In substage III-2, the piston returns against largely increased hydraulic damping force that acts on the piston stem. The governing equations at this stage are described in Equations (5) and (6). Equation (5) describes the response from point 3 to 5 (see Figure 2).

$$M\ddot{y} + C_{f_2}\dot{y} + K_p y + K_p\delta_p = 0 \tag{5}$$

where $y(0) = y_{max}$, and $\dot{y}(0) = 0$. The response beyond point 5 in hydraulic damping region follows the response of Equation (6).

$$M\ddot{y} + C_{f_2}\dot{y} + K_p(y + \delta_p) = A_p P_p + A_{cap} P_{oil} - (A_p + A_{cap}) P_{atm} \tag{6}$$

where P_{oil} is a constant in substage III-1. But it is a function of flow out area in the hydraulic damper in substage III-2. The detail derivation of P_{oil} can be found in [1].

B. Level Two Model Validation

The simulation and experimental responses of the level two model are compared in Figure 3. The thin valve curve is the experimental response; and the thick one is the simulated response using level two model. Damping ratio at opening stage, C_{f_1}, and damping ratio at closing stage, C_{f_2} are identified manually by trial and error in this simulation. In the real time implementation, these damping coefficients will be adaptively identified online since they vary significantly with respect to temperature, fluid viscosity and engine operational conditions. The two curves close to the x axis are the measured solenoid currents, where the solid line is the dwell current of solenoid 1 and the dash line is that of solenoid 2. There are delays between the activation of the solenoids and the actual mechanical motions. The total delay associated with solenoids 1 and 2 are defined as Δt_1 and Δt_2 respectively. As shown in Figure 3, total delay of each solenoid rises in two steps. Taking solenoid 1 current as an example, the first rise is from the starting point to the first peak which represents the electrical delay; and the second rise is from the first peak to the second peak which represents the magnetic delay. Algorithms were developed to detect Δt_1 and Δt_2 at each cycle. Δt_1 is used to follow reference opening timing by compensating the valve opening delay. Both Δt_1 and Δt_2 are used to modify the pulse width of air pressure force input δ_1 associated with the valve lift control. This will be discussed in the next section.

III. CONTROL STRATEGY

The control strategy of valve timing, duration, and lift is addressed in this section. An adaptive parameter identification algorithm using model reference technique and MIT rule [3] played an important role in the control process. The identified parameters are then used to modify parameters in the closed-loop controller. Some approximations are introduced to obtain analytical solutions of control input in terms of the estimated parameters. To further reduce the computational efforts, only stages I and III of level two

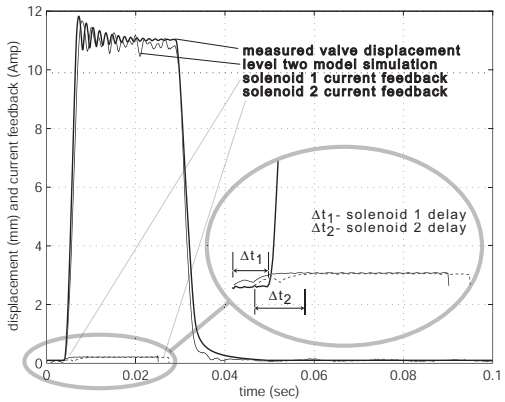

Fig. 3. Level two model simulation and experiment responses

model were used in the controller. (see Figure 2). Parameters involved in the control process were investigated and defined for three possible cases. The closed-loop control scheme is proposed and the concept is validated in simulation for closed-loop valve lift control. The closed-loop valve open and close timing control portion is similar to the valve lift control, and the results are not repeated in this section.

A. Parameter Definition

Figure 4 defines the parameters involved in control strategy. At low engine speed, the valve lift profile has all three stages as shown in the left diagram, where the holding period exists. This kind of response is categorized in case 1 (with holding). As engine speed increases, the holding period reduces. At certain engine speed, the holding period disappears, and the valve lift profile consists of only the opening and closing stages as shown in the right diagram. That is named as case 2 (without holding). In this case, solenoid 1 was deactivated shortly after its activation. It discharges the cylinder and allows valve to return before the hydraulic latch is engaged. In these two cases, both solenoids 1 and 2 are needed to control the valve event. There is another special case in which only solenoid 1 was used. The cylinder was simply charged with supply air when solenoid 1 is energized and discharged when solenoid 1 is de-energized. This occurs when the engine speed is so high that the activation duration of solenoid 1 becomes very small. The valve lift control is implemented by regulating air supply pressure in this case. Note that in both cases 1 and 2, the air supply pressure remains unchanged throughout the process. This special case is not the subject of discussion in this paper. As displayed in the left diagram of Figure 4, control pulses of solenoids 1 and 2 are generated based upon $DefA$ and $DefB$ pulses that are synchronized with engine crank angle. $DefB$ appeared to be nonzero during the time $DefA$ was sent, when the system needs to utilize both solenoids 1 and 2. $DefA$ and $DefB$ pulses carry the control information and they will be converted to solenoid command pulses.

The convention of this transformation is defined as follows. The first and second rising edges of $DefA$ correspond to the activation of solenoids 1 and 2. The first and second

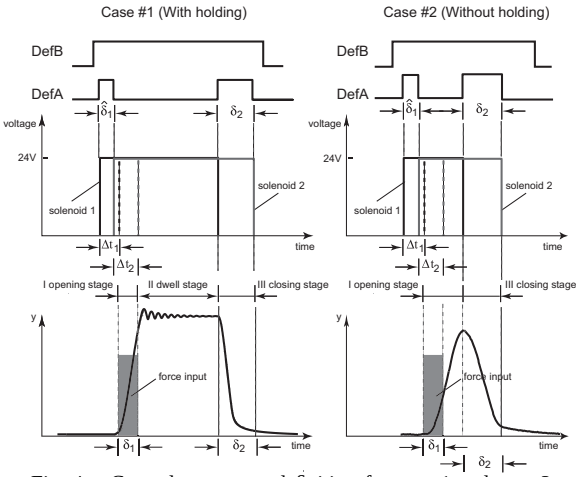

Fig. 4. Control parameter definition for case 1 and case 2

falling edges of $DefA$ correspond to the deactivation of solenoids 1 and 2. The first pulse width of $DefA$ is denoted as $\hat{\delta}_1$ and the second pulse width of $DefA$ is denoted as δ_2. $\hat{\delta}_1$ is the time duration between the activation of two solenoids. The second falling edge of $DefA$, which is also the falling edge of solenoid 2 pulse, is defined to be the desired valve closing time. δ_2 represents the time needed for the valve to return after the deactivation of solenoid 1 (at valve return point). Activation of solenoids 1 and 2 begins their impact on the system after time delays Δt_1 and Δt_2 respectively. The air pressure in the piston cylinder rises and forms a pulse force input to the system with a pulse width δ_1. Therefore, $\hat{\delta}_1$ associates with δ_1 through the expression $\hat{\delta}_1 = \delta_1 + (\Delta t_1 - \Delta t_2)$, given the fact that Δt_1 is always greater than Δt_2. The parameter convention described in the right diagram of Figure 4 for case 2 is similar to case 1. For both cases, desired valve opening and closing timing and desired valve lift are known variables.

B. Adaptive Parameter Identification

The architecture of adaptive parameter identification is illustrated in Figure 5, where $G_m(S)$ is the model and $G_p(S)$ is the plant. The goal of this estimator is to identify the damping ratios C_{f_1} and C_{f_2}, where C_{f_1} is for the opening stage and C_{f_2} is for the closing stage. The error e between model and plant outputs reduces as the estimated parameters converge. The excitation force u is a pulse input with PE of order infinity that meets the persistent excitation condition in the adaptive identification. The identification controller based on MIT rule utilizes the error between the model and plant outputs and generates the estimated C_{f_1} or C_{f_2}, where C_{f_1} and C_{f_2} update at every step during the identification period.

1) MIT rule: MIT rule states as follows.

$$J(\theta) = \frac{1}{2}e^2 = \frac{1}{2}[y(t) - y_m(t)]^2 \tag{7}$$

$$\dot{\theta} = -\gamma \nabla_\theta J(\theta) = -\gamma e \nabla_\theta e = -\gamma e \frac{\partial e}{\partial \theta} \tag{8}$$

where y, valve displacement, is the plant output and y_m is the model output of valve displacement, e is the error between

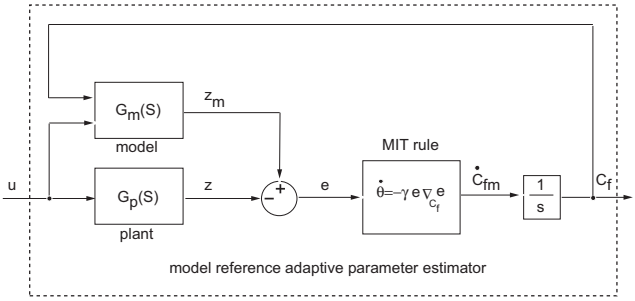

Fig. 5. Model reference adaptive parameter identification scheme

the model and plant outputs, θ is the estimated parameter, and $\gamma > 0$ is the adaptive gain. In this case,

$$\theta = \begin{cases} C_{f_1}, & \text{for opening stage} \\ C_{f_2}, & \text{for closing stage} \end{cases}$$

2) Adaptive law at opening stage: In this section and the following section, the adaptive law at opening and closing stage is developed based on the MIT rule. The governing equation of the system at this stage is expressed in Equation (9).

$$M\ddot{y} + C_{f_1}\dot{y} + K_p y + K_p \delta_p = u(t) \tag{9}$$

where $y(0) = -\delta_p$, $\dot{y}(0) = 0$, and $u(t) = F(t) - F(t - \delta_1)$ by Equation (1). To change the coordinate, let

$$z = y + \delta_p \tag{10}$$

Equation (9) can be re-written in z coordinate as below:

$$M\ddot{z} + C_{f_1}\dot{z} + K_p z = u(t) \tag{11}$$

where $z(0) = \dot{z}(0) = 0$. Laplace transform of Equation (11) results in Equation (12):

$$MS^2 + C_{f_1}SZ(S) + K_p Z(S) = U(s) \tag{12}$$

The transfer function takes the following form:

$$G(S) = \frac{Z(S)}{U(S)} = \frac{1}{MS^2 + C_{f_1}S + K_p} \tag{13}$$

The error between the model output and the plant output in Laplace domain $E(S)$ can be expressed in the equation below:

$$E(S) = Z(S) - Z_m(S) = \frac{1}{MS^2 + C_{f_1}S + K_p}U(S) - \frac{1}{MS^2 + C_{fm_1}S + K_p}U(S) \tag{14}$$

where Z and Z_m are the plant and model outputs, and C_{f_1} and C_{fm_1} are the plant and model damping ratios. Let $P(S) = \frac{\partial E(S)}{\partial C_{fm_1}}$. We obtain $P(S)$ by taking partial derivative of $E(S)$ with respect to C_{fm_1}:

$$P(S) = \frac{U(S)}{MS^2 + C_{fm_1}S + K_p}\frac{S}{MS^2 + C_{fm_1}S + K_p} \tag{15}$$

Since $\frac{U(S)}{MS^2+C_{fm_1}S+K_p} = Z_m(S)$ by Equation (14), Equation (15) can be rearranged into Equation (16) :

$$P(S) = Z_m(S)\frac{S}{MS^2 + C_{fm_1}S + K_p} = Z_m(S)\frac{1}{MS + C_{fm_1} + \frac{K_p}{S}} \quad (16)$$

Taking the inverse Laplace transform of Equation (16) to obtain the adaptation law of $\dot{p}(t)$ results in Equation (17).

$$\dot{p}(t) = \frac{1}{M}\big(z_m(t) - C_{fm_1}p(t) - K_p\int p(t)dt\big) \quad (17)$$

The adaptation law of C_{f1} at opening stage is summarized below:

$$\begin{cases} \dot{C}_{fm_1} = -\gamma_1 p(t)e \\ \dot{p}(t) = \frac{1}{M}\big(z_m(t) - C_{fm_1}p(t) - K_p\int p(t)dt\big) \\ e = z - z_m = y - y_m \end{cases}$$

with $\gamma_1 > 0$ chosen to be an adaptive gain. The adaptation takes place between point 1 and the first peak on the valve response as indicated in Figure 2.

3) Adaptive law at closing stage: The adaptive law of C_{f2} at the closing stage can be derived in a similar way to the opening stage, and the result is presented below.

$$\begin{cases} \dot{C}_{fm_2} = -\gamma_2 q(t)e \\ \dot{q}(t) = \frac{1}{M}\big(z_m(t) - C_{fm_2}q(t) - K_p\int q(t)dt - \int z(0)dt\big) \\ e = z - z_m = y - y_m \end{cases}$$

with $\gamma_2 > 0$ being an adaptive gain and C_{fm_2} being the model damping ratio. The adaptation occurs between points 3 and 4 as indicated in Figure 2, since the valve experiences a pure free return in this portion of the response.

C. Closed-Loop Control Scheme

Valve opening timing control can be achieved by compensating the identified solenoid 1 delay Δt_1 at every cycle. Controller design in this subsection focuses on the valve lift and closing timing control. These involve the adjustment of $\hat{\delta}_1$ and δ_2.

1) Closed-loop valve lift and closing timing control: Since the estimated damping ratios are available due to adaptive parameter identification, the closed-loop valve timing and lift control scheme is developed based upon the identified parameters and the lift control algorithm is validated in simulation. The structure of the closed-loop controller with the parameter estimator is shown in Figure 6. The control goal is to let the plant output y track the desired input y_{desire} and the desired closing timing. The nominal values of $\hat{\delta}_{1_o}$ and δ_{2_o} are computed based on the estimated C_{f_1} and C_{f_2}. They are the feedforward control signals to the system. The error between y_{max} and y_{desire} passes through an integrator and then adds onto the nominal $\hat{\delta}_{1_o}$. That produces $\hat{\delta}_1$ as a feedback signal to the system for valve lift control. The integral action is added to achieve the zero steady state tracking error and at the same time to reject the step type of disturbance. $u(\hat{\delta}_{1_o}, \delta_{2_o})$ can be depicted as a function that converts $\hat{\delta}_{1_o}$ and δ_{2_o} to the force input u. In the same manner, δ_2 is constructed as a feedback signal. This allows the closed-loop controller to track the desired closing timing. K_1 and K_2 are two closed-loop gains. The control system operates in an open loop using pre-determined $\hat{\delta}_{1_i}$ and δ_{2_i} until the parameter identification algorithm converges, and then, switches to closed-loop control to minimize the tracking error. A

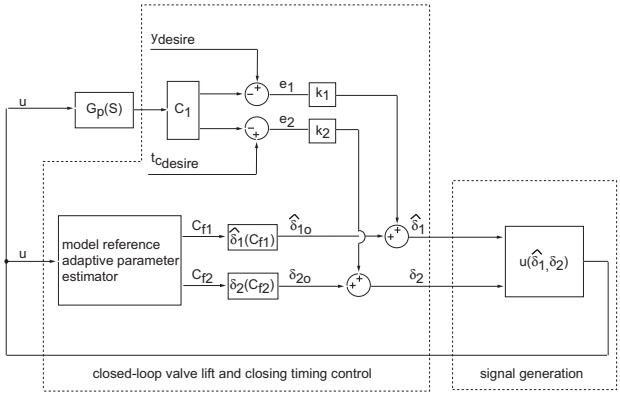

Fig. 6. Closed-loop valve lift and timing control scheme

detailed control scheme is presented in Figure 7. System inputs include valve displacement, solenoids 1 and 2 current feedback, and supply pressure P_{supply}. Desired outputs are valve opening crank angle, valve closing crank angle, and valve lift height. This diagram includes the adaptive estimator that identifies both C_{f_1} and C_{f_2}, and an algorithm developed to detect critical points including maximum valve lift height, valve opening and closing locations and peak displacement, etc. These results are used by the following algorithm to identify Δt_1, Δt_2, $\hat{\delta}_1$ and δ_2. These four parameters are used to generates $DefA$ and $DefB$ pulses. $DefA$ and $DefB$ are then converted to solenoid commands sent to the valve actuator. It is critical to provide a suitable adaptation

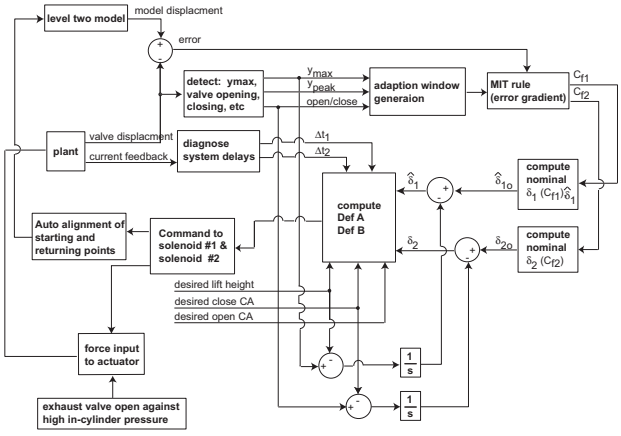

Fig. 7. Control scheme with parameter identification based on model reference adaptation method

window which determines the start and end of adaptive identification at opening and closing stages. Moreover, the returning point at closing stage could be affected by a number

of factors. It greatly depends on hydraulic latch performance, for instance, when the latch is released or whether there is certain oil leak in the latch. Inaccurate locations of the start point at opening stage and the return point at closing stage may cause instability of parameter identification. Algorithms were designed to allocate these locations automatically. This increases the robustness of parameter identification. The adaptive parameter identification algorithm is used to generate feedforward control signals. The feedback closed-loop control will be applied in real time to obtain the initial conditions close enough to the true values so that small adaptive gains can be used to acquire stability.

2) Solutions of $\hat{\delta}_{1_o}$ and δ_{2_o}: In order to compute $\hat{\delta}_{1_o}$ and δ_{2_o}, analytical solutions need to be established. It was found that the system damping ratio is between over-damped and slightly under-damped cases based upon the identified values. Therefore, two first order systems are employed to approximate the second order systems for both opening and closing stages in the region of interest. The closed-form analytical solutions are developed based on the first order system. The formulas of computing $\hat{\delta}_{1_o}$ in terms of C_{f_1} are provided by Equations (18), (19) and (20).

$$\hat{\delta}_{1_o} = \delta_1 - (\Delta t_1 - \Delta t_2) \tag{18}$$

$$\delta_1 = \frac{2}{\sigma} \ln(\frac{a}{a - y_{max}}) \tag{19}$$

$$a = \frac{f_0}{K_p} - \delta_p \tag{20}$$

where $f_0 = A_p P_p + A_{cap} P_{oil} - (A_p + A_{cap}) P_{atm}$ is defined by Equation (1). The formula of solving δ_{2_o} in terms of C_{f_2} is provided in Equation (21).

$$\delta_{2_o} = \frac{100}{C_{f_2}\sigma} \ln(\frac{\delta_p}{y_{max} + \delta_p}) \tag{21}$$

In Equations (19) and (21), σ is derived accordingly for three cases as follows:

$$\sigma = \begin{cases} \frac{C_f}{2M}, C_f^2 < 4K_pM & \text{underdamped} \\ \frac{C_f}{2M}, C_f^2 = 4K_pM & \text{critically damped} \\ |\frac{-C_f + \sqrt{C_f^2 - 4K_pM}}{2M}|, C_f^2 > 4K_pM & \text{overdamped} \end{cases}$$

with $C_f = C_{f_1}$ at opening stage or $C_f = C_{f_2}$ at closing stage.

3) Open-loop parameter estimation and Closed-loop lift control simulation: The adaptive parameter estimation algorithm was simulated for 40 cycles and the results are presented in Figure 8 and Figure 9. The system was simulated with $80psi$ air supply pressure, $5ms$ lag between the activation of solenoids 1 and 2, $100ms$ solenoid period (equivalent to 1200RPM) and $25ms$ solenoid active duration. Figure 8 shows that C_{f_1} and C_{f_2} converge to 80 and 85 respectively. Note that these values are the damping ratios set in the plant model which served as the control target for simulation purposes. The error between the model and the plant outputs converges to a set tolerance in less than ten cycles. Figure 9 shows that after $\hat{\delta}_{1_o}$ and δ_{2_o} were evaluated with the solution based upon the identified C_{f_1} and C_{f_2}, they converge to $5ms$ (top) and $3ms$ (bottom) approximately. The estimated $\hat{\delta}_{1_o}$ is close to the true lag ($5ms$) used in the plant, and δ_{2_o} is also approached to the $3ms$ model plant closing duration.

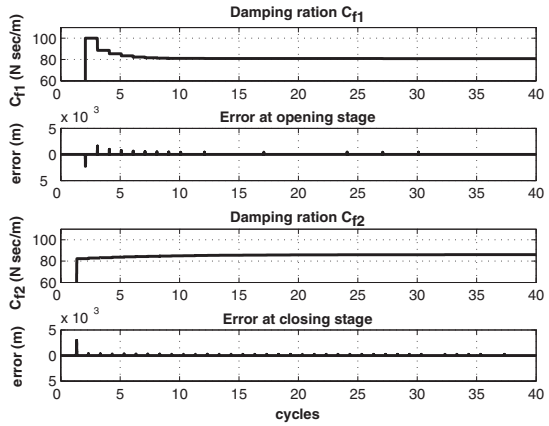

Fig. 8. C_{f_1} and C_{f_2} identification simulation with fixed valve operation at 1200RPM

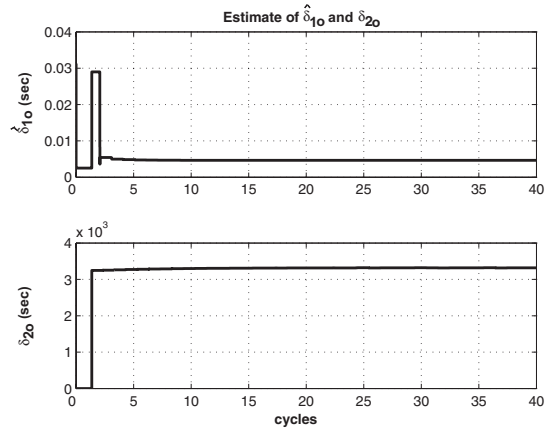

Fig. 9. $\hat{\delta}_{1_o}$ and δ_{2_o} estimation simulation with fixed valve operation at 1200RPM

The closed-loop lift controller is validated in a 40 cycle simulation using the level two model. The simulation results are presented in Figure 10. The system was simulated with $80psi$ air supply pressure, $5ms$ lag between the activation of solenoids 1 and 2 during the open-loop parameter identification period, $100ms$ solenoid period (equivalent to 1200RPM) and $25ms$ solenoid active duration. The desired valve lift y_{desire} is $5mm$. The top diagram in Figure 10 displays the valve lift converging to the $5mm$ set point with zero tracking error. It can also observed from the middle diagram that that the nominal control input $\hat{\delta}_{1_o}$ is estimated to be $3.6ms$ based on the desired valve lift. As displayed in the bottom diagram of this figure, the plant is operated in an open loop condition to achieve the parameter convergence in the first ten cycles. The closed-loop control input $\hat{\delta}_1$ dropped from its initial value to $3.68ms$ at the eleventh cycle. This indicates the beginning of the closed-loop control and the system detects the reference input at this point. In the next

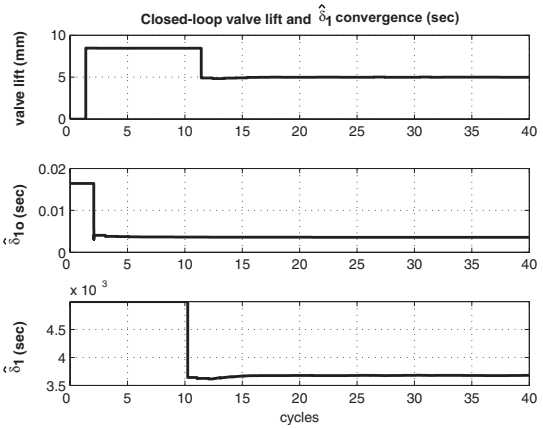

Fig. 10. Closed-loop valve lift control at 1200RPM

cycle, the valve lift was brought down to $5mm$. This one cycle transient response is one of the design criteria.

IV. EXPERIMENTAL IMPLEMENTATION

A. Control System Hardware Configuration

An $Opal-RT^{TM}$ real-time control system was employed as a real time controller for the hardware-in-loop bench tests. This system consists of two 3.2GHz CPU's equipped with two 16 channel A/D and D/A boards and one 16 channel digital I/O board. The communication between the two CPU's is a high performance serial bus IEEE 1934 fire wire with the data transfer rate at 400MHz per bit. CUP $\#1$ is used for engine controls and CPU $\#2$ is dedicated for controlling the EPVA.

B. Valve Actuator Driving Circuit

The solenoid driving circuit was designed to amplify the signal from the D/A outputs of the real time controller and to sense the solenoid current. The circuit is required to have a short solenoid release time and fast switching capability with low noise. The circuit was made of switching MOSFETs (Metal-Oxide Semiconductor Field-Effect Transistor) and NPN BJT (Bipolar Junction Transistors).

C. Verification of Parameter Identification Convergence

EPVA bench tests were conducted using a cylinder head of 5.4 liter 3 valve V8 engine. 200 cycle data was recorded at different engine speeds. The convergence of adaptive parameter identification algorithm was verified using the bench test data. There are two sets of data equivalent to engine speed at 1200RPM and 5000RPM. At 1200RPM, the test parameters are $80psi$ air supply pressure, $100ms$ solenoid period with $25ms$ solenoid active duration. The lag between the activation of solenoids 1 and 2 was $5ms$. The parameter identification resulting at 1200RPM are presented in Figures 11, 12 and 13. Figure 11 shows that C_{f_1} and C_{f_2} converge to 55 and 65, where the error between model and plant outputs reduce to less than the given tolerance. Figure 12 displays $\hat{\delta}_{1_o}$ and δ_{2_o} computed with the estimated C_{f_1} and C_{f_2}. Both parameters converges to about $5.8ms$ and $3ms$ respectively and they are close to the true lag of $5ms$ and the measured return time of $3ms$. The last cycle of valve response with the model response is displayed in Figure 13. The two rectangular windows are the parameter identification regions for opening and closing stages. The adaptive algorithm is inactive outside these two windows. The test parameters at 5000RPM are $80psi$ air supply pressure and $24ms$ solenoid period with $6ms$ solenoid active duration. The lag between the activation of solenoids 1 and 2 was $5ms$. The parameter identification resulting at 5000RPM is presented in Figures 14, 15 and 16. Again, Figure 14 shows the convergence of C_{f_1} and C_{f_2}. Figure 15 shows that $\hat{\delta}_{1_o}$ and δ_{2_o} reach steady state values that are quite close to the true values. Figure 16 presents the last valve lift with reference model outputs and the identification windows.

The closed-loop lift control algorithm was implemented in a prototype controller, and validated on a valve test bench with multiple reference valve lift set points at both $1200rpm$ and $5000rpm$ engine speeds. The experiment results are shown in [16].

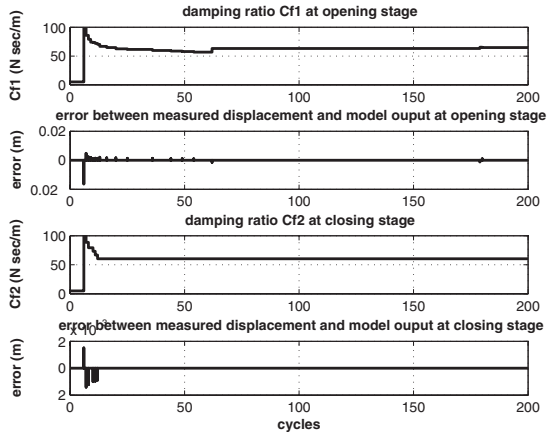

Fig. 11. C_{f_1} and C_{f_2} identification with 200 cycle valve bench data at 1200RPM

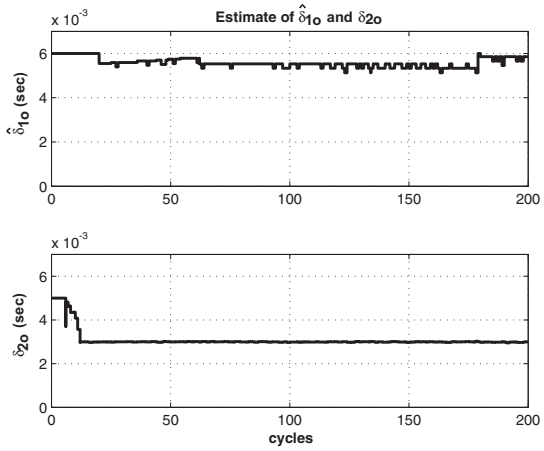

Fig. 12. $\hat{\delta}_{1_o}$ and δ_{2_o} estimation with 200 cycle valve bench data at 1200RPM

V. CONCLUSION

A control oriented model called level two model was developed for model reference parameter identification. This

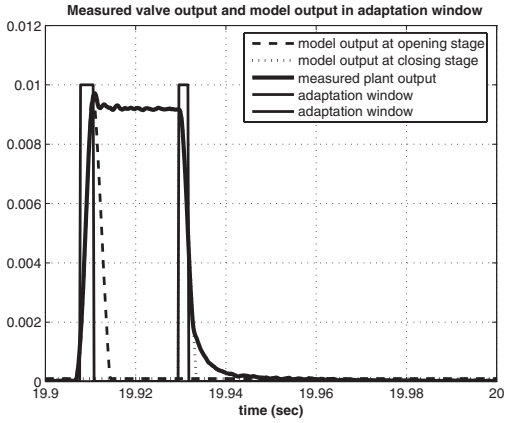

Fig. 13. The last valve lift profile at 1200RPM with the reference model output

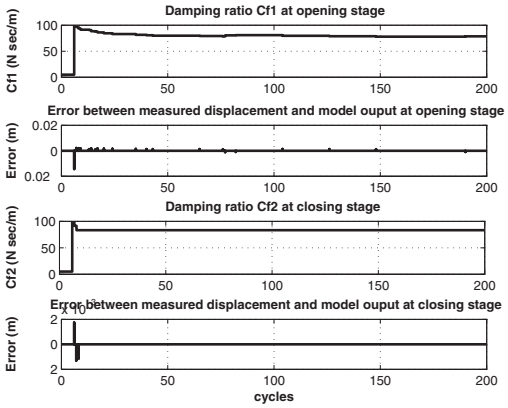

Fig. 14. C_{f_1} and C_{f_2} identification with 200 cycle valve bench data at 5000RPM

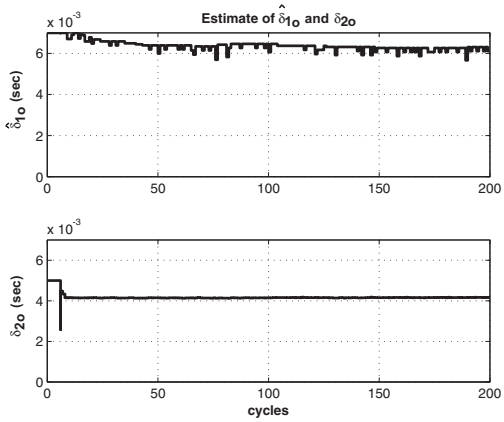

Fig. 15. $\hat{\delta}_{1_o}$ and δ_{2_o} estimation with 200 cycle valve bench data at 5000RPM

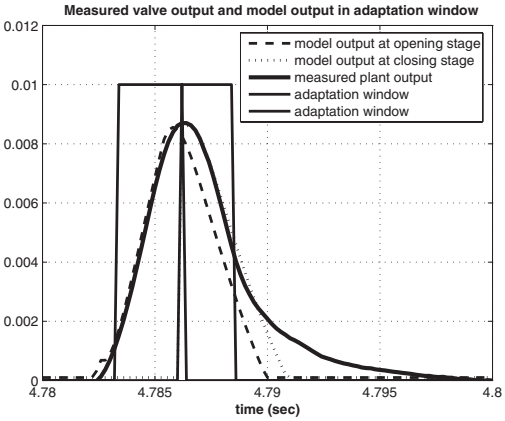

Fig. 16. The last valve lift profile at 5000RPM with the reference model output

level two model is a piece wise linearized model based upon a previously developed nonlinear model which was built using Newton's law, mass conservation and thermodynamic principles. The level two model reduces computational throughput and enable real time implementation. A model reference adaptive scheme was employed to identify valve parameters required to generate real time control signals. The convergence of adaptive parameter identification algorithms was experimentally verified using the test bench data at 1200RPM and 5000RPM engine speed. Parameter convergence was achieved within 40 cycles. Error between the model and plant outputs were converged to set tolerances. Closed-loop lift control strategy was developed and validated in simulation. One cycle transient response and zero steady state tracking error was achieved in simulation.

REFERENCES

[1] Jia Ma, Harold Schock, Urban Carlson, Anders Hoglund and Mats Hedman, "Analysis and Modeling of an Electronically Controlled Pneumatic Hydraulic Valve for an Automotive Engine," *SAE 2006-01-0042*, 2006.

[2] William T. Thomson, *Theory of vibration with applications (5th edition)*, Prentice Hall, Upper Saddle River, New Jersey, 1998.

[3] Karl Johan Astrom, Bjorn Wittenmark, *Adaptive control (2nd edition)*, Addison-Wesley Publishing Company, Boston, MA, 1995

[4] K. Inoue, K. Nagakiro, Y. Ajiki, and N. Kishi, "A High Power Wide Torque Range Efficient Engine with a Newly Developed Variable Valve Lift and Timing Mechanism," *SAE 890675*, 1989.

[5] Y. Moriya, A. Watanabe, U. Uda, H. Kawanura, M. Yoshioka, and Adachi, "A Newly Developed Intelligent Variable Valve Timing System Continuously Controlled Cam Phasing as Applied to a New 3 Liter Inline 6 Engine," *SAE 960579*, 1996.

[6] R. Flierl and M. Kluting, "The Third Generation of New Fully Variable Valvetrain for Throttle Free Load Control", *SAE 2000-01-1227*, 2000.

[7] M. Theobald, B. Lequesns, and R. Henry, "Control of Engine Load via Electromagnetic Valve Actuators," *SAE 940816*, 1994.

[8] C. Boie, H. Kemper, L. Kather, and G. Corde, "Method for Controlling a Electromagnetic Actuator for Achieving a Gas Exchange Valve On a Reciprocating Internal Combustion Engine," *US Patent 6,340,008*, 2000.

[9] L. Schneider, "Electromagnetic Valve Actuator with Mechanical End Position Clamp or Latch," *US Patent 6,267,351*, 2001.

[10] I. Haskara, L. Mianzo, and V. Kokotovic, "Method of Controlling an Electromagenatic Valve Actuator," *US Patent 6,644,253*, 2003.

[11] G. Wright, N. Schecter, and M. Levin, "Integrated Hydraulic System for Electrohydraulic Valvetrain and Hydraulicly Assisted Turbocharger," *US Patent 5,375,419*, 1994.

[12] O. Sturman, "Hydraulic Actuator for an Internal Combustion Engine," *US Patent 5,638,781*, 1994.

[13] Z. Sun and D. Cleary, "Dynamics and Control of an Electro-Hydraulic Fully Flexible Valve Actuation System," *Proceedings of American Control Conference*, Denver, Colorado, June, 2003.

[14] M. Anderson, T. C. Tsao, M. Levin, "Adaptive Lift Control for a Camless Electrohydraulic Valvetrain," *SAE 981029*, 1998.

[15] K. Misovec, B. Johnson, G. Mansouri, O. Sturman, and S. Massey, "Digital Valve Technology Applied to the Control of an Hydraulic Valve Actuator," *SAE 1999-01-0825*, 1999.

[16] Jia Ma, Guoming Zhu, Tom Stuecken, Harold Schock, Jim Winkelman, "Model Reference Adaptive Control of a Pneumatic Valve Actuator for Infinitely Variable Valve Timing and Lift," *SAE 2007-01-1297*, 2007.

Model-Based Predictive Control of an Electro-Pneumatic Exhaust Valve for Internal Combustion Engines

Jia Ma, Guoming Zhu, Andrew Hartsig, and Harold Schock

Abstract— **Variable valve actuation of Internal Combustion (IC) engines is capable of significantly improving their performance. Variable valve actuation can be divided into two main categories: variable valve timing with cam shaft(s) and camless valve actuation. For camless valve actuation, research has been centered in electro-magnetic, electro-hydraulic, and electro-pneumatic valve actuators. This research studies the control of the electro-pneumatic valve actuator. The modeling and control of intake valves for the Electro-Pneumatic Valve Actuators (EPVA) was shown in early publications and this paper extends the EPVA modeling and control development to exhaust valves for both valve timing and lift control. The control strategy developed utilizes model-based predictive techniques to overcome the randomly variable in-cylinder pressure against which the exhaust valve opens.**

I. INTRODUCTION

Variable intake valve timing and lift can be used to optimize engine performance over a wide operating range, for instance, to reduce engine pumping losses, deactivate selected cylinder(s), and control flame speed by manipulating in-cylinder turbulence. Exhaust valve timing and lift control makes it possible to vary the amount of Residual Gas Recirculation (RGR) and control valve overlap when combined with intake valve control. Variable valve timing and lift control is also a key technology for HCCI (Homogenous Charge Compression Ignition) combustion control.

Variable valve actuation can be achieved with mechanical (cam-based), electro-magnetic (electric mechanical), electro-hydraulic, and electro-pneumatic valvetrain mechanisms. The cam-based variable valve actuation is able to provide either a multiple stepping or a continuously changing valve timing phase shift. See [1], [2] and [3]. Infinitely variable valvetrain, often referred to as camless valvetrain, includes electro-magnetic ([4], [5], [6], [7], and [8]), electro-hydraulic ([9] [10] and [11]), and electro-pneumatic actuation ([12]). The electro-pneumatic valve actuator (EPVA) utilizes the supplied air pressure to actuate either the intake or exhaust valve by electronically controlling solenoids that control the motion of the actuator's piston. For both electro-hydraulic and electro-pneumatic valves, there is a potential issue of having a repeatable valve lift over the life of an engine.

Valve lift control for electro-hydraulic valvetrain actuation has been investigated by a number of researchers. Adaptive peak lift control was presented in [15], and digital valve technology was applied to control of a hydraulic valve actuator in [17]. The modeling and control of intake valves for the electro-pneumatic valve actuators was shown in [12], [13] and [14].

Unlike the intake valve, the exhaust valve opens against an in-cylinder pressure that varies as a function of the engine operational conditions with cycle-to-cycle combustion variations. This pressure disturbance slows down the valve actuator response and as a result, it increases the variation of valve opening delay. In fact, this disturbance makes it difficult to maintain repeatable valve opening timing and lift. As a result, unrepeatable valve lift affects the closing timing control which is critical for RGR control. Therefore, this work addresses exhaust valve lift control.

A mathematical in-cylinder pressure model at exhaust opening was developed and integrated with the exhaust valve model for control development. The thermodynamics data was obtained using WAVE^{TM} simulation [20]. The WAVE^{TM} model was calibrated and validated using experimental in-cylinder pressure data. The mathematical in-cylinder pressure model is then used to develop the model-based predictive control scheme for exhaust valve lift. The controller consists of two parts: feedforward and closed loop controls. The feedforward control is used to provide a nominal lift control based upon the predicted valve opening trajectory, while the closed loop controller is used to minimize the mean control error. The closed-loop control strategy was developed and verified in simulation using the combined mathematical model of exhaust valve and in-cylinder pressure.

The paper is organized as follows. First, an exhaust valve dynamic model is presented in Section II. Next, the feedforward and closed loop control strategies are discussed in Section III. Third, the simulation validation results are shown in Section IV, and finally, conclusions are drawn.

II. EXHAUST VALVE DYNAMIC MODEL

A physics-based nonlinear model, called a level one model, was built component-by-component based upon the flow and fluid dynamics. The details of the level one model and its verification can be found in [12]. This model provides an insight to the operation of the pneumatic/hydraulic mechanical actuation system. A piecewise linearized level two model was then created based on the level one model to reduce the computational throughput for control system development purposes. The details of the level two model are described in [13]. The level two model was used as

This work was supported by Department of Energy

Jia Ma is with Delphi Corporation. This work was completed as part of her Ph.D. study at Michigan State University, USA jia.ma@delphi.com

Guoming Zhu, Andrew Hartsig, and Harold Schock are with Mechanical Engineering, Michigan State University, Engineering Research Complex South, East Lansing, MI 48824, USA zhug@egr.msu.edu, hartsiga@msu.edu and schock@egr.msu.edu

the actuator model for the intake valve in the previous studies. Here, it is used for the exhaust valve actuator modeling. The exhaust valve opens against a high in-cylinder combustion pressure with large cycle-to-cycle variations. This in-cylinder pressure produces a force on the face of the exhaust valve that affects the valve dynamics. This in-cylinder pressure is modeled and integrated with the exhaust valve actuator model to capture the exhaust valve dynamics. The system dynamics illustrated here focuses

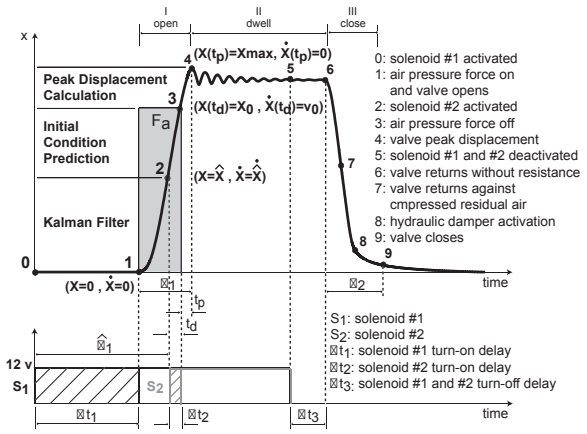

Fig. 1. Valve lift profile with the solenoid command chart and exhaust valve lift control strategy

on the relationship between the solenoid control commands and the exhaust valve response. It follows the same analysis as that of the level two model which simplifies the system dynamics used for the level one model analysis. As shown in Figure 1, the valve response can be divided into three stages. They are the opening stage (I), dwell stage (II), and closing stage (III). Solenoid $\#1$ is activated at point 0 first. It induces a high air pressure force to push the valve open at point 1 after Δt_1. Solenoid $\#2$ is then activated (point 2) with a time lag $\hat{\delta}_1$. It removes this air pressure force Δt_2 time after solenoid $\#2$ is activated (point $\#3$). Note that the interplay between two solenoids results in a pulse force input to the actuator valve piston with pulse width δ_1 between points 1 and 3. The increment of the pulse width increases valve lift. Now, with zero input, the valve movement continues until it reaches its peak lift at point $\#4$, the valve equilibrium. This ends the open stage. Next, the valve enters the dwell stage where it is held open by a hydraulic latch mechanism. At the end of the dwell stage, solenoid $\#1$ is deactivated at point $\#5$. After Δt_3 time, the valve starts to return (point $\#6$). The close stage starts at point $\#6$ and ends at point $\#9$ where the valve is considered closed. The returning duration is δ_2 between these two points.

The two solenoids have electro-mechanical delays after their activation and de-activation (see Figure 1). Δt_1 is defined as the delays for solenoid $\#1$ at activation. Δt_2 is defined as solenoid $\#2$ delay at activation. The de-activation delay for both solenoids are Δt_3. The solenoid commands direct the valve motion after the delays. The time lag applied between the activation of two solenoids is denoted as $\hat{\delta}_1$. This differs from the time lag between two delayed solenoid activations which is denoted as δ_1 since two solenoid delays, Δt_1 and Δt_2, are not equal. The exhaust valve lift control algorithm is to determine when to activate solenoid $\#2$ during exhaust valve opening for each cycle with the varying in-cylinder pressure at the face of the valve and its activation delay in presence. It is impossible to remove the input force F_a instantly upon the activation of solenoid $\#2$ due to its activation delay. An model-based predictive lift control algorithm is developed to make this possible. The details are described in the control strategy section.

The exhaust valve closing timing control requires knowledge of δ_2, the amount of time that the valve takes to close. To guarantee the exhaust valve closing at the desired time requires de-activating solenoid $\#1$ by time δ_2 before exhaust valve closing. δ_2 can be predetermined from the different valve lift set points. In other words, the closing timing control relies on a repeatable valve lift control. Developing a lift control system is the primary emphasis of work described in this paper.

The opening stage exhaust valve actuator model and the in-cylinder pressure model are employed to formulate the model-based predictive lift control scheme. In order to validate the exhaust valve lift control algorithm, the level two model integrated with the in-cylinder pressure model is used as a plant model in simulation. The opening stage exhaust valve actuator model and the in-cylinder pressure model are introduced in the following two subsections.

A. Actuator Model

The opening stage exhaust actuator model with the in-cylinder pressure is studied in this section. This model is expanded based on the level two model [13] to include the in-cylinder pressure dynamics. Figure 2 shows the

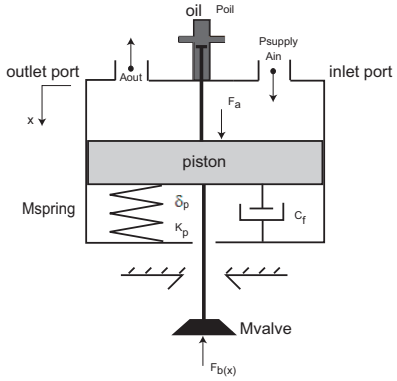

Fig. 2. Actuator piston model

schematic diagram of a single actuating piston for this system. At the opening stage, the valve actuator is modeled as a second order mass-spring-damper system with zero initial conditions. See Equation (1). All pressures used in modeling and control formulation process are gauge pressure in this article.

$$M\ddot{x} + C_f\dot{x} + K_p(x + \delta_p) = F_a(t) - F_b(x) \tag{1}$$

$$F_a(t) = F(t) - F(t - \delta_1), F(t) = \begin{cases} 0, & t < 0 \\ A_p P_p, & t \geq 0 \end{cases} \tag{2}$$

where, P_p is supply air pressure; $F_b(x)$ is the in-cylinder pressure force applied at the back of the exhaust valve; M is the equivalent mass of actuator piston, effective valve spring mass [18], exhaust valve and cap; A_p is the sum of actuator piston and oil passage areas; C_f is the damping ratio approximating energy dissipation due to flow loss and frictional loss; K_p and δ_p are the stiffness and preload of the valve spring respectively; δ_1 is the lag between the activation of solenoids $\#1$ and $\#2$ after solenoid delays as shown in Figure 1.

B. In-cylinder Pressure Model

The in-cylinder pressure $F_b(x)$ needs to be modeled and evaluated in Equation (1). Figure 3 illustrates the dynamics in the combustion chamber with an exhaust valve. A control volume is drawn above the piston, where m_{cyl}, T_{cyl} and P_{cyl} are the mass, temperature and pressure inside the combustion cylinder. A_{cyl} is the engine piston area. $\dot{m}_{ex}$ is the mass flow rate at the exit when the exhaust valve opens. T_{atm} and P_{atm} are the atmospheric temperature and pressure. x and y are the exhaust valve displacement and cylinder piston displacement respectively. The mass flow rate equations at

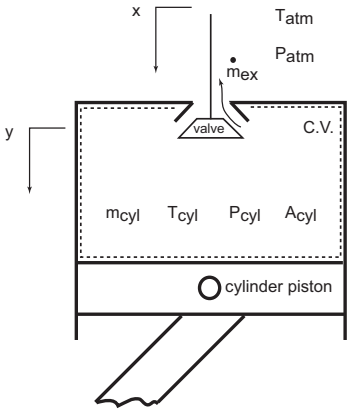

Fig. 3. In-cylinder pressure model

the exit are written for both choked and unchoked flow cases through Equations (3) to (5) following their derivation in [16].

$$\dot{m}_{ex} = C_{d_{ex}} \gamma P_{cyl} A_{ex}(x) \sqrt{\frac{k}{RT_{cyl}}},\ A_{ex} = 2\pi r_{valve} x, \quad (3)$$

where, A_{ex} is the flow area with r_{valve} being the valve radius; $C_{d_{ex}}$ is the flow coefficient at the exit; and R is the residual gas constant. C_p and C_v are the specific heat of the residual gas at constant pressure and constant volume respectively; and $k = \frac{C_p}{C_v}$. When $P_{cyl} \geq (\frac{k+1}{2})^{\frac{k}{k-1}} P_{atm}$, the flow is choked at the exit. In this case, γ is shown in Equation (4)

$$\gamma = \sqrt{(\frac{2}{k+1})^{\frac{k+1}{k-1}}}. \quad (4)$$

When $P_{cyl} \leq (\frac{k+1}{2})^{\frac{k}{k-1}} P_{atm}$, the flow is unchoked and γ is expressed in Equation (5).

$$\gamma = \sqrt{\frac{2}{k-1}(\frac{P_{atm}}{P_{cyl}})^{\frac{k+1}{2k}}[(\frac{P_{atm}}{P_{cyl}})^{\frac{1-k}{k}} - 1]}. \quad (5)$$

The mass of the residual gas inside the combustion cylinder in Equation (6) can be obtained by integrating the calculated mass flow rate. The initial mass m_0 is derived using ideal gas law in Equation (6):

$$m_{cyl} = -\int_0^t \dot{m}_{ex} dt + m_0, \quad m_0 = \frac{P_0 V_0}{R T_{cyl_0}}. \quad (6)$$

where P_0, V_0, R_0 and T_{cyl_0} are the initial in-cylinder gas pressure, volume, gas constant and temperature at the exhaust valve opening. Using the ideal gas law again with the obtained m_{cyl} results in an expression of in-cylinder pressure as shown in Equation (7).

$$P_{cyl} = \frac{m_{cyl} R T_{cyl}}{V_{cyl}}, \quad V_{cyl} = A_{cyl} y, \quad (7)$$

where, k, R and T_{cyl} are variables acquired from the WAVE^{TM} simulation with the same engine configuration and parameters; and y is the piston displacement derived from the cylinder geometry in Equation (8).

$$y = r[1 + \frac{L}{r} - \cos(\theta) - \sqrt{\frac{L}{r} - \sin^2(\theta)}], \quad (8)$$

where

- $A_{cyl} = \pi(\frac{1}{2} \times bore)^2 = 0.0401 m^2$ $(bore = 90.2mm)$,
- L is the connecting rod length $(L = 169.2mm)$,
- r is the crank shaft radius $(r = \frac{1}{2} stroke = 52.9mm)$,
- θ is the engine crank angle.

Therefore, $F_b(x)$ can be expressed in Equation (9) below.

$$F_b(x) = P_{cyl} A_{valve}, \quad (9)$$

where P_{cyl} is defined in Equation (7).

C. Validation of In-cylinder Pressure Model by Simulation

The in-cylinder pressure force F_b is a function of the effective flow out area A_{ex} which varies as the exhaust valve displacement cahnges.

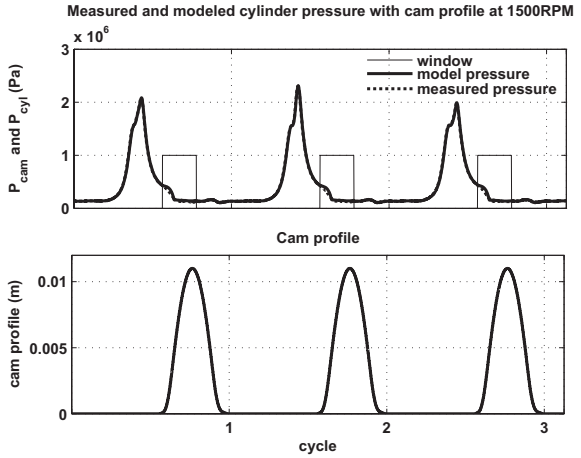

Fig. 4. In-cylinder pressure model validation by simulation

In order to validate the in-cylinder pressure model, combustion experiments were conducted using a 5.4L 3 valve V8 engine with in-cylinder pressure measurement and a conventional camshaft at 1500RPM. The pressure model

was simulated using the conventional cam profile as the valve displacement input. The modeled in-cylinder pressure was then compared with the measured in-cylinder pressure as shown in Figure 4. The top diagram of this figure shows the modeled pressure (solid line) in the rectangular windows and measured in-cylinder pressure (dash line) with satisfactory modeling accuracy. The bottom diagram shows the exhaust cam profile used in the simulation and experiments. The in-cylinder pressure model is then integrated into the pneumatic exhaust valve model and the responses are shown in Figure 5. Here, the pressure model uses the EPVA valve displacement to calculate the corresponding in-cylinder pressure. The modeled pressure (solid line in top diagram) and the associated EPVA valve lift profile (solid line in bottom diagram) are compared with the experiment pressure (dash line) and the cam profile (dash line). The simulation result demonstrates that the in-cylinder pressure drops rather quickly with the EPVA exhaust valve actuation since the EPVA valve opens faster than the conventional cam-based valve. This simulated in-cylinder pressure is used to construct the control signals. The exhaust valve model is used as a plant model and it is integrated with the in-cylinder pressure model in simulations to validate the control algorithm. The modeled in-cylinder pressure is one of the two inputs to the plant (exhaust valve), and the actuation force F_a commanded by the two solenoid control signals is the other input.

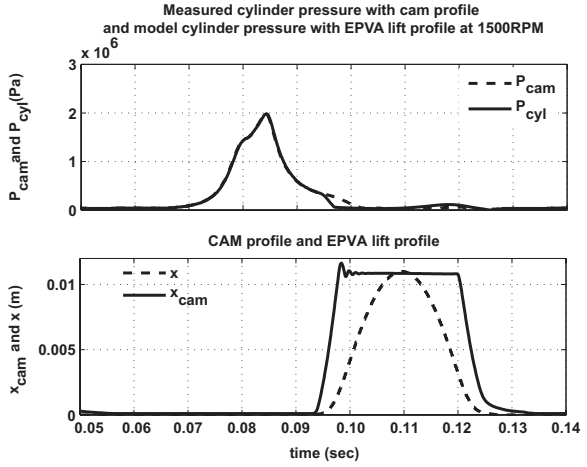

Fig. 5. In-cylinder pressure model integrated into exhaust valve model

III. CONTROL STRATEGY

Since the in-cylinder pressure on the face of the exhaust valve varies significantly from cycle-to-cycle, the valve lift control needs to be adjusted as a function of the current in-cylinder pressure for each individual cycle. As explained in the actuator dynamics section, the exhaust actuator is modeled as a second order mass-spring-damper system at the opening stage. Activating solenoid $\#1$ applies the force F_a on the valve and moves the exhaust valve. Activating solenoid $\#2$ removes the force and the valve continues to open until it reaches the maximum displacement. Solenoid $\#2$ activation timing determines the maximum valve lift. Therefore, the key for valve lift control is to find when to activate solenoid $\#2$. Figure 1 illustrates the idea of the exhaust valve lift control strategy. Solenoid $\#1$ is activated at time 0. After the delay of Δt_1, the input force F_a acts on the system and the exhaust valve starts to open at point 1. Solenoid $\#2$ is then activated at point 2. After Δt_2 delay, force F_a is removed at point 3. The valve moves further until its velocity decreases to 0 at point 4. The second order valve system response from points 3 to 4 can be calculated with zero input and nonzero initial conditions at point 3. In other words, the valve peak displacement at point 4 can be calculated if the initial displacement and velocity at point 3 are known. Once the calculated displacement at point 4 reaches the reference maximum valve lift, point 3 is found to be the right time to remove force F_a. If activating solenoid $\#2$ could turn off the input force F_a immediately, we would only need to activate it whenever the calculated displacement of point 4 reaches the reference lift. But the solenoid delay requires the activation to take place at point 2 with Δt_2 amount of time before point 3. This means that if point 3 is the time to eliminate input force, point 2 is the time to activate solenoid $\#2$. However, the initial conditions at point 3, where the peak displacement of the valve is calculated, are not yet available at point 2. Therefore, an algorithm is derived to predict initial conditions of point 3 at point 2. This strategy of initial condition prediction can be implemented as long as the delay Δt_2 of solenoid $\#2$ is less than the lag $\hat{\delta}_1$ between the activation of two solenoids. The predictive algorithm needs to know both states, valve displacement and velocity, at point 2. A Kalman state estimator was used to estimate them with minimized effect of measurement noise. Now we can determine the time to activate solenoid $\#2$ (point 2), which is served as a feedforward control of the valve actuator. A proportional and integral (PI) scheme is used as a closed-loop feedback lift control system to reduce the steady state lift tracking error.

The flow chart of the feedforward control scheme is shown in Figure 6. First, solenoid $\#1$ is activated. Secondly, the Kalman state estimator provides the current states. Finally, a model-based prediction algorithm uses the estimated states to calculate the states after solenoid $\#2$ delay Δt_2, which is then used to calculate the peak valve displacement. If the calculated peak displacement is greater than or equal to the reference valve lift, solenoid $\#2$ is activated, otherwise, the process repeats until the condition is satisfied. The details of the derivations are discussed in the following four subsections.

A. Peak Displacement Calculation (PDC)

This section describes the solution for the peak displacement at point 4 based on the initial conditions at point 3. Recall that the governing equation of the exhaust valve at the opening stage is presented in Equation (1). The back pressure force $F_b(x)$ equals the product of the exhaust valve area and the modeled in-cylinder pressure. The in-cylinder pressure used in the control algorithm development here is piece-wisely linearized between points 1 and 4 according

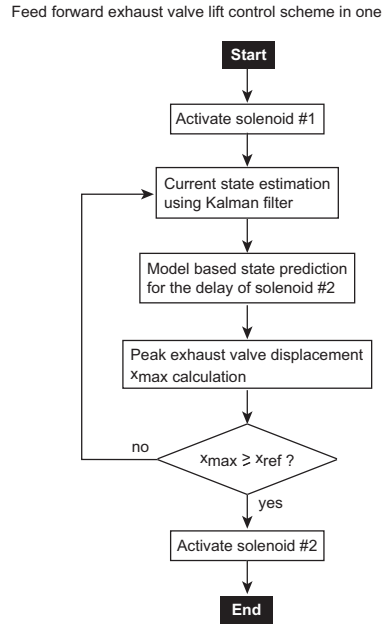

Fig. 6. Feedforward exhaust valve lift control strategy

to the simulated in-cylinder pressure against EPVA exhaust valve profile. Three lines were used for piecewise approximatation of the in-cylinder pressure data, and $F_b(x) = px+q$ ($p \leq 0$ and $q \geq 0$) with

$$\begin{cases} p = p_1,\ q = q_1,\ \ x \leq 0.002m \\ p = p_2,\ q = q_2,\ \ 0.002m < x \leq 0.008m \\ p = p_3,\ q = q_3,\ \ x > 0.008m \end{cases}.$$

Substituting $F_b(x)$ with its linearized expression into Equation (1) results in Equation (10) below.

$$M\ddot{x} + C_f\dot{x} + K_p x = F_a - (px + q) - K_p\delta_p. \tag{10}$$

Move the px term to the left resulting in Equation (11):

$$M\ddot{x} + C_f\dot{x} + (K_p + p)x = F_a - q - K_p\delta_p. \tag{11}$$

Let $K = K_p + p$ and $F_a = 0$, since it is assumed that input force F_a is turned off, to obtain Equation (12) in a general format given the initial condition $x(0) = x_0,\ \dot{x}(0) = v_0$.

$$M\ddot{x} + C_f\dot{x} + Kx = -Q,\ \ Q = K_p\delta_p + q. \tag{12}$$

Recall that p takes three different values, p_1, p_2 and p_3 in three valve displacement regions. K could be either negative, zero or positive depending on the value of p. When K is positive, Equation (12) can be rewritten into Equation (13) as below:

$$\ddot{x} + 2\zeta\omega_n\dot{x} + \omega_n^2 x = -\frac{Q}{M}, \tag{13}$$

where $\omega_n = \sqrt{\frac{K}{M}}$ and $\zeta = \frac{C_f}{2}\sqrt{\frac{1}{MK}}$. In this case, the solution can be categorized into under damped, critically damped and over damped scenarios depending on the value damping ratio ζ, damping coefficient C_f, mass M and equivalent stiffness K in Equation (13). The peak displacement solution derivation of Equation (12) proceeds separately in four cases. They are $K > 0$ with $0 < \zeta < 1$ (case #1), $K > 0$ with $\zeta = 1$ (case #2), $K > 0$ with $\zeta > 1$ (case #3) and $K \leq 0$ (case #4). The initial condition denoted as $x(0) = x_0$ and $\dot{x}(0) = v_0$ in this section are derived in the next section of model-based initial condition prediction.

For under damped PDC case #1 ($K > 0$ and $0 < \zeta < 1$), we start with solving Equation (13) for all three cases where $K > 0$. The homogenous solution x_h can be expressed in Equation (14)

$$x_h = e^{-\zeta\omega_n t}(a_1 e^{i\omega_d t} + a_2 e^{-i\omega_d t}),\ \omega_d = \sqrt{1-\zeta^2}\omega_n. \tag{14}$$

Solving for the particular solution x_p of Equation (13) results in Equation (15)

$$x_p = -\frac{Q}{K}. \tag{15}$$

The complete solution $x(t) = x_p(t) + x_h(t)$ can be expressed in Equation (16).

$$x(t) = e^{-\zeta\omega_n t}(a_1 e^{i\omega_d t} + a_2 e^{-i\omega_d t}) - \frac{Q}{K}. \tag{16}$$

We apply Euler formula $e^{i\alpha} = cos(\alpha) + isin(\alpha)$ and trigonometric identities to the equation above to obtain Equation (17)

$$x(t) = Ae^{-\zeta\omega_n t}\sin(\omega_d t + \theta) - \frac{Q}{K}, \tag{17}$$

where A and θ are determined by the initial conditions as follows:

$$\begin{cases} x(0) = A\sin(\theta) - \frac{Q}{K} = x_0 \\ \dot{x}(0) = -\zeta A\omega_n\sin(\theta) + \omega_d A\cos(\theta) = v_0, \end{cases}$$

$$\begin{cases} A = \sqrt{\frac{(v_0+\zeta\omega_n\chi_0)^2 + \chi_0^2\omega_d^2}{\omega_d^2}}, \chi_0 = x_0 + \frac{Q}{K} \\ \theta = tan^{-1}(\frac{\omega_d\chi_0}{v_0+\zeta\omega_n\chi_0}). \end{cases}$$

The peak displacement $x_p = x(t_p)$ is solved at $\dot{x}(t_p) = 0$ with t_p being the time the valve takes to travel to its maximum displacement (see Figure 1). Taking the time derivative of $x(t)$ and setting it to zero at t_p results in Equation (18).

$$\dot{x}(t_p) = -\zeta\omega_n A e^{-\zeta\omega_n t_p}\sin(\omega_d t_p + \theta) = 0. \tag{18}$$

Solving Equation (18) yields:

$$t_p = \begin{cases} \frac{1}{\omega_d}\left(tan^{-1}(\sqrt{\frac{1}{\zeta^2}-1}) - \theta\right), & tan^{-1}\sqrt{\frac{1}{\zeta^2}-1} > \theta \\ \frac{1}{\omega_d}\left(tan^{-1}(\sqrt{\frac{1}{\zeta^2}-1}) - \theta + 2\pi\right), & otherwise. \end{cases}$$

We substitute t_p into Equation (17) to obtain the peak displacement $x(t_p)$. The solution of the peak displacement is summarized below:

PDC Summary $K > 0$ with $0 < \zeta < 1$
$x(t_p) = Ae^{-\zeta\omega_n t_f}\sin(\omega_d t_p + \theta) - \frac{Q}{K}$ $Q = K_p\delta_p + q,\ K = K_p + p,\ \theta = tan^{-1}(\frac{\omega_d\chi_0}{v_0+\zeta\omega_n\chi_0})$ where, $x_0 = x(t_d),\ v_0 = \dot{x}(t_d)$, $x(t_d)$ and $\dot{x}(t_d)$ are from model-based initial condition prediction

For PDC cases #2, #3, and #4, the results can be derived similarly and are omitted in this paper.

B. Model-Based Initial Condition Prediction (ICP)

The previous section solves for the peak displacement $x(t_p)$ using the displacement and velocity at point 3 as initial conditions (Figure 1). This section derives the formulas to predict the displacement $x(t_d)$ and velocity $\dot{x}(t_d)$ at point 3, given the displacement and velocity at point 2. The displacement and velocity at point 2 are initial conditions denoted as $x(0) = x_0$ and $\dot{x}(0) = v_0$ in this subsection. Their values are estimated by the Kalman state estimator described in the next subsection. Solenoid #2 delay, Δt_2, is the time input and F_a is a constant force input between points 2 and 3. Consider the governing equation again in Equation (1). Given $F_b(x) = px + q$, Equation (1) becomes

$$M\ddot{x} + C_f\dot{x} + K_p x = F_a - (px + q) - K_p\delta_p. \tag{19}$$

Rearrange the equation above to obtain

$$M\ddot{x} + C_f\dot{x} + (K_p + p)x = F_a - q - K_p\delta_p. \tag{20}$$

Let $K = K_p + p$ and $W = q + K_p\delta_p - F_a$, Equation (20) becomes Equation (21).

$$M\ddot{x} + C_f\dot{x} + Kx = -W. \tag{21}$$

It is clear that Equations (12) and (21) have the same form. Previously, Equation (12) was evaluated for the maximum displacement given initial conditions. Now, Equation (21) is evaluated for the displacement and velocity in t_d amount of time with given initial conditions, where $t_d = \Delta t_2$ (see Figure 1). Equation (21) can be solved in a similar way to Equation (12) by replacing Q with W, and the solutions are omitted in this paper.

C. Kalman Filter State Estimation (KFE)

The displacement and velocity at point 2 (see Figure 1) are needed as initial conditions in the previous section. The system is equipped with a displacement sensor which measures the exhaust valve displacement. The velocity obtained through taking a time derivative of the measured displacement is unreliable due to the measurement noise. The observer formulated in this section performs the optimal estimations of both the displacement and velocity at point 2 in the presence of noise using the Kalman state estimator. The estimated displacement and velocity are denoted as $\widehat{x}$ and $\dot{\widehat{x}}$ respectively. The state space notation of the system is expressed below:

$$\begin{aligned} \dot{x} &= Ax + Bu + Gw(t) \\ y &= Cx + v(t) \end{aligned}$$

where $A = \begin{bmatrix} 0 & 1 \\ \frac{-K}{M} & \frac{-C_f}{M} \end{bmatrix}$, $B = \begin{bmatrix} 0 \\ 1 \end{bmatrix}$, $C = \begin{bmatrix} 1 & 0 \end{bmatrix}$ and $x^T = [x_1, x_2]$; $w(t)$ and $v(t)$ represent the process noise and measurement noise. Note that $u = -W$ is the input to the system, $x_1 = x$ and $x_2 = \dot{x}$ are the states representing the valve displacement and velocity. The Kalman state estimator takes the following forms:

$$\begin{aligned} \dot{\widehat{x}} &= A\widehat{x} + Bu + L(y - c\widehat{x}) \\ y &= C\widehat{x}, \quad \widehat{x}(0) = 0, \end{aligned}$$

where L is the observer gain acquired through solving the algebraic Riccati Equation (22); and $\widehat{x}$ is the estimated displacement x_1 and velocity x_2; and G is an identity matrix.

$$AP + PA^T + GWG^T - PC^TV^{-1}CP = 0, \tag{22}$$

$$L = PC^TV^{-1}, where\ W \geq 0\ and\ V > 0, \tag{23}$$

where W and V are covariance matrices of w and v, respectively. If (C, A) is observable, the algebraic Riccati equation has a unique positive definite solution P, and the estimated state $\widehat{x}$ asymptotically approaches true state x.

D. Closed-Loop Control Scheme

The feedforward solution of solenoid #2 activation timing is obtained by implementing the formulas from the peak displacement calculation, model-based initial condition prediction and Kalman filter state estimation subsections. This solution combined with the displacement error compensation from the proportional and integral (PI) feedback scheme forms a closed-loop control signal of solenoid #2 as illustrated in Figure 7.

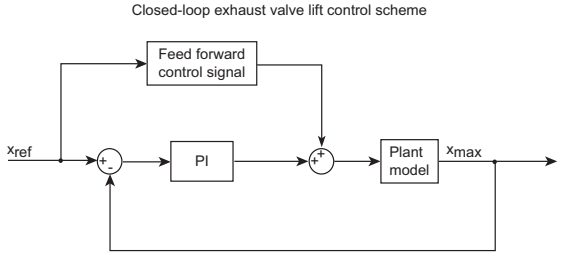

Fig. 7. Closed-loop exhaust valve lift control scheme

IV. SIMULATION RESULT

The developed control algorithms are validated by simulation using the combined valve actuator and the in-cylinder pressure model as the plant model. The three segments of the feedforward control strategy and the closed-loop control scheme are evaluated in sequence.

A. Simulation of Peak Displacement Calculation

Figure 8 demonstrates the simulation results in four out of 80 cycles, where the solenoid #2 is activated when the calculated peak displacement reaches the reference valve peak lift of $11mm$. This tests the open loop feedforward peak displacement calculation algorithm. The model valve displacement and velocity are employed as the known initial condition in this simulation. The top diagram shows that the peak valve lift is maintained at $11mm$, rejecting the in-cylinder pressure variation at the back of the exhaust valve (shown in the bottom diagram) when the feedforward peak displacement calculation is applied.

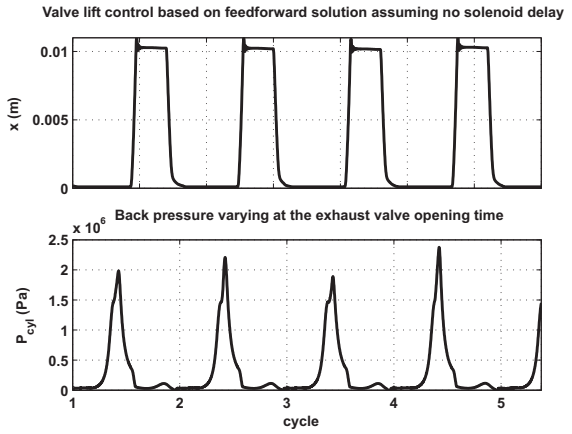

Fig. 8. Feedforward solution simulation without solenoid #2 delay

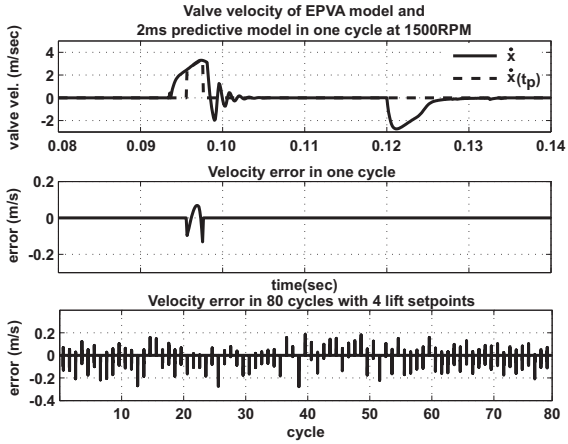

Fig. 10. Simulation validation of velocity prediction $\dot{x}_{0_p}$

B. Simulation of Model-Based Initial Condition Prediction

Figure 9 presents the simulation results of the model-based displacement prediction. The solenoid $\#2$ delay (Δt_2 or t_d) is assumed to be $2ms$ in the simulation. White noise is injected to the plant displacement output to simulate the measurement noise. The plant displacement (solid line) without measurement noise and the predicted displacement (dash line) in the prediction active region are displayed in the top diagram for one cycle. The middle diagram displays the error between the two. The bottom diagram shows the tracking error between the plant and predicted displacement. The lift set points were selected as $11mm$, $6mm$, $8mm$, and again $11mm$. The absolute error is less than $0.7mm$. The

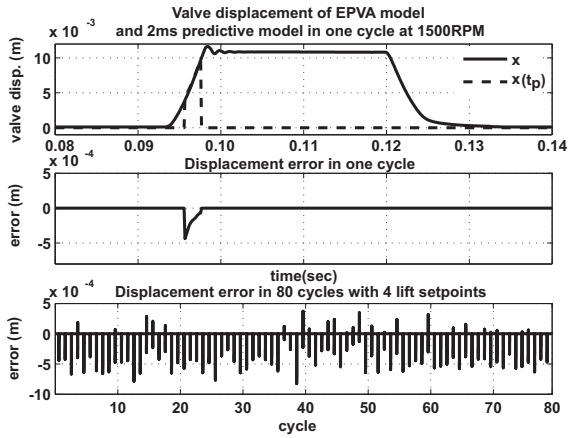

Fig. 9. Simulation validation of displacement prediction x_{0_p}

simulation results of the model-based velocity prediction are shown in Figure 10. The absolute error between the plant and predicted velocity is less than $0.25m/s$ over 80 simulated cycles using the closed-loop lift tracking control with four lift set points.

C. Simulation of Kalman Filter State Estimation

Figure 11 and Figure 12 present the simulation results of the Kalman filter state estimation with the measurement noise present. The top and middle graphs show one cycle response and the estimation error, and the bottom one shows the error over 80 engine cycles. The absolute error over 80 cycles between the plant displacement and the estimated displacement is less than $0.3mm$. The absolute error between the plant and estimated velocity is less than $0.38m/s$ over 80 simulated cycles using the closed-loop lift tracking control with four lift set points.

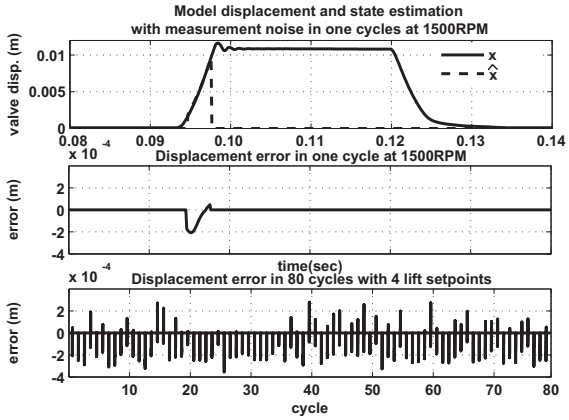

Fig. 11. Kalman filter displacement $(\widehat{x_0})$ estimation simulation

D. Simulation of Closed-Loop Exhaust Valve Lift Tracking

Finally, Figure 13 presents the entire closed-loop lift tracking simulation results with all three feedforward control sequences assembled at four reference lift set points in the presence of measurement noise. The dark and gray lines in the top diagram represent the reference and model valve lift respectively. The bottom diagram demonstrates that the absolute lift tracking error is below $0.6mm$ at steady state. The exhaust valve tracks the reference lift within one engine cycle with the lift error less than $0.6mm$.

It is clear that model-based predictive control is computationally intense. In order to reduce on-line calculation of PDC and ICP algorithms, off-line PDC simulations were conducted for a range of initial displacements and velocities. The simulation results were converted into lookup tables of displacement and velocity as inputs to ICP lookup table

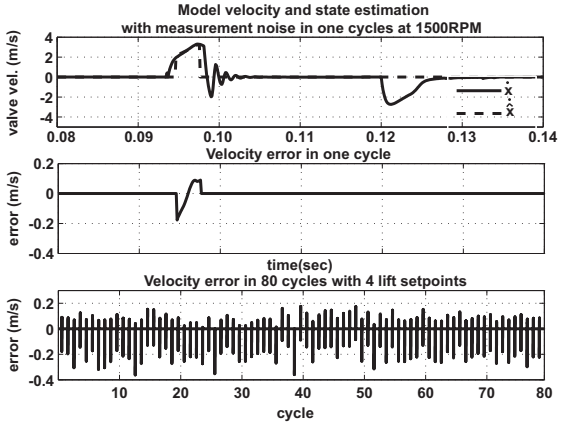

Fig. 12. Kalman filter velocity ($\widehat{x}_0$) estimation simulation

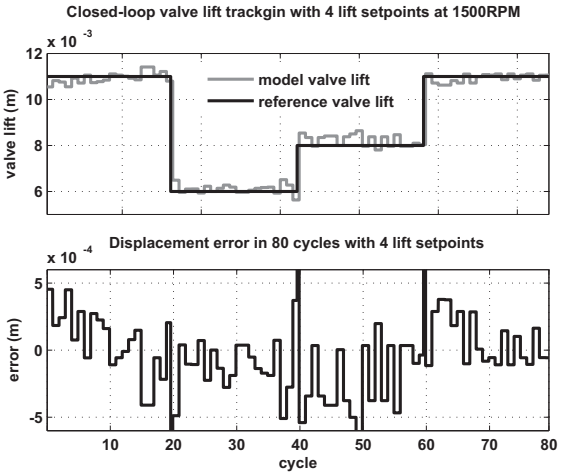

Fig. 13. Closed-loop lift tracking control with four set points

which is calibrated using off-line simulation data. Only the Kalman filter algorithm needs to run on-line. This strategy was implemented into a real-time controller with 40 microsecond sample rate [19].

V. CONCLUSION

A mathematical exhaust valve actuator model and an in-cylinder pressure model have been developed for a model-based predictive lift control of an exhaust valve. The exhaust valve model was approximated by a piecewise-linearized second order spring-mass-damper system. The in-cylinder pressure was modeled during the exhaust valve opening stage. This model was integrated with the exhaust valve actuator model for control development. The thermodynamics data used in this model was obtained with the WAVE^{TM} simulation which was calibrated using experimental in-cylinder pressure data. The in-cylinder pressure model was validated using experimental data and demonstrates satisfactory model accuracy.

A model-based predictive control strategy was developed for feedforward control. This strategy contains three segments; peak displacement calculation, model-based initial condition prediction and Kalman state estimation. Simulations were carried out with the white measurement noise to evaluate the performance of each individual segment and the integrated feedforward algorithm. A proportional and integral controller was used for closed loop control. The closed loop valve lift control system was integrated with model-based predictive feedforward control. Evaluation simulations were conducted at different reference lift set points with the white measurement noise based upon the developed exhaust valve and in-cylinder pressure models.

Simulation results show good robustness against measurement noise. The steady state valve lift error is below $0.6mm$ and the closed loop valve lift control system is able to track the step reference lift within one engine cycle with a lift error less than $0.6mm$.

REFERENCES

[1] K. Inoue, K. Nagakiro, Y. Ajiki, and N. Kishi, "A High Power Wide Torque Range Efficient Engine with a Newly Developed Variable Valve Lift and Timing Mechanism," *SAE 890675*, 1989.

[2] Y. Moriya, A. Watanabe, U. Uda, H. Kawanura, M. Yoshioka, and Adachi, "A Newly Developed Intelligent Variable Valve Timing System Continuously Controlled Cam Phasing as Applied to a New 3 Liter Inline 6 Engine," *SAE 960579*, 1996.

[3] R. Flierl and M. Kluting, "The Third Generation of New Fully Variable Valvetrain for Throttle Free Load Control," *SAE 2000-01-1227*, 2000.

[4] M. Theobald, B. Lequesns, and R. Henry, "Control of Engine Load via Electromagnetic Valve Actuators," *SAE 940816*, 1994.

[5] C. Boie, H. Kemper, L. Kather, and G. Corde, "Method for Controlling a Electromagnetic Actuator for Achieving a Gas Exchange Valve On a Reciprocating Internal Combustion Engine," *US Patent 6,340,008*, 2000.

[6] L. Schneider, "Electromagnetic Valve Actuator with Mechanical End Position Clamp or Latch," *US Patent 6,267,351*, 2001.

[7] I. Haskara, L. Mianzo, and V. Kokotovic, "Method of Controlling an Electromagnetic Valve Actuator," *US Patent 6,644,253*, 2003.

[8] Y. Wang, A. Stefanopoulou, K. Peterson, T. Megli, M. Haghgooie, "Modeling and Control of Electromechanical Valve Actuator," *SAE 2002-01-1106*, 2002.

[9] G. Wright, N. Schecter, and M. Levin, "Integrated Hydraulic System for Electrohydraulic Valvetrain and Hydraulicly Assisted Turbocharger," *US Patent 5,375,419*, 1994.

[10] O. Sturman, "Hydraulic Actuator for an Internal Combustion Engine," *US Patent 5,638,781*, 1994.

[11] Z. Sun and D. Cleary, "Dynamics and Control of an Electro-Hydraulic Fully Flexible Valve Actuation System," *Proceedings of American Control Conference*, Denver, Colorado, June, 2003.

[12] Jia Ma et al., "Analysis and Modeling of an Electronically Controlled Pneumatic Hydraulic Valve for an Automotive Engine," *SAE 2006-01-0042*, 2006.

[13] Jia Ma et al., "Model reference adaptive control of a pneumatic valve actuator for infinitely variable valve timing and lift," *2007 SAE World Congress (SAE 2007-01-1297)*, Detroit, MI, April, 2007.

[14] Jia Ma et al.,"Adaptive control of a pneumatic valve actuator for an internal combustion engine," *2007 American Control Conference*, New York, NY, July, 2007

[15] M. Anderson, T. C. Tsao, M. Levin, "Adaptive Lift Control for a Camless Electrohydraulic Valvetrain," *SAE 981029*, 1998.

[16] J. M. Tressler et al., "Dynamic Behavior of Pneumatic Systems for Lower Extremity Extenders," *Proceedings of the 2002 IEEE International Conference on Robotics & Automation*, Washington, D.C., May 2002.

[17] K. Misovec et al., "Digital Valve Technology Applied to the Control of an Hydraulic Valve Actuator," *SAE 1999-01-0825*, 1999.

[18] William T. Thomson, *Theory of vibration with applications* 5^{th} ed. Prentice Hall, Upper Saddle River, New Jersey, 1998.

[19] J. Ma, G. Zhu, T. Stuecken, A. Hartsig, and H. Schock, "Electro-pneumatic exhaust valve modeling and control for an internal combustion engine," *submitted to 2008 ASME ICE Spring Conference*, Chicago, IL, April, 2008

[20] http://www.ricardo.com/engineeringservices/software.aspx?page=wave

Proceedings of ICES 2008
ASME 2008 International Combustion Engine Spring Technical Conference
April 27-30, 2008, Chicago, IL, USA

ICES2008-1653

ELECTRO-PNEUMATIC EXHAUST VALVE MODELING AND CONTROL FOR AN INTERNAL COMBUSTION ENGINE

Jia Ma, Guoming Zhu, Tom Stuecken, Andrew Hartsig, Harold Schock
Department of Mechanical Engineering
Michigan State University

ABSTRACT

Variable valve actuation of Internal Combustion (IC) engines is capable of significantly improving their performance. It can be divided into two main categories: variable valve timing with cam shaft(s) and camless valve actuation. For camless valve actuation, research has been centered in electro-magnetic, electro-hydraulic, and electro-pneumatic valve actuators. This research studies the control of the electro-pneumatic valve actuator. The modeling and control of intake valves for the Electro-Pneumatic Valve Actuators (EPVA) was shown in early publications and this paper extends the EPVA modeling and control development to exhaust valves for the lift control which is the key to the exhaust valve control since an accurate and repeatable lift control guarantees a satisfactory valve closing timing control. Note that exhaust valve closing timing is a key parameter for controlling engine residual gas recirculation. The exhaust valve lift control challenge is the disturbance from the randomly varying in-cylinder pressure against which the exhaust valve opens. The developed strategy utilizes model based predictive techniques to overcome this disturbance. This exhaust valve lift control algorithm was validated on a 5.4 Liter 3 valve V8 engine head with a pressurized chamber to imitate the in-cylinder pressure. The experimental results demonstrated that the exhaust valve lift tracked the step reference in one cycle with the lift error under 1mm and the steady state lift error was kept below 1mm.

1 INTRODUCTION

Variable intake valve timing and lift can be used to optimize engine performance over a wide operating range, for instance, to reduce engine pumping losses, deactivate selected cylinder(s), and control flame speed by manipulating in-cylinder turbulence. Exhaust valve timing and lift control makes it possible to vary the amount of Residual Gas Recirculation (RGR) and control valve overlap when combined with intake valve control. Variable valve timing and lift control is also a key technology for HCCI (Homogenous Charge Compression Ignition) combustion control.

Variable valve actuation can be achieved with mechanical (cam-based), electro-magnetic (electric mechanical), electro-hydraulic, and electro-pneumatic valvetrain mechanisms. The cam based variable valve actuation is able to provide either a multiple stepping or a continuously changing valve timing phase shift (see [1], [2] and [3]). Infinitely variable valvetrain, often referred to as camless valvetrain, includes electro-magnetic ([4], [5], [6], [7], and [8]), electro-hydraulic ([9], [10] and [11]), and electro-pneumatic actuation ([12]). The electro-pneumatic valve actuator (EPVA) utilizes the supplied air pressure to actuate either the intake or exhaust valve by electronically controlling solenoids that regulate the motion of the actuator's piston. For both electro-hydraulic and electro-pneumatic valves, there is a potential issue of having a repeatable valve lift over the life of an engine.

Valve lift control for electro-hydraulic valvetrain actuation ([22]) has been investigated by a number of researchers. Adaptive peak lift control was presented in [16], and digital valve technology was applied to control of an hydraulic valve actuator in [18]. The modeling and control of intake valves for the electro-pneumatic valve actuators were shown in [12], [13] and [14]. Model-based control scheme has been used to regulate the cylinder air charge of a camless multi-cylinder engine for throttleless operations (see [19]).

Unlike the intake valve, the exhaust valve opens against an

in-cylinder pressure that varies as a function of the engine operational conditions with cycle-to-cycle combustion variations. This pressure disturbance slows down the valve actuator response and as a result, it increases the variation of valve opening delay. In fact, this disturbance makes it difficult to maintain repeatable valve opening timing and lift. As a result, unrepeatable valve lift affects the closing timing control which is critical for RGR control. Therefore, this work addresses exhaust valve lift control.

A mathematical in-cylinder pressure model during exhaust valve opening period was developed and integrated with the exhaust valve dynamic model for control development. The thermodynamics data was obtained using WAVE^{TM} simulations (www.ricardo.com). The WAVE^{TM} model was calibrated and validated using experimental in-cylinder pressure data. The mathematical in-cylinder pressure model is then used to develop the model based predictive control scheme for exhaust valve lift control. In this paper, the model-based predictive control scheme is used to predict the control required to reach desired valve lift under varying exhaust pressure. This is the key to achieve accurate valve lift control since the valve control signal needs to be sent to actuator solenoid before the valve reaches its desired lift due to solenoid electro-magnetic delay. The controller consists of two parts: feedforward and closed loop controls. The feedforward control is used to provide a nominal lift control based upon the predicted valve opening trajectory, while the closed loop controller is used to minimize the mean control error. The closed-loop control strategy was developed and verified in simulation using the combined mathematical model of exhaust valve and in-cylinder pressure, and then, demonstrated on a 5.4 Liter 3 valve V8 engine head with a pressurized chamber.

The paper is organized as follows. First, an exhaust valve dynamic model is presented in Section 2. Next, the feedforward and closed loop control strategies are described in Section 3. Third, the experimental validation results are shown in Section 4, and finally, conclusions are drawn.

2 EXHAUST VALVE DYNAMIC MODEL

A physics based nonlinear model, called a level one model, was built component-by-component based upon the flow and fluid dynamics. The details of the level one model and its verification can be found in [12]. This model provides an insight to the operation of the pneumatic/hydraulic mechanical actuation system. A piecewise linearized level two model was then created based on the level one model to reduce the computational throughput for control system development purpose. The details of the level two model are described in [13]. The level two model was used as the actuator model for the intake valve in the previous studies (see [13] and [14]). In this study, it is used for the exhaust valve actuator modeling. The exhaust valve opens against an in-cylinder combustion pressure with certain cycle-to-cycle variations. This in-cylinder pressure produces a force on the face of the exhaust valve that affects the valve dynamics. This in-cylinder pressure is modeled and integrated with the exhaust valve actuator model to capture the exhaust valve dynamics.

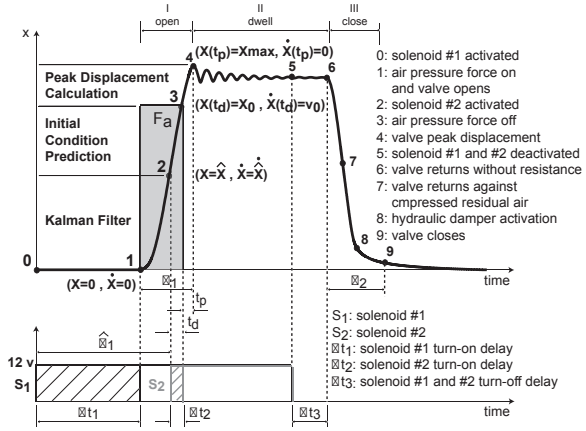

Figure 1. Valve lift profile with the solenoid command chart

The system dynamics illustrated here focuses on the relationship between the solenoid control commands and the exhaust valve displacement. It follows the same analysis as that of the level two model. As shown in Figure 1, the valve response can be divided into three stages. They are the opening stage (I), dwell stage (II), and closing stage (III). Solenoid #1 is activated at point 0 first. It induces a high air pressure force to push the valve open at point 1 after Δt_1. Solenoid #2 is then activated (point 2) with a time lag $\hat{\delta}_1$. It removes this air pressure force Δt_2 time after solenoid #2 is activated (point #3). Note that the interplay between two solenoids results in a pulse force input to the actuator valve piston with pulse width δ_1. Note that this pulse width is proportional to the valve lift. Now, with zero input, the valve movement continues until it reaches its peak lift at point #4, the valve equilibrium. This ends the open stage. Next, the valve enters the dwell stage where it is held open by a hydraulic latch mechanism. At the end of the dwell stage, solenoid #1 is deactivated at point #5. After Δt_3 time, the valve starts to return (point #6). The close stage starts at point #6 and ends at point #9 where the valve is considered closed. The returning duration is δ_2 between these two points.

The two solenoids have electro-mechanical delays after their activation and de-activation (see Figure 1). Δt_1 is defined as the delays for solenoid #1 at activation. Δt_2 is defined as solenoid #2 delay at activation. The de-activation delay for both solenoids are Δt_3. The solenoid commands direct the valve motion after the delays. The time lag applied between the activation of two solenoids is denoted as $\hat{\delta}_1$. This differs from the time lag between two delayed solenoid activations which is denoted as δ_1 since two

solenoid delays, Δt_1 and Δt_2, are not equal. The exhaust valve lift control algorithm is to determine when to activate solenoid #2 during exhaust valve opening for each engine cycle with the varying in-cylinder pressure at the surface of the valve and its activation delay in presence. It is impossible to remove the input force F_a instantly upon the activation of solenoid #2 due to its activation delay. An model based predictive lift control algorithm is developed to make this possible. The details are described in the control strategy section.

The exhaust valve closing timing control requires knowledge of δ_2, the amount of time that the valve takes to close. To guarantee the exhaust valve closing at the desired time requires de-activating solenoid #1 by time δ_2 before exhaust valve closing. δ_2 can be predetermined from the different valve lift set points. In other words, the closing timing control relies on a repeatable valve lift control. Developing a lift control system is the primary emphasis of work described in this paper.

The opening stage exhaust valve actuator model and the in-cylinder pressure model are employed to formulate the model based predictive lift control scheme. In order to validate the exhaust valve lift control algorithm, the level two model integrated with the in-cylinder pressure model is used as a plant model in simulation. The opening stage exhaust valve actuator model and the in-cylinder pressure model are introduced in the following two subsections.

2.1 Actuator Model

The opening stage exhaust actuator model with the in-cylinder pressure as external disturbance is studied in this subsection. This model is expanded based on the level two model [13] to include the in-cylinder pressure dynamics. Figure 2

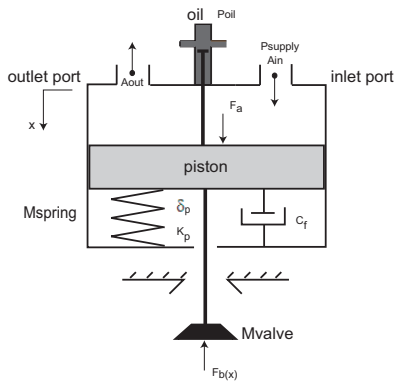

Figure 2. Actuator piston model

shows the schematic diagram of a single actuating piston for this system. At the opening stage, the valve actuator is modeled as a second order mass-spring-damper system with zero initial conditions, see Equation (1). All pressures used in modeling and control formulation process are gauge pressure in this article.

$$M\ddot{x} + C_f\dot{x} + K_p(x+\delta_p) = F_a(t) - F_b(x) \tag{1}$$

$$F_a(t) = F(t) - F(t-\delta_1), F(t) = \begin{cases} 0, & t < 0 \\ A_p P_p, & t \geq 0 \end{cases} \tag{2}$$

where, P_p is supply air pressure; $F_b(x)$ is the in-cylinder pressure force applied at the exhaust valve surface; M is the sum of equivalent mass of actuator piston, effective valve spring mass, exhaust valve and cap; A_p is the sum of actuator piston and oil passage areas; C_f is the damping ratio approximating energy dissipation due to flow loss and frictional loss; K_p and δ_p are the stiffness and preload displacement of the valve spring respectively; δ_1 is the lag between the activation of solenoids #1 and #2 after solenoid delays as shown in Figure 1.

2.2 In-cylinder Pressure Model

The in-cylinder pressure force $F_b(x)$ needs to be modeled and evaluated in Equation (1). Figure 3 illustrates the dynamics in the combustion chamber with an exhaust valve. A control volume is drawn above the piston, where m_{cyl}, T_{cyl} and P_{cyl} are the mass, temperature and pressure inside the combustion cylinder. A_{cyl} is the engine piston area. $\dot{m}_{ex}$ is the mass flow rate at the exit when the exhaust valve opens. T_{atm} and P_{atm} are the atmospheric temperature and pressure. x and y are the exhaust valve displacement and cylinder piston displacement respectively. The mass

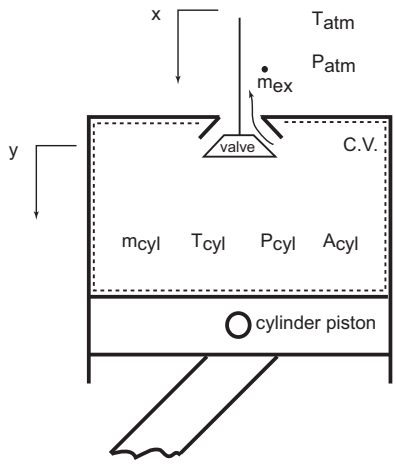

Figure 3. In-cylinder pressure model

flow rate equations at the exit are written for both choked and unchoked flow cases through Equations (3) to (5) following their derivation in [16].

$$\dot{m}_{ex} = C_{d_{ex}}\gamma P_{cyl} A_{ex}(x)\sqrt{\frac{k}{RT_{cyl}}}, A_{ex} = 2\pi r_{valve} x, \tag{3}$$

where, A_{ex} is the flow area with r_{valve} being the valve radius; $C_{d_{ex}}$ is the flow coefficient at the exit; R is the residual gas constant. C_p and C_v are the specific heat of the residual gas at constant pressure and constant volume respectively; and $k = \frac{C_p}{C_v}$. When $P_{cyl} \geq (\frac{k+1}{2})^{\frac{k}{k-1}} P_{atm}$, the flow is choked at the exit. In this case, γ is shown in Equation (4)

$$\gamma = \sqrt{(\frac{2}{k+1})^{\frac{k+1}{k-1}}}. \quad (4)$$

When $P_{cyl} \leq (\frac{k+1}{2})^{\frac{k}{k-1}} P_{atm}$, the flow is unchoked and γ is expressed in Equation (5).

$$\gamma = \sqrt{\frac{2}{k-1}} (\frac{P_{atm}}{P_{cyl}})^{\frac{k+1}{2k}} [(\frac{P_{atm}}{P_{cyl}})^{\frac{1-k}{k}} - 1]. \quad (5)$$

The mass of the residual gas inside the combustion cylinder in Equation (6) can be obtained by integrating the calculated mass flow rate. The initial mass m_0 is derived using ideal gas law, where P_0, V_0, R_0 and T_{cyl_0} are the initial in-cylinder gas pressure, volume, gas constant and temperature at the exhaust valve opening.

$$m_{cyl} = -\int_0^t \dot{m}_{ex} dt + m_0, \quad m_0 = \frac{P_0 V_0}{R T_{cyl_0}}. \quad (6)$$

Using the ideal gas law again with the obtained m_{cyl} results in an expression of in-cylinder pressure as shown in Equation (7).

$$P_{cyl} = \frac{m_{cyl} R T_{cyl}}{V_{cyl}}, \quad V_{cyl} = A_{cyl} y, \quad (7)$$

where, k, R and T_{cyl} are variables acquired from the WAVE^{TM} simulation with the same engine configuration and parameters; and y is the piston displacement derived from the engine geometry in Equation (8).

$$y = r[1 + \frac{L}{r} - \cos(\theta) - \sqrt{\frac{L}{r} - \sin^2(\theta)}], \quad (8)$$

where

- $A_{cyl} = \pi(\frac{1}{2} \times bore)^2 = 0.0401 m^2$ ($bore = 90.2mm$) ,
- L is the connecting rod length ($L = 169.2mm$),
- r is the crank shaft radius ($r = \frac{1}{2} stroke = 52.9mm$),
- θ is the engine crank angle.

Therefore, $F_b(x)$ can be expressed in Equation (9) below.

$$F_b(x) = P_{cyl} A_{valve}, \quad (9)$$

where P_{cyl} is defined in Equation (7).

2.3 In-cylinder Pressure Model Validation

The in-cylinder pressure force F_b is a function of the exhaust valve displacement since the flow out area A_{ex} is a function of the exhaust valve displacement.

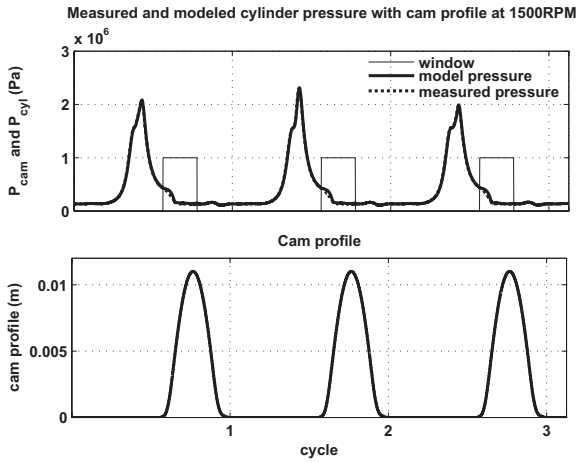

Figure 4. In-cylinder pressure model validation by simulation

In order to validate the in-cylinder pressure model, combustion experiments were conducted using a 5.4L 3 valve V8 engine with in-cylinder pressure measurement and a conventional cam shaft at 1500RPM. The pressure model was simulated using the conventional cam profile as the valve displacement input. The modeled in-cylinder pressure was then compared with the measured in-cylinder pressure as shown in Figure 4. The top diagram of this figure shows the modeled pressure (solid line) in the rectangular windows and measured in-cylinder pressure (dash line). The bottom diagram shows the exhaust cam profile used in the simulation and experiments. The in-cylinder pressure model is then integrated into the pneumatic exhaust valve model and the responses are shown in Figure 5. Here, the pressure model uses the EPVA valve lift profile to calculate the corresponding in-cylinder pressure. The modeled pressure (solid line in top diagram) and the associated EPVA valve lift profile (solid line in bottom diagram) are compared with the experiment pressure (dash line) and the cam profile (dash line). The simulation results demonstrated that the in-cylinder pressure reduces rather quickly with the EPVA exhaust valve actuation since the EPVA valve opens much faster than the conventional cam based valve.

This simulated in-cylinder pressure is used to construct the control signals. The exhaust valve model is used as a plant model and it is integrated with the in-cylinder pressure model in simulations to validate the control algorithm. The modeled in-cylinder pressure is one of the two inputs to the plant (exhaust valve) and the actuation force F_a commanded by the two solenoid control signals is the other input.

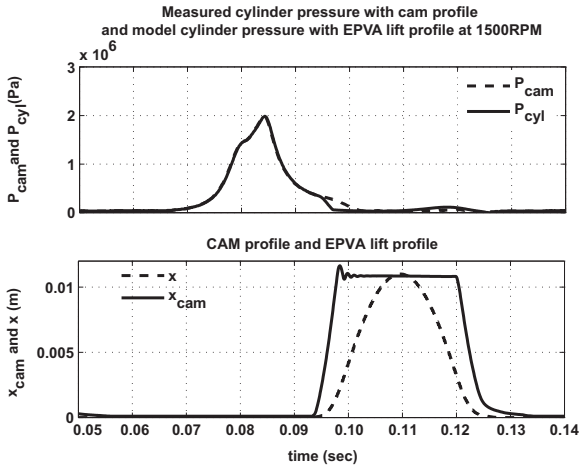

Figure 5. In-cylinder pressure model integrated into exhaust valve model

3 CONTROL STRATEGY

Since the in-cylinder pressure on the face of the exhaust valve varies significantly from cycle-to-cycle, the valve lift control needs to be adjusted as a function of the current in-cylinder pressure for each individual cycle. As explained in the actuator dynamics section, the exhaust actuator is modeled as a second order mass-spring-damper system at the opening stage. Activating solenoid #1 applies the force F_a on the valve and moves the exhaust valve. Activating solenoid #2 removes the force and the valve continues to open until it reaches the maximum displacement. Solenoid #2 activation timing determines the maximum valve lift. Therefore, the key for valve lift control is to find when to activate solenoid #2. Figure 1 illustrates the idea of the exhaust valve lift control strategy. Solenoid #1 is activated at time 0. After the delay of Δt_1, the input force F_a acts on the system and the exhaust valve starts to open at point 1. Solenoid #2 is then activated at point 2, after Δt_2 delay, force F_a is removed at point 3. The valve moves further until its velocity decreases to 0 at point 4. The second order valve system response from points 3 to 4 can be calculated with zero input and nonzero initial conditions at point 3. In other words, the valve peak displacement at point 4 can be calculated if the initial displacement and velocity at point 3 are known. Once the calculated displacement at point 4 reaches the reference maximum valve lift, point 3 is found to be the right time to remove force F_a. If activating solenoid #2 could turn off the input force F_a immediately, we would only need to activate it whenever the calculated displacement of point 4 reaches the reference lift. But the solenoid delay requires the activation to take place at point 2 with Δt_2 amount of time before point 3. This means that if point 3 is the time to eliminate input force, point 2 is the time to activate solenoid #2. However, the initial conditions at point 3, where the peak displacement of the valve is calculated, are not yet available at point 2. Therefore, an algorithm is derived to predict initial conditions of point 3 at point 2. This strategy of initial condition prediction can be implemented as long as the delay Δt_2 of solenoid #2 is less than the lag $\hat{\delta}_1$ between the activation of two solenoids. The predictive algorithm needs to know both states, valve displacement and velocity, at point 2. A Kalman state estimator was used to estimate them with minimized effect of measurement noise. Now we can determine the time to activate solenoid #2 (point 2), which is served as a feedforward control of the valve actuator. A proportional and integral (PI) scheme is used as a closed-loop feedback lift control system to reduce the steady state lift tracking error.

The flow chart of the feedforward control scheme is shown in Figure 6. First, solenoid #1 is activated. Secondly, the Kalman state estimator provides the current states (valve displacement and its velocity). Finally, a model based prediction algorithm uses the estimated states to calculate the states after solenoid #2 delay Δt_2, which is then used to calculate the peak valve displacement. If the calculated peak displacement is greater than or equal to the reference valve lift, solenoid #2 is activated, otherwise, the process repeats until the condition is satisfied. The details of the derivations are discussed in the following four subsections.

3.1 Peak Displacement Calculation (PDC)

This section describes the solution for the peak displacement at point 4 based on the initial conditions at point 3. Recall that the governing equation of the exhaust valve at the opening stage is presented in Equation (1). The back pressure force $F_b(x)$ equals the product of the exhaust valve area and the modeled in-cylinder pressure. The in-cylinder pressure used in the control algorithm development here is piece-wisely linearized according to the simulated in-cylinder pressure against EPVA exhaust valve profile, where $F_b(x) = px+q$ ($p \leq 0$ and $q \geq 0$) with

$$\begin{cases} p = p_1,\ q = q_1,\ x \leq 0.002m \\ p = p_2,\ q = q_2,\ 0.002m < x \leq 0.008m \\ p = p_3,\ q = q_3,\ x > 0.008m \end{cases}.$$

Substituting $F_b(x)$ with its linearized expression into Equation (1) results in Equation (10) below.

$$M\ddot{x} + C_f\dot{x} + K_p x = F_a - (px+q) - K_p\delta_p. \qquad (10)$$

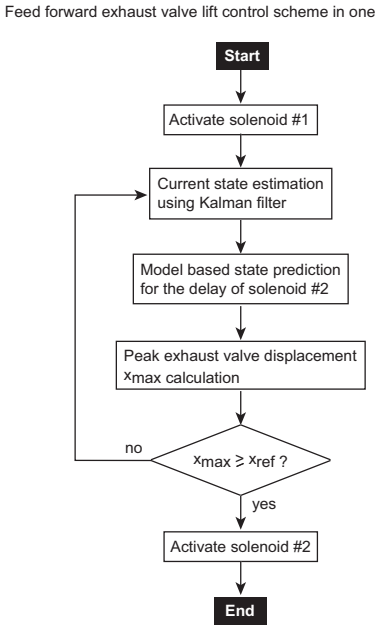

Figure 6. Feedforward exhaust valve lift control strategy

Move term px to the left resulting in Equation (11):

$$M\ddot{x}+C_f\dot{x}+(K_p+p)x=F_a-q-K_p\delta_p. \tag{11}$$

Let $K=K_p+p$ and $F_a=0$, since it is assumed that input force F_a is turned off, to obtain Equation (12) in a general format given the initial condition $x(0)=x_0,\ \dot{x}(0)=v_0$.

$$M\ddot{x}+C_f\dot{x}+Kx=-Q,\ \ Q=K_p\delta_p+q. \tag{12}$$

Recall that p takes three different values, p_1, p_2 and p_3 in three valve displacement regions. K could be either negative, zero or positive depending on the value of p. When K is positive, Equation (12) can be rewritten into Equation (13) as below:

$$\ddot{x}+2\zeta\omega_n\dot{x}+\omega_n^2x=-\frac{Q}{M}, \tag{13}$$

where $\omega_n=\sqrt{\frac{K}{M}}$ and $\zeta=\frac{C_f}{2}\sqrt{\frac{1}{MK}}$. In this case, the solution can be categorized into under damped, critically damped and over damped scenarios depending on the value damping ratio ζ, damping coefficient C_f, mass M and equivalent stiffness K in Equation (13). Based upon the system dynamic equations shown in (13), the peak displacement solution can be derived for four cases (see [15] for details). They are $K>0$ with $0<\zeta<1$ (case #1), $K>0$ with $\zeta=1$ (case #2), $K>0$ with $\zeta>1$ (case #3) and $K\leq 0$ (case #4). The initial condition denoted as $x(0)=x_0$ and $\dot{x}(0)=v_0$ in this section are derived in the next section of model based initial condition prediction.

3.2 Model Based Initial Condition Prediction (ICP)

The previous section solves for the peak displacement $x(t_p)$ using the displacement and velocity at point 3 as initial conditions (Figure 1). This section derives the formulas to predict the displacement $x(t_d)$ and velocity $\dot{x}(t_d)$ at point 3, given the displacement and velocity at point 2. The displacement and velocity at point 2 are initial conditions denoted as $x(0)=x_0$ and $\dot{x}(0)=v_0$ in this subsection. Their values are estimated by the Kalman state estimator described in the next subsection. Solenoid #2 delay, Δt_2, is the time input and F_a is a constant force input between points 2 and 3. Consider the governing equation again in Equation (1). Given $F_b(x)=px+q$, Equation (1) becomes

$$M\ddot{x}+C_f\dot{x}+K_px=F_a-(px+q)-K_p\delta_p. \tag{14}$$

Rearrange the equation above to obtain

$$M\ddot{x}+C_f\dot{x}+(K_p+p)x=F_a-q-K_p\delta_p. \tag{15}$$

Let $K=K_p+p$ and $W=q+K_p\delta_p-F_a$, Equation (15) becomes Equation (16).

$$M\ddot{x}+C_f\dot{x}+Kx=-W. \tag{16}$$

It is clear that Equations (12) and (16) have the same form. Previously, Equation (12) was evaluated for the maximum displacement given initial conditions. Now, Equation (16) is evaluated for the displacement and velocity in t_d amount of time with given initial conditions, where $t_d=\Delta t_2$ (see Figure 1). Equation (16) can be solved in a similar way to Equation (12) by replacing Q with W, and the solutions are omitted in this paper. The techniques of solving analytical solutions for a second order mass-spring-damper system can be found in [21].

3.3 Kalman Filter State Estimation (KFE)

The displacement and velocity at point 2 (see Figure 1) are needed as initial conditions in the previous section. The system is equipped with a displacement sensor which measures the exhaust valve displacement. The velocity obtained through taking a time derivative of the measured displacement is unreliable due to the measurement noise. The observer formulated in this section performs the optimal estimations of both the displacement and velocity at point 2 in the presence of noise using Kalman state estimator (see [20]). The estimated displacement and velocity are denoted as $\widehat{x}$ and $\widehat{\dot{x}}$ respectively. The state space notation of the system is expressed below:

$$\dot{x}=Ax+Bu+Gw(t)$$
$$y=Cx+v(t)$$

where $A = \begin{bmatrix} 0 & 1 \\ \frac{-K}{M} & \frac{-C_f}{M} \end{bmatrix}$, $B = \begin{bmatrix} 0 \\ \frac{1}{M} \end{bmatrix}$, $C^T = \begin{bmatrix} 1 \\ 0 \end{bmatrix}$, $x = \begin{bmatrix} x_1 \\ x_2 \end{bmatrix}$, and G is an identity matrix; $w(t)$ and $v(t)$ represent the process noise and measurement noise. Note that $u = -W$ is the input to the system, $x_1 = x$ and $x_2 = \dot{x}$ are the states representing the valve displacement and velocity. The Kalman state estimator takes the following forms:

$$\dot{\widehat{x}} = A\widehat{x} + Bu + L(y - c\widehat{x})$$
$$\widehat{y} = C\widehat{x}, \quad \widehat{x}(0) = 0,$$

where L is the observer gain acquired through solving the algebraic Riccati Equation (17); and $\widehat{x}$ is the estimated displacement x_1 and velocity x_2.

$$AP + PA^T + GW_pG^T - PC^TV^{-1}CP = 0, \tag{17}$$
$$L = PC^TV^{-1}, where \;\; W \geq 0 \;\; and \;\; V > 0, \tag{18}$$

where W_p and V are covariance matrices of w and v, respectively. If (C,A) is observable, the algebraic Riccati equation has a unique positive definite solution P, and the estimated state $\widehat{x}$ asymptotically approaches true state x.

3.4 Closed-Loop Control Scheme

The feedforward solution of solenoid #2 activation timing is obtained by implementing the formulas from the peak displacement calculation, model based initial condition prediction and Kalman filter state estimation subsections. This solution combined with the displacement error compensation from the proportional and integrator (PI) feedback scheme forms a closed-loop control signal of solenoid #2 as illustrated in Figure 7.

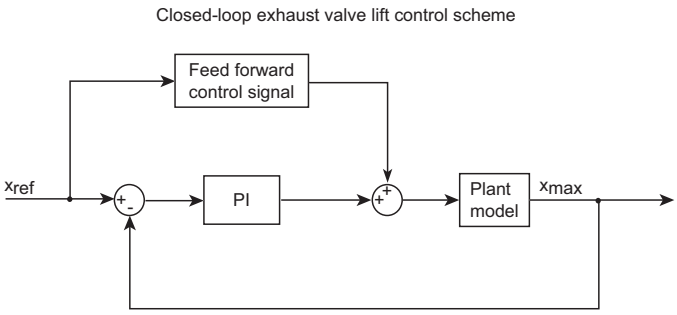

Figure 7. Closed-loop exhaust valve lift control scheme

4 EXPERIMENTAL IMPLEMENTATION

The developed control algorithms was validated in simulation using the combined valve actuator and the in-cylinder pressure model as the plant model (see [14]), where the three-segment feedforward control strategy and the closed-loop control scheme are evaluated in sequence. In this section, the closed-loop lift control strategy was implemented in a prototype controller and evaluated by experiments. The feedforward lift control signals were precalculated and implementation in a form of lookup tables to reduce the real-time calculation throughput. Note that both ICP and PDC calculations require only system initial states, and they can be precalculated to reduce realtime processing throughput.

4.1 Experiment Setup

4.1.1 Mechanical system configuration Experiments were conducted on a 5.4L 3 valve (2 intake valves and 1 exhaust valve) V8 engine head. As displayed in Figure 8, the cam and cam shaft were removed from the engine head. Three electro-pneumatic actuators were installed on the top of each valve to manage both intake and exhaust valve events. Micro-Epsilon^{TM} point range sensors were mounted under each valve to measure the valve displacements (see Figure 9).

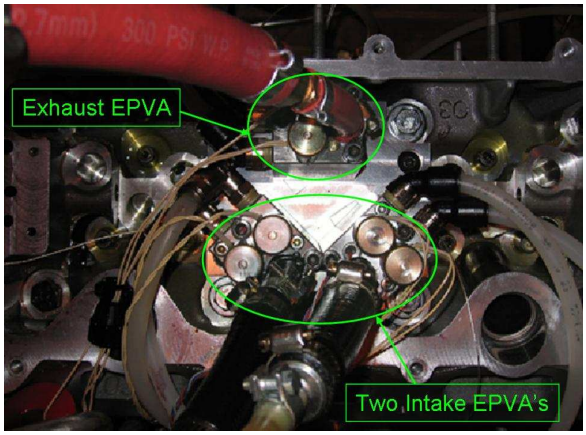

Figure 8. Top view of EPVA installed on the 5.4L 3V V8 engine head

To test the exhaust valve control system, a pressurized chamber was build and installed under the cylinder head, which imitates the in-cylinder pressure acting at the back of the exhaust valve. The pressure chamber is shown in Figure 9. It was pressurized with the supplied compressed air at $4.48 \times 10^5 Pa$ ($65 psi$). The pressure inside chamber drops quickly when the exhaust valve opens and builds up when it closes. The exhaust lift control experiments were performed at $600 RPM$ that is lower enough to ensure that the chamber pressure can recover close to $4.14 \times 10^5 Pa$ ($60 psi$) at every cycle. An optical window was built underneath the exhaust valve on the bottom of the chamber. The exhaust valve laser sensor sends and receives laser beam through this optical window to measure the exhaust valve displacement

(see Figure 9). A pressure transducer was mounted on the cylinder head close to the exhaust valve.

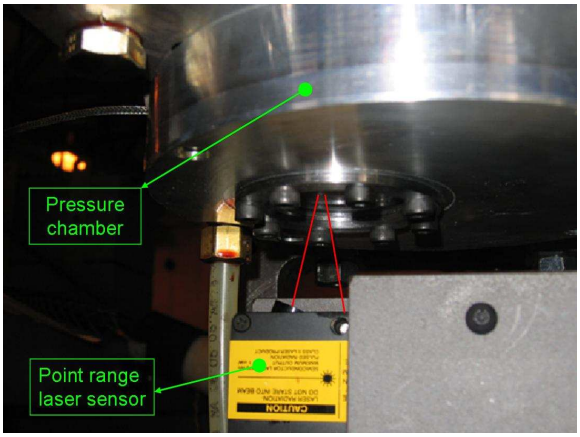

Figure 9. Pressure chamber under the valves

4.1.2 Control system hardware configuration A realtime Opal-RT^{TM} prototype control system was employed for the EPVA exhaust valve bench tests. The system consists of:

- Two 3.2GHz CPU's
- An IEEE 1934 fire wire serial bus with the data transfer rate at 400MHz per bit
- Two 16 channel A/D and D/A boards with less than 1 μs conversion rate
- One 16 channel digital I/O board at 50 ns sampling rate

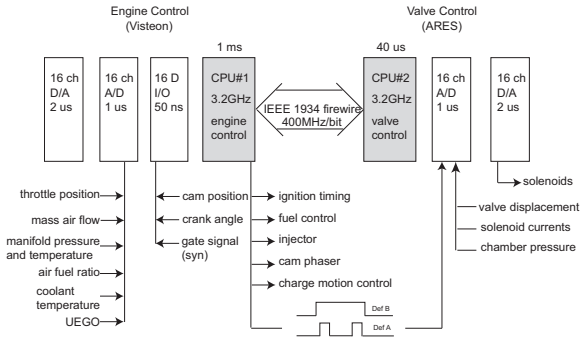

Figure 10. Modular control system configuration

Figure (10) displays the hardware configuration of the system. CPU #1 is used for engine controls and CPU #2 is dedicated to the valve actuator (EPVA) control. An IEEE 1934 fire wire serial bus is used for communication between CPU #1 and CPU #2. CPU #1 is configured to be updated every $1ms$ and to execute the engine control strategy every combustion cycle. This means that this CPU updates input and updates analog outputs every $1ms$, but calculates the engine control parameters every engine combustion event. The digital inputs and outputs of CPU #1 are synchronized with the engine crank angle with one-third crank degree resolution. The crank angle calculation is completed within the digital I/O card of CPU #1 utilizing digital inputs from cam sensor, gate and crank signals from an encoder. The CPU #1 digital outputs are spark pulse, fuel injection pulse, charge motion control, and intake and exhaust valve timing pulses, especially the pulses $DefA$ and $DefB$ that synchronize the valve control between the engine and valve control system. The inputs of the 16 channel analog I/O board include ionization signal, pressure signal, throttle position, mass air flow rate, coolant temperature, manifold pressure and temperature, and air-to-fuel ratio from universal exhaust gas oxygen (UEGO) sensor.

The valve control CPU #2 is configured to operate at $40\mu s$ sample rate, which is close to one-sixth crank degree at $600RPM$. CPU #2 executes most of the valve control algorithms and generates the control signals for the pneumatic valve actuators. A 16 channel A/D board reads crank synchronized $DefA$ and $DefB$ pulse signals from CPU #1, valve lift signal from valve lift point range position sensors, solenoid current signals from their drive circuits, and supply air pressure signal. The solenoid control pulses and the exhaust valve pressure (which is needed to calculate the feedforward lift control inputs in simulation) are the output from a 16 channel D/A board.

The solenoid driving circuit for the exhaust valve used the peak and hold scheme to minimize the solenoid electro-magnetic delays. The total solenoid delay including the electro-magnetic and mechanical delays was kept below $2ms$.

4.2 Feedforward Lift Control Input Calculation

The damping ratio of the exhaust valve model at the opening stage is needed in constructing the feedforward lift control signal using the developed model based predictive lift control strategy. To identify this model parameter, open loop lift control tests were conducted on the exhaust valve test bench at $600RPM$. The maximum pressure at the back of exhaust valve was set to be $4.14 \times 10^5 Pa$ $(60psi)$, the supply air and oil pressure was at $8.28 \times 10^5 Pa$ $(120psi)$ and the target lift was $10mm$. The valve back pressure varies randomly from cycle to cycle with the variation as large as $10^5 Pa$ $(14.5psi)$. The measured valve back pressure was used in the exhaust valve model simulation. The lag between the activation of two solenoids remained unchanged in both simulations and tests for parameter identification purpose. The experiment and simulation valve responses are displayed in Figure 11. The bottom diagram shows the model (dot line) and the measured (solid line) valve lift profiles in five cycles. The top diagram shows the corresponding pressure against with the ex-

haust valve opens. The damping ratio was chosen in such a way that the model valve responses agree with the experimental valve responses as demonstrated in this figure. The developed model

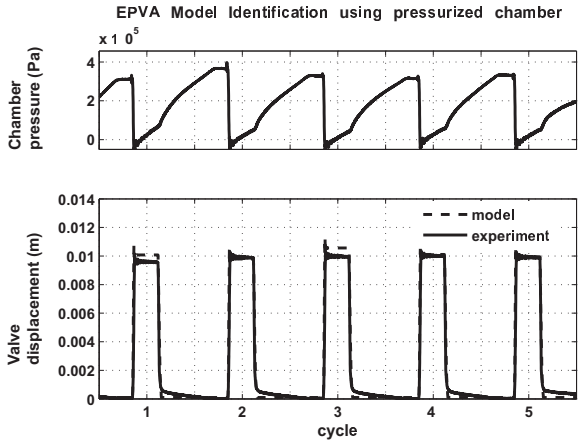

Figure 11. Exhaust valve model identification

based predictive control strategy can be used to determine the activating timing of the second solenoid and use this timing as a feedforward lift control input in realtime. In order to reduce realtime computational throughput, the developed strategy was used to calculate the lag between the activation of the first and the second solenoids for different lift set points in off-line simulations to precalculate for all possible initial conditions. In realtime applications, this lag was the feedforward lift control input, combined with the feed back PI compensation, to form a closed-loop lift control input. The measured valve back pressure in the pressurized chamber was piecewisely linearized and used in the feedforward control input calculation. The measured pressure was multiplied by the area of the exhaust valve to obtain the pressure force applied at the exhaust valve surface. This force was plotted in Figure 12 (grey curves) against the valve displacement for 20 cycles. As shown in this figure, they were linearized in three segments (solid lines) during the exhaust valve opening to approximate the averaged forces. The coefficients, p_1, q_1, p_2, q_2, p_3 and q_3, were used to construct the feedforward lift control input through the model based predictive control algorithm.

¿From Figure 12 we can observe that the pressure force applied to the face of exhaust valve varies between $260N$ and $410N$. This is equivalent to that the exhaust back pressure varies between $2.28 \times 10^5 Pa$ ($33.1 psi$) and $3.57 \times 10^5 Pa$ ($51.7 psi$). The control strategy was developed based upon the averaged exhaust pressure profile, but the experimental validation using the pressurized chamber simulates a variable in-cylinder pressure, that the exhaust valve opens against, between $2.28 \times 10^5 Pa$ ($33.1 psi$) and $3.57 \times 10^5 Pa$ ($51.7 psi$). Therefore, even though the control strategy is based upon a mean pressure model, the control strategy is demonstrated under certain cycle-to-cycle pressure variations. Evaluation of this controller against cycle-to-cycle variation is going to be part of our future study.

Simulations were performed to determine the lags between the activation of two solenoids according to the given reference lifts. The exhaust valve model was identified earlier and used as the plant in the simulations. The measured back pressure during exhaust valve opening was used to make the simulation consistent with experimental results. The Riccati equation was solved off-line with three different stiffness coefficient K. The results are displayed in Figure 13. The diagrams in the left column are the valve lift output from the exhaust valve model. Those in the right column are the calculated feedforward lift control inputs which are the calculated lags between the activation of the first and second solenoids. The lag was found to be about $3.8ms$ (top right), $4.1ms$ (middle right) and $4.8ms$ (bottom right) to achieve the target lift of $6mm$ (top left), $8mm$ (middle left) and $10mm$ (bottom left).

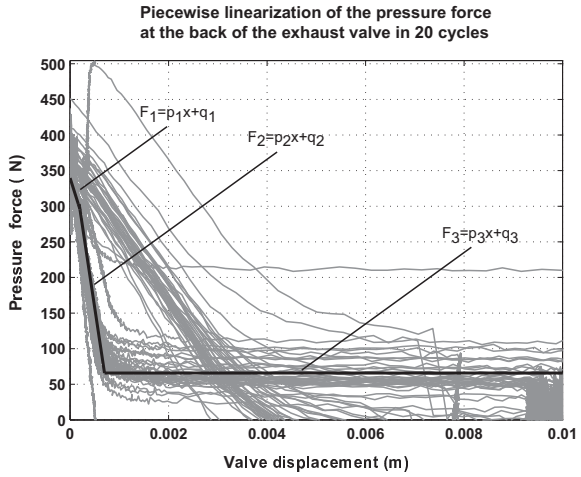

Figure 12. Piecewise linearized valve back pressure force

4.3 Experimental Results of Closed-Loop Exhaust Valve Lift Tracking

Finally, Figures 14 to 17 present the closed-loop lift tracking control results with the feedforward control. 150 cycles of valve responses were recorded with sequences assembled at three reference lift set points in Figure 14. The reference valve lift varies every 50 engine cycles from $8mm$ to $6mm$, $6mm$ to $10mm$, and $10mm$ to $8mm$. The complete sequences of lift tracking responses are presented in Figures (14). The responses at every set point were enlarged through Figures 15 to 17 to illustrate their transient and steady state performance. On the top diagram of every figure, the black line is the reference valve lift,

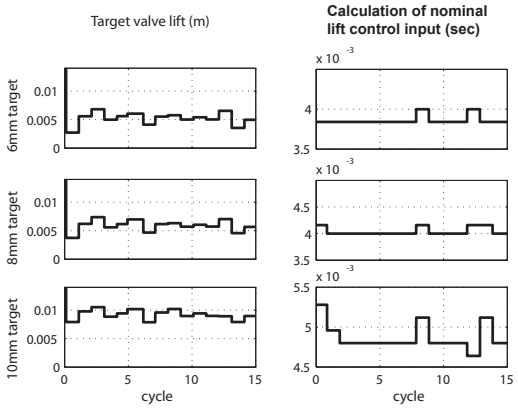

Figure 13. Feedforward exhaust valve lift control calculation

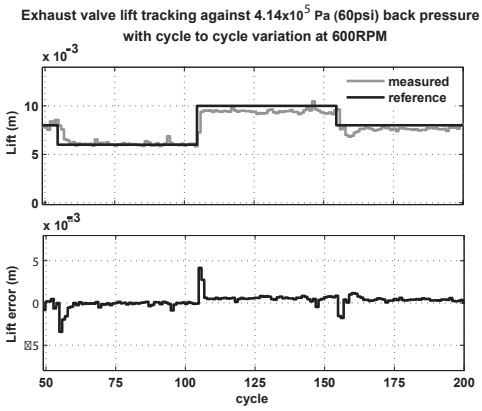

Figure 14. Experimental responses: three set points

and the grey line is the actual valve lift. The bottom diagram shows the lift error between the reference and the actual valve lifts. Figure 15 shows that the exhaust valve follows the reference lift of $6mm$ in two engine cycles with the lift error less than $0.7mm$. Figures 16 and 17 show that the exhaust valve tracks the reference lift of $10mm$ and $8mm$ in one engine cycle with the lift error less than $0.7mm$. It can also be observed from Figures 16 and 17 that steady state errors were not converged to zero. This is mainly due to small integration gain used for this set of the tests. The enlarged responses display that the absolute steady state lift tracking errors of all three set points are below $1mm$. Here, an accurate feedforward controlled input ensures a fast transient responses. The valve responses at low lift is more sensitive to the error in the calculated feedforward controlled input, which has relatively greater fraction in the entire input (the lag between the activation of solenoid #1 and #2). A slight error in the feedforward input calculation due to the model uncertainty, measurement inaccuracy or numerical error leads to a significant deviation of the actual valve lift from its desired lift in transition. Therefore, the valve at low reference lift exhibits a slower transient response than that at high reference lift.

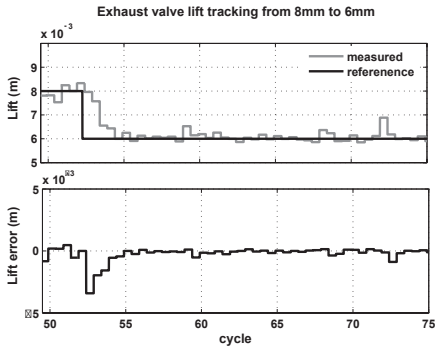

Figure 15. Experimental responses: transient from $8mm$ to $6mm$

5 CONCLUSIONS

A mathematical exhaust valve actuator model and an in-cylinder pressure model have been developed for a model based predictive lift control of an exhaust valve. The exhaust valve model was approximated by a piece-wisely linearized second order spring-mass-damper system. The in-cylinder pressure was modeled during the exhaust valve opening stage. This model was integrated with the exhaust valve actuator model for control development. The thermodynamics data used in this model was obtained using WAVE^{TM} simulation which was calibrated using experimental in-cylinder pressure data. The in-cylinder pressure model was validated using experimental data and demonstrated satisfactory modeling accuracy.

A model based predictive control strategy was developed for feedforward control. This strategy contains three segments: peak displacement calculation, model based initial condition prediction and Kalman state estimation. The acquired feedforward input combined with the closed loop proportional and integral control forms the closed-loop lift control signal to accomplish the exhaust valve lift tracking. The exhaust valve model was calibrated using the measured exhaust valve back pressure signal to obtain piecewisely linearized parameters required for the feedforward input calculation. Experiments were conducted on a 5.4L 3 valve V8 engine head at $600RPM$ to evaluate the closed-loop lift control system. A pressurized chamber was installed under the cylinder head which imitates the in-cylinder pressure acting at the back of the exhaust valve. The actual chamber pressure that the exhaust valve opens against varies between $2.28 \times 10^5 Pa$ ($33.1psi$) and $3.57 \times 10^5 Pa$ ($51.7psi$). Therefore, even though the control strategy is based upon a mean pressure model, the

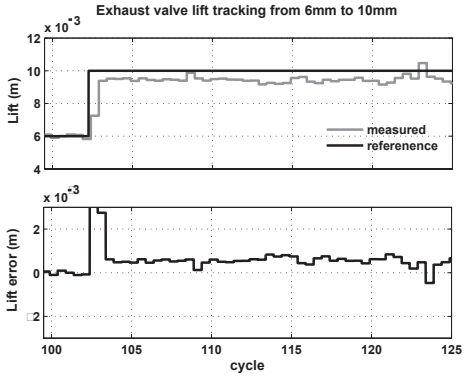

Figure 16. Experimental responses: transient from $6mm$ to $10mm$

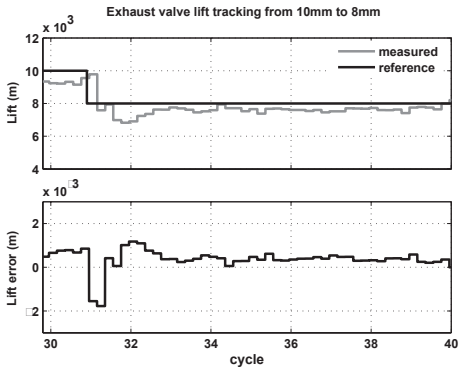

Figure 17. Experimental responses: transient from $10mm$ to $8mm$

control strategy is demonstrated with certain cycle-to-cycle pressure variations. The experimental results with three lift reference points showed that the steady state valve lift error is below $1mm$. The exhaust valve tracks the reference lift in a single engine cycle at high reference lift (greater than $8mm$) and two engine cycles at low reference lift ($6mm$) with a lift error less than $0.7mm$.

ACKNOWLEDGMENT

The authors gratefully acknowledge the support for this work from the U.S. Department of Energy, National Energy Technology Laboratory, Energy Efficiency and Renewable Energy Division, Samuel Taylor, Project Manager.

REFERENCES

[1] K. Inoue et al., "A High Power Wide Torque Range Efficient Engine with a Newly Developed Variable Valve Lift and Timing Mechanism," *SAE 890675*, 1989.

[2] Y. Moriya et al., "A Newly Developed Intelligent Variable Valve Timing System Continuously Controlled Cam Phasing as Applied to a New 3 Liter Inline 6 Engine," *SAE 960579*, 1996.

[3] R. Flierl and M. Kluting, "The Third Generation of New Fully Variable Valvetrain for Throttle Free Load Control," *SAE 2000-01-1227*, 2000.

[4] M. Theobald, B. Lequesns, and R. Henry, "Control of Engine Load via Electromagnetic Valve Actuators," *SAE 940816*, 1994.

[5] C. Boie et al., "Method for Controlling a Electromagnetic Actuator for Achieving a Gas Exchange Valve On a Reciprocating Internal Combustion Engine," *US Patent 6,340,008*, 2000.

[6] L. Schneider, "Electromagnetic Valve Actuator with Mechanical End Position Clamp or Latch," *US Patent 6,267,351*, 2001.

[7] I. Haskara, L. Mianzo, and V. Kokotovic, "Method of Controlling an Electromagenatic Valve Actuator," *US Patent 6,644,253*, 2003.

[8] Y. Wang, A. Stefanopoulou, K. Peterson, T. Megli, M. Haghgooie, "Modeling and Control of Electromechanical Valve Actuator," *SAE 2002-01-1106*, 2002.

[9] G. Wright, N. Schecter, and M. Levin, "Integrated Hydraulic System for Electrohydraulic Valvetrain and Hydraulicly Assisted Turbocharger," *US Patent 5,375,419*, 1994.

[10] O. Sturman, "Hydraulic Actuator for an Internal Combustion Engine," *US Patent 5,638,781*, 1994.

[11] Z. Sun and D. Cleary, "Dynamics and Control of an Electro-Hydraulic Fully Flexible Valve Actuation System," *Proceedings of American Control Conference*, Denver, Colorado, June, 2003.

[12] Jia Ma et al., "Analysis and Modeling of an Electronically Controlled Pneumatic Hydraulic Valve for an Automotive Engine," *SAE 2006-01-0042*, 2006.

[13] Jia Ma et al., "Model reference adaptive control of a pneumatic valve actuator for infinitely variable valve timing and lift," *2007 SAE World Congress (SAE 2007-01-1297)*, Detroit, MI, April, 2007.

[14] Jia Ma et al., "Adaptive control of a pneumatic valve actuator for an internal combustion engine," *2007 American Control Conference*, New York, NY, July, 2007

[15] Jia Ma et al., "Model Based Predictive Control of an Electro-Pneumatic Valve Actuator for Internal Combustion Engines," *Submitted to 2008 American Control Conference*, Seattle, WA, June, 2008.

[16] M. Anderson, T. C. Tsao, M. Levin, "Adaptive Lift Control

for a Camless Electrohydraulic Valvetrain," *SAE 981029*, 1998.

[17] J. M. Tressler et al., "Dynamic Behavior of Pneumatic Systems for Lower Extremity Extenders," *Proceedings of the 2002 IEEE International Conference on Robotics & Automation*, Washington, D.C., May 2002.

[18] K. Misovec et al., "Digital Valve Technology Applied to the Control of an Hydraulic Valve Actuator," *SAE 1999-01-0825*, 1999.

[19] M.-S. S. Ashhab, A. G. Stefanopoulou, J. A. Cook, and M. B. Levin, "Control of Camless Intake ProcessPart II," *Journal of Dynamic Systems, Measurement, and Control, Vol. 122, Issue 1, pp. 131-139*, 2000.

[20] D. S. Naidu, "Optimal Control Systems," *Electrical Engineering Textbook Series* CRC Press, Boca Raton, FL, USA, 2003

[21] W. T. Thomson, "Theory of vibration with applications," (5th edition), Prentice Hall, Upper Saddle River, New Jersey, 1998.

[22] C. Turner, G. Babbitt, C. Balton, and M. Raimao, "Design and Control of a Two-Stage, Electro-Hydraulic Valve Actuation System," *SAE 2004-01-1265*, 2004.

2007-01-1411

A High Speed Flow Visualization Study of Fuel Spray Pattern Effect on Mixture Formation in a Low Pressure Direct Injection Gasoline Engine

David L.S. Hung, Guoming G. Zhu and James R. Winkelman
Visteon Corporation

Tom Stuecken and Harold Schock
Michigan State University

Andrew Fedewa
Mid-Michigan Research, LLC

ABSTRACT

In developing a direct injection gasoline engine, the in-cylinder fuel air mixing is key to good performance and emissions. High speed visualization in an optically accessible single cylinder engine for direct injection gasoline engine applications is an effective tool to reveal the fuel spray pattern effect on mixture formation The fuel injectors in this study employ the unique multi-hole turbulence nozzles in a PFI-like (Port Fuel Injection) fuel system architecture specifically developed as a Low Pressure Direct Injection (LPDI) fuel injection system. In this study, three injector sprays with a narrow 40° spray angle, a 60° spray angle with 5° offset angle, and a wide 80° spray angle with 10° offset angle were evaluated. Image processing algorithms were developed to analyze the nature of in-cylinder fuel-air mixing and the extent of fuel spray impingement on the cylinder wall. Test data reveal that for a given cylinder head, piston configuration and intake air port flow characteristics, injector spray pattern plays a dominating role in how the fuel-air mixture is formed. If an appropriate injector spray pattern is chosen, the in-cylinder fuel mixing can be enhanced by minimizing fuel impingement on cylinder wall, piston top, and intake valves, thus producing a more homogeneous fuel-air mixture prior to the ignition. Engine designers can select a specific spray pattern to improve the fuel-air mixture optimized for specific parameters such as engine head, piston, valve configuration, intake air flow characteristics, fuel injection strategy, injector mounting and operating conditions.

INTRODUCTION

Developing a high efficiency and clean combustion engine with enhanced combustion performance, improved fuel economy and reduced engine emissions has been a principal goal of vehicle manufacturers and component suppliers. Among many enablers advancing the current internal combustion engine technology to achieve such goals is the development of direct injection (DI) gasoline engines. As fuel is injected directly into the engine cylinder, this engine technology offers great flexibility to control the fuel injection strategy with respect to various engine operation modes. In particular, the fuel-air mixture preparation in the combustion chamber has also been identified as one of the key factors that greatly influence the combustion characteristics of the engine performance [1]. Hence, optimizing the fuel mixture homogeneity is a key engine design parameter.

Recently, there has been a resurgent effort by various vehicle manufacturers and suppliers to develop and manufacture a second generation DI gasoline engines which overcome the challenges of the first generation production engines [2]. The main focus has been shifted to the stoichiometric homogeneous-charge engines which are designed particularly for the North American automobile markets [3]. For homogeneous combustion mode, the injection timing occurs during the intake stroke and a homogeneous fuel-air mixture is generally formed. The mixture is therefore maintained at stoichiometric condition in the cylinder prior to the ignition event. A homogeneous mixture can generally be formed by creating a spray with moderate to wide cone angle, well-atomized drops, and an appropriate level of spray tip penetration for optimizing the fuel-air mixing. In addition, the fuel injection timing window has to be precisely controlled in order to minimize any cylinder wall and/or piston wetting while maintaining the charge homogeneity in the cylinder.

When developing combustion systems for DI gasoline engines, it is important to achieve optimal fuel-air mixture for ignition. Depending upon the combustion chamber

configuration and the engine operating modes, the fuel mixture strategy may require different levels of control over key spray characteristics including spray pattern, cone angle, penetration, and drop size. If the injectors can be designed to offer spray tailoring flexibility, engine designers may utilize the injectors to deliver the specific flow and spray requirements without major compromises and limitations when running the engine at its optimized configuration.

High speed imaging has evolved as a primary optical diagnostic technique for investigating the characteristics of ultra-fast motion events. The short time duration between frames and high image quality with good image resolution make high speed imaging an ideal optical tool to study the highly transient fuel spray characteristics applicable in an engine configuration. Earlier research by Hamady et al. [4] studied the fuel spray characteristics from various injector nozzles using a high speed imaging system. Using a similar technique, Kawajiri et al. [5] were able to investigate the interaction between spray and air motion in a cylindrical vessel with swirling intake gas motion similar to that in an engine. In addition, high speed imaging visualization from consecutive cycles was also applied to study fuel distribution, ignition, and combustion characteristics [6-8] under realistic engine speed and load configurations. More recently, Hung et al. [9] combined high speed imaging with time-resolved laser diffraction to characterize the transient nature of the gasoline pulsing sprays under atmospheric condition. Transient characteristics such as drop sizing, intra-pulse and pulse-to-pulse interactions throughout and in between consecutive injection cycles were readily resolved.

Hardware improvement has also been a key contributor to the major advances in imaging technology over the past decade. The technology of high speed camera systems has also shifted from a traditional 16 mm film camera such as a rotating prism cine camera at a maximum rate of around 10,000 frames per second to advanced CMOS or CCD based sensors with digital image format at a frame rate exceeding 100,000 frames per second with kilo pixel resolution. Visible and ultra-violet laser light sources have also been advanced to operate at repetition rates as high as 50 kHz. These powerful illumination sources work very well with the intensified or regular cameras, enabling visible imaging or planar laser induced fluorescence (PLIF) imaging on fuel spray to be performed. Timing devices have also been improved significantly such that the timing of the injection events can be reliably synchronized with the camera and light source. In addition, sophisticated algorithms and innovative analysis techniques have also been developed. Large quantities of digitized images can be stored and analyzed efficiently, thus allowing both qualitative and quantitative information to be extracted. For example, mechanisms of fuel film formation on the cylinder wall have been identified as a potential source of smoke and hydrocarbon emissions from DI gasoline engines. Various studies have been performed [10, 11] to focus on investigating the mechanisms of the fuel film formation. In particular, Drake and Fansler [12] used high speed imaging at a rate of 4,500 frames per second to visualize the fuel film deposition on piston top from two different types of fuel injectors. Using a RIM (Refractive Index Matching) technique, they were able to process the images and quantify the fuel film area, thickness and volume deposited on piston top as a function of engine crank angle. They concluded that the spray structure could be a dominant factor in affecting the amount of film deposited on piston for stratified charge combustion during late injection.

The objective of this paper is to investigate how spray pattern would affect the fuel mixture preparation in a DI gasoline engine under realistic speed and load conditions. Several key parameters including the injector spray pattern, injection timing, and fuel pressure are evaluated. The observations are based upon the fuel distribution in the combustion chamber as well as fuel impingement on the cylinder wall as a function of crank angle degree. Further, imaging analysis techniques are presented to reveal cylinder wall impingement. The results will be used to correlate the engine combustion and emissions performance in the subsequent single cylinder dynamometer combustion testing, which will be reported in a future study.

LPDI FUEL SYSTEM AND MULTI-HOLE FUEL INJECTORS

The multi-hole fuel injectors are developed as part of a patented Low Pressure Direct Injection (LPDI) fuel delivery system for DI gasoline engines [13, 14]. The LPDI fuel delivery architecture is very similar to the current port fuel injection (PFI) fuel system in production, i.e., no engine driven pump is required. This LPDI fuel system is designed for an engine to run in stoichiometric homogeneous-charge combustion mode and to achieve improved combustion, better fuel economy, and reduced emissions. It consists of a high-efficiency in-tank positive displacement pump and motor module, fuel injectors and fuel rail with an integral pulse damping feature and controls. The in-tank fuel pump delivers a nominal fuel pressure of 2 MPa to the fuel injectors connected to a common-rail through a chassis fuel line. An injector driver integrated into a powertrain control module (PCM) controls the fuel injection, timing and duration. A pressure sensor mounted on a fuel rail provides fuel pressure feedback to the PCM and the fuel pump controller to regulate fuel flow and fuel rail pressure using a closed-loop control.

One of the key components in this fuel system is the multi-hole high turbulence fuel injectors that inject fuel in relatively well-atomized drops directly into the cylinder at much lower pressures than competing high pressure DI fuel systems. It has been shown in a previous study [15] that multi-hole fuel injectors offer the spray pattern tailoring flexibility over other existing fuel injectors using either the swirl or slit nozzles. This is because the hole pattern, hole orientation, internal flow cavity, and number of holes on a multi-hole nozzle can all be precisely designed to control individual spray plumes and the

overall spray distribution. This injector utilizes a novel high-turbulence multi-hole nozzle to produce a soft spray at 2 MPa fuel system pressure with relatively well-atomized drops. Since this pressure is significantly lower than that of other existing high pressure gasoline DI systems, it enables an attractive cost effective solution for DI fuel system implementation by eliminating the expensive high-pressure fuel pump and related parts.

The fuel spray characteristics of current production intent injectors used in this study are produced by an eight-hole nozzle configuration. The internal nozzle geometry and geometrical parameters have been designed to offer different spray characteristics. Prior to running these injectors in the optical engine, injector spray tests were performed to evaluate the spray geometry, drop sizing, and injector dynamic flow characteristics in a test bench. Whenever possible, the spray measurement and characterization were carried out according to the test setup, procedure and reporting guidelines based on the SAE Gasoline Fuel Injection Standards Committee recommendations [16]. Images of spray pattern formation were recorded using a spray imaging system. Direct illumination on the spray was provided by a strobe light located at a slight angle from the direction of the camera. Spray geometrical parameters such as spray angle, offset angle, and spray trip penetration were extracted from the Mie-scattered spray images. The spray drop sizing was performed using Phase Doppler Interferometry. Statistical drop diameters and volume flux were measured and reported. In addition to the spray characteristics, an automated injector flow stand was used to measure the dynamic flow rate of the injector as a function of the injection pulse width. The static flow rate was extracted from the dynamic flow curve. The test fuel used in the spray characterization tests was n-Heptane and the fuel pressure was set at 2 MPa. The injection pulse width for the spray characterizations was set to 1.5 ms.

Figures 1 to 3 show the spray images of three spray patterns produced with various multi-hole nozzle configurations. These images were recorded at the same time delay of 1.5 ms after the start of the injection (SOI) pulse. Each spray is shown as an ensemble average image by averaging ten individual images. The image size in these figures is approximately 55 mm wide by 65 mm high. The baseline narrow spray with a spray angle 40° and 0° offset angle (denoted as 40/0) is depicted in Figure 1. As expected, this spray exhibits a strong symmetry along the injector axis. Figure 2 shows a wider spray with the spray angle of 60° and a 5° offset angle (denoted as 60/5). The offset angle of this spray is achieved by designing the valve seat and nozzle configurations without distorting the basic symmetry of the spray. Similar to the narrow spray, the spray pattern is also symmetric with respect to the injector axis, tilted by the designed offset angle of 5°. The front end of the spray is relatively uniform across the spray tip. The overall spray angle is wider because each inclined spray plume from an individual hole is increased proportionally from that of the baseline nozzle. As a result, the spray is hollower in the inner core region. Using the similar design principle, a spray with a much larger spray angle of 80° and a 10° offset angle (denoted as 80/10) can be produced, as shown in Figure 3. It is worth mentioning that even though these sprays are generated using the same basic eight-hole nozzle configurations, the fact that different spray patterns can be achieved due to different internal geometrical configurations in the nozzles demonstrates the capability to tailor the spray pattern by using the multi-hole nozzles.

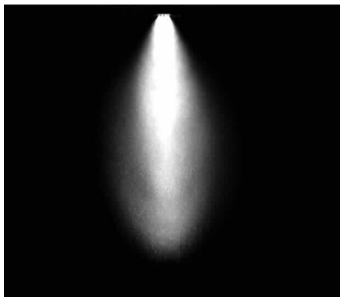

Figure 1. Spray with 40° spray angle / 0° offset angle

Figure 2. Spray with 60° spray angle / 5° offset angle

Figure 3. Spray with 80° spray angle / 10° offset angle

Figure 4 shows the axial penetrations of three different injector sprays. The penetration length was determined as the axial location of the spray tip from the injector axis. As expected, the 40/0 spray penetrates longer than the other two sprays with larger spray angles. Both 60/5 and 80/10 sprays have very similar penetration characteristics. Figure 5 shows the volume flux and Figure 6 depicts the sauter mean diameter (SMD) distribution of three injector sprays. The measurements were achieved along a line scan perpendicular to the injector axis at 30 mm below the injector tip. Each scan was made at a 2 mm spatial step. The narrow spray shows a Gaussian-like flux distribution with the peak flux along the centerline of the injector axis while the other two wider sprays depict a similar dual peak distribution

near the edges of the spray with less flux distribution (hollow) along the injector axis. The peaks on the line scan also show the locations of the plumes which somewhat correspond to the spray angle. The peak-to-peak distance of the volume flux is largest for the 80/10 spray. The SMD values of the 40/0 spray range from 28 to 44 microns; whereas for the 60/5 and 80/10 sprays, the SMD values are between 20 and 42 microns. To convert the radial scan point-wise SMD measurements into a single, line-of-sight value, the SMD was re-processed by weighing the measurement at each location with its corresponding flux density and then normalized. Calculated SMD values for all three sprays are quite similar: that of the 40/0 is about 33.1 microns, whereas the SMD for the 60/5 and 80/10 are 33.4 and 31.8 microns, respectively.

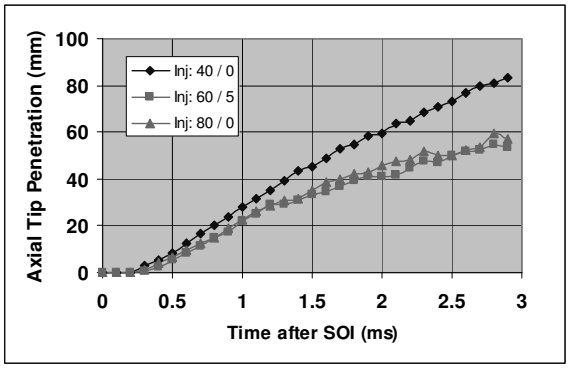

Figure 4. Axial spray tip penetration

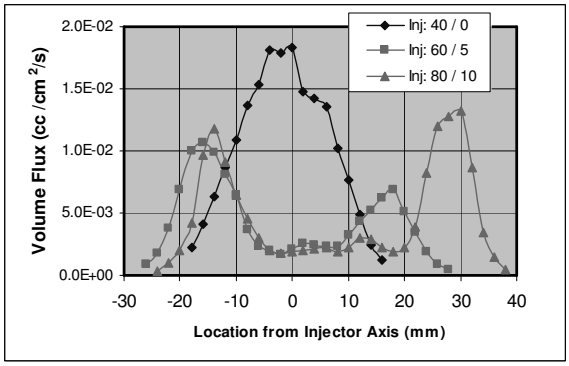

Figure 5. Volume flux distribution

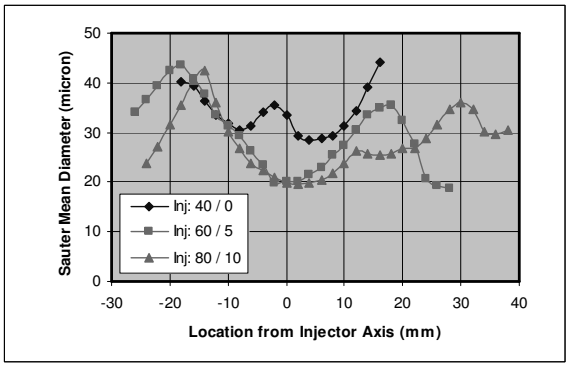

Figure 6. Sauter mean diameter distribution

EXPERIMENTAL SETUP AND TEST CONDITION

SINGLE CYLINDER OPTICAL ENGINE AND FLOW VISUALIZATION DIAGNOSTICS

The 5.4 liter V8 engine rig studied is shown in Figure 7. A production intake air manifold is used and the cylinder head has been modified to accept the low pressure direct injector. Three of the four cylinders on this half cylinder head bank have been deactivated by grinding off their lobes on the camshaft. The head is mounted on top of a single cylinder crank case that has been re-stroked to 105.7 mm to match the crankshaft geometry of the engine as well as to utilize the original connecting rod. Located between the cylinder head and the reciprocating assembly are the quartz cylinder and piston with a quartz insert. Both the cylinder and piston are designed to provide optical access to the inside of the engine cylinder while retaining the original cylinder bore of 90.2 mm. The engine is held at speed by a 15 hp AC motor with a variable speed drive. An optical shaft angle encoder is used to determine crankshaft orientation for the fuel injection control which is accomplished through the use of a timing controller. Both the high speed camera and the fuel injector are triggered from the output signal of the controller.

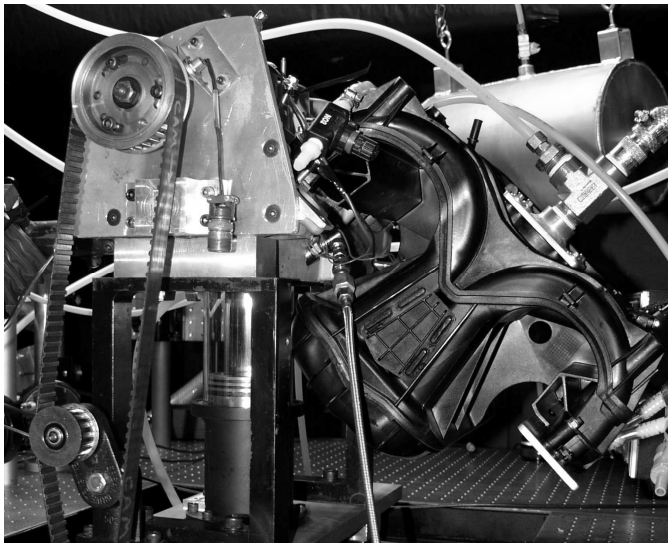

Figure 7. View of the single cylinder optical engine

Figure 8 shows the geometry of the single cylinder head and port configuration. This cylinder head has two intake valves and one exhaust valve. The spark plug is located near the center of the roof. Figure 9 shows the middle section view of the cylinder head. This view shows both the orientation and mounting locations for the injector and the spark plug. The outlines of the three injector spray orientation are also depicted in the same figure. The injector was side-mounted onto the cylinder head at an angle of 35° from the horizontal axis. The mounting location was selected such that there was no interference between the fuel injector and the existing coolant passage surrounding the cylinder head.

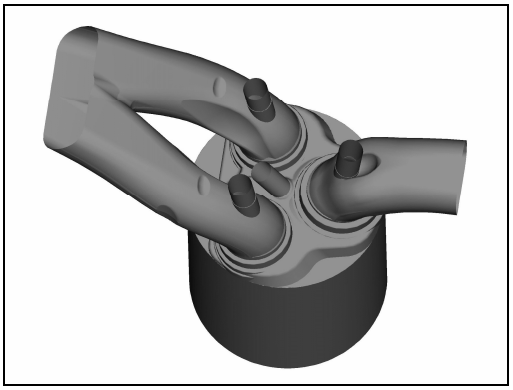

Figure 8. Single cylinder head configuration with intake and exhaust ports

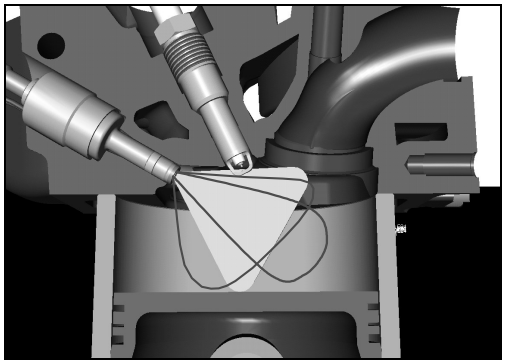

Figure 9. Placement of spark plug and fuel injector (with spray configurations outlined)

EXPERIMENTAL PROCEDURE

All fuel spray imaging tests were performed with the engine motored only. A Mie scattering technique was used to visualize the liquid phase of the fuel dispersion inside the combustion chamber through the quartz cylinder liner wall as well as the quartz piston insert. The fuel spray was imaged with a non-intensified high speed digital video camera. The camera was set to operate at 10 kHz which provides an image resolution of 512 by 512 pixels to cover a spatial imaging area of approximately 123 by 123 mm. A high repetition rate pulsed copper vapor laser, synchronized with the high speed camera and the fuel injection timing logic, was used to illuminate the liquid fuel dispersion. A fiber optics cable was used to direct the laser pulse through the quartz piston insert into the cylinder, as shown in Figure 10. This arrangement maximized the illumination quality inside the cylinder and minimized much of the secondary scattering from the internal reflection of the quartz wall. The 20 Watt laser provided the high intensity short pulse duration (about 25 ns) for visualization. This equates to an energy level of approximately 2 mJ per laser pulse.

For this series of optical engine tests, a laboratory type fuel supply system was used which consisted of a fuel bladder, pressure regulator, and compressed nitrogen bottle. Premium grade gasoline was used as test fuel and it was delivered to the fuel injector at which the injection pressure was regulated to either 2 or 3 MPa, which was dictated by different fuel flow and fuel charge mixing requirements at various engine load conditions. Two engine speed and load points were selected for this study: a part load, 1500 RPM point at a manifold air pressure (MAP) of 45.5 kPa absolute, and a full load, 2500 RPM at wide open throttle (WOT). For each test condition, the engine was first motored to reach the desired RPM. Once the engine was stabilized, a signal from the controller was sent out to the fuel injector to trigger the start of injection (SOI) at a specific crank angle of piston location. The same signal was also used to trigger the high speed camera to start recording the image sequence. Based on the previous test data of fuel flow and lambda calculation on this firing engine, the fuel injection duration was adjusted at each load condition to achieve a stoichiometric air fuel ratio. For each imaging test, 300 consecutive frames from each injection cycle were recorded to visualize the fuel dispersion during the intake and compression strokes. Five injection cycles were normally filmed to allow for a quick assessment of cycle-to-cycle variation. The optical chamber was cleaned periodically to ensure that there was no debris remained in the chamber to affect the image background quality. The test matrix in Table 1 summaries the key parameters studied in this investigation. In addition, an in-depth in-cylinder flow field investigation on this engine head and cylinder configuration was made using the Molecular Tagging Velocimetry (MTV) as previously demonstrated by Schock et al. [17]. This investigation will be reported in a future study.

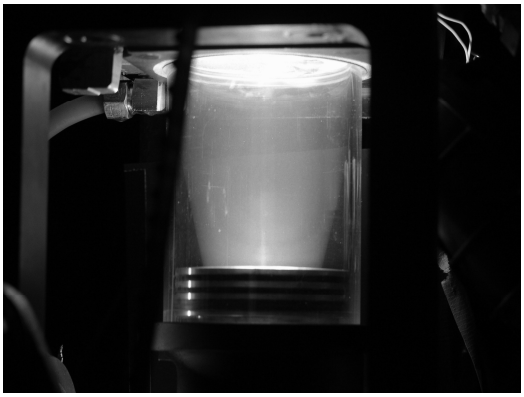

Figure 10. Illumination of the cylinder through the quartz piston insert

Parameter	Description
Fuel Injector Type	40 / 0 (spray angle / offset angle) 60 / 5 80 / 10
Fuel Injection Pressure	2 MPa 3 MPa
Injection Timing	330° CA BTDC (Intake Stroke) 300° CA BTDC (Intake Stroke) 270° CA BTDC (Intake Stroke)
Engine Load	Part Load: 1500 RPM / 45.5 kPa MAP Full Load: 2500 RPM / WOT
Injection Pulse Width	Part Load: 1 – 2 ms (nominal) Full Load: 4 – 7 ms (nominal)

Table 1 Test parameters for the optical study

RESULTS AND DISCUSSIONS

SPRAY PATTERN EFFECT ON IN-CYLINDER FUEL MIXTURE FORMATION

Figure 11 shows the comparison of three injector sprays on fuel mixture distribution in the combustion chamber at the engine part load condition of 1500 RPM and a MAP pressure of 45.5 kPa absolute. If the single cylinder engine was combusting, this MAP pressure would correspond to about 3.3 Bar IMEP (Indicated Mean Effective Pressure). Previous test data on this single cylinder engine of 3.3 Bar IMEP at 1500 RPM corresponded to a 2.62 Bar BMEP (Brake Mean Effective Pressure), which is normally referred to as the World Wide Mapping Point (WWMP). The injection pressure was regulated to a baseline level of 2 MPa. The SOI was set at 300° crank angle (CA) before top dead center (BTDC). With the adjusted cam phasing timing, the intake valve was lifted to about 8 mm at this SOI. The injection pulse width (duration) was set to correspond to lambda one (stoichiometric) condition. These images were recorded within an injection cycle at different crank degrees. It is worth mentioning that the injector driver has a 1 ms pre-charge delay, and so it corresponded to the delay of either 9 CAD/ms (at 1500 RPM) or 15 CAD/ms (at 2500 RPM) before the fuel spray was observed at the top of the cylinder. The first image of the sequence was shown at 277.5° BTDC, where the initial portion of the spray entering the cylinder was found to be about the same for all three sprays. The intake air did not have much effect on the beginning of the spray. The narrow spray of 40/0 showed a slightly stronger axial penetration along the injector axis into the cylinder. At 255° BTDC, the fuel charge started to show some noticeable differences in the fuel distribution. The 40/0 spray penetrated more directly across the cylinder towards the liner wall while the 60/5 and 80/10 sprays were moving more towards the central region of the cylinder. They produced very minimal fuel impingement on the opposite side of the liner wall. It also shows that at this SOI timing, the leading portion of the sprays impinged slightly on the piston top. However, as the cycle progressed to 210° BTDC, the fuel distributions among all three sprays were quite similar.

The fuel distribution at 2500 RPM with full load WOT is displayed in Figure 12. The SOI was again set at 300° BTDC. In this case, the fuel injection pressure was increased to 3 MPa. At full load, the images show that both the spray angle and offset angle were critical factors to affect how fuel was dispersed. In addition, the effect of intake air on fuel mixing was more dominant when the engine was running at full load condition. When the intake valves opened, the intake air diverted the spray slightly towards the direction of moving piston. The initial spray dispersion at an early CA of 262.5° BTDC seemed to be quite similar for all three sprays. However, as the cycle progressed to 225° BTDC, the liquid fuel of the 40/0 spray moved directly towards the opposite side of the cylinder wall. The 60/5 spray penetrated more towards the central region of the cylinder and less on the cylinder wall. The spray was tilted more towards the piston and it created a slightly better fuel dispersion within the cylinder. The impinging location of fuel on the cylinder wall was further away from the top of the cylinder along the stroke than the previous 40/0 spray. It is believed that the enhanced dispersion is due to two factors: Firstly, a wider spray angle improves the fuel dispersion; and secondly, the additional spray offset angle of 5° from the injector axis moves the spray even more towards the piston direction. As expected, the 80/10 spray directed the fuel dispersion even more towards the central region of the cylinder without any noticeable fuel impingement on the cylinder wall. At 197.5° BTDC, the fuel impingement of the 40/0 spray was very pronounced. At 150° BTDC, both intake valves were almost fully closed. The fuel dispersion of the 40/0 spray was quite localized in the upper half of the cylinder closer to the exhaust valve. The 60/5 spray improved the fuel distribution slightly, but the 80/10 spray seemed to provide the best fuel air mixing in the cylinder.

The images, particularly at high load point, confirm that the spray pattern has a dominant effect on how fuel is dispersed inside the cylinder. The narrow spray of 40/0 created a significantly reduced core dispersion of fuel droplets in the central region of the cylinder. A narrower spray usually has a higher axial spray penetration. Since the spray penetration was along its injector axis which was mounted at an angle of 35° inclined from horizontal, the tip of the spray penetrated directly across the cylinder along the injector mounting axis and impinged on the opposite side of the cylinder wall at a location somewhere near the middle of the cylinder. This impingement location was found to be closely related to the geometrical mounting of the injector. A wider angle of fuel spray not only produced a more homogeneous fuel-air mixture by dispersing the mixture formation more in the upper to central region of the cylinder, it also reduced the penetration along its injector axis. In addition, since the spray was designed to bend towards the piston by either 5° or 10°, the spray was able to propagate more directly towards the piston. However, for all three sprays, it was also noticed that there was a lack of fuel distribution in the upper half of the cylinder closer to the intake valves. It is believed that the lack of fuel dispersion was partially due to the constraint of the injector mounting orientation.

For an existing configuration of injector mounting orientation and cylinder geometry in this engine, a wider spray angle with an offset angle bent towards the piston made the spray less likely to impinge on the cylinder wall. It is likely to reduce any liquid fuel film formation on liner walls which usually leads to a high level of unburned hydrocarbon and other smoke particulates. The fuel impingement on the piston top is strongly dependent upon the SOI timing. The potential fuel impingement on the piston top may also be minimized if the injection timing can be retarded further up to a reasonable level without degrading the fuel mixture quality.

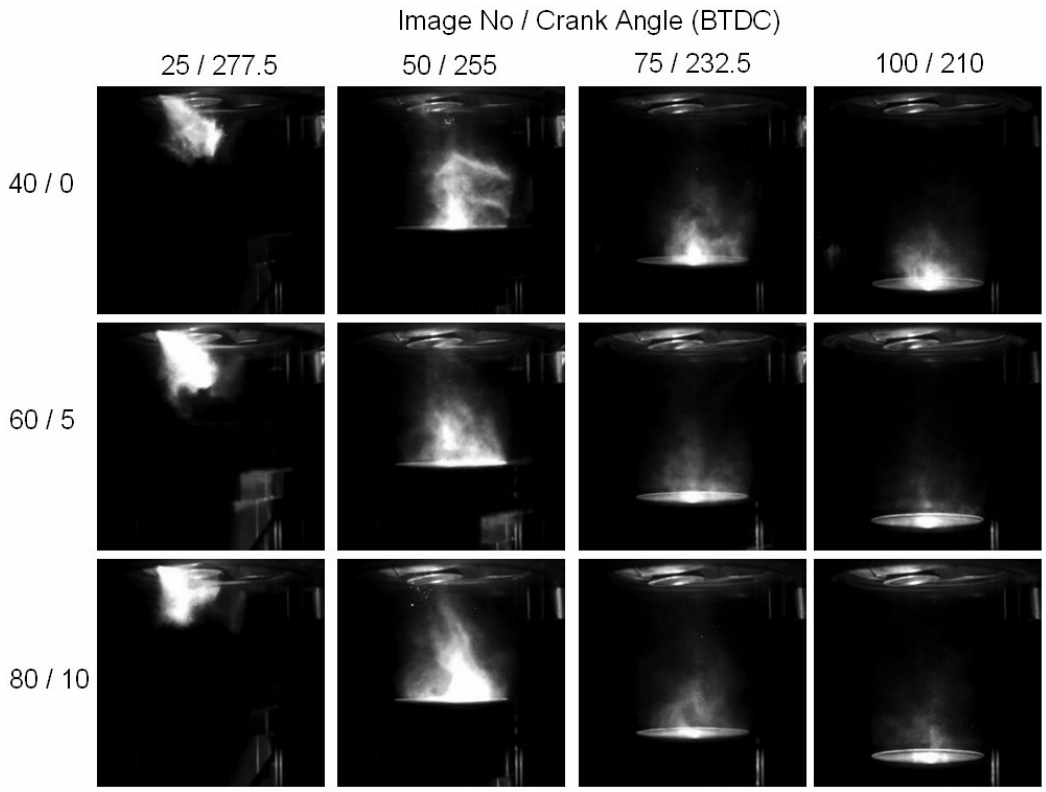

Figure 11. In-cylinder fuel mixture formation at 1500 RPM / 45.5 kPa MAP / 2 MPa fuel pressure / SOI at 300° CA BTDC

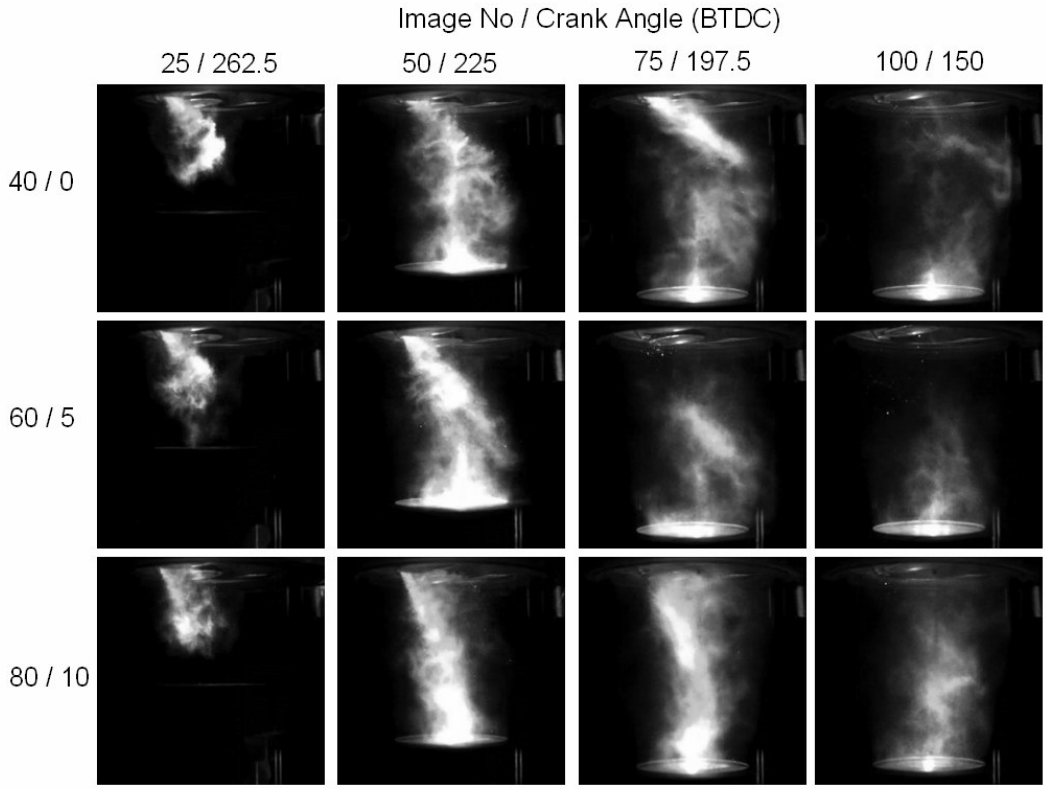

Figure 12. In-cylinder fuel mixture formation at 2500 RPM / WOT / 3 MPa fuel pressure / SOI at 300° CA BTDC

The 80/10 spray produced a better fuel mixture in the cylinder. However, it was also found that due to the close proximity of the injector tip to the intake valves, the larger spray angle also caused a slight amount of fuel spray impingement on the inner side of both intake valves, as shown in Figure 13.

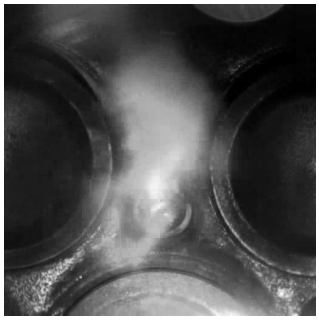

Figure 13. Slight fuel impingement on intake valves due to larger spray angle

FUEL IMPINGEMENT ANALYSIS ON CYLINDER LINER WALL

Based on the distinct features depicted in Figures 11 and 12, it is possible to identify and extract more information on the mixture formation from these images with image processing. Therefore, image processing algorithms have been developed to measure the semi-quantitative information such as the magnitude of fuel spray impingement on cylinder wall and piston top, and fuel-air mixture homogeneity.

For example, to analyze the fuel impingement magnitude on the cylinder wall, a fuel impingement index on the cylinder wall can be defined based upon the illumination intensity of the location (pixel) on the image near the cylinder wall. The methodology of the fuel impingement on the cylinder wall is briefly outlined next. Figure 14 depicts the measurement areas shown as a gray bar along the cylinder wall where the illumination intensity of each pixel in the image is extracted. The size of this area depends on the image orientation and measurement location of interest. For the analysis of fuel impingement on cylinder wall, a thin area band was chosen to be 5 pixels (i^{th}) wide by 300 pixels (j^{th}) long. Then, an average intensity is computed by averaging the pixel intensity across the width (i.e., across the i^{th} direction) of the area at each j^{th} pixel as follows:

$$\bar{I}_{ave,j} = \frac{\sum_{i=1}^{N} I_{i,j}}{N} \qquad (1)$$

where $I_{i,j}$ is the intensity of an individual pixel in the measurement area. N is the number of pixels along the width and it is equal to 5 for this analysis.

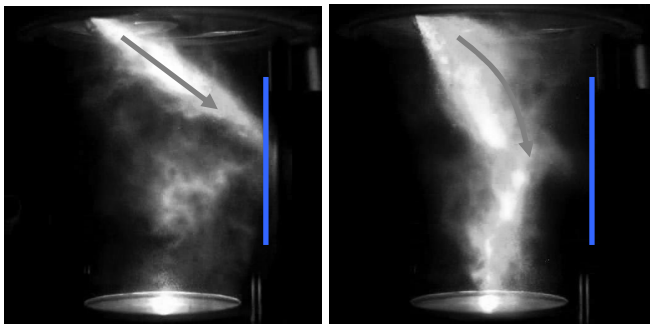

Figure 14. Location of the fuel impingement analysis (illustrated by the measurement region) (Left: 40/0 spray; Right: 80/10 spray)

Figure 15 shows the comparison of the average intensity between the two spray patterns along the measurement line. For both sprays, there was no fuel impingement near the top of the cylinder wall. However, it can be seen that for the 40/0 spray, the average intensity along the cylinder wall started to increase abruptly at about one-third of the stroke distance, and it peaked at about halfway of the cylinder. After the peak, the intensity continued to decrease toward the bottom of the cylinder. Fuel impingement was found to spread more on the lower half of the cylinder wall. Conversely, for the wider spray of 80/10, there was almost no impingement of fuel along the cylinder wall. The average intensity remained very minimal and constant along the entire analysis location.

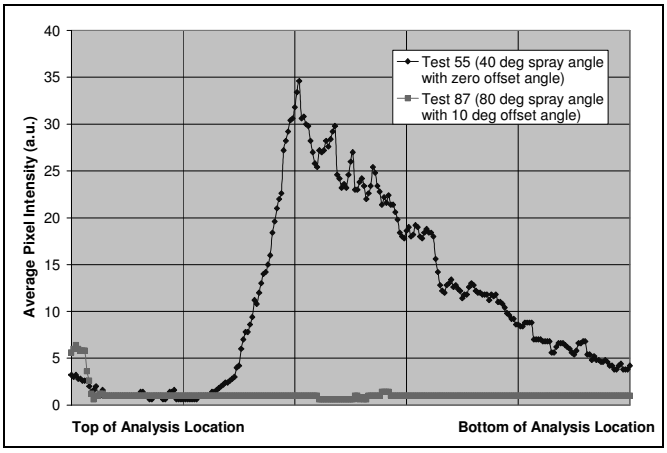

Figure 15. Comparison of ensemble average intensity on wall impingement when piston is at BDC

Since the fuel impingement is strongly transient and it is rapidly changing at different crank angles within an engine cycle, an overall fuel impingement index (FII) at a specific crank angle can also be defined based on the ensemble average intensity over the entire location along j^{th} direction of the measurement domain:

$$FII_{CA} = \frac{\sum_{j=1}^{M} \bar{I}_{ave,j}}{M} \qquad (2)$$

where M is the number of pixels along the length of the measurement domain. M is equal to 300 for this analysis.

This index can be used to track and analyze the extent of fuel impingement at each crank angle degree over the injection cycle. Figure 16 shows such a plot of crank angle resolved fuel impingement index on the cylinder wall. This figure also reveals several useful facts about the characteristics of such as the sequence and the duration of the fuel impingement. The injection logic pulse started at 270° BTDC when the image sequence was commenced. Taking the injector driver pre-charge delay into account, the fuel spray entered the cylinder at about 246° BTDC. The spray then propagated directly across the cylinder and started to impinge on the cylinder wall at about 210° BTDC. The impingement index started to increase as the piston continued to sweep downwards. For both sprays, even though the peak of impingement was observed to be between 140° and 130° BTDC, the narrow spray with 40/0 resulted in substantially higher cylinder wall impingement than the wider spray of 80/10. Impingement continued to decrease for both sprays as the piston reached about 100° BTDC. Beyond this crank angle, the fuel impingement for both sprays was found to be very minimal.

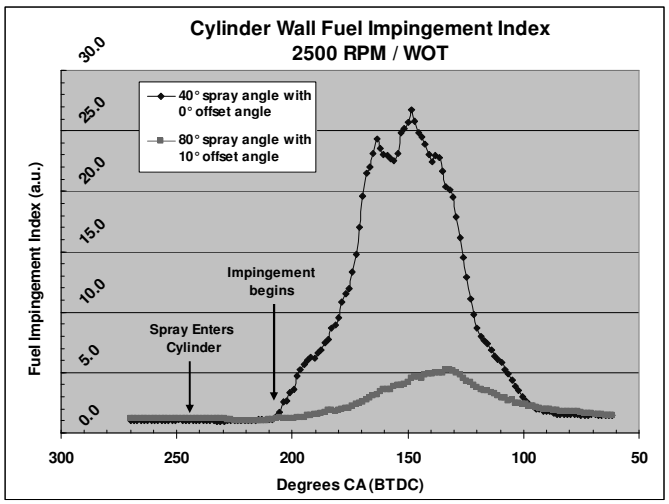

Figure 16. Crank angle resolved fuel impingement index on cylinder liner wall

Similar to any other image analysis methods based on light intensity extracted from the pixels of an image, it is important to realize that this fuel impingement analysis technique mentioned above also requires a consistent light illumination and background in the region of interest in order to minimize any possible inaccuracy or uncertainty. For example, any fuel droplets populated in the bottom of the liner wall or in the shadow of the piston quartz insert may not be accounted for equally due to the uneven light intensity distribution inside the cylinder. In addition, any residual fuel left behind from previous cycles may remain in the cylinder or be deposited on the walls as the cycle progresses. This could potentially over-estimate the quantity and location of the fuel impingement at a particular crank angle. Therefore, a proper background subtraction may be needed to eliminate any contribution of the residual fuel from previous cycles.

Even though this fuel impingement index cannot be used directly to correlate the amount of fuel impinged on the wall, this value indicates the extent as well as the location of the fuel impingement at a specific crank angle within a cycle. Since it is based on the illumination intensity of the pixel, once the images are properly adjusted to correct for any illumination deviation in the imaging setup, it may be useful for comparing other fuel mixing quality between different conditions.

CONCLUSION

High speed imaging was performed to visualize the spray pattern effect on fuel mixture formation as a function of crank angle in a single cylinder engine for direct injection gasoline applications. With the use of the imaging diagnostics to differentiate the fuel mixing characteristics produced by three different spray patterns, it was found that the spray angle, offset angle, and injector mounting orientation had pronounced effects on the fuel mixture preparation. The fuel mixture inside the combustion chamber was affected more by the spray pattern at full load than on part load condition. A narrow spray with 40° spray angle was not able to create a homogeneous fuel mixture in the cylinder. Fuel was found to impinge on the cylinder wall. The location of the impingement was strongly dependent on how the injector was mounted in the cylinder head. However, the widest spray angle of 80° with 10° offset angle produced a better fuel mixture in the cylinder with more homogeneous distribution and less cylinder liner wall impingement. Due to the wide spray angle, a small amount of fuel was also found to impinge on the intake valves. Moreover, for all three spray patterns, there was still a lack of fuel dispersion in the upper part of the region near the intake valves. It is believed that the lack of fuel dispersion was partially due to the constraint of the injector mounting orientation. For this cylinder head configuration, a steeper (more vertical) injector mounting angle may help improve the fuel mixture distribution and overall homogeneity.

Fuel impingement on cylinder liner walls was also investigated by using image processing and analysis algorithms. Using high speed imaging, the transient nature of fuel impingement was resolved as a function of crank angle degree. If a consistent light intensity through the image was ensured, the location and extent of fuel impingement of various spray patterns could be differentiated and compared. Similar image analysis methods may also be applied to evaluate the fuel impingement on the top of the piston. A new injector spray pattern is currently being revised which will not only minimize the fuel impingement on liner wall and intake valves, but enhance the overall fuel distribution. These results will be used to correlate the engine combustion and emission performance in the subsequent single cylinder dynamometer combustion testing.

ACKNOWLEDGMENTS

The authors gratefully acknowledge the support for this work from the U.S. Department of Energy, National Energy Technology Laboratory, Energy Efficiency and Renewable Energy Division, with Samuel Taylor as the Project Manager. Technical assistance from the staff members of Visteon Corporation and the Automotive Research Experimental Station at Michigan State University is greatly appreciated.

REFERENCES

1. Zhao, F.Q., Harrington, D.L., and Lai, M.C., *Automotive Direct-Injection Gasoline Engines*, Society of Automotive Engineers Press, 2002.
2. Yamaguchi, J, "Direct-Injection Resurgence," *Automotive Engineering International*, January 2005, SAE International.
3. Carney, D., "Internal-combustion engineering," *Automotive Engineering International*, May 2004, SAE International.
4. Hamady, F.J., Hahn, J.P., Hellman, K.H., and Gray, C.L., Jr., "High Speed/High-Resolution Imaging of Fuel Sprays from Various Injector Nozzles for Direct injection Engines," SAE 950289.
5. Kawajiri, K., Yonezawa, T., Ohuchi, H., Sumida, M., and Katashiba, H., "Study of Interaction Between Spray and Air Motion, and Spray Wall Impingement," SAE 2002-01-0836.
6. Jansons, M., Lin, S., and Rhee, KT., "High-speed Imaging from Consecutive Cycles," SAE 2001-01-3486.
7. Smith, J.D., and Sick, V., "Crank-Angle Resolved Imaging of Fuel Distribution, Ignition and Combustion in a Direct-Injection Spark-Ignition Engine," SAE 2005-01-3753.
8. Wyszynski, P., Aboagye, R., Stone, R., and Kalghatgi, G., "Combustion Imaging and Analysis in a Gasoline Direct Injection Engine," SAE 2004-01-0045.
9. Hung, D.L.S., Humphrey, W., Markle, L, Chmiel, D., Ospina, C., and Brado, F., "A Novel Transient Drop Sizing Technique for Investigating the Role of Gasoline Injector Sprays in Fuel Mixture Preparation," SAE 2004-01-1349.
10. Kim, M., Cho, H., and Min, K., "Computational and Optical Investigation of Liquid Fuel Film on the Cylinder Wall of an SI Engine," SAE 2003-01-1113.
11. Ghandhi, J. and Park, S., "Fuel Film Temperature and Thickness Measurements on the Piston Crown of a Direct-Injection, Spark-Ignition Engine," SAE 2005-01-0649.
12. Drake, M.C., and Fansler, T.D., "Piston Wall Film Formation and Evaporation in a Motored SIDI Engine: Comparison of High-Pressure Swirl and Multihole Injectors," ILASS Americas, 16th Annual Conference on Liquid Atomization and Spray Systems, Monterey, CA, May 2003.
13. Xu, M., Porter, D., Daniels, C., Panagos, G., Winkelman, J., and Munir, K., "Soft Spray Formation of a Low-Pressure High-Turbulence Fuel Injector for Direct Injection Gasoline Engines," SAE 2002-01-2746.
14. "Low Pressure Direct Injection Engine System," US Patent 6712037, 2003.
15. Hung, D.L.S., Mara, J.P., and Winkelman, J.R., "Spray Pattern Tailoring Flexibility of Multi-hole Injector for Direct Injection Spark Ignition Engines," ILASS Americas, 17th Annual Conference on Liquid Atomization and Spray Systems, Arlington, VA, May 2004.
16. Society of Automotive Engineers, "Gasoline Fuel Injector Spray Measurement and Characterization," *SAE J2715*, to be published by SAE.
17. Schock, H.J., Shen, Y., Timm, E., Stuecken, T., Fedewa, A., and Keller, P., "The Measurement and Control of Cyclic Variations of Flow in a Piston Cylinder Assembly," SAE 2003-01-1357.

DEFINITIONS, ACRONYMS, ABBREVIATIONS

BDC	Bottom Dead Center
BMEP	Brake Mean Effective Pressure
BTDC	Before Top Dead Center
CA	Crank Angle
CAD	Crank Angle Degree
CMOS	Complementary Metal Oxide Semiconductor
CCD	Charge Coupled Device
DI	Direct Injection
FII_{CA}	Fuel Impingement Index
IMEP	Indicated Mean Effective Pressure
LPDI	Low Pressure Direct Injection
MAP	Manifold Air Pressure
MTV	Molecular Tagging Velocimetry
PCM	Powertrain Control Module
PFI	Port Fuel Injection
PLIF	Planar Laser Induced Fluorescence
RPM	Revolution Per Minute
SOI	Start of Injection
SMD	Sauter Mean Diameter
WOT	Wide Open Throttle
WWMP	World Wide Mapping Point

CONTACT

David L.S. Hung, Ph.D.
Visteon Corporation
One Village Center Drive
Van Buren Township, MI 48111-5711, USA
Email: dhung1@visteon.com
Phone: 1-734-710-5445

Numerical Study of the Mixture Preparation Process in a 5.4L V8 GDI Engine

Yuxin Zhang and Harold Schock
Automotive Research Experiment Station (ARES)
Michigan State University East Lansing, MI 48823

David LS Hung*
Visteon Corporation
Van Buren Township, MI 48111

INTRODUCTION

A KIVA-3V based numerical simulation has been performed to study the in-cylinder flow field and fuel mixture formation process in a 5.4L V8 3-valve low pressure direct injection gasoline engine. GRIDGEN®, which is a commercial grid generator software program, was used to build a fine mesh for the single cylinder with over a half million computational cells configured in 50 blocks. To resolve the problems of fine moving mesh in KIVA-3V, a new rezoner methodology was implemented. Simulation results show that the effect of injector spray pattern, enabled by the use of multi-hole fuel injectors to achieve spray tailoring flexibility, is a key factor to improve the fuel charge homogeneity in the cylinder.

FLOWCHART OF KIVA-GRIDGEN SIMULATION

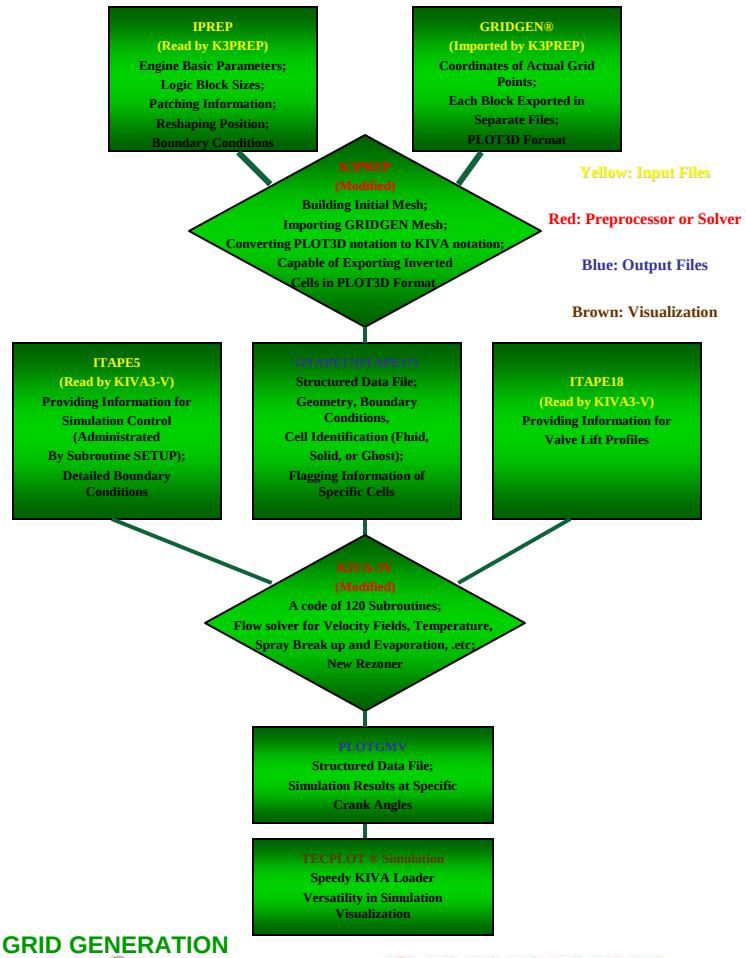

GRID GENERATION

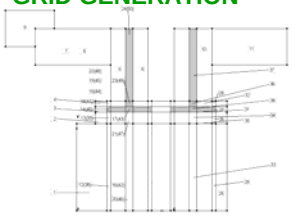
Engine block template


Blocks

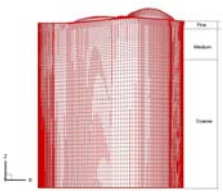
Mesh Density Variation in Z direction

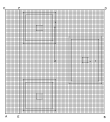
Logical mesh of block1

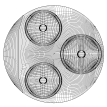
Actual mesh of block1

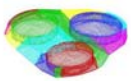
Block3 before joining


Block3 after joining

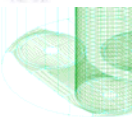
Mesh before local adjustment

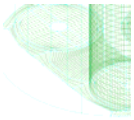
Mesh after local adjustment

SIMULATION RESULTS AND MTV * VALIDATION

Velocity field in the tumble plane (above: simulation, unit(cm/s); below: MTV, unit: m/s)

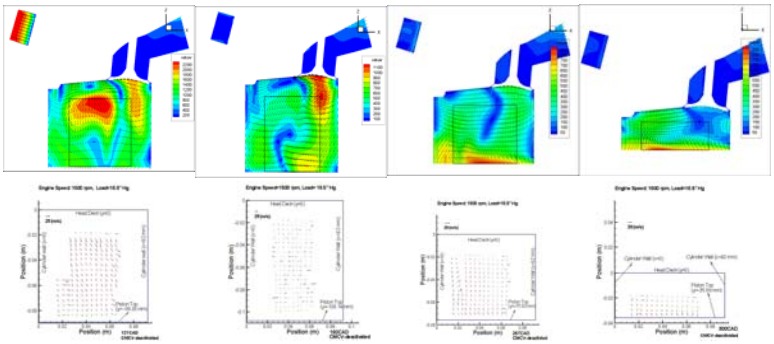
121CAD ATDC 192CAD ATDC 257CAD ATDC 300 CAD BTDC

Velocity field in the swirl plane (above: simulation, unit: cm/s; below: MTV, unit: m/s)

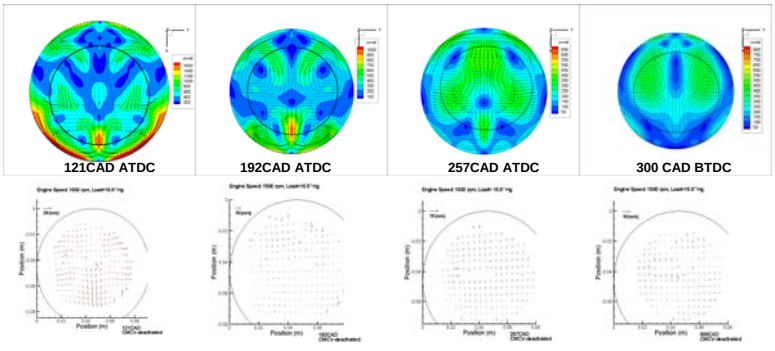
121CAD ATDC 192CAD ATDC 257CAD ATDC 300 CAD BTDC

Droplet distribution (Y direction)

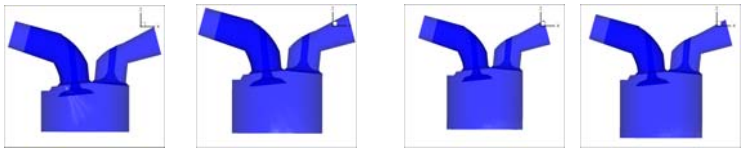
121CAD ATDC 192CAD ATDC 257CAD ATDC 300 CAD BTDC

Iso surface of ignitable region (equivalence ratio=1.0)

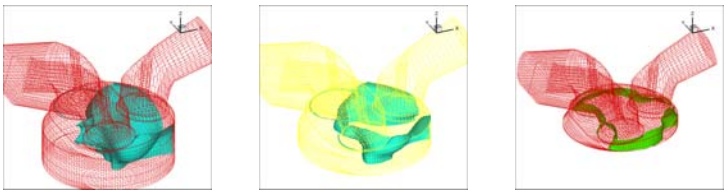
300CAD ATDC 330CAD ATDC 360CAD ATDC

SUMMARY/CONCLUSIONS

- The GRIDGEN-KIVA simulation of the internal combustion engine was more complicated than the commercial CFD 3-dimensional software analysis tools.
- The original $\kappa - \varepsilon$ model included in KIVA3V could not provide simulation accuracy like LES.
- Local mesh quality was carefully checked in the block building process to avoid the failing of convergence for specific cells, which results in negative internal energy or unrealistic temperature point. Considerable work was done to improve the spray region mesh quality.
- K3 prep was modified to detect and export inverted and non concaved cells in PLOT3D format.
- Reshaping was done in the GRIDGEN mesh building process.
- Local manual adjustments on specific cells were widely practiced.

*MTV: Molecular Tagging Velocimetry

ILASS Americas
20th Annual Conference on Liquid Atomization and Spray Systems
Chicago, USA, May 2007

MICHIGAN STATE UNIVERSITY

MECHANICAL ENGINEERING AT MICHIGAN STATE UNIVERSITY